Relationship between thermomechanical performances of bituminous binders and mixtures with focus on the binder-aggregate adhesion

Gabriel Orozco

N°d'ordre NNT : 2020LYSET013

THÈSE de DOCTORAT DE L'UNIVERSITÉ DE LYON

opérée au sein du

Laboratoire de Tribologie et Dynamique des Systèmes (UMR 5513)

à

l'Ecole Nationale des Travaux Publics de l'Etat

École Doctorale 162
Mécanique, Energétique, Génie civil et Acoustique

Spécialité / discipline de doctorat :
Génie civil

Soutenue publiquement le 23/10/2020
par :
Gabriel OROZCO

Relation entre les performances thermomécaniques des liants et des enrobés bitumineux avec prise en compte de l'adhésion liant-granulat

(Manuscrit)

Mme. MADEO Angela, Pr., INSA Lyon	Présidente
M. MASAD Eyad, Pr., Texas A&M University at Qatar	Rapporteur
M. CARTER Alan, Pr., ETS Montréal	Rapporteur
M. POUGET Simon, Dr., Eiffage Route	Examinateur
M. DI BENEDETTO Hervé, Pr., ENTPE	Directeur de thèse
M. SAUZEAT Cédric, HDR, ENTPE	Directeur de thèse

N° d'ordre NNT : 2020LYSET013

Ph.D. THESIS OF THE UNIVERSITY OF LYON

carried out at

Laboratoire de Tribologie et Dynamique des Systèmes (UMR 5513)

in

Ecole Nationale des Travaux Publics de l'Etat

École Doctorale 162
Mécanique, Energétique, Génie civil et Acoustique

Specialty:
Civil Engineering

Publicly defended on October 23rd, 2020
by
Gabriel OROZCO

Relationship between thermomechanical performances of bituminous binders and mixtures with focus on the binder-aggregate adhesion

(Manuscript)

Pr. MADEO Angela, INSA Lyon	President
Pr. MASAD Eyad, Texas A&M University at Qatar	Reviewer
Pr. CARTER Alan, ETS Montréal	Reviewer
Dr. POUGET Simon, Eiffage Infrastructures	Examiner
Pr. DI BENEDETTO Hervé, ENTPE	Supervisor
Pr. SAUZEAT Cédric, ENTPE	Supervisor

Table of contents

Figures

Tables

1 Introduction

Bituminous mixture is the most popular material to build the surface course, and very often the base course of pavement structures in industrialised countries. The bearing capacity and the durability of the pavement structures comes down to the strong binding capacity of the bituminous binder to hold the aggregate skeleton together. An important part of paving technologists' work is the laboratory characterisation of the bituminous mixtures to ensure *in-situ* good performances and cost-effective pavement design. The development and the standardisation of thermomechanical tests on bituminous mixtures in a rational, mechanistic approach started over six decades ago and is still being improved, as our understanding of their complex behaviour progresses. Many current developments are trying to figure out how the thermomechanical performances of mixtures (workability, stiffness, resistance to fatigue, resistance to rutting…etc.) arise from the following elements: the bitumen properties, the aggregate properties, the mix design parameters (granular stacking, void contents…) and the binder-aggregate interface properties. The rational approach consists of studying the influence of one particular aspect of one of these categories (for example varying the grading curve of the aggregate skeleton) without changing the other mixture features (in this example: same bitumen, same aggregate source and same mixture fabrication procedure). This exercise can be challenging and requires to innovate in test methods, especially regarding the role of binder-aggregate interface; indeed, how can someone modify the binder-aggregate adhesion in a mixture without changing the nature of its constituent materials? Eventually, the identification of the underlying mechanisms and the key parameters that ultimately determine the performances of mixtures is one of the biggest challenge of paving technologists, as it would provide powerful predictive tools to optimise costs and resource consumption.

This thesis problematic was to identify the determining factors of three of the most important thermomechanical properties of mixtures: the linear viscoelastic (LVE) behaviour, the resistance to fatigue and in a less important manner the water sensitivity. Two main objectives were established.

- First Objective: Understand the influence of binder and aggregate properties on mixtures. In that scope, the relationship between the thermomechanical performances of mixtures and of their constituent bitumen, studied with classical and advanced tests, constituted the main focus of this study.
- Second Objective: Develop experimental techniques to characterise the binder-aggregate interface, and ultimately evaluate its role on the thermomechanical performances of the bituminous mixtures.

This manuscript is decomposed in eight chapters. Following this introduction, Chapter 2 consisted in a literature review about the thermomechanical characterisation of bituminous materials and the bitumen-aggregate adhesion. In Chapter 3, experimental devices and tested materials are introduced. In Chapters 4, 5, 6 and 7, four different research campaigns are presented and analysed (one per chapter). Although often related to each other, each campaign was constructed independently with their own set of objectives, experimental plans, results and conclusions. Campaign I investigated the influence of bitumen and aggregate on the bituminous mixture thermomechanical performances: Stiffness, resistance to fatigue and water sensitivity. Campaign II focused on characterising and comparing the behaviours in LVE domain and during Load and Rest Periods (LRP) of bitumens and bituminous mastics made with glass beads. In Campaign III, a new rheological test to characterize the bitumen interface with bitumen thin film was developed and the first experimental results were presented. Campaign IV studied the binder-aggregate adhesion by exploring the influence of aggregate surface treatment (with silanes) on the thermomechanical performances of bituminous mastics and mixtures. From the general perspective, Campaign I and II were designed to complete the first objective of this thesis, whereas Campaign III and IV addressed the second objective. Eventually, Chapter 8 summarises the conclusions of the four campaigns and draw some perspectives that arose from this work.

2 Literature review

2.1 Overview on bituminous materials

2.1.1 Bitumen

2.1.1.1 Definition

Bitumen is defined by the Permanent International Association of Road Congresses (PIARC 2019) as a "Very viscous or nearly solid, virtually non-volatile, adhesive and waterproofing organic material derived from crude petroleum or present in natural asphalt, which is completely or nearly completely soluble in toluene". It consists of the heaviest part of crude oil. Bitumen is also referred to as "asphalt" in American English literature.

2.1.1.2 Origin and production

Bitumen can be found at earth surface in oil seepage or trapped in rock asphalt. However, most bitumens are manufactured from crude oil through a vacuum distillation process (Read and Whiteoak 2003) schematized in Figure 2-1. Crude oil is first heated at 300 to 350°C and distilled at atmospheric pressure, where the lighter parts are separated to produce gases (propane, butane…) and liquid fuels (naphtha, kerosene…). The atmospheric residue is then heated again and distilled in a vacuum column at 1/10 bar, where gas oil and other distillates such as paraffin are collected. The residue of this second distillation is named "straight run bitumen" that can be post-processed through air-blowing or de-asphalting to achieve specific composition before storage. Not all crude oil may be used to produce bitumen and bitumens present different properties depending on the origin of crude oil.

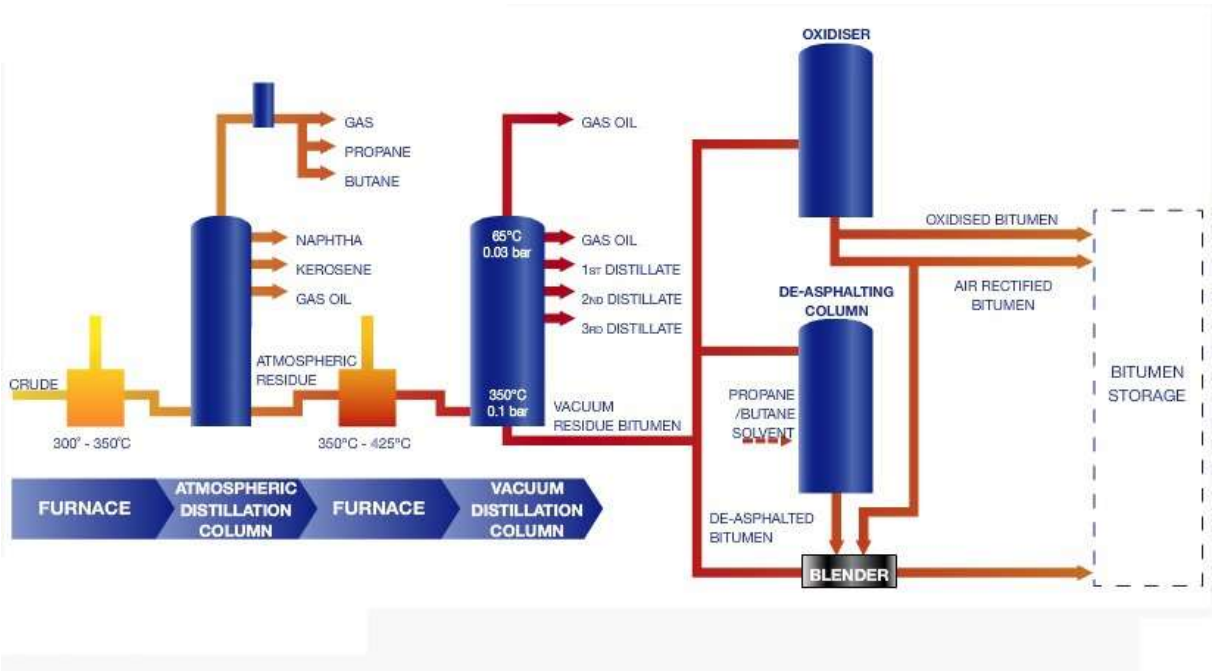

Figure 2-1 *Schematic representation of bitumen production process* (cypraegean-neftegaz Ltd 2020)

2.1.1.3 Anthropic use of bitumen

The oldest evidence of anthropic use of bitumen is from the middle Palaeolithic era, as hafting material for cutting or piercing tools (Boëda, Connan, and Muhesen 2002). Bitumen has been significantly exploited during the Neolithic era: as mortar in construction and art or as sealant to waterproof vessels, rooftops, jars, etc., and was a valuable traded resource through all Near East region (Connan and Van de Velde 2010). Although bitumen has already served as binder in road materials in the Ancient era, its extensive use in pavement started in early 19th Century in Europe. Vacuum distillation of crude oil, developed in 1910, provided an additional source to natural bitumen quarries (Krchma and Gagle 1974). The fast-increasing global demand of oil since the beginning of the 20th Century led to a simultaneously growing disposal of residue. The combined availability of large quantity and interesting thermomechanical properties of bitumen allowed paving technologists to make bituminous materials predominant for road surface construction. The Asphalt Institute in the U.S. and Eurobitume estimated the world production of bitumen in 2015 around 87Mtons, of which approximately 85% were indeed used as road material (10% for roofing, 5% for various purposes) (Asphalt Institute and Eurobitume 2015). The U.S. paved roads network, the world's longest, for a total length of 2.7 million miles, is indeed covered at 93% with bituminous mixture (Federal Highway Administration 2014).

2.1.1.4 Bitumen composition and structure

Bitumen is a mix of various molecules, mainly composed of Carbon (82-88%), Hydrogen (8-11%), Sulphur (0-6%), Oxygen (0-1.5%) and Nitrogen (0-1%), and contains traces of metallic elements such as Aluminium, Iron, Nickel, etc. (Corté and Di Benedetto 2004). The huge variety of composing molecules makes the complete molecular identification for one given bitumen impossible. Practically, chemical compounds are separated in several groups. The most common technique, schematized in Figure 2-2, consists of separating the "SARA" fractions, i.e. Saturates, Aromatics, Resins and Asphaltenes. Bitumen is first dissolved in *n*-heptane. The asphaltenes form the insoluble solid residue of this dissolution, whereas the soluble part, the maltenes, are filtered and then separated using chromatography. Saturates, aromatics and resins are eluted with different solvents. Read and Whiteoak (Read and Whiteoak 2003) remind that these fractions have different properties and that their concentration can vary a lot between bitumens:

- Saturates (constituting 5 to 20% of total bitumen mass) are non-polar, liquid, viscous oils, mainly composed of aliphatic hydrocarbons chains and saturated ring systems.
- Aromatics (40 to 60%) are also non-polar viscous liquids, with a dominating proportion of unsaturated ring systems.
- Resins (13 to 25%) are polar, semi-solid or solid. Their high polarity confers adhesiveness to the bitumen.
- Asphaltenes (5% to 25%) are insoluble, polar, amorphous solids. Their concentration strongly influences the microstructure and the rheology of bitumen.

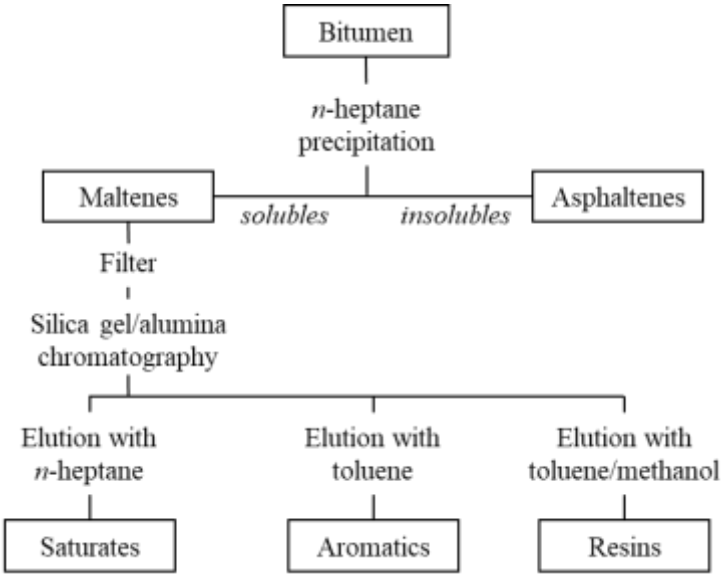

Figure 2-2 *Schematic representation of SARA fractions separation procedure, adapted from* (Corté and Di Benedetto 2004)

Although SARA fractions are only defined than by their separation process, with overlap between groups, these categories fit well in the most consensual structure description of bitumen: the colloidal model (Lesueur 2009); The asphaltenes forms the solid micelles and the maltenes composes the liquid viscous matrix. Two potential microstructures emerge from this description (see Figure 2-3):

- A sol-type structure, with low asphaltenes concentration, disconnected from eachother.
- A gel-type structure, with high asphaltenes concentration, typically in air-blown bitumen, creating an internal structure.

The structure of bitumen is greatly influenced by its temperature. The significant change of structure at the Glass Transition Temperature T_g (varying from -40 to -10°C) is well known and has been extensively studied in the literature (Kriz, Stastna, and Zanzotto 2008). Moreover, Claudy and co-workers (Claudy et al. 1992) showed by Thermomicroscopy and Diffenrential Scanning Calorimetry techniques that wax cristalisation occurs in a large range of temperature from T_g up to 90°C. These microstructural changes explain the extreme variability of the rheological behaviour of bitumen as the temperature varies.

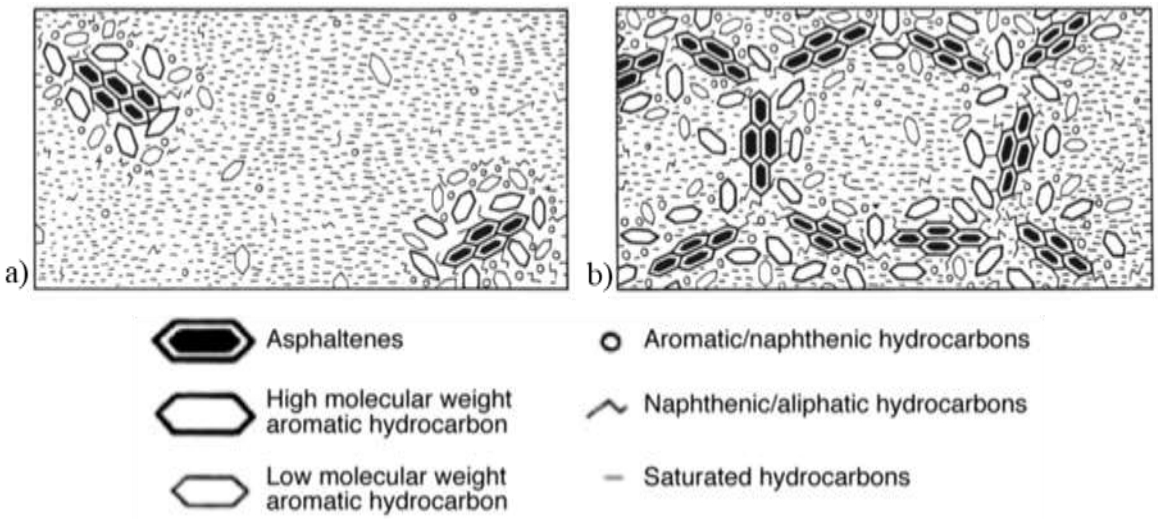

Figure 2-3 *Schematic representation of a) sol-type bitumen, b) gel-type bitumen*

2.1.1.5 Classical tests and classification of bitumen

In an effort to classify bitumen for practical uses, various tests have been developed. The European approaches differs from the North American one.

European countries adopted a commercial standardisation of bitumen based upon the Needle Penetration test (AFNOR 2018a). It consists of measuring the penetration depth, *pen* in 10^{-1}mm, of a loaded needle into a bitumen cup at 25°C. According to the *pen* value, bitumens are sorted in different categories, named Penetration Grade, e.g. 35/50, 50/70 or 160/220. This test gives an indication of their consistency at ambient temperature, "stiff" for low Grades, "soft" for high Grades. The Temperature of softening point or "Ring and Ball" test (AFNOR 2018b) determines a temperature T_{RB} of equivalent plastic deformability between bitumens. Based on *pen* and T_{RB} values of a vast quantity of bitumens, Pfeiffer and Van Doormaal (Pfeiffer and Van Doormaal 1936) proposed a Penetration Index *PI*, which indicates the thermal sensitivity of bitumen. This index is calculated according to Equation (2.1). Bitumens with high temperature susceptibility exhibit *PI* values of around -3, whereas less temperature susceptible bitumens around 7. The Fraas breaking point test (AFNOR 2018c) provides the low temperature behaviour of a bending bitumen film. In addition to all these empirical tests, the determination of kinematic viscosity at 60°C and 135°C (AFNOR 2014) gives precious rheological information.

$$PI = \frac{1952 - 500 \log_{10} pen - 20 T_{RB}}{50 \log_{10} pen - T_{RB} - 120} \tag{2.1}$$

The American Strategic Highway Research Program (SHRP) led to the SUPERPAVE Performance Grading (PG) system (AASHTO M 320 2017; SHRP 1994) in the early 1990s. Following a series of different thermomechanical tests (AASHTO T 313 2019; AASHTO T 314 2012; AASHTO T 315 2019) on original and laboratory aged bitumen, the PG specifies two extreme service temperatures for a bituminous mixture composed of the tested bitumen.

2.1.1.6 Polymer-modified Bitumen

The globally increasing traffic during the second half of the 20th Century pushed paving technologists to enhance the mechanic performances and durability of bituminous materials (Polacco et al. 2015). Polymer-modified bitumen (PmB) were developed to tackle these issues. A standard PmB is a mix of pure bitumen and polymer (3 to 7% of total weight), composed of either elastomers (e.g. Styrene-Butadiene-Styrene, SBS), plastomers (e.g. Ethylene-Vinyl Acetate, EVA), or a combination of these categories.

Polymer modification is well known to improve high temperature thermomechanical performance of bitumen (Brulé, Brion, and Tanguy 1988; Collins et al. 1991) and resistance to ageing (McNally 2011; Singh and Kumar 2019). Studies on the effects of polymer modification on low-temperature performance of bitumen showed both significant (F. Zhang, Yu, and Wu 2010) or negligible (X. Lu, Isacsson, and Ekblad 2003) improvement.

New tests to characterise PmB have been introduced, such as the determination of the elastic recovery *ER* (%). It consists of measuring the percentage of recovered deformation of a standardised bitumen sample, stretched and then cut at a precise level using a ductilometer apparatus (AFNOR 2017b). While pure bitumens usually exhibit purely viscous flow (*ER*≈0%), PmB can show important elastic recovery (up to 90%).

Concerning mixtures performances using PmB, many sources point out a better resistances to fatigue and rutting (McNally 2011; Hassan Baaj, Di Benedetto, and Chaverot 2005; Qabur 2018; Ahmed et al. 2019), which are generally attributed to the change of bitumen rheology. The mixture resistance to moisture damage could also be enhanced by polymer modification (Kok and Yilmaz 2009; Al-Humeidawi, Aodah, and Hameed 2016).

2.1.2 Bituminous mixtures

A bituminous mixture is a mix of ≈95% road aggregates (in total weight), bonded together with ≈5% bitumen (Corté and Di Benedetto 2004).

2.1.2.1 Aggregates

Road aggregates are sands, gravel or crushed rocks of various petrographic origin. They are separated by size in homogeneous granular fractions. Paving technologists usually design the granular skeleton of a bituminous mixture from these fractions to fulfil specific performances. Each fraction is characterized by a minimal diameter *d* and a maximal diameter *D* corresponding to the size of the sieves used during Particle Size Distribution analysis (AFNOR 2012a). A "grading curve" represents the evolution of the passing mass percentage of aggregates with the sieve size. To maximize aggregate skeleton density, all fractions have to be represented; the grading curve is labelled "continuous", or "well graded". EME ("Enrobé à Module Elevé", high-modulus bituminous mixture) are typically designed with continuous grading curves. On the other hand, "poorly graded" or "gap-graded" curves show one or several discontinuities. It is favoured in Stone Mastic Asphalt (SMA) (AFNOR 2006) or GB5® (Olard 2012).

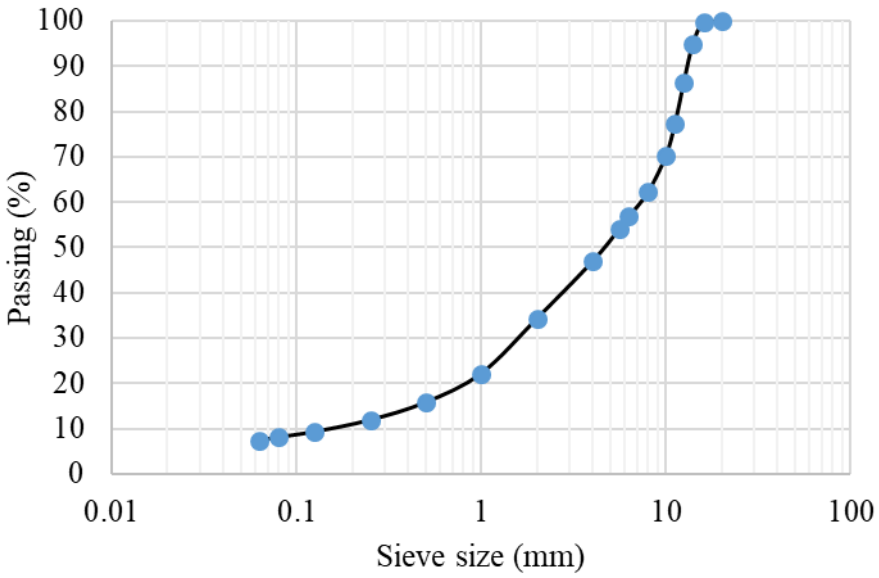

Figure 2-4 *Continuous aggregate grading curve of an EME. Data provided by Eiffage*

To ensure important mixture performances such as stiffness, resistances to rutting, moisture, ravelling…, road aggregates have to meet some requirements regarding their geometrical and physical properties such as:

- Shape (AFNOR 2008a; 2012b)
- Angularity (AFNOR 2005)
- Resistance to wear (AFNOR 2011)
- Resistance to fragmentation (AFNOR 2010)
- Assessment of fines (AFNOR 2013a; 2015)

2.1.2.2 Filler

The smallest particles of an aggregate skeleton constitutes the filler, namely the fractions that fill the gaps between larger aggregates. The size criterion can vary from different sources, but European paving technologists consider all particles passing the 0.063mm sieve as filler (AFNOR 2008b). The filler usually represents around 7% of the aggregate skeleton (Di Benedetto and Corté 2005), although this value can vary a lot (2% to 12% (Lesueur 2009)).

2.1.2.3 Bituminous mastics

Mastic is the mix of bitumen and filler. The main role of mastic is to reduce the average thickness of bitumen layer between two aggregates and to increase the density of granular skeleton as well as the stiffness of the mixture. The mastic can be considered as an homogeneous material at intermediate scale (>500µm) between bitumen scale (≈10nm for biggest asphaltenes molecules, ≈10µm for waxes crystal structures (Lesueur 2009)) and mixture scale (>5-10cm). Many studies emphasise the importance of mastic properties in mixtures performance such as the resistances to fatigue, permanent deformation or moisture damage (Khandal, Lynn, and Parker Jr. 1998) (Chaturabong and Bahia 2018).

2.1.2.4 Key parameters for bituminous mixtures mix design

Paving technologists have to adapt to the variability of the bitumens and aggregates at their disposal. Several parameters can be used to optimize mix design and achieve expected mixture performances/requirements:

- The grading curve (Section 2.1.2.1).

- The binder content *BC* (%). It is defined as the ratio of bitumen mass to the total mass of the mixture, in percent. Some sources also uses the "external" binder content BC_{ext}, i.e. the ratio of bitumen mass to the total dry aggregate mass, in percent. All mixtures require a minimal binder content to ensure complete coating of aggregates. Additionally, a *Module de Richesse* ("Richness Modulus") *K*, based on specific surface area of the aggregate skeleton and external binder content, has been developed to compare the average thickness of bitumen film around aggregates (Delorme, de la Roche, and Wendling 2007). It could be calculated as explained in Equations (2.2) to (2.4)

$$K = \frac{BC_{ext}}{\alpha \sqrt[5]{\Sigma}} \tag{2.2}$$

$$\Sigma = \frac{0{,}25\,\mathrm{G} + 2{,}3\,\mathrm{S} + 12\,\mathrm{s} + 150\,\mathrm{f}}{100} \tag{2.3}$$

with *G* the proportion of aggregate particles bigger than 6.3mm,
S between 6.3mm and 0.250mm
s between 0.250mm and 0.063mm
f smaller than 0.063

$$\alpha = \frac{2.65}{\rho_{agg}} \tag{2.4}$$

with ρ_{agg} the density of aggregate

Many studies showed the crucial role of the binder content (Pell and Taylor 1962; Epps and Monismith 1969; Brennan, Lohan, and Golden 1990; Harvey and Tsai 1996) on mixtures performances. Epps and Monismith (Epps and Monismith 1969) established for Californian bituminous mixtures that resistance to fatigue increases with binder content until an optimum ($BC \approx 7\%$). This optimum may be dependent of the aggregate skeleton. Moutier (Moutier 1992), cited by Di Benedetto and Corté (Di Benedetto and Corté 2005), confirmed these results on French mixtures. He also found a similar trend for mixture stiffness (complex modulus), maximised at a certain optimum of binder content.

- Air voids content *VC* (% of compacted mixture volume). It is not a proper mix design parameter, as it results of the combination of factors (materials, grading curve, mixture production mode and compaction procedure), but remains critical for mix design and plays an important role in mixture performances. A lower void content yields systematically to a higher stiffness (Bazin and Saunier 1967; H. Di Benedetto and de la Roche 1998). The role of void content regarding fatigue life depends on the density of the mixture. Harvey and co-workers (Harvey and Tsai 1996; Harvey et al. 1995) showed that an increase of the external void content from 1-3% to 7-8% can significantly diminish the fatigue life (up to 200%) in. To put in perspective, this effect is of the same order of magnitude as the decrease of fatigue life with a loss of 1% of binder content (6% to 5%) in this study.

2.2 Road pavements

2.2.1 General description

The role of road pavement is to provide a safe, durable and efficient structure of transportation. Three type of structures are generally used: rigid, semi-rigid, and flexible pavements. A rigid pavement is composed of a thick layer of concrete (reinforced or slabs) which single-handedly distributes the traffic loads to the subgrade. On the opposite, flexible pavement is a pile of different bound and unbound layers (Figure 2-5). The natural subgrade supports the compacted mineral subgrade layer. The subbase course is either made of aggregates, either unbound or treated with hydraulic binder. In roadways and highways, the base course is made of bituminous mixture, where a high modulus and a good resistance to fatigue are expected. Finally, the last course is composed a bituminous wearing course at surface, ensuring user comfort and safety as well as specific water sealing properties, and of an optional binder course.

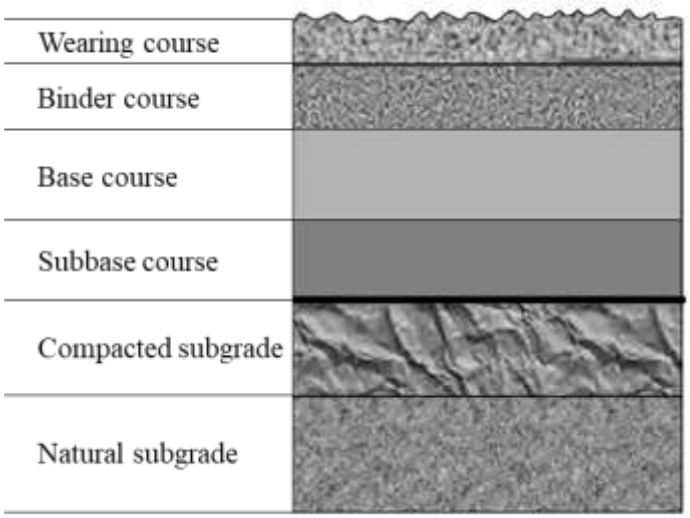

Figure 2-5 *Schematic view of flexible pavement layers*

A semi-rigid pavement is a combination of rigid and flexible pavements, typically a bituminous wearing course on top of a concrete base course.

2.2.2 Thermomechanical loads on flexible pavement structure

Traffic and temperature variations are the two main sources of thermomechanical load applied to pavement structure. Under a vehicle load, successive bituminous layers are subjected to a combination of flexion and vertical compression (Figure 2-6). Although the exact stress and strain distribution is complex to characterise (Di Benedetto and Corté 2005), the paving technologists following the French method use a simplified model of infinite linear elastic isotropic layers developed by Burmister (Burmister 1945), since the observed in-situ strains barely surpasses 10^{-4}. This model only requires the Young's moduli E and the Poisson's ratio v of all layers and the interface conditions (perfectly bound, or perfectly sliding).

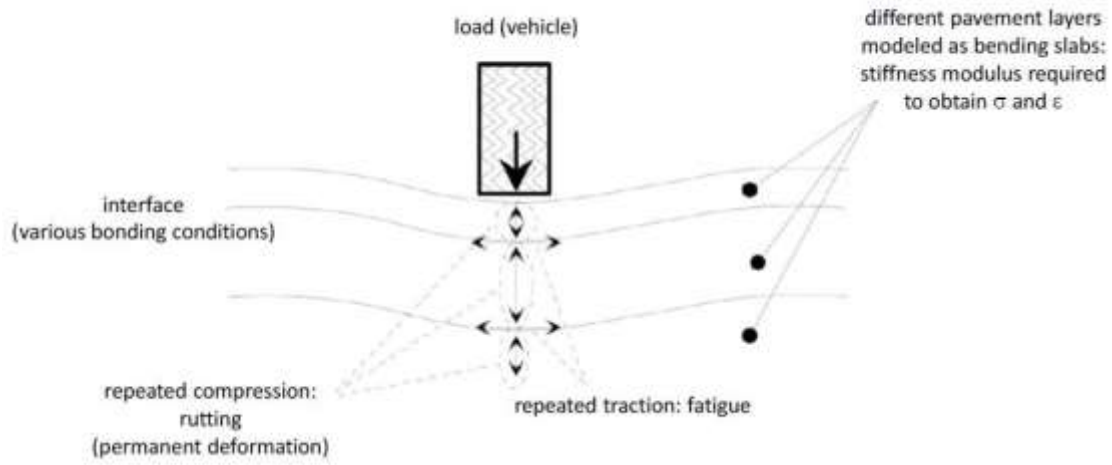

Figure 2-6 *Schematic representation of a flexible pavement response subjected to traffic load (Mangiafico 2014)*

Climate induces important temperature variations within the pavement structure (Figure 2-7). On a daily basis, bituminous layers can experience oscillation of tens of centigrade degrees, mainly due to a high solar radiation absorption (albedo of bituminous mixture surface ranges from 0.04 to 0.16) (Minhoto et al. 2005). With a typical coefficient of 1-dimensional thermal contraction of approximately 3.10^{-5} per centigrade degree (Islam and Tarefder 2015), thermally induced strains are far from being negligible. Additionally, it should be noted that temperature variations in bituminous materials lead to significant thermomechanical behaviour changes, such as for stiffness. This susceptibility to temperature will be addressed in section 2.3

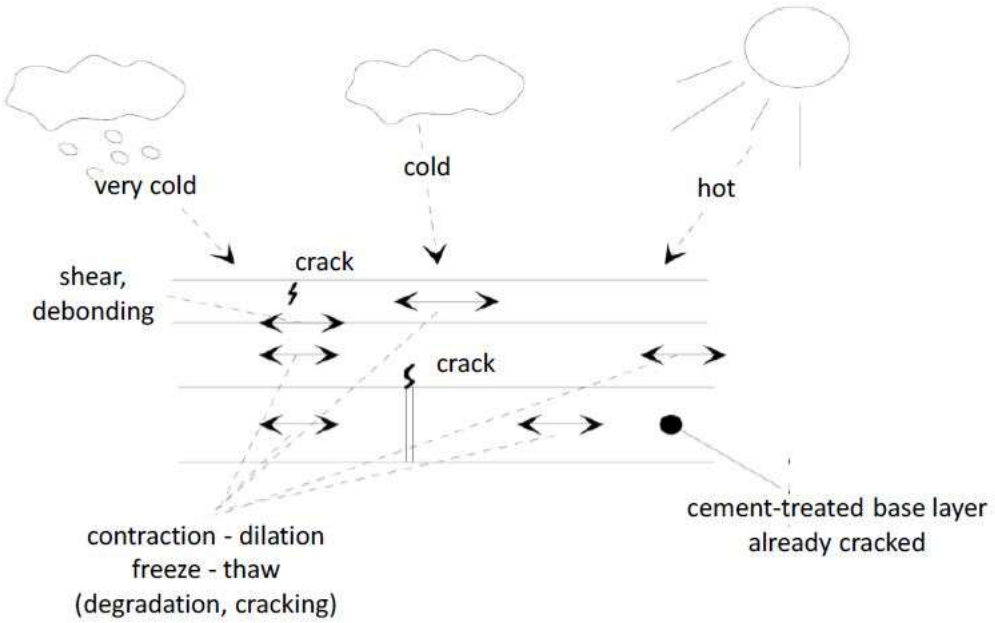

Figure 2-7 *Schematic representation of a flexible pavement response subjected to temperature variation (Mangiafico 2014)*

2.2.3 Main distresses in flexible pavement bituminous layers

2.2.3.1 Rutting

Rutting is the result of permanent deformation under repeated traffic loading (Figure 2-8), which increase with temperature. It affects user's comfort and in the worst case, its safety (generating bumps and puddles). The rutting potential of a bituminous pavement layer is both external (traffic flow, driving speed, tyre pressure, temperature…) and internal: inherent to the constituent bituminous mixture. The rutting potential of a mixture is usually based on empirical test simulating repeated traffic load (AFNOR 2013c; AASHTO T 324 2019). The evaluation of intrinsic permanent deformation potential of mixture using homogeneous thermomechanical tests has also been proposed. These tests do not recreate the complex stress distribution patterns caused by a passing loaded wheel, but intend to develop and calibrate rheological models taking into account viscoplastic behaviour of such materials (Di Benedetto and Corté 2005). Models could be used to analyse with numerical tools the pavement behaviour.

Figure 2-8 *Example of rutting by a trolleybus* (http://transporturbain.canalblog.com/ 2019)

2.2.3.2 Fatigue cracking

Fatigue is defined as the loss of material integrity under a large number of applied cycles of "limited" load amplitude. Repeated traction due to layer flexion (Figure 2-6) causes the formation of microscopic cracks that eventually coalesce into macroscopic cracks, synonym of material failure. "Crocodile cracking" of the wearing course (Figure 2-9) is a typical result of fatigue cracking (Miller and Bellinger 2014). Since the study of fatigue in bituminous materials is central in this thesis, a detailed description of this complex phenomenon and of its evaluation is given in section 2.3.4

Figure 2-9 *Example of severe fatigue cracking* (Miller and Bellinger 2014)

2.2.3.3 Thermal cracking

As explained previously in Section 2.2.2, thermal dilatation-contraction cycles can lead to significant strains. The corresponding stresses depend on the material behaviour. In case of elastic, temperature-independent behaviour such as for concrete, contraction joints with potential dowel bars are necessary. On the opposite, the viscoelastic nature of bituminous materials provides a valuable stress relaxation ability (discussed in Section 2.3). However, when temperature falls, the bitumen rigidifies until reaching its glass transition and the resulting mixture similarly becomes more elastic and stiffer (the storage modulus usually increases above 30GPa) (Di Benedetto, Olard, et al. 2004). This decreasing relaxation capability, coupled with this increasing thermal stresses generation due to higher stiffness, results in thermal cracking. This thermomechanical phenomenon can be the principal cause of pavement distress in cold regions (Aschenbrener 1995b). Paving technologists proposed a simulation test of thermal cracking to evaluate and compare the performances between mixtures in laboratory: the Thermal Stress Restrained Specimen Test (TSRST) (AFNOR 2013d). It consists of a cylindrical mixture specimen with restrained longitudinal deformation (ensured with a press system) submitted to a certain negative temperature ramp until failure.

2.2.3.4 Distresses caused by moisture damage

Moisture damage is the loss of integrity of a material in presence of water (Caro et al. 2008a). Although bitumen is hydrophobic and insoluble in water, moisture in bituminous mixtures can migrate at the bitumen-aggregate interface and cause a loss of adhesion, also named “stripping”. Pavement distress such as ravelling or shelling are possible outcomes of moisture damage. In more severe cases, it synergises with fatigue cracking, accelerating the pavement deterioration. Since the study of binder-aggregate adhesion is central in this thesis, a detailed description of moisture susceptibility of bituminous mixtures and of its evaluation is given in section 2.4.3

2.3 Thermomechanical characterisation of bituminous materials

The thermomechanical characterisation of bituminous materials presented in this section is based on continuum mechanics. Indeed, bitumen, mastic and mixtures can be considered continuous and homogeneous at a macroscopic scale (Di Benedetto and Corté 2005).

2.3.1 Thermomechanical behaviour domains of bituminous materials

2.3.1.1 Bitumen

Bitumen behaves in very different ways depending on three factors:

- Temperature T. It determines the microstructure of bitumen (see Section 2.1.1.4). Under its transition glass temperature ($T_g \approx$ -20°C), bitumen exhibits a solid, elastic state. Over its wax crystallisation temperature ($\approx$ 90°C), bitumen shows a purely viscous state. At intermediate temperatures, the mechanical behaviour of bitumen is viscoelastic.
- Strain amplitude ε_0. Strain dependence of bitumen viscoelastic behaviour at low temperature has been established (Airey, Rahimzadeh, and Collop 2003; Babadopulos et al. 2019); nonlinearity appears over a certain strain amplitude limit.
- Number of cycle N in case of cyclic loading. Repeated cycles can induce fatigue cracking or permanent deformation depending on the loading mode.

The typical domains of mechanical behaviour of bitumen are displayed in Figure 2-10 and Figure 2-11. It should be emphasised that the domains limits are only indications of the order of magnitude, and that the shift from a domain to another is rather continuous than abrupt (e.g. for the linear and nonlinear domain (Q. T. Nguyen, Di Benedetto, and Sauzeat 2014))

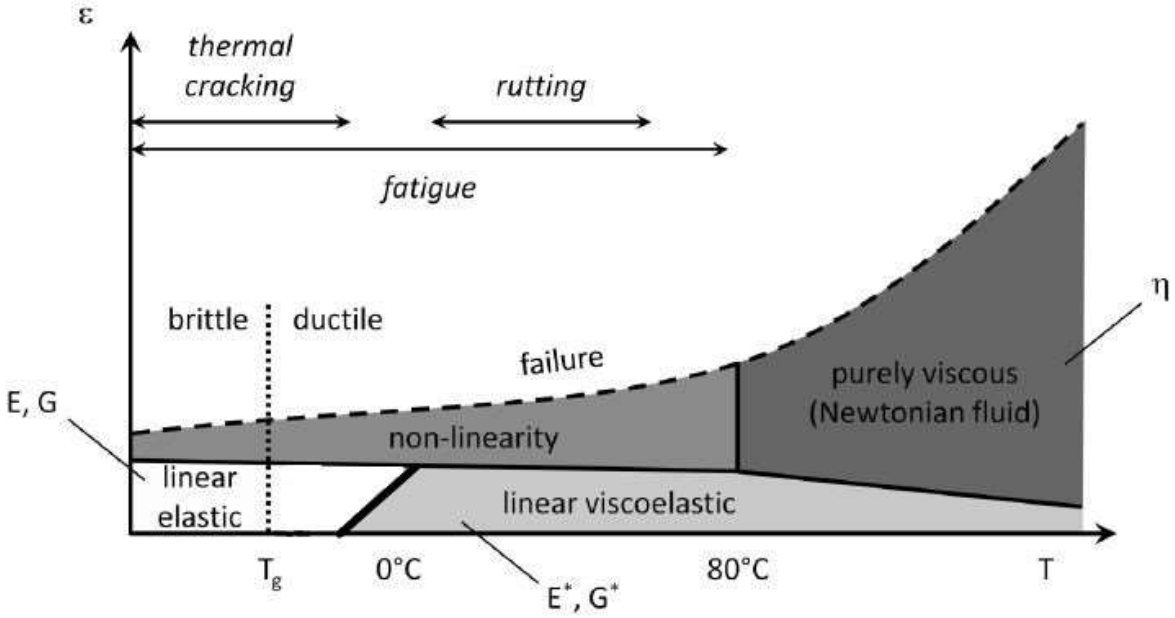

Figure 2-10 *Typical mechanical behaviour domains of bitumen as a function of temperature and strain amplitude, adapted from Mangiafico* (Salvatore Mangiafico 2014)

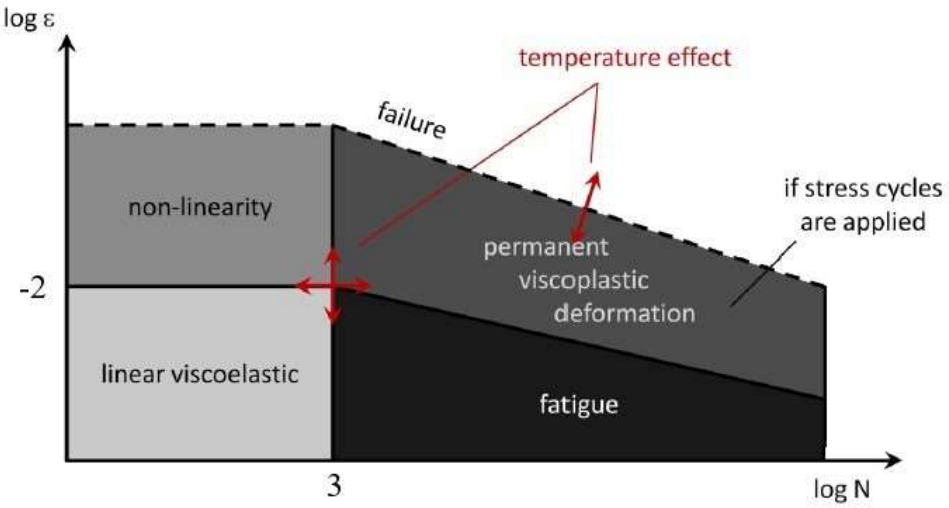

Figure 2-11 *Typical mechanical behaviour domains of bitumen at intermediate temperature as a function of number of cycles and strain amplitude, adapted from Mangiafico* (Salvatore Mangiafico 2014)

2.3.1.2 Bituminous mixture

The mechanical behaviour of mixtures can be separated in four domains, depending on strain amplitude ε_0 and number of applied cycle N (Figure 2-12). for a small number of cycles at small strain amplitude, bituminous mixtures can be considered linear viscoelastic. As for bitumen, nonlinearity appears at a certain level of strain amplitude (discussed in section 2.3.3). The fatigue domain is usually observed for $N > 10^4$ at moderate strain amplitude. In case of cyclic stress loadings generating moderate to important strains, mixtures are susceptible to rutting.

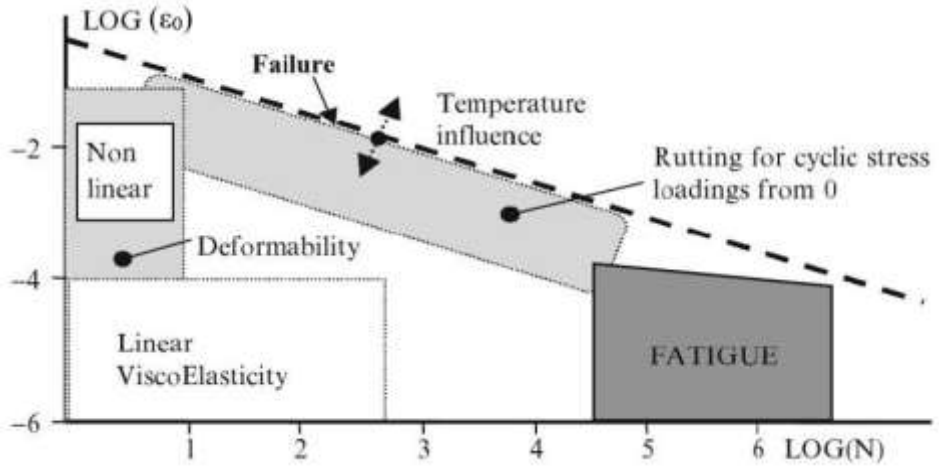

Figure 2-12 *Typical mechanical behaviour domains of bituminous mixtures* (Di Benedetto and Corté 2005)

The following sections 2.3.2, 2.3.3 and 2.3.4 elaborate respectively on linear viscoelasticity, nonlinear viscoelasticity and fatigue domains.

2.3.2 Small strain amplitude load domain: Linear viscoelasticity (LVE)

2.3.2.1 Theory of unidimensional viscoelasticity

The concept of viscoelasticity has been developed to characterise the behaviour of numerous materials that can simultaneously exhibit energy storage (elastic response) and energy dissipation over time (viscous flow response) when subjected to a deformation. Indeed, many polymers present these two fundamental characteristics, and the ubiquitous use of these materials in modern industry pushed for a practical description of viscoelasticity (R. M. Christensen 1982). Notwithstanding the deep microscopic (usually molecular) origin of such mechanical behaviour, physicists invented a theory of viscoelasticity in the framework of continuum mechanics that has been proven relevant over the 20th Century, including for bituminous materials. Therefore, the following sections introduce this theory in its unidimensional form, with a particular attention to the linear viscoelasticity.

2.3.2.1.1 Creep compliance function

Considering an unloaded material submitted to an instantaneous stress step of σ_0 at t_0; The stress $\sigma(t)$ is then a Heaviside function, delayed of t_0 as expressed in Equation (2.5). The creep compliance function $J(t_0, t, \sigma_0)$ is defined as the strain response $\varepsilon(t)$ divided by stress amplitude (Equation (2.6)). This response to a creep test illustrates the relationship between strain and the history of stress for viscoelastic materials, whereas in the elastic case only the instantaneous stress value at *t* is required.

$$\sigma(t) = \sigma_0 Y(t - t_0) = \sigma_0 Y_{t_0}(t) \quad (2.5)$$

$$\varepsilon(t) = \sigma_0 J(t_0, t, \sigma_0) \quad (2.6)$$

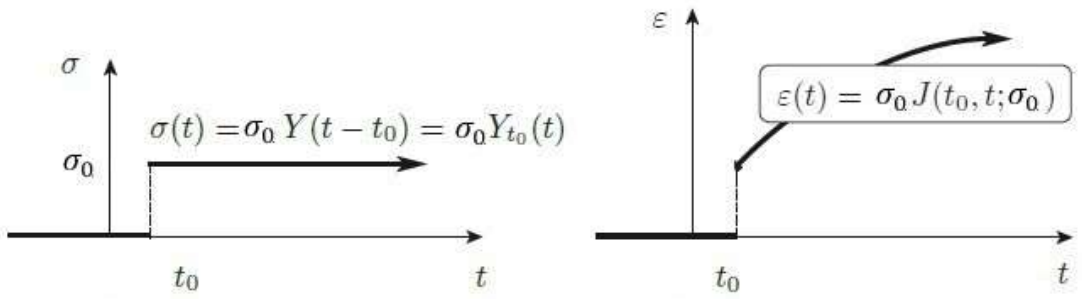

Figure 2-13 *Creep test (adapted from Salençon* (Salençon 2009)*)*

2.3.2.1.2 Stress relaxation function

Similarly, the stress relaxation function $R(t_0, t, \varepsilon_0)$ is defined as the stress response to a strain step function of ε_0 at t_0, divided by the amplitude as expressed in Equations (2.7) and (2.8).

$$\varepsilon(t) = \varepsilon_0 Y_{t_0}(t) \tag{2.7}$$

$$\sigma(t) = \varepsilon_0 R(t_0, t, \varepsilon_0) \tag{2.8}$$

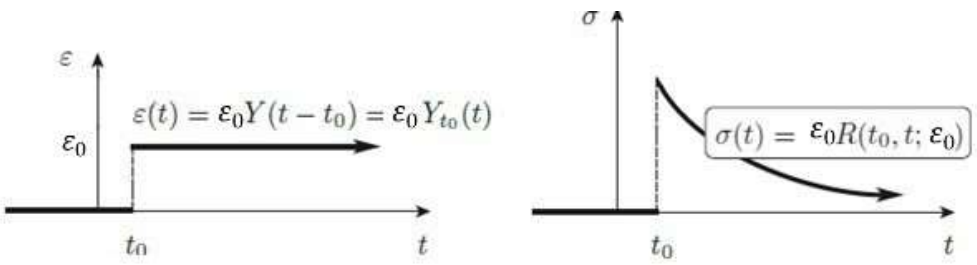

Figure 2-14 *Relaxation test*

2.3.2.1.3 Boltzmann's superposition principle

During the 19th Century, physicists (including great contributors like Maxwell, Boltzmann or Kelvin) had performed many mechanical tests on viscoelastic materials such as glasses or rubbers, with various history of loading in small perturbations framework (McCrum, Buckley, and Bucknall 1997). Experimental observations led to Boltzmann's superposition principle: the response to the superposition of loading is equal to the the sum of the responses of each separated loading. Materials that present such behaviour are called "linear viscoelastic" (LVE), or less frequently "Boltzmannian". From a mathematical point of view, this principle postulates the linearity of the functional that link the histories of strain and stress (Salençon 2009). This implies that both the creep compliance function and the stress relaxation function are independent of loading amplitude. Indeed, for any σ_0 and t_0, considering a creep test of amplitude $k\sigma_0$ (k being any real number $\neq 0$) at t_0, the strain response is expressed in Equation (2.9), and in Equation (2.10) according to the superposition principle. The creep compliance function J is therefore independent of stress amplitude, as expressed in Equation (2.11). The same result applies for the relaxation function R.

$$\varepsilon'(t) = k\sigma_0 J(t_0, t, k\sigma_0) \tag{2.9}$$

$$\varepsilon'(t) = k\varepsilon(t) = k\sigma_0 J(t_0, t, \sigma_0) \tag{2.10}$$

$$J = J(t_0, t) \tag{2.11}$$

These fundamental properties permit the expression of the strain response as a function of the stress history, and of the stress response as a function of the strain history. With the reasonable hypothesis of differential continuity almost everywhere for both stress and strain functions, any stress loading history can be interpreted as an addition of successive infinitesimal step functions of amplitude $d\sigma$ and instantaneous step $[\![\sigma]\!]_i$ (see Figure 2-15). Thus, the loading history is expressed as in Equation (2.12), which is the definition of the Stieltjes integral, which can be written with the time derivative of the stress $\dot{\sigma}$, considered as a distribution function in Equation (2.13).

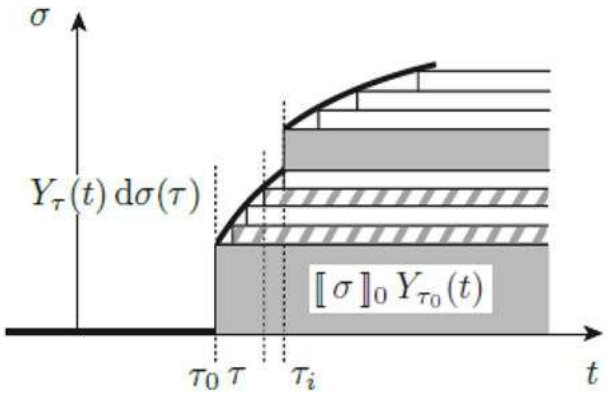

Figure 2-15 *Example of stress history*

$$\sigma(t) = \int_{\tau_0^+}^{t} d\sigma(\tau) Y_\tau(t) + \sum_{\tau_i \le t} [\![\sigma]\!]_i Y_{\tau_i}(t) \tag{2.12}$$

$$\sigma(t) = \int_{-\infty}^{t} \dot{\sigma}(\tau) d\tau \tag{2.13}$$

Thanks to the unicity of the creep compliance function in respect with the stress amplitude, the response to this stress history is expressed as in Equations (2.14) and (2.15). Since $J(\tau, t)$ is null for $\tau > t$, and $\sigma(\tau)$ is also null for $\tau < \tau_0$, the strain response can be expressed as the Stieltjes integral (Equation (2.16)).

$$\varepsilon(t) = \int_{\tau_0^+}^{t} J(\tau, t) d\sigma(\tau) + \sum_{\tau_i \le t} J(\tau_i, t) [\![\sigma]\!]_i \tag{2.14}$$

$$\varepsilon(t) = \int_{\tau_0^-}^{t} J(\tau, t) \dot{\sigma}(\tau) d\tau \tag{2.15}$$

$$\varepsilon(t) = \int_{-\infty}^{+\infty} J(\tau, t) \dot{\sigma}(\tau) d\tau \tag{2.16}$$

Moreover, Equation (2.14) can be rearranged with integration by parts into the Boltzmann formulation (Equation (2.17)), where an instantaneous elastic response part and a "memory" term emerge for any stress loading history. Following the same process Equation (2.16) becomes Equation (2.18).

$$\varepsilon(t) = J(t,t)\sigma(t) - \int_{\tau_0}^{t} \frac{\partial J}{\partial \tau}(\tau,t)\sigma(\tau)d\tau \tag{2.17}$$

$$\varepsilon(t) = -\int_{-\infty}^{+\infty} \frac{\partial J}{\partial \tau}(\tau,t)\sigma(\tau)d\tau \tag{2.18}$$

Applying the same reasoning with relaxation test, the stress response can be written as in Equations (2.19) and (2.20)

$$\sigma(t) = R(t,t)\varepsilon(t) - \int_{\tau_0}^{t} \frac{\partial R}{\partial \tau}(\tau,t)\varepsilon(\tau)d\tau \tag{2.19}$$

$$\sigma(t) = -\int_{-\infty}^{+\infty} \frac{\partial R}{\partial \tau}(\tau,t)\varepsilon(\tau)d\tau \tag{2.20}$$

2.3.2.1.4 Non-ageing materials

The behaviour of non-ageing materials does not change for two identical experiment delayed in time. For classical tests on bituminous materials, this is a valid assumption. Therefore, the value of $J(\tau,t)$ only depends on the time difference between *t* and the start of the loading *τ*, as shown in equation (2.21). The start of any test is arbitrarily set to $\tau_0 = 0$ for simplification purpose.

$$J(\tau,t) = J(t-\tau) \tag{2.21}$$

Equations (2.17) to (2.20) become in this case Equations (2.22) to (2.25)

$$\varepsilon(t) = J(0)\sigma(t) + \int_{\tau_0}^{t} \dot{J}(t-\tau)\sigma(\tau)d\tau \tag{2.22}$$

$$\varepsilon(t) = \int_{-\infty}^{+\infty} \dot{J}(t-\tau)\sigma(\tau)d\tau \tag{2.23}$$

$$\sigma(t) = R(0)\varepsilon(t) + \int_{\tau_0}^{t} \dot{R}(t-\tau)\varepsilon(\tau)d\tau \tag{2.24}$$

$$\sigma(t) = \int_{-\infty}^{+\infty} \dot{R}(t-\tau)\varepsilon(\tau)d\tau \tag{2.25}$$

2.3.2.1.5 Laplace-Carson transformation

From the Equations (2.23) and (2.25), the response functions identify as the convolution products expressed in Equations (2.26) and (2.27). The Laplace-Carson transformation is defined for any function *g* in Equation (2.28) and possesses a fundamental property written In Equation (2.29): to simplify the convolution product including a time derivative to a simple function product in Laplace space.

$$\varepsilon(t) = \left(\sigma * \dot{J}\right)(t) \tag{2.26}$$

$$\sigma(t) = \left(\varepsilon * \dot{R}\right)(t) \tag{2.27}$$

$$\tilde{g}(p) = p\int_{-\infty}^{+\infty} g(t)e^{-pt}dt \tag{2.28}$$

$$\widetilde{(\dot{g}_1 * g_2)}(p) = \widetilde{(g_1 * \dot{g}_2)}(p) = \widetilde{g_1}(p)\widetilde{g_2}(p) \tag{2.29}$$

Hence, the strain is expressed in Equation (2.30). With the same mathematical developments for stress, equation (2.31) is obtained. These two equations are analogous to the elastic case in time domain, where $\tilde{R}$ is equivalent to the modulus *E* and $\tilde{J}$ to a compliance E^{-1}. The transformed relaxation function is simply the inverse of the transformed compliance function (Equation (2.32).

$$\tilde{\varepsilon}(p) = \tilde{J}(p)\tilde{\sigma}(p) \tag{2.30}$$

$$\tilde{\sigma}(p) = \tilde{R}(p)\tilde{\varepsilon}(p) \tag{2.31}$$

$$\tilde{R}(p)\tilde{J}(p) = 1 \tag{2.32}$$

2.3.2.1.6 LVE response to sinusoidal load

The previous expressions in Laplace space can be exploited for well-selected loading functions, especially sinusoidal loading. Consider the sinusoidal strain loading starting at $t = 0$ expressed in equation (2.33) as the real part of a complex function. The stress response is calculated in Equation (2.34) using Equation (2.27). After calculations (Equations (2.35) to (2.38)), the expression of stress is obtained, separated in two parts, one being the real part of the original strain complex function multiplied by the transformed relaxation function taken at $p = i\omega$, the other one a residual term *a(t)* converging to 0 when $t \to +\infty$ (primarily because *R* is bounded and monotone). The first part corresponds to the steady state response, which is sinusoidal, and the second one to a transient term in the response.

$$\varepsilon(t) = \varepsilon_0 \cos(\omega t)Y(t) = \varepsilon_0 Re\left(e^{i\omega t}\right)Y(t) \tag{2.33}$$

$$\sigma(t) = \left(\dot{R} * \varepsilon\right)(t) = \int_{-\infty}^{+\infty} \dot{R}(\tau)\varepsilon(t-\tau)d\tau \tag{2.34}$$

$$\sigma(t) = \int_{-\infty}^{+\infty} \dot{R}(\tau)\varepsilon_0 Re\left(e^{i\omega(t-\tau)}\right)Y(t-\tau)d\tau \tag{2.35}$$

$$\sigma(t) = \varepsilon_0 Re\left[\int_{-\infty}^{+\infty} \dot{R}(\tau)e^{i\omega(t-\tau)}Y(t-\tau)d\tau\right] \tag{2.36}$$

$$\sigma(t) = \varepsilon_0 Re\left[e^{i\omega t}\int_{-\infty}^{+\infty} \dot{R}(\tau)e^{i\omega\tau}d\tau - e^{i\omega t}\int_{t}^{+\infty} \dot{R}(\tau)e^{i\omega\tau}d\tau\right] \tag{2.37}$$

$$\sigma(t) = \varepsilon_0 Re\left[\tilde{R}(i\omega)e^{i\omega t}\right] + a(t) \tag{2.38}$$

2.3.2.1.7 Complex modulus

The previous section proves that the LVE response to a sinusoidal strain loading (Equation (2.39)) is also sinusoidal in steady state. The complex modulus $E^*(\omega)$ is defined as the transformed relaxation function for $p = i\omega$ (Equation (2.40)). Physically, its norm $|E^*|$ equals the ratio of stress and strain amplitude, and its phase angle φ represents the delay between these two harmonic functions (Equation (2.41)). This result can be visualised in Figure 2-16, whereas in Figure 2-17, the strain-stress ellipses (Lissajou curves) of materials with different phase angle are plotted. For $\varphi = 0°$, the material is linear elastic (Hooke's law), and for $\varphi = 90°$, the material is purely viscous.

$$\varepsilon^*(t) = \varepsilon_0 e^{i\omega t} \tag{2.39}$$

$$\sigma^*(t) = \tilde{R}(i\omega)\varepsilon^*(t) = E^*(\omega)\varepsilon^*(t) = \sigma_0 e^{i(\omega t+\varphi)} \tag{2.40}$$

$$E^* = |E^*(\omega)|e^{i\varphi(\omega)} = \frac{\sigma_0}{\varepsilon_0}e^{i\varphi} \tag{2.41}$$

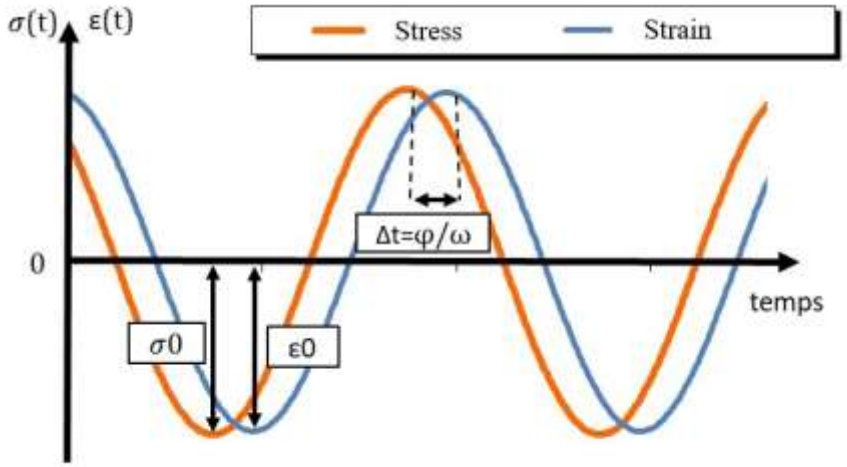

Figure 2-16 *Schematic response of LVE materials to harmonic loading as a function of time*

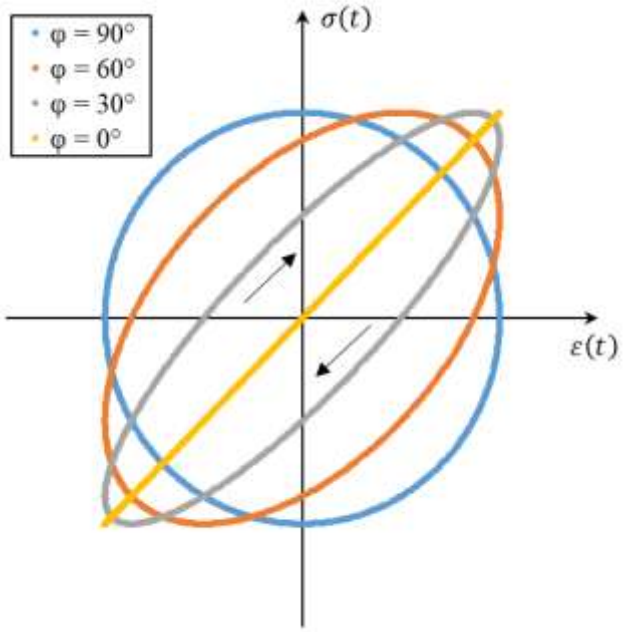

Figure 2-17 *Schematic response to harmonic loading for LVE materials with different phase angle in strain-stress plane*

The real part of the complex modulus E_1 is the "storage" modulus, whereas the imaginary part E_2 is the "loss" modulus (respectively written in Equations (2.42) and (2.43)). The energy dissipated per cycle w_i calculated in equation (2.44) is proportional to the loss modulus and equals the surface area under the strain-stress ellipses in Figure 2-16.

$$E_1 = Re(E^*) \tag{2.42}$$

$$E_2 = Im(E^*) \tag{2.43}$$

$$\begin{aligned} w_i &= \int_0^{\frac{2\pi}{\omega}} \sigma(t)\,\dot{\varepsilon}(t)dt = \pi\sigma_0\varepsilon_0 \sin\varphi \\ &= \pi{\varepsilon_0}^2|E^*| \sin\varphi = \pi{\varepsilon_0}^2 E_2 \\ &= \pi\frac{{\sigma_0}^2}{|E^*|}\sin\varphi \end{aligned} \tag{2.44}$$

The complex modulus defined in the frequency domain (where ω is the angular pulsation and $f = \frac{\omega}{2\pi}$ the frequency) is the fingerprint of the LVE behaviour. The relaxation function in time domain can be obtained with the inverse of the Laplace-Carson transformation (Mandel 1955):

$$R(t) = \frac{2}{\pi}\int_0^{+\infty} \frac{Re\left(E^*(\omega)\right)\sin\omega t}{\omega}\,d\omega \tag{2.45}$$

Eventually, the complete mechanical characterisation of a LVE material is equivalently possible either in time domain with infinite relaxation and creep tests or in frequency domain with a complex modulus test over an infinite range of frequencies. In practice, tests are obviously restricted in time and frequency, but LVE models can account for asymptotic behaviours (see section 2.3.2.4).

2.3.2.2 Time and temperature dependence of LVE behaviour of bituminous materials

LVE materials are by definition time-dependent. Additionally, the LVE behaviour of bituminous materials varies as a function of temperature. This section aims at showing the influence and the relationship between frequency and temperature on the complex modulus of bituminous materials based on the example of a typical French "*BBSG*" (Semi-coarse asphaltic concrete) (Di Benedetto and Corté 2005).

2.3.2.2.1 Time dependence of LVE behaviour

The frequency dependence of complex modulus can be grasped with complex modulus isotherm curves (Figure 2-18). The kinetic susceptibility of mixture at different temperature is displayed, with dramatic variations of $|E^*|$ up to an order of magnitude between 1Hz and 30Hz, for instance at 30°C. This kinetic susceptibility is less important at low temperature, the mixture becoming more elastic as seen previously.

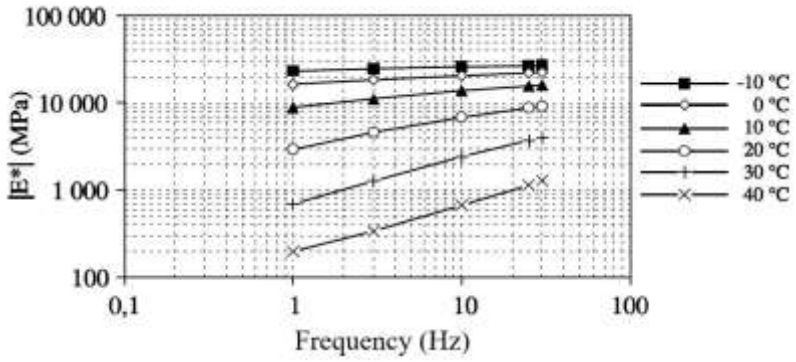

Figure 2-18 *Isotherms of complex modulus* (Di Benedetto and Corté 2005)

2.3.2.2.2 Temperature dependence of LVE behaviour

The same data as in the previous section are rearranged to illustrate the temperature influence on complex modulus isochrones curves, i.e. for fixed frequency.

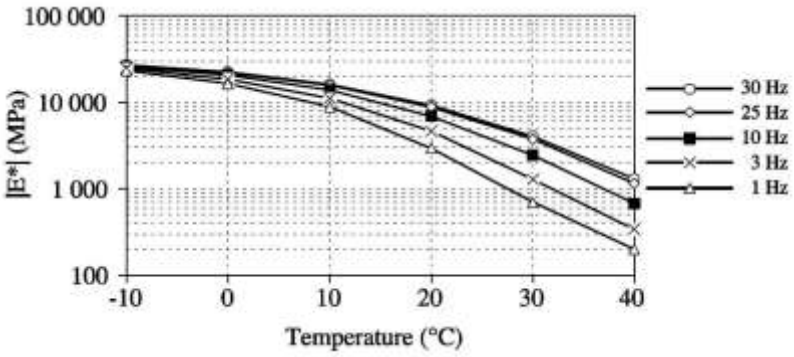

Figure 2-19 *Isochrones of complex modulus* (Di Benedetto and Corté 2005)

2.3.2.2.3 Time-Temperature Superposition Principle

For thermorheologically simple materials (defined in section 2.3.2.3), there is an equivalence between a temperature change and a frequency variation on LVE behaviour. These materials follow the Time-Temperature Superposition Principle (TTSP). This permits the introduction of an equivalent frequency $a_T.f$ for any given reference temperature T_{ref} (see equation (2.46) to (2.48)).

$$E^*(f,T) = E^*\left(a_T.f, T_{ref}\right) \tag{2.46}$$

$$a_T = a_T(T, T_{ref}) \tag{2.47}$$

$$a_{T_{ref}} = a_T\left(T_{ref}, T_{ref}\right) = 1 \tag{2.48}$$

Based on the isotherm curves of complex modulus in logarithmic scale from Figure 2-18, a_T acts as a shift factor on the frequency horizontal axis for each temperature. All isotherm curves can be shifted to form a unique master curve in the equivalent frequency domain, as shown in Figure 2-20, illustrating the TTSP. The reference temperature for which the shift is null is arbitrary.

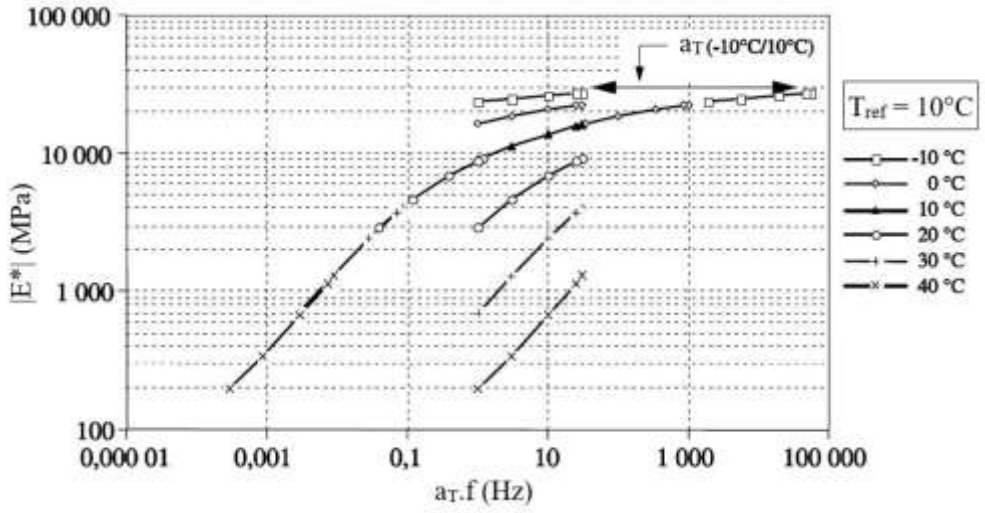

Figure 2-20 *Master curve of the norm of complex modulus at T_{ref} =10°C* (Di Benedetto and Corté 2005)

It should be noted that the TTSP can also be verified in other domains of behaviour for bituminous materials (e.g. nonlinear viscoelasticity), as discussed in (L. Babadopulos 2017).

2.3.2.2.4 Time-temperature equivalence models

Several models are suitable to fit the experimental observations of shift factor as a function of temperature for bituminous materials. Among others, two models are often used by paving technologists (Md. Yusoff, Chailleux, and Airey 2011; Forough, Nejad, and Khodaii 2014):

- The first one uses Arrhenius' law (Equation (2.49)), originally developed to model chemical kinetics (Arrhenius 1889). $\bar{R}$ is the gas constant and the fitting parameter δH represents the activation energy of the material.

$$\log a_T = \frac{\delta H}{\bar{R}}\left(\frac{1}{T} - \frac{1}{T_{ref}}\right) \tag{2.49}$$

- The second one (Equation (2.50)) is the William-Landel-Ferry (WLF) equation (Williams, Landel, and Ferry 1955). C1 and C2 are two fitting parameters. This empirical model simulates well a wide range of temperature for bituminous materials; an example for a bituminous mixture is shown in Figure 2-21.

$$\log a_T = \frac{-C_1\left(T - T_{ref}\right)}{\left(T - T_{ref}\right) + C_2} \tag{2.50}$$

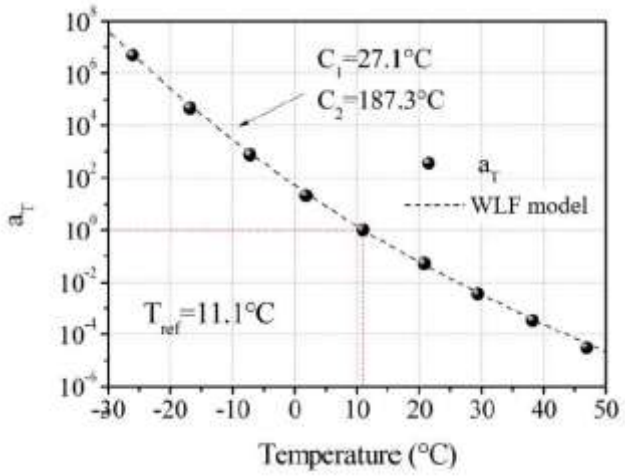

Figure 2-21 *Example of shift factors and WLF curve fit of a bituminous mixture (adapted from Nguyen* (Q. T. Nguyen 2011)*)*

2.3.2.3 Complex modulus representation in complex diagrams

Huet spotted that the complex modulus obtained from sinusoidal loading in steady state (equation (2.40)) is analogous to an electrical impedance (Huet 1963). Two classical representations in electrical engineering can be used to describe the LVE behaviour of bituminous materials:

- the Cole-Cole plot (Cole and Cole 1941), where the loss modulus is plotted against the storage modulus (this corresponds to the complex plane).

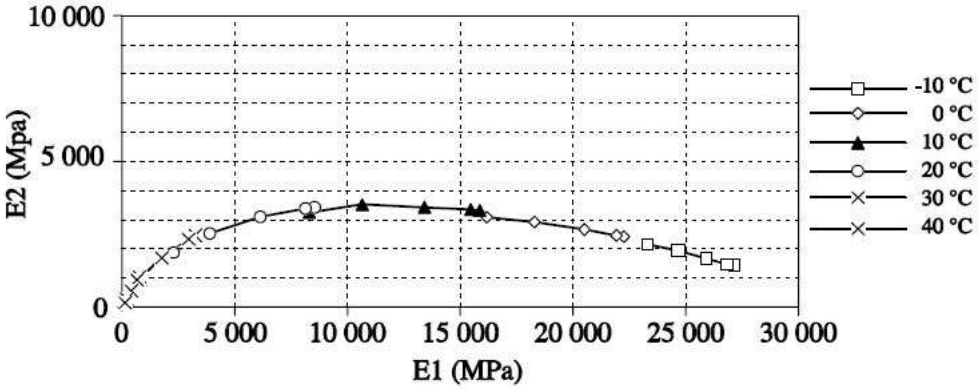

Figure 2-22 *Complex modulus in Cole-Cole plot* (Di Benedetto and Corté 2005)

- The Black space, where the norm of complex modulus is plotted against the phase angle

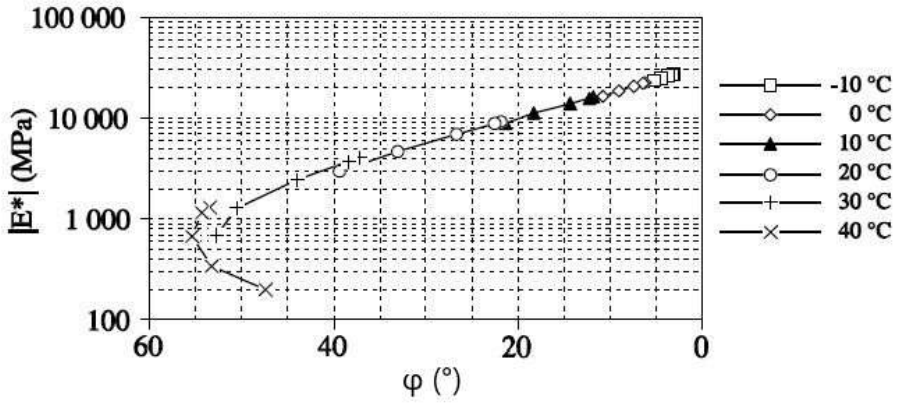

Figure 2-23 *Complex modulus in Black Space* (Di Benedetto and Corté 2005)

If the plot for a set of temperature and frequency couples describes a unique curve in those planes, the material is considered "thermorheologically simple". Moreover, the TTSP is consequently valid. Pure bitumens are thermorheologically simple, whereas some PmB may not possess a unique complex modulus curve in complex planes (Read and Whiteoak 2003).

2.3.2.4 Linear viscoelastic rheological models

A reliable simulation of the LVE behaviour of bituminous materials is essential for paving technologists. As mentioned above, the complex modulus is analogous to an electrical impedance. Like in electric engineering, analogical models are built from fundamental analogical elements to approximate the LVE behaviour of bituminous materials.

2.3.2.4.1 Models with discrete relaxation spectrum

Two basic elements are available to build analogical LVE models:

- the linear elastic spring, where stress and strain are proportional.

$$\sigma(t) = E\varepsilon(t)$$
$$E^*(\omega) = E \tag{2.51}$$

- the dashpot, where stress and strain rate are proportional.

$$\sigma(t) = \eta\frac{d\varepsilon}{dt}(t)$$
$$E^*(\omega) = i\omega\eta \tag{2.52}$$

Any combination of one or more of these elements in parallel or in series constitutes an analogical LVE model. The Maxwell and the Kelvin-Voigt (KV) models are the combination of one spring and one dashpot, respectively in series and in parallel. When two elements are put in series, their creep compliance functions add up. On the other hand, when they are put in parallel, their relaxation functions add up. Therefore, the complex moduli, the creep compliance and the stress relaxation functions of the Maxwell and KV models are given by Equations (2.53) and (2.55). A relaxation time τ is introduced in equation (2.54). It gives an estimate of the order of magnitude of the reaction time scale of the model. This is illustrated in Equation (2.53) with the exponential decay of the relaxation function of the Maxwell model in time domain.

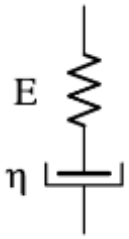

Figure 2-24 *Schematic representation of the Maxwell model*

$$\left.\begin{aligned} E^*_{Maxwell}(\omega) = R^*(i\omega) = \frac{1}{f^*(i\omega)} = \frac{1}{\frac{1}{E}+\frac{1}{i\omega\eta}} = E\frac{i\omega\tau}{1+i\omega\tau} \\ R_{Maxwell}(t) = Ee^{-\frac{t}{\tau}}Y(t) \\ J_{Maxwell}(t) = \left(\frac{1}{E}-\frac{t}{\eta}\right)Y(t) \end{aligned}\right\} \quad (2.53)$$

$$\tau = \frac{\eta}{E} \quad (2.54)$$

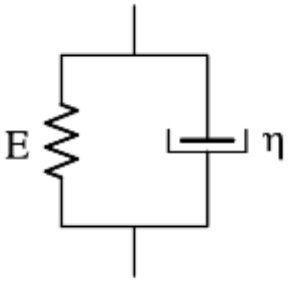

Figure 2-25 *Schematic representation of the Kelvin-Voigt model*

$$\left.\begin{aligned} E^*_{KV}(\omega) = R^*(i\omega) = E + i\omega\eta = E(1+i\omega\tau) \\ R_{KV}(t) = EY(t) + \eta\delta(t) \\ J_{KV}(t) = \frac{1}{E}\left(1-e^{-\frac{t}{\tau}}\right)Y(t) \\ \text{with } \delta(t) \text{ the Dirac distribution function} \end{aligned}\right\} \quad (2.55)$$

Several Maxwell or Kelvin-Voigt elements can be assembled to form more complex models. The generalised Maxwell model consists of *n* Maxwell elements all in parallel with a spring E_0 and a dashpot η_∞ (Figure 2-26). This model, also called Prony series if $\eta_\infty = 0$, is widely used for all kinds of LVE materials. Each Maxwell element possesses a specific relaxation time that allows, along with the variable number of elements, fitting complex experimental stress relaxation curves.

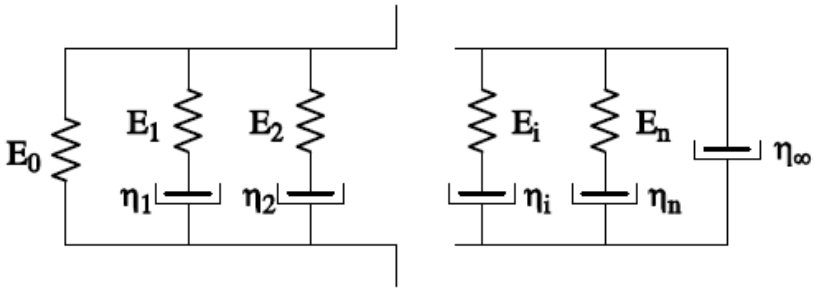

Figure 2-26 *Schematic representation of the generalized Maxwell model*

$$\left.\begin{aligned} E^*_{generalised\ Maxwell}(\omega) &= E_0 + i\omega\eta_\infty + \sum_{i=1}^{n} E_i \frac{i\omega\tau_i}{1+i\omega\tau_i} \\ R_{Generalised\ Maxwell}(t) &= E_0 Y(t) + \eta_\infty \delta(t) + \sum_{i=1}^{n} E_i e^{-\frac{t}{\tau_i}} Y(t) \end{aligned}\right\} \quad (2.56)$$

Similarly, the generalised Kelvin-Voigt model is composed of *n* KV elements all in series with a spring and a dashpot.

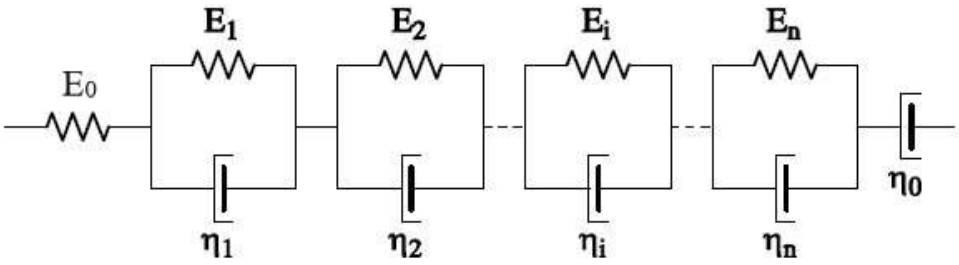

Figure 2-27 *Schematic representation of the generalized Kelvin-Voigt model*

$$\left.\begin{aligned} E^*_{generalised\ KV}(\omega) &= \frac{1}{\frac{1}{E_0} + \frac{1}{i\omega\eta_0} + \sum_{i=1}^{n} \frac{1}{E_i(1+i\omega\tau_{i)}}} \\ J_{Generalised\ KV}(t) &= \frac{1}{E_0} Y(t) + \frac{t}{\eta_0} Y(t) + \sum_{i=1}^{n} \frac{1}{E_i}\left(1 - e^{-\frac{t}{\tau_i}}\right) Y(t) \end{aligned}\right\} \quad (2.57)$$

Park and Schapery (S.W. Park and Schapery 1999) showed that any combination of spring and dashpot elements is reducible to either a generalised Maxwell model or a generalised KV model. Moreover, these two models are equivalent and the use of one expression over the other depends on the studied phenomenon (Salençon 2009). The relaxation spectrum is the distribution associated with the set of relaxation times $\{\tau_i\}_{i\in[\![1,n]\!]}$. For the previous cases, the spectrum is discrete.

2.3.2.4.2 Models with continuous relaxation spectrum

If the number of Maxwell (or KV) elements is virtually infinite, we can assume the continuity of the relaxation spectrum. Thus, the Equation (2.56) is generalised in Equation (2.58), where $H(\tau)$ is the distribution function of the continuous relaxation spectrum (Di Benedetto and Corté 2005). This formalism permits to describe any type of LVE behaviour.

$$E^*(\omega) = \int_{\ln\tau=-\infty}^{\ln\tau=+\infty} H(\tau)\frac{i\omega\tau}{1+i\omega\tau} d\ln\tau \quad (2.58)$$

The parabolic element is one example of continuous relaxation spectrum. Its creep compliance function is the biparametric power law (Equation (2.59)) and the complex modulus is expressed in equation (2.60), with a positive τ and $0 < h < 1$, and where Γ is the gamma function as expressed in (2.61)

Figure 2-28 *Schematic representation of a parabolic element*

$$J(t) = \left(\frac{t}{\tau}\right)^h \quad (2.59)$$

$$E^*(\omega) = \frac{(i\omega\tau)^h}{\Gamma(1+h)} \quad (2.60)$$

$$\Gamma(h) = \int_0^{+\infty} x^{h-1}e^{-x}dx \quad (2.61)$$

The first use of parabolic elements to successfully model LVE behaviour of bituminous materials was proposed by Huet (Huet 1963). The so-called Huet model uses 2 parabolic elements and one spring in series. The creep compliance function (2.62) and the complex modulus (2.63) are rearranged to have a simplified expression as a function of τ (defined in Equation (2.64)).

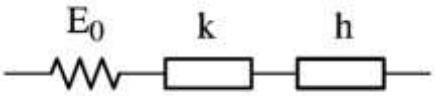

Figure 2-29 *Schematic representation of the Huet model*

$$J(t) = \frac{1}{E_0} + \left(\frac{t}{\tau_k}\right)^k + \left(\frac{t}{\tau_h}\right)^h$$

$$J(t) = \frac{1}{E_0}\left(1 + \delta\frac{\left(\frac{t}{\tau}\right)^k}{\Gamma(1+k)} + \frac{\left(\frac{t}{\tau}\right)^h}{\Gamma(1+h)}\right) \tag{2.62}$$

$$E^*(\omega) = \frac{E_0}{1 + \delta(i\omega\tau)^{-k} + (i\omega\tau)^{-h}} \tag{2.63}$$

$$\tau = \tau_k \delta^{-\frac{1}{k}}\left(E_0\Gamma(1+k)\right)^{\frac{1}{k}} = \tau_h\left(E_0\Gamma(1+h)\right)^{\frac{1}{h}} \tag{2.64}$$

Such model is suitable for materials following the TTSP to the condition that only τ depends on the temperature and is proportional to the shift factor:

$$\tau(T) = \tau_0 a_T(T, T_{ref}) \tag{2.65}$$

The equivalent angular frequency is indeed $\omega\tau(T)$. E_0 is the asymptotic elastic modulus at low temperature or high frequency, also called "glassy" modulus. This modulus is a physical parameter that can be determined experimentally by extrapolation with sufficient data (for instance in Cole-Cole plot in Figure 2-22) or even simulated from a homogenisation model for LVE granular materials (M. D. Nguyen et al. 2016). The Huet model proved to be useful for bituminous materials (Huet 1963), although it fails to correctly simulate the behaviour of mixtures at high temperature or low frequency. Unlike bitumens, which tend to become purely viscous, mixtures exhibit an asymptotic elastic modulus E_{00}, also named static modulus, due to the granular skeleton. An improvement of the Huet model has been proposed by Sayegh (Sayegh 1965), with a supplementary spring in parallel of the existing model; This forms the Huet-Sayegh model. No simple analytical expression of both creep and relaxation functions is available, but the complex modulus is given in equation (2.66).

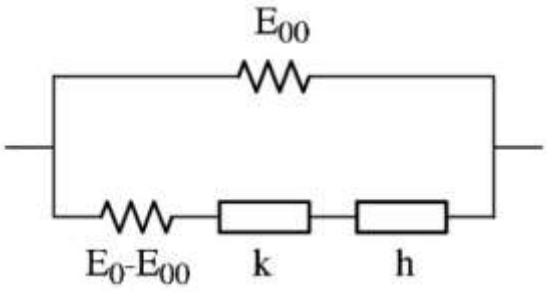

Figure 2-30 *Schematic representation of the Huet-Sayegh model*

$$E^*(\omega) = E_{00} + \frac{E_0 - E_{00}}{1 + \delta(i\omega\tau)^{-k} + (i\omega\tau)^{-h}} \tag{2.66}$$

2.3.2.4.3 2S2P1D model

Olard and Di Benedetto (Olard and Di Benedetto 2003) proposed to add a dashpot to the Huet-Sayegh model to better simulate the asymptotic Newtonian viscous flow of the bitumen at high temperature or low frequency. The resulting "2S2P1D" model (2 springs, 2 parabolic elements, 1 dashpot) has proven to be versatile enough to model successfully the LVE behaviour of bituminous materials, from bitumens to mixtures (Di Benedetto, Olard, et al. 2004; Delaporte et al. 2007; Md. Yusoff, Monieur D., and G. D. 2010; Md. Yusoff et al. 2013), and precise enough to study the influence of different phenomena on LVE behaviour, such as short or long-term aging (Wang et al. 2019). A total of seven constants (E_0, E_{00}, τ_0, k, h, δ, β) are required to fully describe the LVE behaviour of bituminous materials. If the WLF equation is used to simulate the TTSP, two additional parameters are necessary (C_1 and C_2).

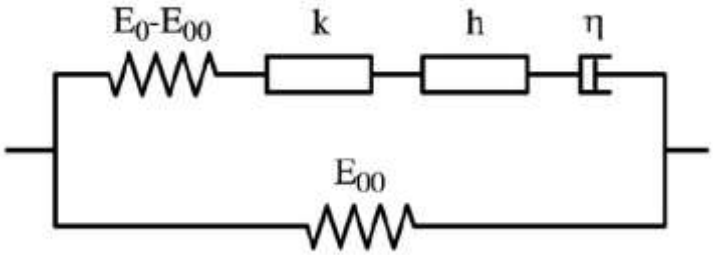

Figure 2-31 *Schematic representation of the 2S2P1D model*

$$E^*(\omega) = E_{00} + \frac{E_0 - E_{00}}{1 + \delta(i\omega\tau)^{-k} + (i\omega\tau)^{-h} + (\beta i\omega\tau)^{-1}} \qquad (2.67)$$

, with

$$\beta = (E_0 - E_{00})\eta\tau \qquad (2.68)$$

Other continuous spectrum LVE models with remarkable efficiency for bituminous are used (N. I. Md. Yusoff, Airey, and Hainin 2010), such as the Christensen and Anderson model (D. W. Christensen and Anderson 1992), or the generalized logistic sigmoidal model (G. M. Rowe, Baumgardner, and Sharrock 2008). Nevertheless, the analogical structure of the 2S2P1D model allows the inclusion of physical parameters (e.g. E_0, E_{00}, τ, η), and the influence of each constant on the complex modulus curve can be identified in Figure 2-32.

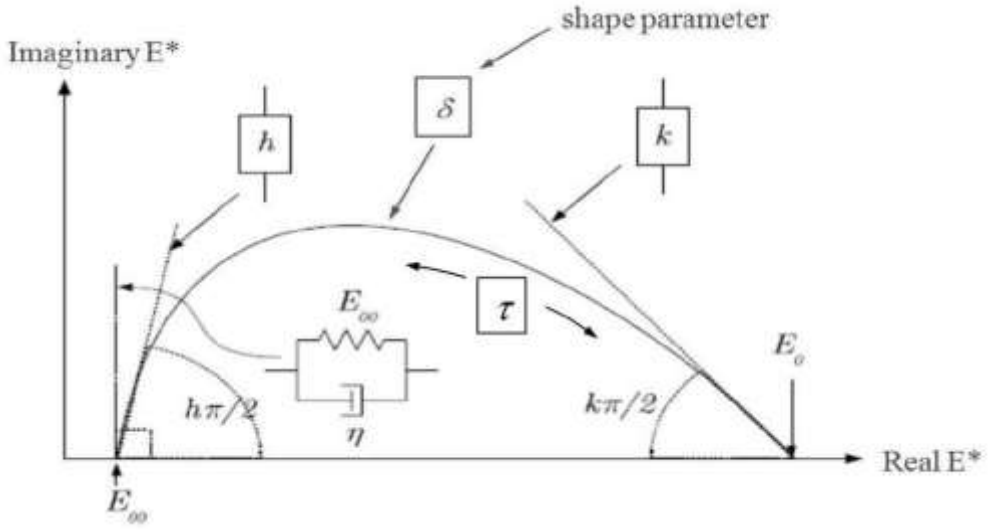

Figure 2-32 *Influence of 2S2P1D constants on the complex modulus curve in Cole-Cole plot*

2.3.2.5 Relationship between binder and mixture LVE behaviours

Characterising the LVE behaviour of mixtures is expensive and time-consuming. Therefore, the prediction of the complex modulus of bituminous mixtures from the bitumen behaviour has been investigated.

2.3.2.5.1 Mechanistic-empirical predictive models

Several models include the bitumen stiffness and mix design volumetric parameters as variables, among others: Hekeulom and Klomp model (Hekeulom and Klomp 1964), Ugé et al. (Ugé et al. 1977) Hirsch model (D. W. Christensen, Pellinen, and Bonaquist 2003) and its improved version (Donald W. Christensen and Bonaquist 2015). These mechanistic-empirical models establish the relationship between the LVE behaviours of bitumen and mixture for a given temperature and frequency couple, and may need recalibration for different conditions. The Witzcak model (Witczak and Fonseca 1996; Bari and Witczak 2006), using the TTSP, takes into account the influence of the equivalent frequency on the predicted modulus based on the logistic sigmoidal model.

2.3.2.5.2 SHSTS transformation

Following the observation that the LVE behaviour of bituminous mastics and mixtures are directly dependent of the behaviour of the constituting bitumen, Di Benedetto et al. (Di Benedetto, Olard, et al. 2004) proposed a geometrical transformation to predict the complex modulus of mixture from the binder modulus values. The SHSTS (Shift, Homothety, Shift, Time Shift) transformation only requires the asymptotic moduli of the mixture $E_{0,mix}$ and $E_{00,mix}$, plus a time shift parameter α, as shown in Equation (2.69). This transformation does not depend on any particular LVE model for the mixture.

$$E^*_{mix}(\omega,T) = E_{0,mix} + \left[E^*_{binder}(10^{\alpha}\omega,T) - E_{00,binder}\right]\frac{E_{00,mix} - E_{00,mix}}{E_{0,binder} - E_{00,binder}} \qquad (2.69)$$

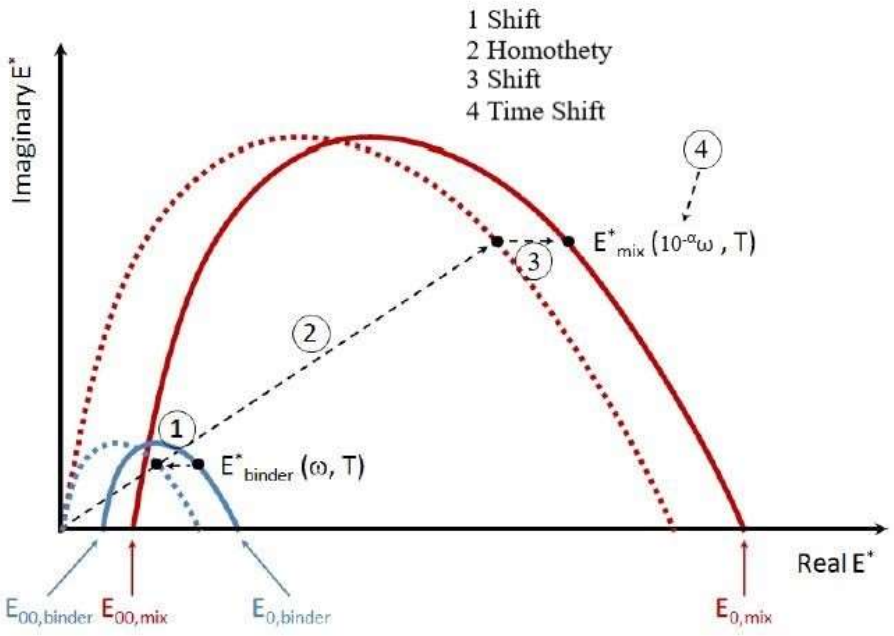

Figure 2-33 *SHSTS transformation in Cole-Cole plot, adapted from Mangiafico* (Salvatore Mangiafico 2014)

The SHSTS transformation has been tested in several studies (Di Benedetto, Olard, et al. 2004; Ramirez Cardona et al. 2015; Riccardi et al. 2017) with good results and α values between 3 and 3.5. This implies that the time and temperature dependence of the LVE behaviours of the bitumen and of the corresponding mixture is similar; their shift factors are proportional of 10^{α} for the same T_{ref}, which is potentially attributed to the mix design and/or aging during fabrication (Delaporte 2007).

2.3.3 High strain amplitude load domain: Nonlinear viscoelasticity

Bituminous materials exhibit LVE behaviour under certain strain and/or stress limits. This section focuses on the material's response analysis in the nonlinear domain and on the LVE domain limits from bitumen to mixtures.

2.3.3.1 Constitutive equations of nonlinear viscoelasticity (NVLE)

Based on a large experimental evidence in polymer science, many viscoelastic materials present nonlinear behaviour, i.e. dependent on strain and/or strain rate. Extending the thermodynamic theory of linear irreversible processes of Biot (Biot and Company 1958) to nonlinear materials, Schapery (R. Schapery 1966; R. A. Schapery 1969) proposed the following constitutive stress-strain Equation (2.70):

$$\varepsilon(t) = g_0 J_0 \sigma(t) + g_1 \int_0^t \Delta J(\xi - \xi') \frac{d\left(g_2 \sigma(\xi')\right)}{d\xi'} d\xi' \tag{2.70}$$

with J_0 the instantaneous creep compliance, and ΔJ the delayed part of the creep compliance function

$$J_0 = J(t,t) = J(t-t) = J(0) \tag{2.71}$$

$$\Delta J(t-\tau) = J(t-\tau) - J_0 \tag{2.72}$$

g_0, g_1, g_2 stress dependent functions and ξ the reduced time

$$\xi(t) = \int_0^t \frac{d\tau}{a_\sigma} \tag{2.73}$$

With a_σ a time scale factor also stress dependent.

The linear case is found again for $g_0 = g_1 = g_2 = a_\sigma = 1$ in equation (2.74), which is a rearrangement of the previous expression (2.15) in LVE theory.

$$\varepsilon(t) = J_0 \sigma(t) + \int_0^t \Delta J(t-\tau) \dot{\sigma}(\tau) d\tau \tag{2.74}$$

2.3.3.2 "Equivalent" complex modulus

The loss of the Boltzmann superposition principle for high strain amplitudes has critical theoretical implications; the response to a harmonic loading function is not *a priori* harmonic itself. The complex modulus is not properly defined in NLVE. Nevertheless, stress-strain curves of bituminous materials during "high" strain amplitude loading may still fit harmonic functions well; an "equivalent" modulus is defined with the amplitudes and the phase angles between the stress and strain cycles, just as the LVE complex modulus is obtained (Equation (2.41)). The semantic difference between the equivalent and the actual complex modulus is not always established in the literature, but should be considered as implicit. In this thesis, for readability and the reader's sake, the term "equivalent complex modulus", written E^*_{eq}, will only be introduced to make a necessary distinction with the real LVE complex modulus E^*(which should be considered as a limit when the strain amplitude tends towards 0). Otherwise, E^* will be used to describe both moduli. Researchers use the change of the equivalent modulus as a function of the loading amplitude to characterise nonlinearity in bituminous mixtures (Doubbaneh 1995; Airey, Collop, and Dongre 2002; Airey, Rahimzadeh, and Collop 2003; Gauthier et al. 2010; Nguyen, Di Benedetto, and Sauzeat 2014; Nguyen, Di Benedetto, and Sauzéat 2015). It is interesting to note that other effects, and not only nonlinearity, can affect the equivalent modulus. An extensive description of the physical phenomena involved during cyclic loading (self-heating and thixotropy) is given in section 2.3.4.6. However, if the number of cycles at high amplitude of loading is limited, these phenomena are negligible (Gauthier et al. 2010; L. F. de A. L. Babadopulos et al. 2019) compared to nonlinearity effects. Continuous or discontinuous strain sweep tests are typically applied to study the influence of loading amplitude on the equivalent modulus.

2.3.3.3 Limits of LVE domain of bituminous materials

Nonlinearity in bituminous materials systematically decreases the norm and increases the phase angle of the equivalent modulus as a response to an increase of the loading amplitude level. The limits of LVE domain of bituminous materials, either in term of stress or strain, are usually defined as the amplitude level where an arbitrary fraction of the norm of the complex modulus (i.e. the equivalent modulus for very small loading amplitude) is reached. Threshold value of 95% of the complex modulus is very common since the American SHRP proposed it (Anderson et al. 1994) (this value was already used in soil mechanics. The strain amplitude limit $\varepsilon_{0\_95\%}$ is around 100µm/m for bituminous mixtures in axial tension-compression (G. D. Airey, Rahimzadeh, and Collop 2003), whereas the distortion amplitude limit $\gamma_{0\_95\%}$ is about 10000µm/m, i.e. 1% deformation, for bitumens tested on Dynamic Shear Rheometer (Airey, Collop, and Dongre 2002). The directions of loading (axial vs. shear) do not seem to cause different nonlinearity effects on their respective moduli (E^* vs. G^*), since the complex Poisson's ratio of bituminous mixtures appears independent of strain amplitude in 3-D experimental results (Nguyen, Di Benedetto, and Sauzéat 2015).

The limits of LVE domain of bituminous materials are time and temperature dependent. Recent work showed that they also respect the TTSP, with the same shift factor as used for the complex modulus (Nguyen, Di Benedetto, and Sauzéat 2015; Babadopulos et al. 2019). For binders (bitumen and mastic), $\gamma_{0\_95\%}$ increases with the equivalent frequency (same direction as the modulus), whereas for mixtures, $\varepsilon_{0\_95\%}$ decreases with the equivalent frequency (opposite direction to the modulus). The authors point out that monitoring the evolution of LVE domain limits as a function of time and temperature with stresses rather than strains yields to similar directions for both binders and mixtures.

One could challenge the existence of an actual LVE domain for bituminous materials, since the threshold value is arbitrary. Researchers have tested nonlinearity at very small strain amplitude that are usually limited by the precision of the sensors or the command controlling system. Mangiafico and co-workers showed the existence of measurable nonlinearity effects in mixtures from 10µm/m to 110µm/m (Mangiafico et al. 2018). In the same publication, linear laws for the change of the norm and the phase angle of the equivalent modulus as a function of strain amplitude was proposed to model nonlinearity effects. For bituminous materials (and probably most of the other viscous materials) pure LVE behaviour can be considered as an asymptotic behaviour when strain amplitude tends toward 0.

2.3.4 Repeated loading cycles domain: Fatigue

Fatigue cracking may appear in pavement under repeated traffic loading. A most recent and extensive state of the art in fatigue cracking evaluation of asphalt concrete pavements has been proposed by the AAPT (Braham and Underwood 2016). This section introduces the phenomenon of fatigue in general and the main features concerning the fatigue of bituminous materials.

2.3.4.1 Description of fatigue phenomenon

Fatigue is defined as the loss of integrity of a material submitted to repeated loading cycles under its ultimate strength, eventually leading to failure. Historically, this behaviour has been studied first for metals in industrial cyclic processes (Rankine 1843; Braithwaite 1854; Wöhler 1890). For these elastic solid materials, fatigue is exclusively associated with irreversible damage; the repeated cycles initiate matter dislocation and induce microcracks that propagate and then coalesce into visible cracks (Ewing and Humphrey 1903). For composite materials, the cracks propagate from pre-existing internal flaws. The complete description of the microscopic phenomena occurring during cyclic loading is generally too complex to be properly related to observed macroscopic properties (e.g. change in stiffness, overall fatigue life…etc.), especially in heterogeneous media (Murakami 2012). Two approaches were developed to interpret fatigue damage : Continuum damage mechanics (Kachanov 1958; 1986) and fracture mechanics (Griffith 1921; Clark 1971). Continuum mechanics introduces the concept of distributed damage usually associated with the loss of resistant cross-section area. The apparent stiffness is monitored during test to evaluate damage evolution. Fracture mechanics focuses on crack propagation in various geometries (e.g. bending beam) and tries to link the fracture characteristics to the fatigue behaviour (Hartman and Gilchrist 2004).

Describing the evolution of fatigue damage with one of the two latter approaches is quite advanced; it remains a research topic and it is not yet developed for practitioners. The classical method to characterise fatigue is to study the fatigue life (i.e. the number of applied cycle N_f before failure) of material specimens subjected to continuous cyclic loading. The stress or strain amplitude level of the loading primarily influences the fatigue life. The display of the loading amplitude versus the N_f forms the Wöhler curve (Wöhler 1890). It should be noticed that this curve depends on the test geometry (e.g. axial versus flexural), as well as the loading mode; indeed, because fatigue always causes a loss of stiffness, a strain-controlled test leads to decreasing stress, whereas a stress-controlled test exhibits increasing strain (illustrated in Figure 2-34).

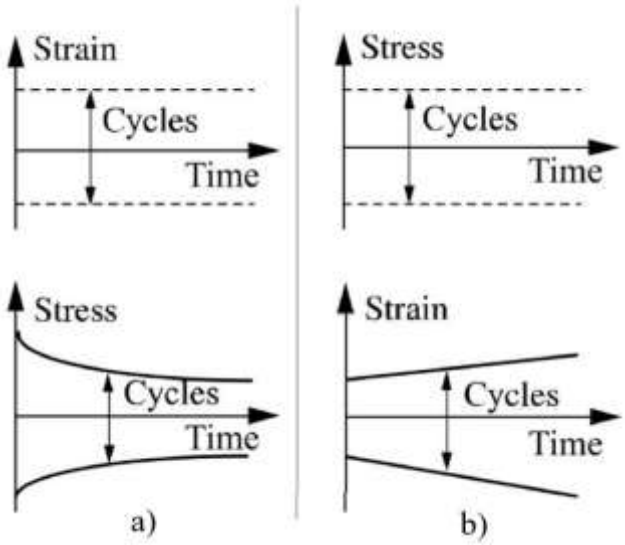

Figure 2-34 *Schematic representation of fatigue test in: a) strain-controlled mode, b) stress-controlled mode*

2.3.4.2 Response of bituminous materials to continuous cyclic loading

During fatigue tests on bituminous materials, three distinct phases are observed (Di Benedetto, Roche, et al. 2004; Hassan Baaj 2002), illustrated in Figure 2-35 and Figure 2-36.

- Phase I: Fast, nonlinear decrease of the norm of equivalent modulus, coupled with an increase of phase angle as well as internal heating due to viscous dissipation. The change in modulus is primarily due to reversible phenomena over actual damage.
- Phase II: Quasi-linear decrease of the norm of complex modulus in respect with *N*. During this stage, the evolutions of the phase angle and of the internal temperature are somewhat stabilised. This corresponds well to the predominance of the effects of damage on modulus change (typically understood as a loss of resistant cross section) over the reversible phenomena. Microcracks appear and expand during phase II. This phase is obviously of utmost importance to test or calibrate damage models (Hassan Baaj, Di Benedetto, and Chaverot 2005; H. Baaj 2003).
- Phase III: clear indication of a brutal change in the material associated with the creation of macrocrack. At this point, the continuum mechanics is not relevant anymore as the homogeneity of the material is lost (values of modulus in phase III are just indications of the severity of the failure).

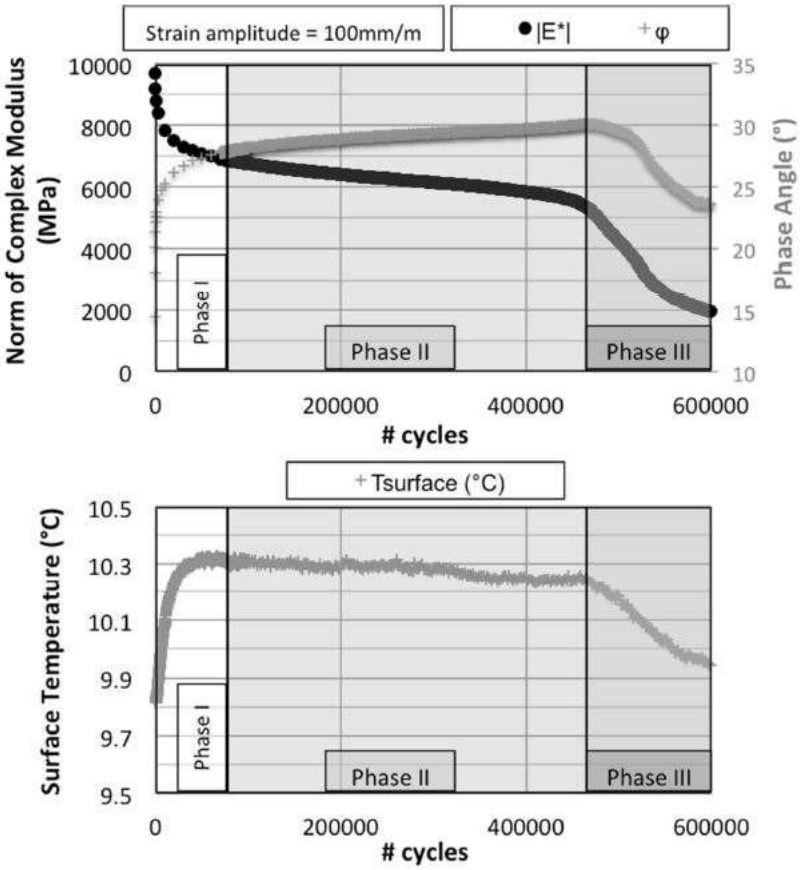

Figure 2-35 *Example of the evolution of the equivalent modulus and the sample surface temperature during a continuous fatigue test on bituminous mixture* (Tapsoba 2012)

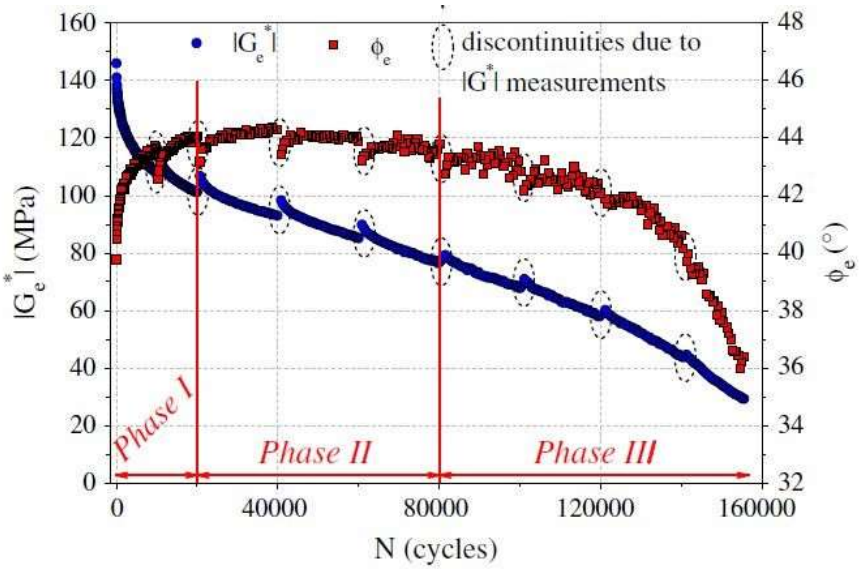

Figure 2-36 *Example of the evolution of equivalent modulus during a discontinuous fatigue test on a bituminous mastic* (Van Rompu et al. 2012)

2.3.4.3 Prediction of fatigue life

The fatigue life N_f is the number of cycles until the failure of the material. From the perspective of the previous section, N_f indicates the shift from phase II to phase III. The apparition of a macrocrack at specific location arises from heterogeneities inherent to either the sample or the material itself. Therefore, it is not surprising to observe considerable scattering of N_f up to one order of magnitude for a constant loading amplitude (Di Benedetto and Corté 2005). Nevertheless, the Wöhler curve (Wöhler 1890) (also named S-N curve) of bituminous materials can be established with sufficient fatigue test repetitions over several loading amplitudes.

For high number of cycles (>10^4), the fatigue life follows Basquin's law (Basquin 1910), i.e. is a power law function of the loading amplitude, usually represented as a linear relationship in log-log scale. This broadly used model is expressed in Equation (2.75) in the case of imposed strain amplitude test (where ε replaces the usual ε_0 for strain amplitude). The expression can be rearranged in Equation (2.76), where ε_6 is the strain amplitude that yields to a fatigue life of one million cycles. This value ε_6 is critical in French pavement design; it is used as the criterion to assess the resistance to fatigue of bituminous mixtures (AFNOR 2012c). The slope factor b is generally around 5 (Di Benedetto and Corté 2005).

$$\log N_f = a + b \log \varepsilon \tag{2.75}$$

$$\varepsilon = \varepsilon_6 \left(\frac{N_f}{10^6}\right)^{-\frac{1}{b}} \tag{2.76}$$

2.3.4.4 Failure criteria used for bituminous materials

The fatigue life N_f, determined by the failure of the material is reached before the total destruction of the test sample. Several failure criteria for bituminous mixtures are used in the literature:

- The classical "half-modulus" criterion. Regardless of the test conditions, the failure is supposed to be reached when half of the initial material stiffness is lost. Although $N_{f,\,50\%}$ is essentially arbitrary, early studies showed that this value is close to the complete failure of the sample in stress-controlled tests. This is less true for strain-controlled tests, where half of the modulus can be reached long before the actual sample failure (Doan 1977). It could also appear not reliable when taking into account all effects appearing during the phase I of tests. Nevertheless, the half-modulus method is used in European standards (AFNOR 2012c).
- Energy-based criteria. The main idea is that the apparition of a macrocrack in the material is accompanied by a brutal change in the Dissipated Energy Ratio (*DER*), defined in Equation (2.77)

$$DER = \frac{\sum_1^N w_i}{w_N} \tag{2.77}$$

with w_i the dissipated energy during cycle *i*. This ratio increases linearly until the considered failure, after a number of cycles noted N_{DER}, where a clear change of rate appears. This criterion is suitable for both stress and strain-controlled tests.

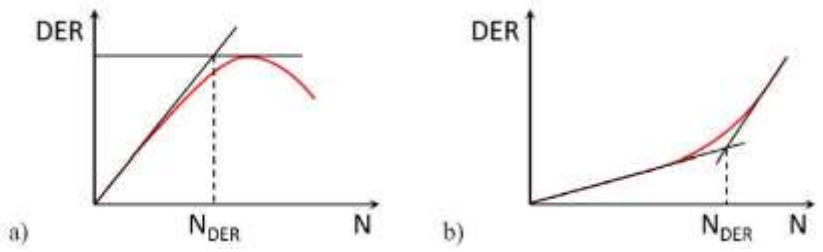

Figure 2-37 *Schematic representation of DER as a function of N during fatigue test in: a) stress-controlled mode, b) strain controlled mode* (Salvatore Mangiafico 2014)

A modification of DER is proposed by Rowe (G. Rowe 1993), followed by Pronk (Pronk and Waterbouwkunde 1995).

$$DER = \frac{Nw_1}{w_N} \tag{2.78}$$

Some authors pointed out that in general, the identification of a clear change of rate of *DER* might be challenging (Di Benedetto and Corté 2005).

- The local criteria. Some test set-ups allow measuring more than a single force-displacement value couple. A classical axial tension-compression (TC) test on cylindrical specimen generally involves several axial displacement (or deformation) measuring devices to calculate an average value on the specimen. Soltani (Soltani 1998) and then Baaj (Hassan Baaj 2002) have used the signals of three extensometers to spot a loss of homogeneity in their samples, synonym of macrocrack formation. Two local criteria were proposed for the failure: when one of the extensometer amplitude deviates of 25% of the average or when one of the extensometer phase angle deviates of 5°. An example of the use of these fatigue life criteria, respectively noted $N_{f,\Delta\varepsilon}$ and $N_{f,\Delta\varphi}$, is displayed in Figure 2-38

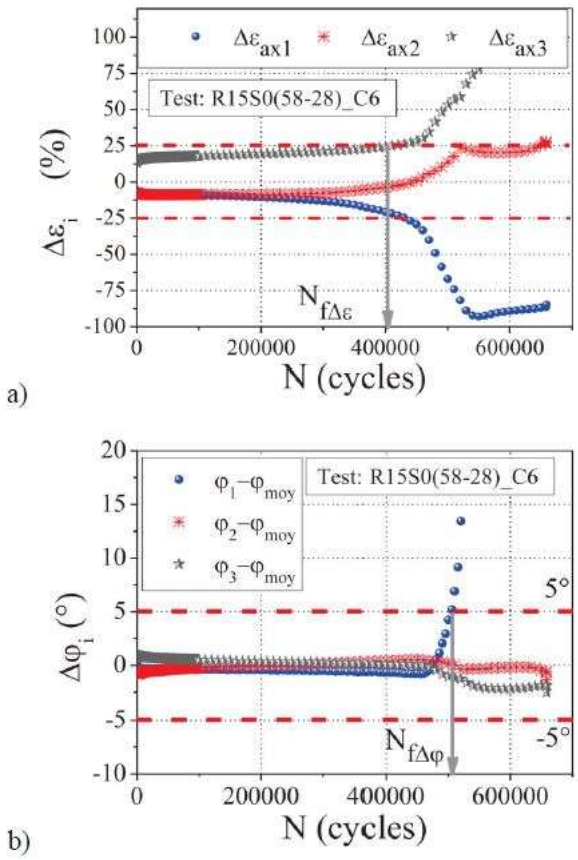

Figure 2-38 *Example of local failure criteria measured for bituminous mixture fatigue test* (Tapsoba 2012)

Regardless of the failure criterion, the establishment of Wöhler curve remains technically expensive and time-consuming, as many specimens undergo millions of cycles. Moreover, it is impossible a priori to link the fatigue parameters *a* and *b* between different test conditions (control mode, geometry…etc.). It is possible to bypass both these challenges with damage models that predicts fatigue life.

2.3.4.5 Fatigue damage modelling

Damage models usually describe the evolution of the material stiffness as a decrease of resistant cross-section $\hat{A}$ using a loss of integrity function *D*, and *A* the initial intact cross-section (Equation (2.79))

$$\hat{A} = A(1 - D) \tag{2.79}$$

The stress-strain relationship applied on the material becomes

$$\sigma = (1 - D)\hat{\sigma} = (1 - D)E\varepsilon \tag{2.80}$$

with $\hat{\sigma}$ the effective stress applied on the material (sigma and epsilon being the apparent stress and strain, measured on the specimen considered intact). This expression in the elastic case is obviously transposable to viscoelasticity, as the effective stress is simply proportional to the apparent stress. This usual description suggests implicitly that damage does not influence the time-dependency of the material's response (i.e. the phase angle of the equivalent modulus for continuous cyclic tests). Indeed, classical damage models do not predict how φ behaves. As for the physical origin of its increase during fatigue test, some theories distinguish the combination of viscoelastic nonlinearities and damage (Masad et al. 2008), while other sources with experimental study on load and rest periods on bitumen (L. F. de A. L. Babadopulos et al. 2019) suggest that it is almost entirely due to reversible phenomena. Previous studies of the same type on mixtures also supported the predominance of reversible phenomena (Q. T. Nguyen 2011). Details on this subject are provided in section 2.3.4.6

Nevertheless, several damage models predict the integrity function $(1 - D)$ either directly as a function of the applied cycles, or via an intrinsic damage parameter *S*.

2.3.4.5.1 Miner's rule

The Miner's rule (Miner 1945) (or Palmgren-Miner linear damage law) is one simple and yet most used model to predict fatigue damage. It assumes that damage cumulates linearly, regardless of the sequence of *n* loading amplitude L_i.

$$D = \sum_{i=1}^{n} \frac{n_i}{N_i} \tag{2.81}$$

, with n_i the number of cycle applied at loading amplitude L_i and N_i the number of cycle until total failure of the material at this amplitude (stress or strain). However, studies showed that the linear cumulative damage is not verified for mixtures (Doan 1977). The amplitude sequence is also known to be important (Di Benedetto and Corté 2005).

2.3.4.5.2 DGCB approach

Starting from the 3-phase description of the fatigue test in section 2.3.4.2, Di Benedetto et al. (Di Benedetto, Soltani, and Chaverot 1996) proposed a model to calculate the rate of actual change of stiffness attributed to damage (corrected from biasing effect of reversible phenomena). The damage function is defined by the change in stiffness relatively to the initial modulus E_0.

$$D(N) = \frac{E_0 - E(N)}{E_0} \tag{2.82}$$

During phase II, *D(N)* is considered linear on successive interval *i*. For each interval, the rate of damage is a_{Ti} and the extrapolated initial modulus is E_{00i}. The fact that a_T varies from one interval to another is due to nonlinearity of the damage phenomena.

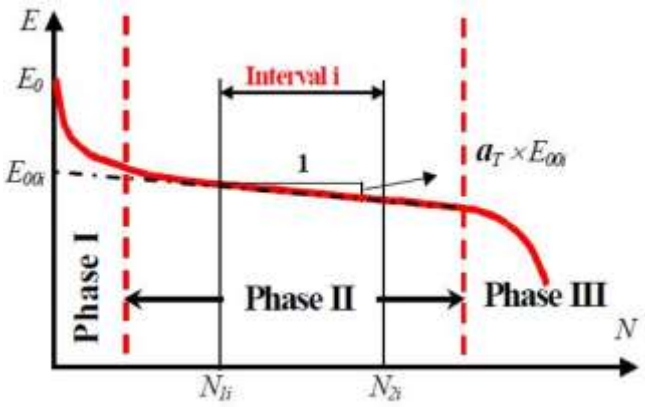

Figure 2-39 *Scheme of the calculation of the rate of total damage during the i[th] interval* (Hassan Baaj, Di Benedetto, and Chaverot 2005)

This rate of damage can be decomposed; during phase II, biasing effects of reversible phenomena can still alter the stiffness of the material with a rate of a_{Bi} (the rate of actual damage is then a_{Fi}).

$$a_{Ti} = a_{Fi} + a_{Bi} \tag{2.83}$$

The authors considered that the biasing effects on the stiffness is proportional to the dissipated power after phase I. Therefore, during phase II, the rate of damage due to biasing effect is proportional to the rate of change in dissipated energy per cycle a_{wi} (Equation (2.84) for strain control test). This rate (positive or negative) depends on the controlling mode.

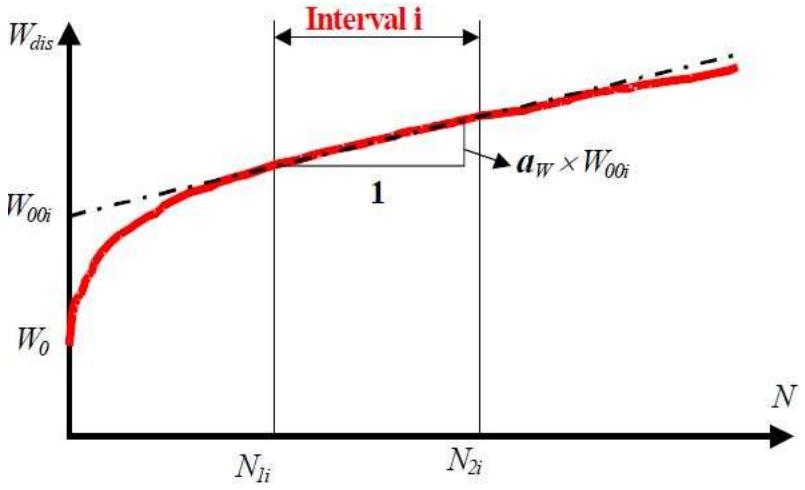

Figure 2-40 *Scheme of the calculation of the rate of dissipated energy during the i[th] interval* (Hassan Baaj, Di Benedetto, and Chaverot 2005)

$$a_{Fi} = a_{Ti} + a_{wi} C_i \frac{E_0 - E_{00i}}{E_{00i}} \tag{2.84}$$

where C_i is a factor taking in account nonlinearity of the actual damage. The interval usually studied for mixtures are between cycles 50 000 and 150000, and between cycles 150000 and 300000. This damage law has proven to be independent of the controlling mode (Hassan Baaj 2002).

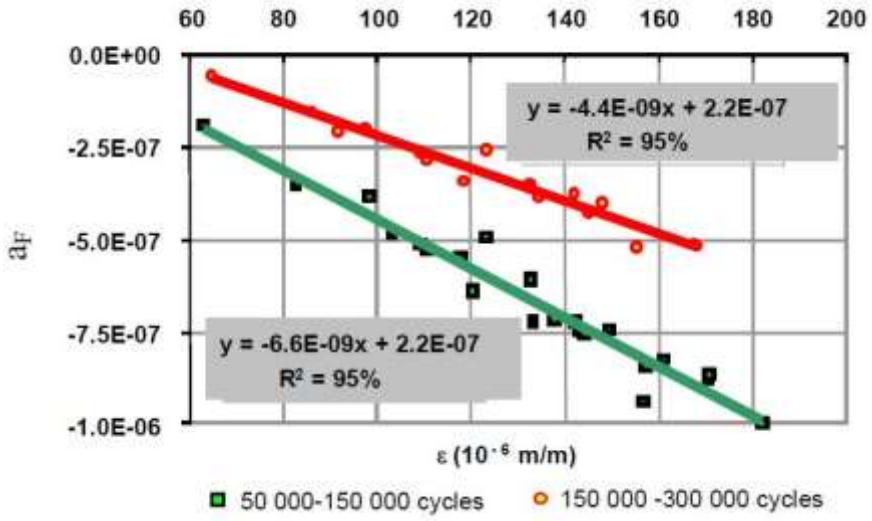

Figure 2-41 *Rate of damage with combined strain and stress-controlled fatigue tests on bituminous mixture. Interval 1 = [50000-150000], interval 2 = [150000-300000]* (Di Benedetto, Soltani, and Chaverot 1996)

2.3.4.5.3 ViscoElastic Continuum Damage model

The ViscoElastic Continuum Damage (VECD) model describes the evolution of an internal damage parameter *S* based on Schapery's generalisation of fracture mechanics to distributed flaws in nonlinear viscoelastic materials (R. A. Schapery 1975; R. Schapery 1981; R. A. Schapery 1987). The VECD model (Y. R. Kim and Little 1990; Sun Woo Park, Richard Kim, and Schapery 1996; Daniel and Kim 2002), is built around four key equations:

- The pseudo strain function, with ξ the reduced time and E^R the reference pseudo modulus,

$$\varepsilon^R = \frac{1}{E^R}\int_0^t R(\xi - \xi')\frac{d\varepsilon}{d\xi'}d\xi' \tag{2.85}$$

- The stress-pseudo strain relationship, with C the pseudo secant modulus,

$$\sigma = C\varepsilon^R \tag{2.86}$$

- The pseudo strain energy density function

$$W^R = \frac{1}{2}(\varepsilon^R)^2 C \tag{2.87}$$

- The damage evolution law, similar to Paris' law in fracture mechanics

$$\frac{dS}{d\xi} = \left(-\frac{\partial W^R}{\partial S}\right)^{\alpha} \tag{2.88}$$

Combining equation (2.87) and (2.88) gives the relationship between the damage parameter *S* and the material integrity function (pseudo stiffness) *C*. For continuous cyclic tests, *C* is simply the ratio of the observed equivalent modulus and the initial LVE complex modulus:

$$C(N) = \frac{\left|E^*_{eq}(N)\right|}{\left|E_{ini}{}^*\right|} \tag{2.89}$$

The strength of the VECD approach is that the characteristic damage curve *C(S)* is unique for a material regardless of the tests performed to evaluate it, promising to reduce considerably the duration of the evaluation of resistance to fatigue. More recently, a simplified viscoelastic continuum damage (S-VECD) model was proposed by Underwood et al. (Underwood, Kim, and Guddati 2010) to study especially and efficiently the resistance to fatigue of bituminous materials.

The major downside of the VECD approach is the difficulty to take into account biasing effects of the reversible phenomena occurring during continuous cyclic tests. Indeed, all the change of stiffness during fatigue test is supposedly attributed to damage. Experimental studies on mixtures found that the *C(S)* is not unique in practice, a result attributed then to self-heating due to viscoelastic energy (Lundström and Isacsson 2004). The evolution of the phase angle change is also very challenging to the VECD approach (which focus on the norm of equivalent modulus), and yet appears important to separate the physical phenomena occuring during fatigue tests (L. F. de A. L. Babadopulos et al. 2019; Shan et al. 2011).

2.3.4.6 Reversible phenomena occurring during fatigue tests of bituminous materials

The resistance to fatigue of bituminous materials in laboratory is characterised with continuous, accelerated, low-amplitude-level fatigue tests. These test conditions are very different from what the material experiences in situ: loading cycles with resting span between cycles, whose duration may vary from less than one second to more than some minutes. During laboratory tests, reversible phenomena are known to appear and bias the fatigue damage analysis (Di Benedetto, Soltani, and Chaverot 1996; De la Roche 1996; Hassan Baaj 2002; Q. T. Nguyen 2011; S. Mangiafico et al. 2015; L. Babadopulos 2017). This section introduces these phenomena and a method to separate and quantify their effects from actual damage.

2.3.4.6.1 Reversible phenomena

Three distinct reversible phenomena occur during continuous cyclic tests on bituminous materials:

- Nonlinearity. This phenomenon and its interpretation in cyclic tests by means of an equivalent complex modulus have been detailed in section 2.3.3. Nevertheless, a semantic clarification is necessary, as the term nonlinearity can cover several phenomena in the literature. In this thesis, nonlinearity is defined as the phenomenon causing "instantaneous", fully reversible change in equivalent modulus as a function of loading amplitude. Because of transient effects inherent to viscoelastic materials, the equivalent modulus can be evaluated only after few cycles (e.g. after 3 to 4 cycles at 10°C/10Hz) (Gayte et al. 2015). During this short lap of time, one could not differentiate a truly instantaneous nonlinear behaviour (initial conditioning of the material) from the effect of a very fast, reversible microstructural breakdown over time (later defined as thixotropy). Regardless of their physical origin description, nonlinearity curves established with Strain Amplitude Sweep (SAS) tests in the literature always describe a decrease in equivalent modulus of several percent of the LVE complex modulus coupled with an increase of several degrees in phase angle, in both bitumen (L. Babadopulos et al. 2019; L. F. de A. L. Babadopulos et al. 2019) and mixtures (Q. T. Nguyen 2011; Q. T. Nguyen, Di Benedetto, and Sauzéat 2015; S. Mangiafico et al. 2018). Studies on the subject also pointed out that other reversible phenomena presented hereafter take place very fast and simultaneously at the beginning of continuous cyclic loading tests (L. F. de A. L. Babadopulos et al. 2019; S. Mangiafico et al. 2018; L. F. de A. L. Babadopulos, Sauzéat, and Di Benedetto 2017) and emphasise on the great care of experimental data analysis to separate and quantify these phenomena properly.

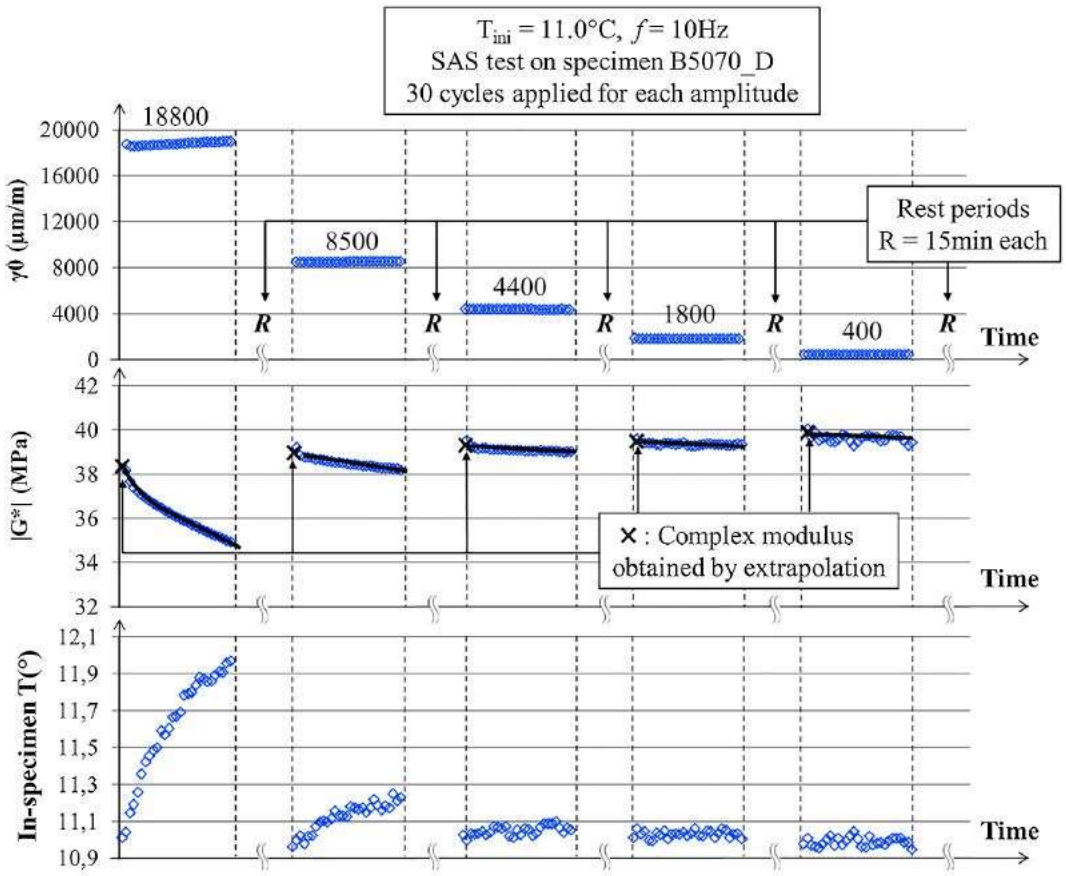

Figure 2-42 *Typical SAS test results on a 50/70 pure bitumen* (L. F. de A. L. Babadopulos et al. 2019)

- Self-heating. During continuous cyclic test on viscoelastic materials, energy is dissipated into heat (see section 2.3.2.1.7), causing a temperature increase in the specimen. Consistent experimental evidence of this phenomena has been reported from bitumen to mixture (Van Rompu et al. 2012; Soltani 1998; Lundström and Isacsson 2004; Piau and Rousset 1983). The temperature susceptibility of bituminous materials can yield to considerable change in equivalent modulus due to self-heating; for instance, Babadopulos et al. (L. F. de A. L. Babadopulos et al. 2019) recorded an internal temperature increase of +5°C during a continuous cyclic shear test on 50/70 pure bitumen at 20000µm/m after only 10000 cycles at 10Hz (thermal chamber T=10°C). According to the authors' previous LVE characterisation of the same bitumen, this temperature increase explained 70% of the modulus loss, as well as 50% of the phase angle increase. In bituminous mixtures, an increase of 1°C roughly corresponds to a loss of 5% of the modulus at intermediate temperature (Salvatore Mangiafico 2014). Self-heating is a major source of stiffness reduction, especially in accelerated, moderate-amplitude-level fatigue tests, that should not be discarded in fatigue damage analysis. Self-heating is highly dependent on loading amplitude, the dissipated energy per cycle w_i is indeed proportional to the square of the strain amplitude. Hence, this phenomenon is limited at low amplitude.

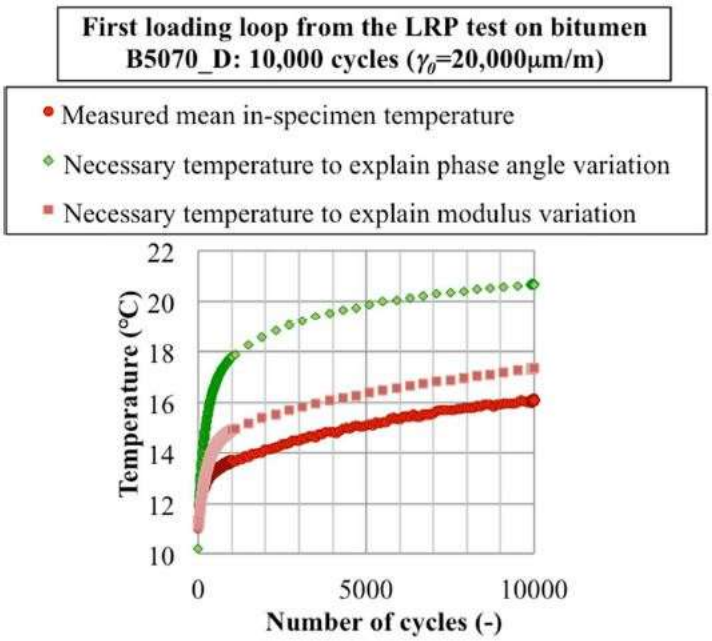

Figure 2-43 *Temperature evolution in bitumen during continuous cyclic test and calculated temperature increases necessary to explain the total phase angle variation and the total modulus variation* (Babadopulos 2017).

- Thixotropy. Thixotropy is defined in fluid rheology as the "the continuous decrease of viscosity with time when flow is applied to a sample that has been previously at rest and the subsequent recovery of viscosity in time when the flow is discontinued" (Mewis and Wagner 2009). This phenomenon is one particular case of the more general term "shear-thinning behaviour", which does not necessarily imply time dependency. The recovery part during rest is also called "build-up". This phenomenon arises from the microstructural breakdown due to shear during mechanical tests, and then fully recovered during rest. The magnitude of the breakdown depends on the loading amplitude. In that sense, thixotropy can be seen as the shift over time of the steady state of the material response as a function of the loading amplitude (see Figure 2-44 and Figure 2-45).

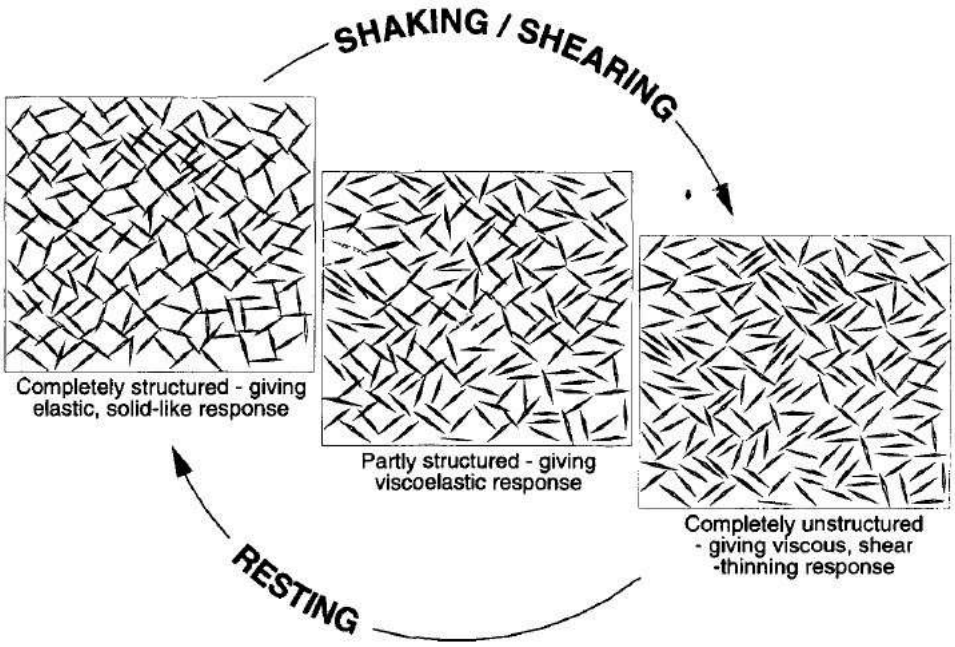

Figure 2-44 *Scheme of the breakdown and the build-up of a thixotropic material* (Barnes 1997)

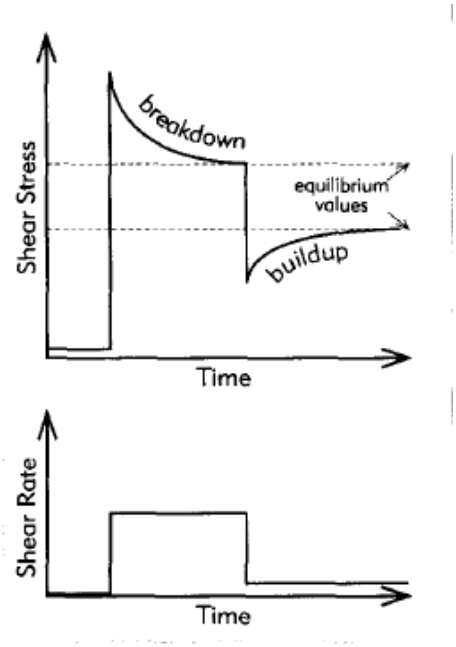

Figure 2-45 *Scheme of a thixotropic material response to shear rate step tests* (Barnes 1997)

Bitumen, like many other colloidal systems (Mewis and Wagner 2011), exhibits thixotropy during continuous cyclic tests (Shan et al. 2011; Van Rompu et al. 2012; Mouillet et al. 2012; L. F. de A. L. Babadopulos et al. 2019). Bituminous mixtures inherit this thixotropic behaviour from the bitumen which can lead to significant, reversible modulus decrease during fatigue tests (Di Benedetto, Soltani, and Chaverot 1996; De la Roche 1996; Q. T. Nguyen 2011; S. Mangiafico et al. 2015). For all bituminous materials, thixotropy causes modulus loss and phase angle increase.

2.3.4.6.2 Separation and quantification of reversible phenomena and damage during load and rest periods

Nonlinearity, self-heating and thixotropy all can bias the actual damage evaluation during continuous cyclic tests. Researchers from ENTPE (University of Lyon) have developed a general framework to separate and quantify all the reversible phenomena effects from damage effects on equivalent modulus, based on Load and Rest Periods (LRP) tests (Q. T. Nguyen 2011; Salvatore Mangiafico 2014; L. Babadopulos 2017). This approach was proposed by Nguyen (Q. T. Nguyen 2011) in a cumulative form:

$$\begin{aligned}\left|E^*_{eq}(\varepsilon_0, T, N)\right| = |E^*_{LVE}(0, T_{ini}, 1)| + \Delta\left|E^*_{nonlinearity}\right| + \Delta\left|E^*_{heating}\right| \\ + \Delta\left|E^*_{thixotropy}\right| + \Delta\left|E^*_{fatigue}\right|\end{aligned} \quad (2.90)$$

The effect of nonlinearity is calculated based on previous Strain Amplitude Sweep (SAS) test (by difference with the asymptotic LVE modulus)

$$\Delta\left|E^*_{nonlinearity}\right| = \left|E^*_{eq}(\varepsilon_0, T_{ini}, 1)\right| - |E^*_{LVE}(0, T_{ini}, 1)| \quad (2.91)$$

The effect of self-heating during load and of cooling during rest are estimated with a measurement of the specimen internal temperature and a previous LVE characterisation of the undamaged material.

$$\Delta\left|E^*_{heating}\right| = \left|E^*_{eq}(\varepsilon_0, T, 1)\right| - \left|E^*_{eq}(\varepsilon_0, T_{ini}, 1)\right| \quad (2.92)$$

The effect of thixotropy is deduced as the share of all the recovered modulus that is not explained by the cooling.

$$\begin{aligned}\Delta\left|E^*_{thixotropy}\right| = \left|E^*_{eq}(\varepsilon_0, T, N, rested)\right| - \left|E^*_{eq}(\varepsilon_0, T, N)\right| \\ = \left|E^*_{eq}(\varepsilon_0, T, N, rested)\right| - \left|E^*_{eq}(\varepsilon_0, T_{ini}, N)\right| + \Delta\left|E^*_{heating}\right|\end{aligned} \quad (2.93)$$

Finally, the real damage is the unrecovered part of the modulus after the rest period. It is identified as the real fatigue damage

$$\Delta\left|E^*_{fatigue}\right| = \left|E^*_{eq}(\varepsilon_0, T_{ini}, 1)\right| - \left|E^*_{eq}(\varepsilon_0, T_{ini}, N + rest)\right| \quad (2.94)$$

In previous equations, T_{ini} is the initial temperature of equilibrium of the material in the thermal chamber. It is recovered after several hours of rest for classical TC tests on cylindrical specimen.

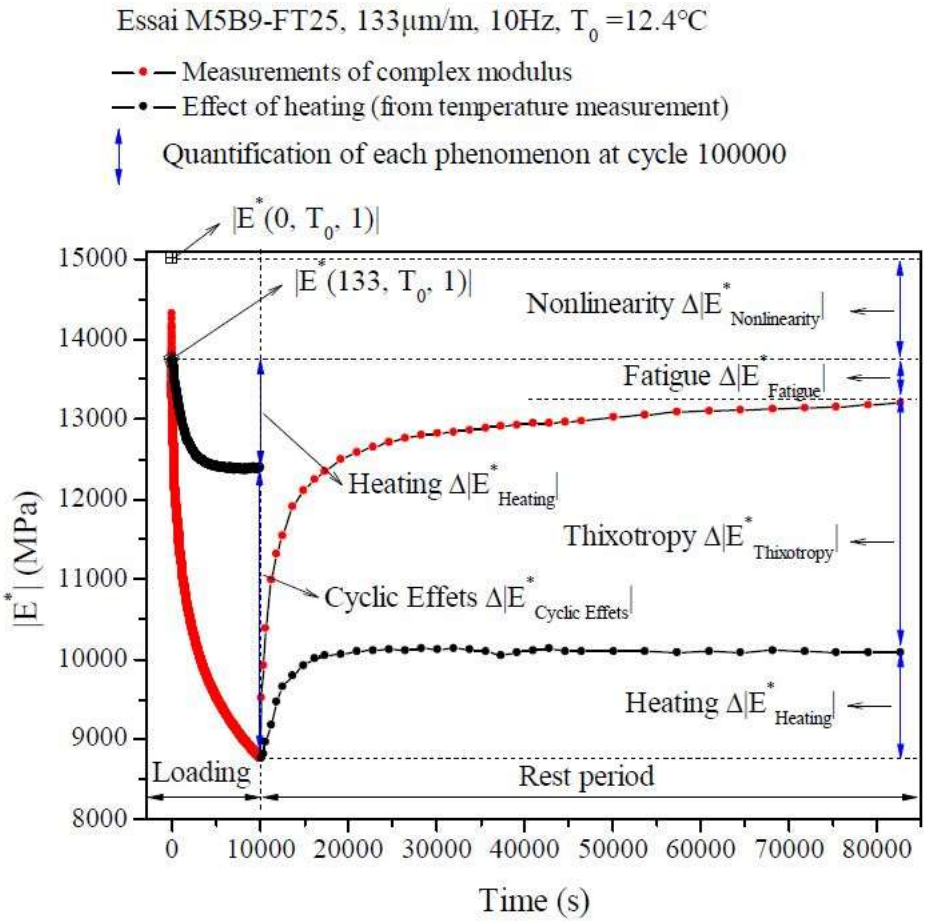

Figure 2-46 *Results and analysis of the contribution of reversible phenomena and damage in modulus change in LRP test. Initial equilibrium temperature T_{ini} is noted T_0 here* (Q. T. Nguyen 2011)

The same cumulative relationship is assumed for the phase angle

$$\varphi(\varepsilon_0, T, N) = \varphi(0, T_{ini}, 1) + \Delta\varphi_{nonlinearity} + \Delta\varphi_{heating} + \Delta\varphi_{thixotropy} + \Delta\varphi_{fatigue} \quad (2.95)$$

Although this formulation is a great tool to estimate the role of each phenomenon, it ignores possible effects combination. Babadopulos et al. (L. F. de A. L. Babadopulos et al. 2019) proposed to work on LRP results on bitumen, corrected from different effects. The authors defined an equivalent modulus corrected from temperature effects $E^*_{T-corrected}$ based on the relative change of modulus due to temperature in the LVE case.

$$E^*_{T-corrected}(\varepsilon_0, T_{ini}, N) = E^*_{eq}(\varepsilon_0, T, N)\frac{E^*_{LVE}(0, T_{ini}, 1)}{E^*_{LVE}(0, T, 1)} \quad (2.96)$$

With five successive loop of 10000-cycle load and 4-hour rest periods, the authors were able to observe the linearity of damage (unrecovered modulus after the 4-hour rest) from one loop to the other, the rate of damage depending on the loading amplitude. They extrapolated this observation to model a linear damage per cycle Δd and were then able to correct fatigue damage effects from the observed equivalent modulus. The correction term for damage is real and therefore in accordance with the classical interpretation of loss of resistant cross section by micro cracking. Indeed, the phase angle of bitumen after each rest period returned to its initial value. For bituminous mixture, the phase angle is not completely recovered after rest (Q. T. Nguyen 2011; Hassan Baaj 2002).

$$E^*_{D-corrected}(\varepsilon_0, T, 1) = E^*_{eq}(\varepsilon_0, T, N)\frac{1}{1 - D(N)} \qquad (2.97)$$
$$D(N) = \Delta d(\varepsilon_0)N$$

The equivalent modulus corrected from combined temperature and damage effects describe the "thixotropy curves" at constant amplitude (nonlinearity happens instantaneously). The authors noticed that thixotropy and the subsequent build-up occur very fast in bitumen (few minutes), and that nonlinearity and thixotropy share the same direction in complex planes, possibly suggesting a common physical origin.

In summary, the ENTPE approach to separate and quantify reversible phenomena and damage during continuous cyclic tests requires:

- LVE characterisation and modelling to calculate the effect of temperature change due to self-heating and cooling during respectively load and rest periods.
- Nonlinearity characterisation via a strain amplitude sweep test
- Loading and Rest Periods (LRP) test with an accurate measure of the specimen temperature. Homogenous tests are mandatory to avoid complex thermomechanical analysis.

2.3.4.7 Healing

Healing is the phenomenon of repair from cracking effects. The theory of microcracks healing in polymer that corresponds to macroscopic observations (material integrity recovery), elaborated by Wool and O'Connor (Wool and O'Connor 1981), distinguished a five-stage mechanism:

a) Rearrangement
b) Surface approach, naturally at the crack tip or forced (i.e. via compression)
c) Wetting
d) Diffusion to an equilibrium distance, material integrity (such as stiffness) recovery
e) Randomisation, total disappearance of previous crack

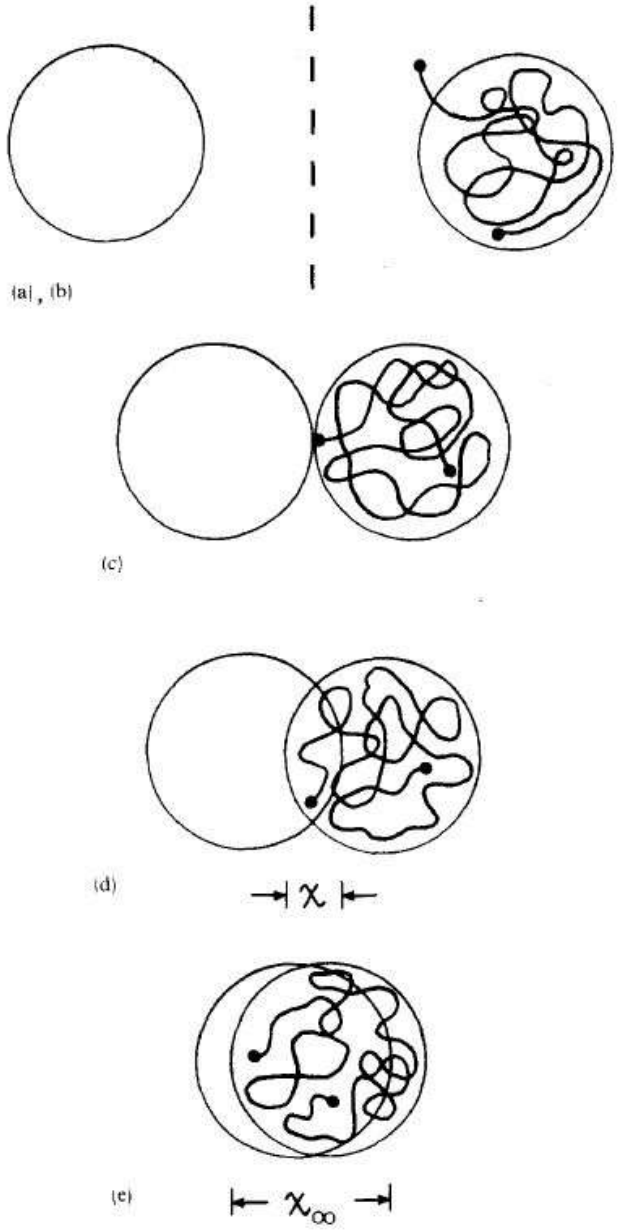

Figure 2-47 *Schematic representation of the five-stage healing of microcracks in polymer* (Wool and O'Connor 1981)

Bituminous materials are well known for their natural (Dallas N. Little and Bhasin 2007) or artificially enhanced (Riara et al. 2018) healing capacity. Researchers developed several tools to quantify the healing potential of bituminous road materials, as this can play a major role in pavement sustainability. Two evaluation approaches can be distinguished:

- Macrocrack reparation. It generally involves a monotonic fracture test where broken surfaces are "glued" back together in specific conditions (with or without compressive force, healing agents, ambient temperature change…etc.). Maximum tensile strength or dissipated energy ratios are typically measured to quantify the healing potential (Riara et al. 2018).

- Continuum micro damage healing. This approach usually involves monitoring the material response during LRP tests (Dallas N. Little and Bhasin 2007; D. N. Little et al. 2001). The classical analysis is very similar to the VECD method, with all the change in pseudo-strain energy being indeed attributed to damage during loading and healing during rest. The Healing Index (HI) is the relative change of pseudo-strain energy during rest.

$$HI = \frac{W^R_{after\ rest} - W^R_{before\ rest}}{W^R_{after\ rest}} \quad (2.98)$$

This continuum healing interpretation cannot include the quantification of reversible phenomena that are not physically due to fatigue cracking damage, described in the ENTPE approach above mentioned. On the other hand, the latter approach does not include healing as a potential independent recovery phenomenon separated from thixotropy during rest. This proves the existence of a semantic struggle between researchers to what "healing", "damage", "reversible phenomena" refers to in rheological tests on bituminous materials. Hopefully this leaves room for contribution in this thesis.

2.4 Binder-aggregate adhesion

The capacity of sustaining thermomechanical loads of bonded granular materials naturally depends on the quality of the binder-aggregate adhesion. This section first introduces general concepts on adhesion, then discusses the characterisation of bituminous binder-aggregate adhesion, the particularly important interface distress due to moisture sensitivity of bituminous mixtures, and finally the role of anti-stripping agents.

2.4.1 Overview on adhesion

An adhesive is defined as a material which, when applied to surfaces of materials (also called substrates or adherends), can join them together and resist separation. The term adhesion refers to the interfacial attraction between an adhesive and a substrate (Kinloch 1987).

2.4.1.1 Physical origins of adhesion

Adams (Adams 2005), in a state of the art review on adhesion, presented the possible mechanisms of adhesion :

- Physical adsorption. Attractive Van der Waals forces at the interface induce adhesion. There are three type of forces: between two molecules with a permanent dipole (Keesom forces), between a molecule with a permanent dipole and a nonpolar molecule with induced dipole (Debye forces), and between two nonpolar molecule with induced dipole (London forces, also called dispersive forces). Although these forces are the weakest of intermolecular electromagnetic forces, they seem to fit well with most adhesive strengths. These weak molecular interactions are at the foundation of the theory of thermodynamic work of adhesion used to characterise binder-aggregate adhesion. Details are provided in section 2.4.1.2
- Chemical bonding. The adhesion would be the result of chemical bond, such as covalent, ionic or hydrogen bonds, or even Lewis acid-base interaction at the interface. For instance, silane-based anti-stripping agents (presented in Section 2.4.5) are linked to substrates with a strong siloxane (Si–O) bond.

- Mechanical interlocking. Porous substrates can absorb adhesives by capillarity and generate interlocking between the two media. If the energy of cohesion (i.e. the amount of energy per unit surface area needed to separate a material in two parts) of both substances is stronger than the work of adhesion between them, mechanical interlocking can greatly increase the interface resistance.
- Adhesion by interdiffusion. This mechanism is possible for two dispersed media (e.g. two polymer above their glass transition temperature), where both diffuse their molecules to the other. The notion of interface (surface) is replaced by an interphase (volume), which possess a specific thickness and its own physical properties. Interdiffusion is a key mechanism in Reclaimed Asphalt Pavement (RAP), where fresh bitumen and rejuvenators are put in contact with the aged binder coated on the RAP aggregates (Kriz et al. 2014).
- Electrostatic theory of adhesion. This approach was originally developed for conductive materials; if two metals are put in contact, electron exchanges create an electrical double layer that results in electrostatic attraction. Even for insulating polymer thin films, evidence of such electrostatic forces and electric sparking after repeated application and stripping was obtained on various substrates (Randow et al. 1997)

All these mechanisms, and more often combination of them, can be invoked as the physical origin of adhesion. This complexity challenges paving technologists to develop a comprehensive characterisation of bituminous binder-aggregate adhesion that can be consistently related to thermomechanical performances of mixtures. In particular, preventing distresses that are directly caused by stripping, such as moisture damage, is essential to improve bituminous paving materials.

2.4.1.2 Surface energy and thermodynamic work of adhesion

In liquids, molecules can move but are kept together because of various intermolecular attractions. Most molecules are completely surrounded by others and therefore the total applied force is null, and the molecules do not move. If the liquid is in contact with air (or vacuum), the molecules at the interface are submitted to little (or no) forces from outside of the liquid phase, causing an overall force perpendicular to the interface towards the "centre" of the liquid phase. This disequilibrium explains why water droplets naturally takes a spherical shape: to minimise their contact surface area with air.

Liquids have extra energy associated with their surface. The surface energy γ_L (expressed in energy per surface unit), also called surface tension (then expressed in force per length unit), represents the amount of energy required to create a unit area of new surface (A. Hefer and Little 2005). The work of cohesion W^c of this liquid, i.e. the minimum work necessary to split a sample of unit cross sectional area in two (Figure 2-48). This work of cohesion is simply twice the surface energy, because two unit surface areas are created after splitting. From the point of view of thermodynamics, it also corresponds to the opposite of the change of Gibbs' free energy (Adamson 1977).

$$W^c = 2\gamma_L = -\Delta G^c \tag{2.99}$$

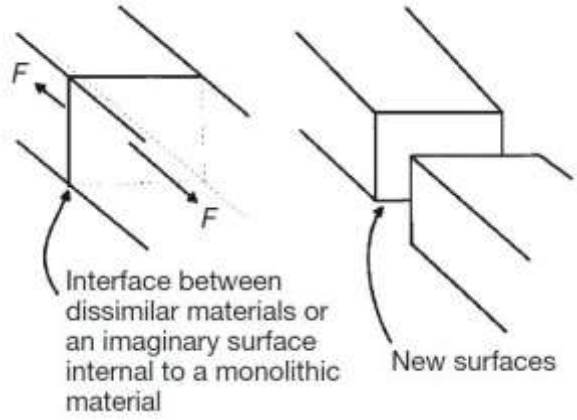

Figure 2-48 *Schematic representation of the force necessary to break an interface*

Adamson (Adamson 1977), cited by Pocius (Pocius 2012), provides a molecular description of the origin of the surface energy. For solids, the surface energy is noted γ_S. Although the surface tension can be higher than in liquids, the driving forces that structures solids are generally much stronger.

The work of adhesion W^a between a liquid and a solid (or between two liquids) quantifies the minimum work required to break a surface unit of the interface. It is expressed via the Dupré equation (2.100), and depends on surface tension of both substances, as well as on the interfacial tension noted γ_{SL}(or $\gamma_{L_1L_2}$). It is simply the sum of the surface energies from the created surfaces minus the interfacial energy.

$$W^a = \gamma_S + \gamma_L - \gamma_{SL} \tag{2.100}$$

The value of W^aindicates if the wetting of a surface is thermodynamically favourable or not. For most bitumen-aggregate combination, the work of adhesion is positive in air, the bitumen naturally sticks and covers mineral aggregates (ignoring practical workability and rheological issues during the mix). However, W^a becomes almost always negative in presence of water (Caro et al. 2008a; Bhasin et al. 2006), meaning that mineral substrates "prefer" water over bitumen at the interface. Thus, moisture damage by debonding occurs naturally, although it does not appears necessary everywhere in water saturated bituminous mixtures because of the topological complexity of real aggregate surface (angularity, porosity…).

2.4.1.3 Prediction of surface energies using surface thermodynamics theories

Theories of surface energy introduce a new relationship between γ_{SL} and the substances' surface energies γ_S and γ_L. Fowkes (Fowkes 1964) postulated that all surface energy is comprised of a polar and a dispersive part (London forces) as expressed in Equation (2.101). Then he calculated the work of adhesion of two liquids, with one of them being nonpolar (e.g. hydrocarbons), as expressed in Equation (2.102).

$$\gamma = \gamma^p + \gamma^d \tag{2.101}$$

$$W^a = \gamma_{L_1} + \gamma_{L_2} - \gamma_{L_1L_2} = 2\sqrt{\gamma_{L_1}^d \gamma_{L_2}^d} \tag{2.102}$$

Owens and Wendt (Owens and Wendt 1969) extended the prediction of work of adhesion to solid-liquid systems including polar attractions (Equation (2.103)) :

$$W^a = 2\sqrt{\gamma_S^d \gamma_L^d} + 2\sqrt{\gamma_S^p \gamma_L^p} \quad (2.103)$$

The Owens-Wendt approach has later been refined by Good, Van Oss and Chaundury (GVOC theory) (Van Oss, Chaudhury, and Good 1988; Van Oss et al. 1989), further decomposing the polar part γ^p into an electron acceptor part γ^+ (acid component) and an electron donor part γ^-(basic component), while the dispersive part γ^d was attributed to Lifshitz–Van der Waals forces and renamed γ^{LW}(Equations (2.104) and (2.105))

$$\gamma = 2\sqrt{\gamma^+ \gamma^-} + \gamma^{LW} \quad (2.104)$$

$$W^a = 2\sqrt{\gamma_S^{LW} \gamma_L^{LW}} + 2\sqrt{\gamma_S^+ \gamma_L^-} + 2\sqrt{\gamma_S^- \gamma_L^+} \quad (2.105)$$

These theories allow the determination of surface energies of unknown substrate by the measurement of the work of adhesion with different known liquids. Several techniques available to obtain W^a are described in section 2.4.2.1.

2.4.2 Characterisation of bituminous binder-aggregate adhesion

In this section, methods to characterise the binder-aggregate adhesion are presented.

2.4.2.1 Surface energy related methods

To be able to measure surface tensions and work of adhesion of bitumen and road aggregates, several techniques have been used:

- The Contact Angle measurement with sessile drop (A. W. Hefer, Bhasin, and Little 2006)
- The Wilhelmy Plate tensiometer technique, for solids only (Bhasin 2006)
- The Pendant Drop technique, for liquid bitumen only
- The Universal Sorption Device technique, for high energy solid substrates only (Bhasin and Little 2007)

2.4.2.1.1 Contact angle measurement with sessile drop

The contact angle method needs a detailed description, as it will be used in this thesis. Let us consider a sessile drop of liquid on a solid substrate. The contact angle of the drop is the angle between the solid-liquid interface plane and liquid-vapour interface plane. The surface tensions at the triple interface point are at equilibrium, leading to Young's equation

$$\gamma_{SV} = \gamma_{SL} + \gamma_{LV} \cos\theta \quad (2.106)$$

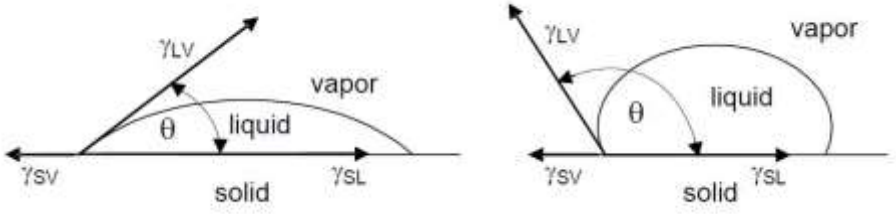

Figure 2-49 *Schematic representation of a sessile drop on a solid substrate*

Figure 2-50 *Water droplets on hydrophobic leaf*

The combined equations (2.100) and (2.106) lead to the so-called Young-Dupré equation

$$W^a = \gamma_L(1 + \cos\theta) \tag{2.107}$$

The work of adhesion is directly obtained with the contact angle and the surface energy of the liquid phase. For $\theta > 180°$, the work of adhesion becomes negative and the drop would not spread on the flat surface. The total wetting ($\theta = 0°$) is attained for certain value of W^a. The measurement of contact angle and calculation of work of adhesion is useful to compare the physicochemical affinity of different bitumen-aggregate couples. The Young-Dupré equation can be coupled with either Owens-Wendt or GVOC approach to calculate the different surface tension components of any substrate with a minimum of respectively two or three known liquids.

Owens-Wendt:
$$\gamma_L(1 + \cos\theta) = 2\sqrt{\gamma_S^d \gamma_L^d} + 2\sqrt{\gamma_S^p \gamma_L^p} \tag{2.108}$$

GVOC:
$$\gamma_L(1 + \cos\theta) = 2\sqrt{\gamma_S^{LW} \gamma_L^{LW}} + 2\sqrt{\gamma_S^+ \gamma_L^-} + 2\sqrt{\gamma_S^- \gamma_L^+} \tag{2.109}$$

However, the authors list two potential biases. First, the calculation of the contribution of polar and dispersive forces from either side of the interface is based on an approximate geometrical mean of forces proposed by Fowkes (Fowkes 1964). Secondly, the approximation of the surface energy for solids: the surface tension γ_{SV} differs from its real surface energy γ_S (with its own vapour) because of the adsorbed vapour (A. Hefer and Little 2005). The difference is the equilibrium spreading pressure π_e, which is a measure of the energy release during adsorption. For liquids, π_e is always assumed null, i.e. $\gamma_{LV} = \gamma_L$. For low surface energy solids, including bitumen, this equilibrium spreading pressure is negligible and set to 0 (Bhasin et al. 2006). For solids of high surface energy however, such as metals and some mineral aggregates, it might become non-negligible.

$$\gamma_{SV} = \gamma_S - \pi_e \quad (2.110)$$

Generalized Owens-Wendt

$$\gamma_L(1+\cos\theta) + \pi_e = 2\sqrt{\gamma_S^d \gamma_L^d} + 2\sqrt{\gamma_S^p \gamma_L^p} \quad (2.111)$$

Generalized GVOC

$$\gamma_L(1+\cos\theta) + \pi_e = 2\sqrt{\gamma_S^{LW} \gamma_L^{LW}} + 2\sqrt{\gamma_S^+ \gamma_L^-} + 2\sqrt{\gamma_S^- \gamma_L^+} \quad (2.112)$$

A goniometer apparatus measures the contact angle of tiny drops (few microliters, noted µL) of known liquids (water, diiodomethane…etc). In this method with sessile drop, the roughness of the surface as well as the porosity can alter the wetting regime of the liquids (Vassaux et al. 2017).

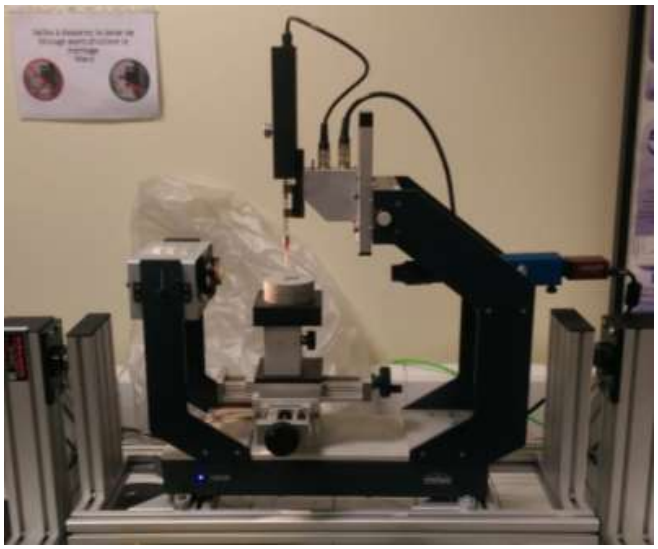

Figure 2-51 *DSA30 goniometer (KRUSS ®) with a cylindrical rock plate sample*

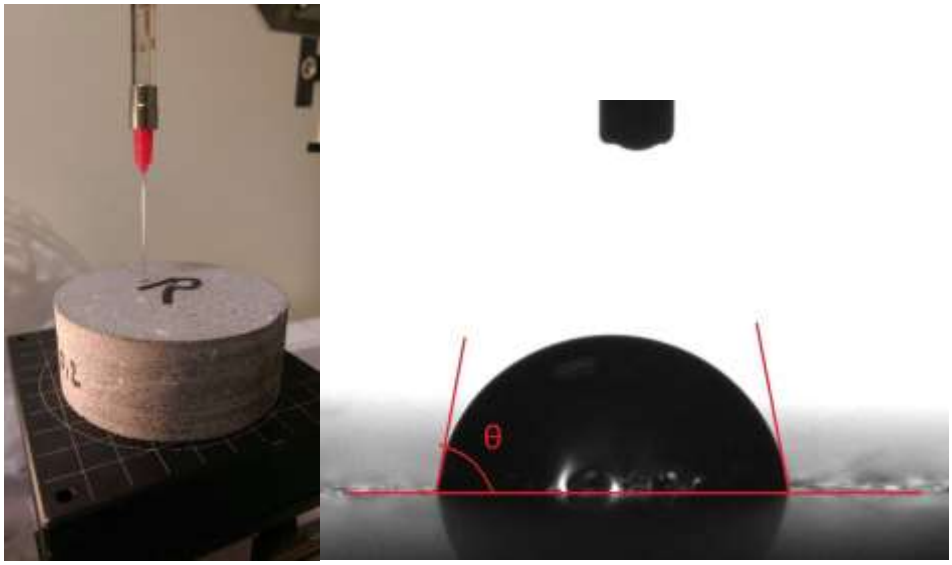

Figure 2-52 *5µL water drop deposit and contact angle measurement*

2.4.2.1.2 Wilhelmy Plate tensiometer technique

The Wilhelmy Plate tensiometer provides an indirect measurement of the dynamic contact angle of a liquid onto a solid substrate. A plate of the tested substrate is suspended to a monitored microbalance, dipped into a recipient of probe liquid and then pulled back out. The force is plotted against the vertical displacement to form hysteresis curves due to the difference of contact angle and meniscus orientation between the advancing phase (downwards) and receding phase (upwards) (Luo et al. 2015). In both cases, the contact angle with the probe liquid is obtained via a simple force equilibrium on the plate, yielding to the equation

$$\cos\theta = \frac{\Delta F + V(\rho_L - \rho_{air})g}{P_S \gamma_L} \tag{2.113}$$

, where ΔF is the weight difference of the plate hanging in air and partially immersed, V is the immersed volume of the substrate, ρ_L the density of the probe liquid, ρ_{air} the density of air, g the local gravitational acceleration and P_S the perimeter of the plate.

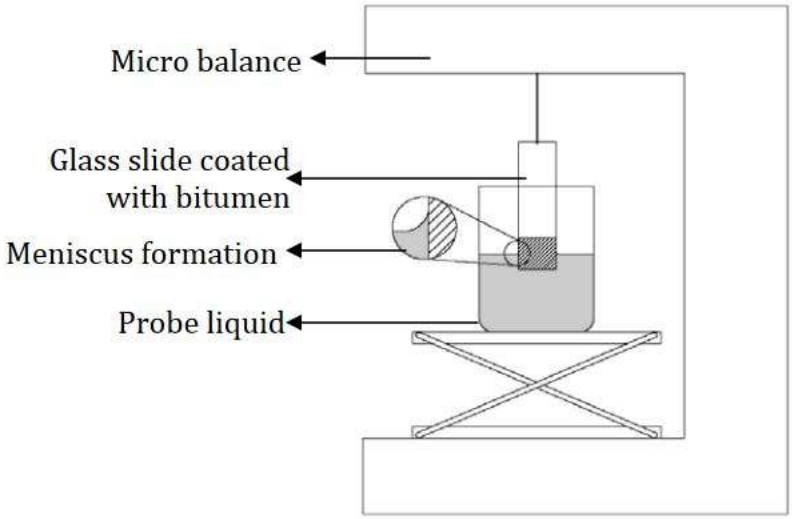

Figure 2-53 *Scheme of the Wilhelmy Plate tensiometer use for bitumen* (Bhasin 2006)

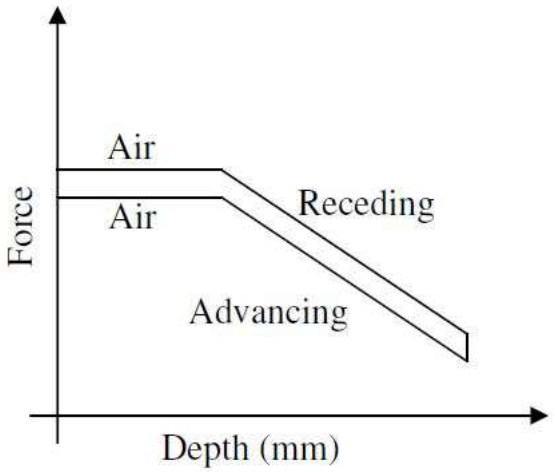

Figure 2-54 *Typical Force-Depth plot obtained with the Wilhelmy Plate tensiometer* (Bhasin 2006)

The Wilhelmy plate method has been used by paving technologists to establish surface tension properties of bitumen (Bhasin 2006; Yildirim 2001). The samples are usually glass plates smoothly covered with the binder. Experimental results show that the advancing contact angle is comparable in trends to the results with the sessile drop technique (Barhamian 2012), although the angle values are not exactly the same.

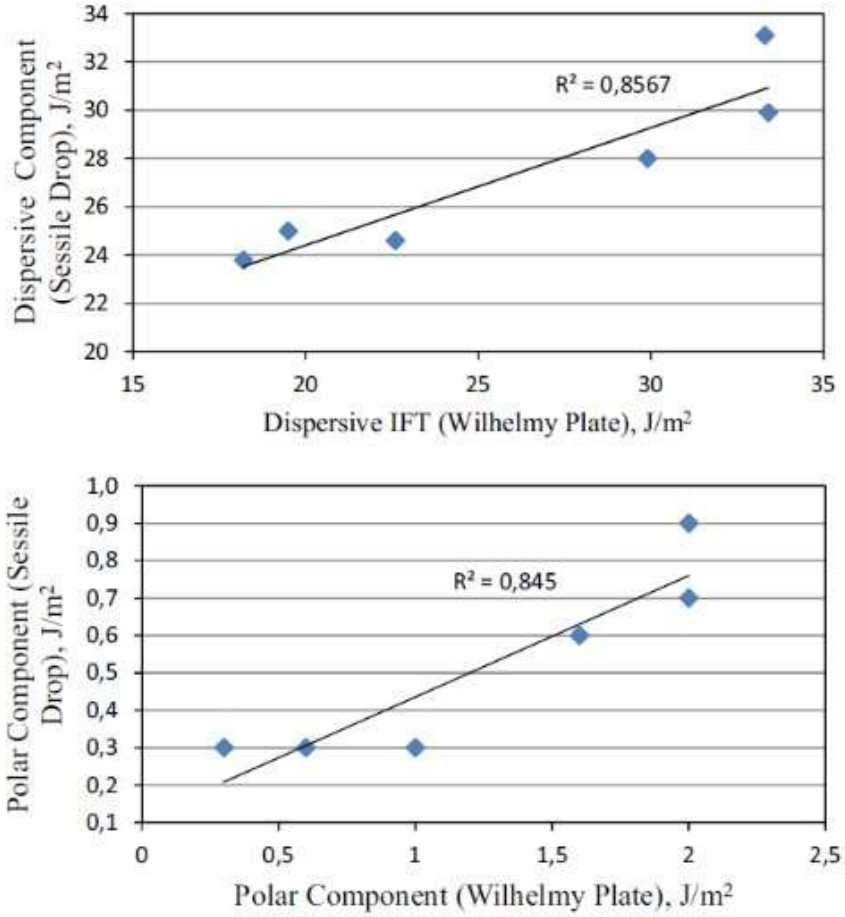

Figure 2-55 *Comparison of surface tension component values obtained with Wilhelmy Plate and Sessile Drop methods on six different 70/100 bitumens at 20°C* (Barhamian 2012)

2.4.2.1.3 Universal Soprtion Device technique

As seen previously, solid substrates may exhibit high surface free energy, possibly leading to the adsorption of the vapour phase when its own surface energy is lower, and characterised by the equilibrium spreading pressure π_e and a contact angle of 0° with most liquids. In this framework, the work of adhesion is given by the equation

$$W^a = 2\gamma_L + \pi_e \qquad (2.114)$$

In opposite to the Young-Dupré equation used for low energy solids and liquids, where π_e was negligible and the contact angle to be determined, the work of adhesion is completely determined by this equilibrium spreading pressure, which can be measured from adsorption isotherm (Jura and Harkins 1944; Bhasin 2006) with the following equation

$$\pi_e = \frac{RT}{MA}\int_0^{p_0}\frac{n}{p}dp \qquad (2.115)$$

, with R the universal gas constant, T the temperature, M the molecular weight of the probe vapour, A the specific surface area of the substrate, n the mass of adsorbed vapour divided per unit mass of substrate and p_0 the saturating vapour pressure of the probe

Adsorption isotherms can be measured with the Universal Sorption Device (USD), described in Figure 2-56. The determination of the surface energy components using Owens-Wendt or GVOC theories is achieved exactly in the same way as for the Sessile Drop or Wilhelmy Plate methods with several probe substances.

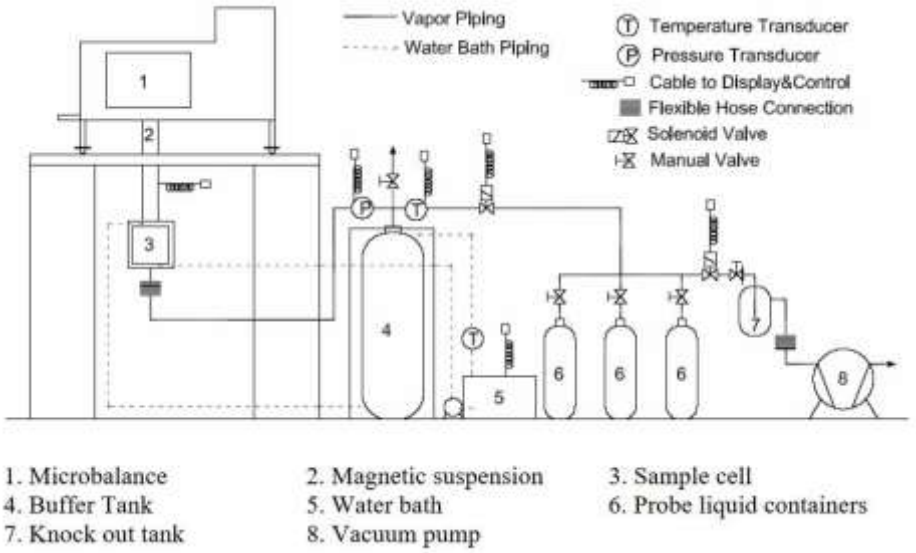

Figure 2-56 *Scheme of the Universal Sorption Device* (Bhasin and Little 2007)

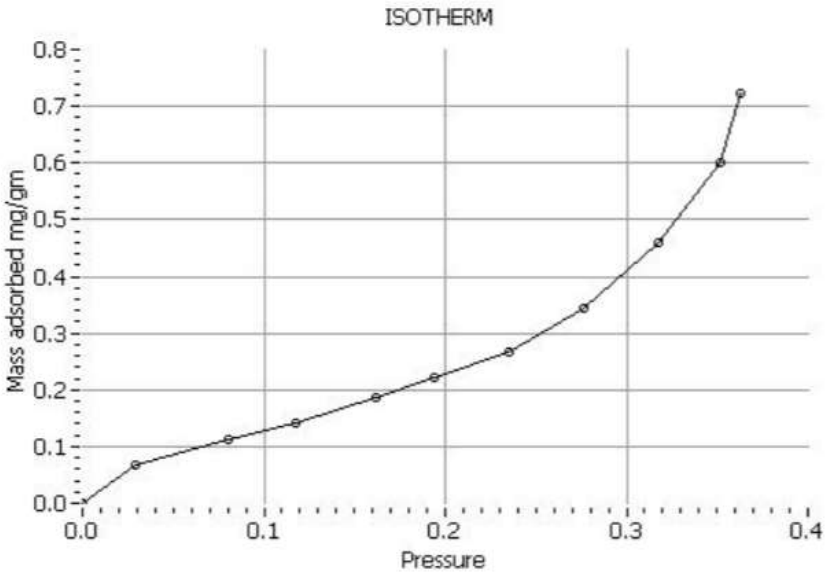

Figure 2-57 *Example of adsorption isotherm* (Lytton et al. 2005)

2.4.2.1.4 Pendant Drop method

The total surface tension of a liquid, such as very hot bitumen, can also be measured using the Pendant Drop method. The curvature of a drop of the studied liquid pending at the tip of a cylindrical syringe create a difference of pressure proportional to the surface tension (Tucker 1938):

$$\Delta P = \gamma_L \left(\frac{1}{R_1} + \frac{1}{R_2} \right) \quad (2.116)$$

, where R_1 and R_2 are the curvature radii in principal directions. The static equilibrium on the lower part of the drop at given altitude z (with $z=0$ at the tip of the drop) yields

$$\pi x^2 \Delta P + (\rho_L - \rho_{air}) g V - 2\pi \gamma_L \sin \varphi = 0 \quad (2.117)$$

, with V the volume of the considered part of the drop. The coordinate system is detailed in Figure 2-58. The surface tension is available with only geometrical considerations on the pendant drop. The same type of goniometer used in the sessile drop method is sufficient to determine the shape of the drop. Measuring the surface energy of hot bitumen (min. 130°C) requires an additional thermal chamber suitable with the optic recording system. Moreover, this method is not used to determine the detailed components of thermodynamic surface energy theories.

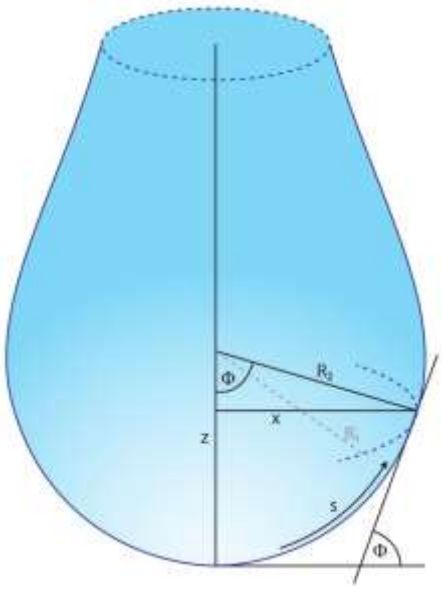

Figure 2-58 *Coordinate system of the pendant drop*

2.4.2.1.5 Surface energy components values of road materials in the literature

Table 2-1 and Table 2-2 are non-exhaustive data collections of surface energies components respectively for aggregates and bituminous binders, with different techniques: Sessile Drop (SD), Wilhelmy Plate (WP) and Universal Sorption Device (USD).

Table 2-1 *Excerpt of surface energy components of aggregates from the literature*

Source	Method	Substrate	γ^{LW} or γ^{d} (mJ/m²)	γ^{+} (mJ/m²)	γ^{-} (mJ/m²)	γ^{AB} or γ^{p} (mJ/m²)	Total γ (mJ/m²)
Koc and Bulut, 2014	SD	Davis limestone	37.23	0.06	11.42	1.66	38.89
	SD	Dolese-Coopeton limestone	37.58	0.13	31.51	4.05	41.63

	SD	Snyder granite	35.15	0.10	8.43	1.84	36.99
	SD	Martin-Mrietta-Mill-Creek granite	35.84	0.42	36.98	7.88	43.72
	SD	Hanson-Davis rhyolite	39.91	0.31	26.26	5.71	45.62
Bhasin, 2006	USD	Limestone	44.10	2.37	259.00	49.55	93.65
	USD	Gravel	57.50	23.00	973.00	299.19	356.69
	USD	Basalt	52.30	0.64	164.00	20.49	72.79
	USD	Granite	48.80	0.00	412.00	0.00	48.80
	USD	Sandstone	58.30	14.60	855.00	223.45	281.75
	USD	Mineral: Albite	47.50	0.70	245.00	21.30	77.10
	USD	Mineral: Calcite	67.00	0.00	427.00	0.00	67.00
	USD	Mineral: Microcline	43.90	0.00	239.00	0.00	46.60
Wasiuddin, 2007	USD	Limestone	51.90	13.00	540.70	167.68	219.58
Lytton et al., 2005	USD	Granite	56.35	43.45	782.70	368.83	425.18
Yildirim, 2001	SD	Montana talc	42.90	0.20	27.40	4.68	47.58
	WP	Montana talc	35.90	0.70	11.10	5.57	41.47
	SD	Vermont talc	44.60	0.10	28.40	3.37	47.97
	WP	Vermont talc	41.40	0.80	13.80	6.65	48.05
Giese and Van Oss, 2002	SD	Na-Montmorillonite	42.40	2.30	33.40	17.53	59.93
Zaidi et al., 2020	USD	Felsic intrusive rock	68.97	17.41	569.68	199.18	268.15

Table 2-2 *Excerpt of surface energy components of bituminous binders from the literature*

Source	Method	Bitumen or mastic	γ^{LW} or γ^{d} (mJ/m²)	γ^{+} (mJ/m²)	γ^{-} (mJ/m²)	γ^{AB} or γ^{p} (mJ/m²)	Total γ (mJ/m²)
Barhamian, 2012	SD	Pure 70/100, "A"	24.80	2.40	6.70	8.02	32.82
	WP	Pure 70/100, "A"	18.16	0.04	4.37	0.82	18.98
	SD	Pure 70/100, "B"	25.40	2.00	5.70	6.75	32.15
	WP	Pure 70/100, "B"	22.58	0.01	4.11	0.41	22.99
	SD	Pure 70/100, "C"	26.30	2.00	5.60	6.69	32.99
	WP	Pure 70/100, "C"	19.55	0.09	4.17	1.19	20.74
	SD	Pure 70/100, "K"	28.20	2.00	5.60	6.69	34.89
	WP	Pure 70/100, "K"	29.89	0.64	7.23	4.30	34.19
	SD	Pure 70/100, "M"	33.30	1.80	5.10	6.06	39.36
	WP	Pure 70/100, "M"	33.32	1.67	8.42	7.50	40.82
	SD	Pure 70/100, "Ref"	30.10	1.90	5.40	6.41	36.51
	WP	Pure 70/100, "Ref"	33.37	0.63	4.42	3.34	36.71
Zaidi et al., 2020	WP	Pure 40/60	19.04	1.32	0.99	2.29	21.33
	WP	Mastic: 50% 40/60 + 50% felsic intrusive rock	23.70	0.35	1.68	1.53	25.23

	WP	Mastic: 50% 40/60 + 40% felsic intrusive rock + 10%HL	28.07	0.01	2.32	0.33	28.40
	WP	Mastic: 50% 40/60 + 30% felsic intrusive rock + 20%HL	28.74	0.00	8.87	0.00	28.74
Bhasin, 2006	WP	PG 64-22	29.90	0.00	1.00	0.00	29.90
	WP	PG 64-28	17.90	0.13	2.88	1.22	19.12
	WP	PG 76-22 "A"	14.70	1.33	1.79	3.09	17.79
	WP	PG 76-22" B"	24.20	0.07	1.31	0.61	24.81
	WP	PG 76-22 "C"	12.10	1.13	2.84	3.58	15.68
	WP	PG 76-22 "D"	21.80	0.63	0.65	1.28	23.08
Hefer et al., 2006	WP	SHRP MRL code: AAB-1	13.50	2.80	0.00	0.00	13.50
	WP	SHRP MRL code: AAD-1	20.20	1.40	0.00	0.00	20.20
	WP	SHRP MRL code: AAF-1	21.40	0.80	0.00	0.00	21.40
	WP	SHRP MRL code: AAM-1	24.80	0.20	0.00	0.00	24.80
	WP	SHRP MRL code: ABD	32.40	0.40	0.00	0.00	32.40

2.4.2.2 Pull-off tests

Adhesive technologists have developed a large variety of mechanical pull-off test setups (Adams 2005). They are used to characterise either the adhesive failure at the binder-substrate interface or the cohesive failure of the binder itself. Paving technologists applied some of these techniques to binder-aggregate interfaces, including:

- Uniaxial pull-off tests. Probably the most direct way to macroscopically quantify adhesion, it consists of pulling a film of the binder perpendicularly to the interface with a flat substrate. The most simple and practical version of this test is the Pneumatic Adhesion Tensile Testing Instrument (PATTI®), that allows measuring only the overall applied pulling force on bitumen films of controlled thickness and surface area on a flat substrate plate. The characterisation of adhesion/cohesion with this device is generally limited to maximal tensile strength. In dry condition, cohesive failure is always expected at tensile strength reaching several thousands of kPa, whereas a partial or total adhesive failure can be obtained when the interface is subjected to a moisture conditioning procedure, with a reduction of tensile strength under 1000 kPa (Canestrari et al. 2010).

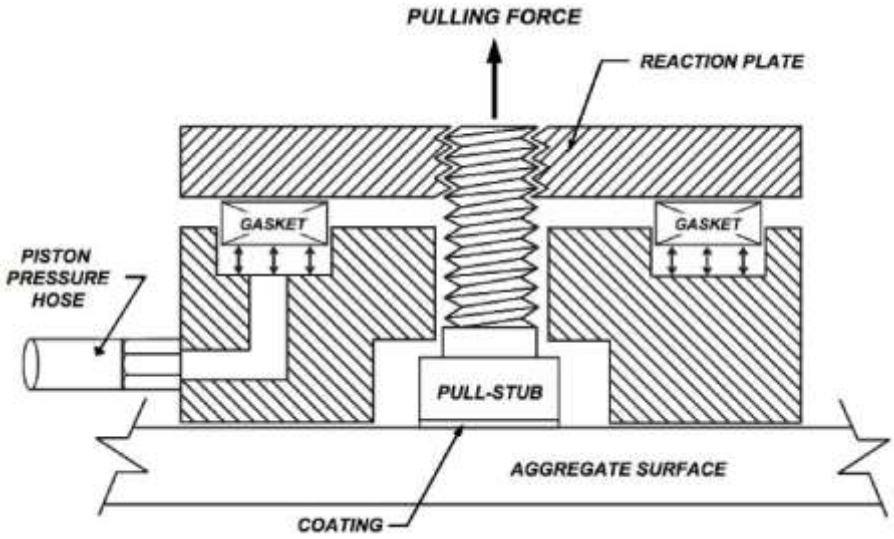

Figure 2-59 *Schematic representation of the PATTI device* (Canestrari et al. 2010)

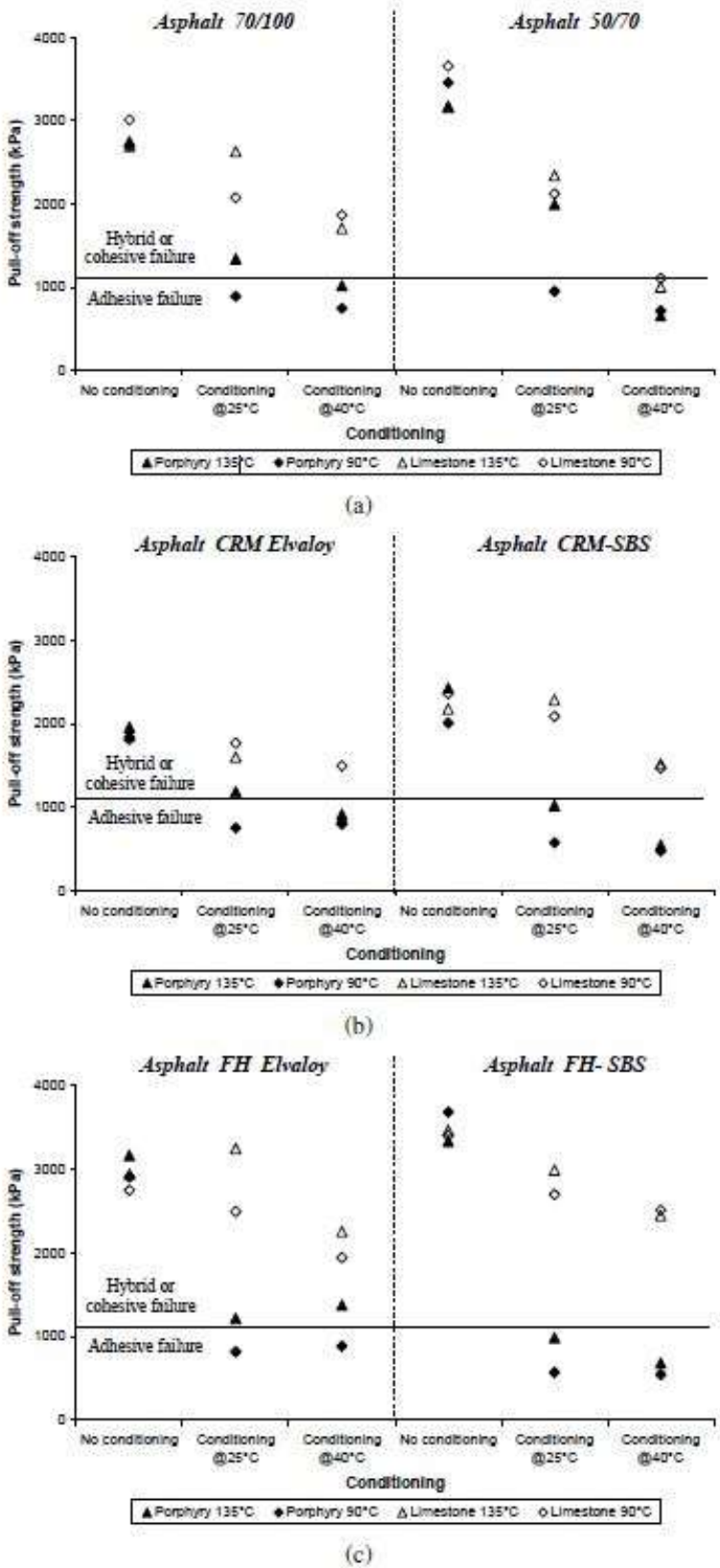

Figure 2-60 *Effect of moisture conditioning on Pull-off test results* (Canestrari et al. 2010)

The “poker-chip” configuration, mounted on an instrumented press, permits to monitor the deformation of the binder as well; a chip of bitumen is “trapped” between two substrate cylinders, which can then be linked to the press axis by clamping jaws (or gluing). With the knowledge of both force and displacement, it is possible to measure and compare adhesion and/or cohesion energies of different binder-aggregate systems. Obviously, the overall dissipated energy needs to be corrected from the part due to viscoelasticity. Moreover, the theoretical calculation of stress-strain distribution in the film reveals important hydrostatic stresses, essentially dependent on the aspect ratio (thickness vs diameter) of the bitumen film (Gent and Lindley 1959; Lindsey et al. 1963; Sultana, Bhasin, and Liechti 2014). These considerations were thoroughly discussed in Campaign III of this thesis (Chapter 6), and in general should be taken into account to perform adhesion tests that are more comparable to the real bitumen-aggregate interface in the mixtures, as experimental evidence confirms (J. Zhang, Airey, and Grenfell 2015).

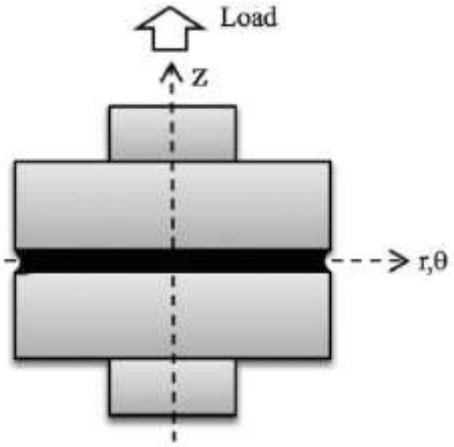

Figure 2-61 *Scheme of the Poker-chip geometry* (Sultana, Bhasin, and Liechti 2014)

More complex geometries for the thin have been proposed, in order to specifically study the healing potential of bitumen after repeated local failure (De la Roche et al. 2003).

- Peel test. A metallic peel arm is bonded to a bitumen film, itself applied on the studied substrate. The arm is then stripped with monitored force and displacement (J. Zhang et al. 2016). The adhesive fracture energy is derived from force-displacement curves, corrected from deformation energy terms of the peel arm.

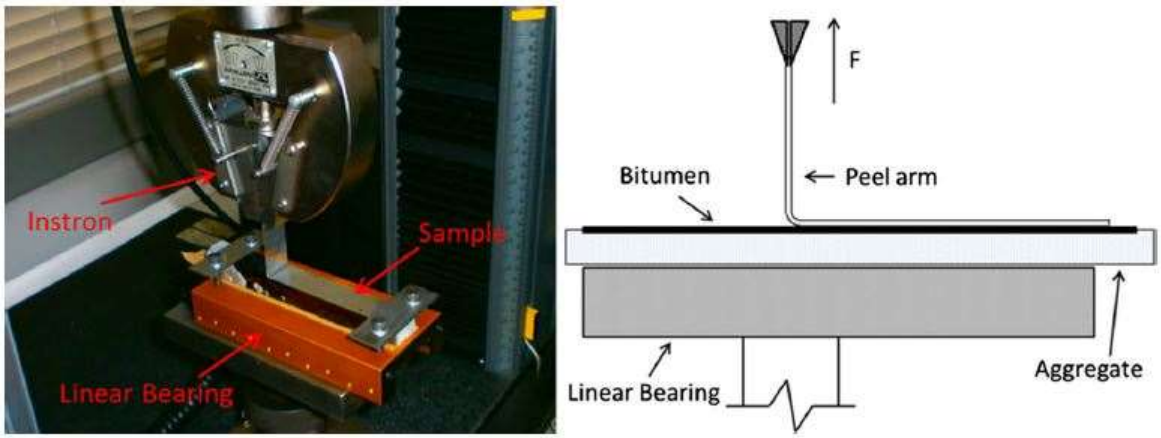

Figure 2-62 *Peel test* (J. Zhang, Airey, and Grenfell 2015)

- Impact fracture tests. The fracture characteristics of bituminous binders have been studied via the Vialit Cohesion Pendulum Test (Geoffrey M. Rowe 2016; AFNOR 2017c). The same method is transposable to the bitumen-aggregate interface. The other type of impact test is the Vialit plate method (Read and Whiteoak 2003). Aggregate particles are pressed to a tray of bitumen laid on a metallic plate. The plate is turned upside down and submitted to steel ball impacts from a controlled height. The percentage of detached aggregate particles after each impact is monitored.

2.4.3 Moisture sensitivity of bituminous mixtures

In the literature, the quality of bitumen-aggregate adhesion in bituminous mixtures is often associated to a low moisture sensitivity, the direct consequence of a good capacity to prevent stripping caused by water migration at the binder-aggregate interface. From the perspective of previous section 2.4.1.2, adhesion in dry and wet conditions are two very different things. However, from a road-engineering point of view, the bitumen-aggregate adhesion in dry condition is *a priori* rarely an issue, whereas moisture-induced damage is a real threat of pavement distress. This is why paving technologists studied in detail the bitumen-aggregate interface in wet conditions and developed testing methods to characterise the moisture sensitivity of bituminous mixtures.

2.4.3.1 Mechanisms of deterioration of bituminous mixtures in presence of water

Caro et al. (Caro et al. 2008a; 2008b) wrote a review of the possible mechanisms of deterioration of bituminous mixtures in pavement due to moisture. These mechanisms possess two phases:

- Phase 1: moisture transport. The main modes of moisture transports are water permeability, water capillarity rise and vapour diffusion. Moisture transport is the result of combined internal (inherent to the mixture) and external parameters (Harvey and Lu 2005). External factors that influence the most moisture transport in pavement mixtures are cumulated rainfall, pavement structure and age. Surprisingly, cumulative truck traffic appears to be marginal. As for internal factors, air void contents, mix type and the use of anti-stripping additives are the most important ones.
- Phase 2: response of the system, ultimately leading to a loss of integrity. Six potential responses are identified (D. N. Little and Jones 2003; Kringos and Scarpas 2005; Kringos, Scarpas, and Kasbergen 2007): Debonding of bitumen, displacement of mastic previously at the interface, weakening of mastic cohesion by long-term loss of material, microcracks in mastic or aggregate, desorption and washing of the outer layers of mastics, and finally spontaneous emulsification of water in bitumen.

2.4.3.2 Characterisation of moisture sensitivity

The laboratory characterisation of moisture sensitivity has widely been studied since the 1960s. The complexity of moisture damage mechanisms and parameters, presented in the previous section, has made it very difficult for paving technologist to design a unique, reliable test, that is also consistently comparable to in situ performance.

The most basic approach is to observe the effect of water on a loose mix; the Boiling Test (ASTM D3625 2012) proposes to visually quantify the percentage of bitumen-stripped surface on aggregate after immersion in boiling water for a short period of time. The Rolling Bottle Test (AFNOR 2013b) uses the same visual evaluation after 6 hours of immersion at ambient temperature.

The most rational approach was to simulate the effect of moisture on compacted bituminous mixtures in laboratory and to measure the loss of thermomechanical properties due to accelerated wet conditioning. Based on this approach, several test methods differ either in sample conditioning and/or tested mechanical property:

- The European Indirect Tensile Strength Ratio test (ITSR) (AFNOR 2018d)
- The Lottman and modified Lottman tests (also based on ISTR) (Aschenbrener 1993; AASHTO T 283 2014)
- The Immersion/Compression (i/C) test, or Duriez test (compressive strength) (AFNOR 2018d)
- Hamburg Wheel-Tracking Device test (rutting by creep flow) (Aschenbrener 1995a; Q. Lu and Harvey 2006)

On-going efforts to improve and rank these tests by sensitivity, reliability and by relatability to in situ performances are fuelled by the possibility of a better understanding of the complex role adhesion in bituminous mixtures and moisture damage (DeCarlo et al. 2020; Moreno-Navarro et al. 2014; Zofka, Maliszewski, and Bernier 2014). Establishing the relationship between the fundamental moisture damage mechanisms, the binder-aggregate adhesion properties and the moisture sensitivity of mixtures are one of the current challenges of paving technologists.

2.4.4 Relationship between binder-aggregate adhesion test results and mixture performances

The surface energy framework presented in section 2.4.2.1 gives a promising quantitative approach to measure the influence of the constituents properties on the adhesion, and ultimately to relate it to the mixture performances (Bhasin 2006; Vassaux et al. 2017; Boulangé, Bonin, and Saubot 2013; Moghadas Nejad, Hamedi, and Azarhoosh 2013; Baldi-Sevilla et al. 2017).

Interesting values retained for analysis of moisture sensitivity are the dry work of adhesion between aggregates and bitumen W_{AB}^{ad}, the work of debonding in presence of water W_{ABw}^{ad} (always negative), as well as the work of cohesion of bitumen W_B^c. Several parameters are proposed by Bhasin to characterise moisture susceptibility of a bitumen-aggregate couple (Bhasin 2006):

$$ER_1 = \left| \frac{W_{AB}^{ad}}{W_{ABw}^{ad}} \right| \tag{2.118}$$

$$ER_2 = \left| \frac{W_{AB}^{ad} - W_B^c}{W_{ABw}^{ad}} \right| \tag{2.119}$$

$$ER_3 = SSA \times ER_1 \tag{2.120}$$

$$ER_4 = SSA \times ER_2 \tag{2.121}$$

$$ER_5 = \sqrt{SSA} \times ER_2 \tag{2.122}$$

,with *SSA* the specific surface area of the aggregate. The parameters using ER_1 are accurate to characterise the moisture sensitivity of well wet interfaces. On the other hand, the wettability is addressed by parameters using ER_2, since the bitumen theoretically spreads on the substrate only if the dry work of adhesion is bigger than the work of cohesion of the bitumen. ER_5 is the parameter that incorporates bitumen wettability and aggregate geometrical properties and best correlates to moisture sensitivity of mixtures based on laboratory tests and field performances (Bhasin 2006).

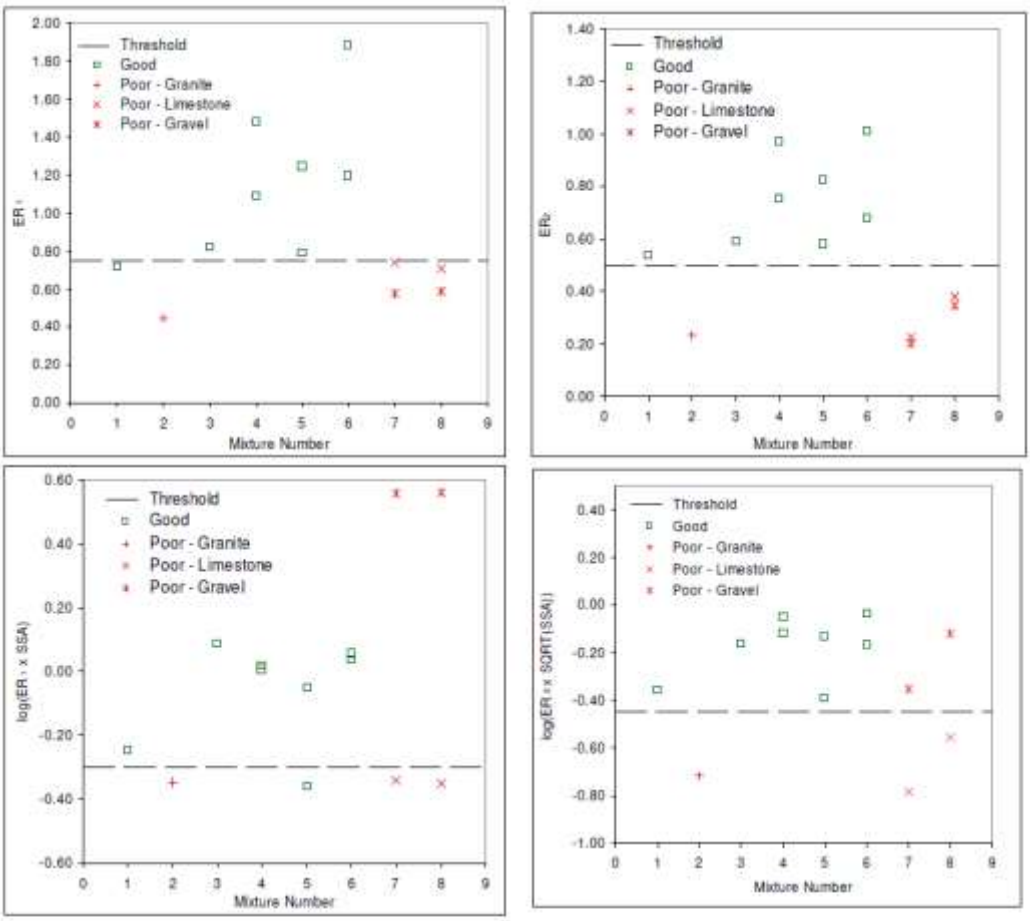

Mix Design No.	Perfor-mance	Asphalt Grade	Aggregate Types	
1	Good	PG 76-22 A	Granite	
2	Poor	PG 76-22 B	Granite	
3	Good	PG 76-22 C	Quartzite	
4	Good	PG 76-22 C	Sandstone A	Sandstone B
5	Good	PG 76-22 C	Gravel A	Limestone A
6	Good	PG 76-22 D	Sandstone A	Sandstone B
7	Poor	PG 64-22	Limestone B	Gravel B
8	Poor	PG 64-28	Limestone B	Gravel B

Figure 2-63 *Bond energy parameters as a function of field evaluation of moisture sensitivity of different mixtures* (Bhasin 2006)

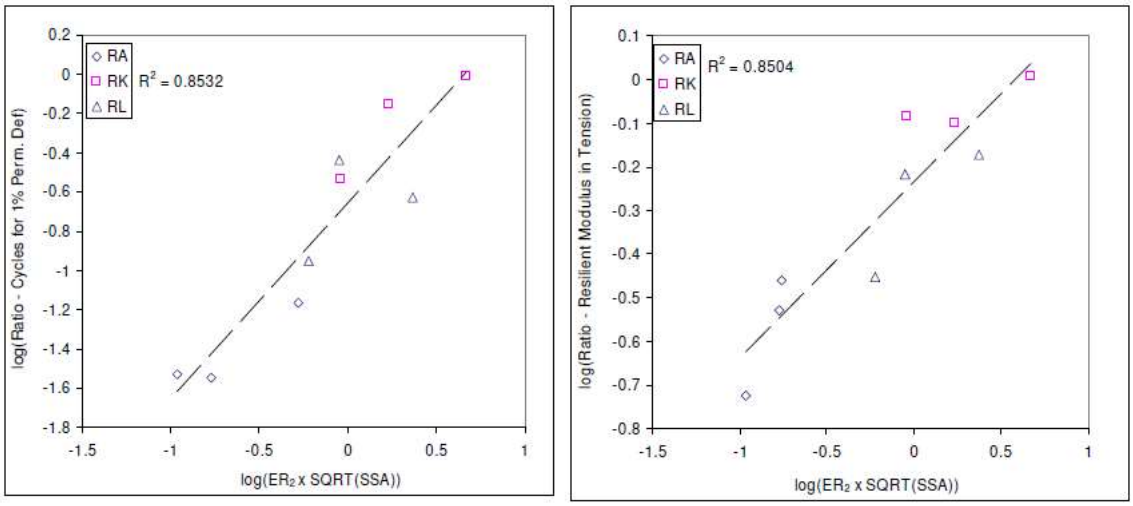

Nine mixtures were selected for the mechanical tests using aggregates RA (granite), RK (basalt) and RL (limestone) and asphalt binders AAB, ABD and AAD.

Figure 2-64 *Bond energy parameters as a function of laboratory evaluation of moisture sensitivity on fatigue and stiffness performance of different mixtures* (Bhasin 2006).

Other works show that the surface energy approach could be adequate to predict fatigue performances of modified materials from unmodified ones (Azarhoosh, Abandansari, and Hamedi 2019). In this study, the incremental use of nano-lime (from 0 to 8% of bitumen weight) increases the base component of bitumen, which with high acid-component substrates, induces an increase of work of adhesion as well as a reduction of work of debonding in presence of water. Fatigue performances are simultaneously enhanced by the increasing use of nano lime in both dry and wet conditioning cases.

2.4.5 Anti-stripping agents

Bitumen-aggregate adhesion depends on the physicochemical affinity between the two phases. The use of anti-stripping agents is sometimes necessary to improve adhesion in dry condition but most importantly to reduce moisture susceptibility of bituminous mixtures in presence of water. Many studies have confirmed the positive impact of these additives in laboratory and in situ conditions (Aschenbrener 1993; Lesueur, Petit, and Ritter 2013). Two types of anti-stripping agents exist: mineral additives in filler that changes the mastic adhesive properties (among others) and anti-stripping liquids that act as surfactant at the bitumen-aggregate interface.

The preferred mineral additive in paving technology is hydrated lime. It has been extensively used for five decades, according to a state of the art review by Lesueur et al. (Lesueur, Petit, and Ritter 2013) and serves as standard for improving bituminous mixtures durability in general. Representing usually 1 to 1.5% of the dry aggregate mass, its use can increase the pavement life duration from 2 to 10 years, according to a survey conducted across many American state Departments of Transport (DOTs) (Hicks and Scholz 2003). The mechanisms behind such performance improvement are detailed in Lesueur's review (Lesueur, Petit, and Ritter 2013). Regarding surface energy aspects, the use of hydrated lime in mastics significantly decreases the work of debonding in presence of water (Zaidi et al. 2020), although the magnitude of the effect depends on the mastic's aggregate nature.

Concerning liquids anti-stripping agents, commercial chemicals are generally a collection of various amine-based agents (Corté and Di Benedetto 2004). They are mixed with the bitumen in very small proportion (approximately 0.1% of bitumen mass) before the mixture fabrication. Once in contact with the aggregate, the anti-stripping agent molecules are adsorbed and can even react with the surface silanol groups to create a strong covalent chemical bond.

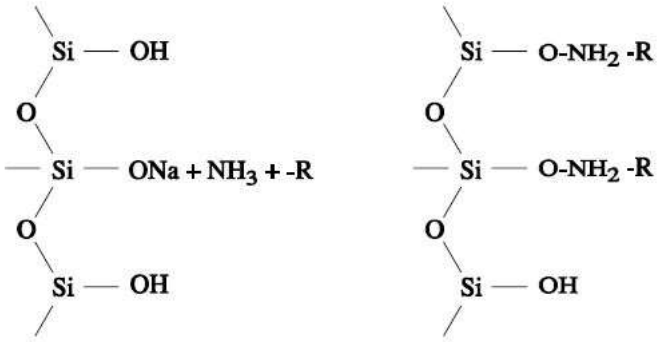

Figure 2-65 *Scheme of amine-based agent possible reactions in contact with siliceous substrate*

Silane-base agents constitute another variety of liquid anti-stripping agent (Plueddemann 1991). Their application technique is the same as amine-base ones, by mixing with bitumen previously to mixture fabrication. The amine reactive part is replaced by a silane that will react with surface silanol to create a siloxane bond; this is the silanisation process (Glass et al. 2011). Silane technology has traditionally been used in textile industry and in the medical field, for its capacity to modify surface properties with monolayers of many molecule types (Arkles 1977; 2011). Very recently, it has been tested to improve bitumen-aggregate adhesion (Min et al. 2015; Rossi et al. 2017; Orozco et al. 2018).

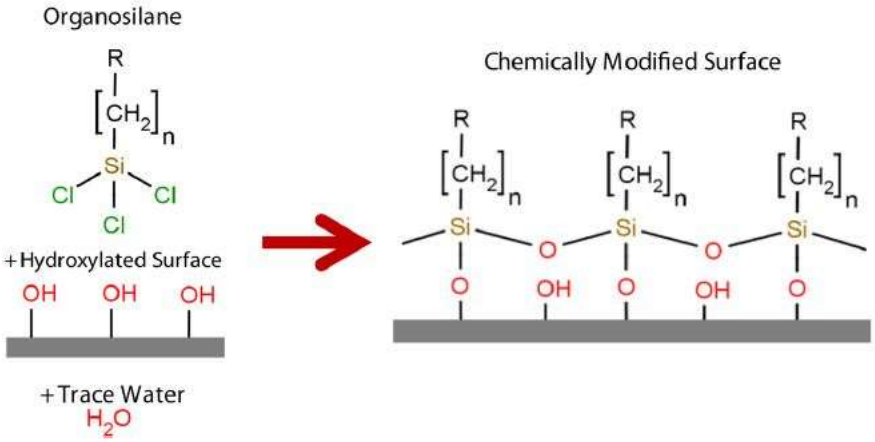

Figure 2-66 *Scheme of silanisation process* (Glass et al. 2011)

3 Experimental devices and tested materials

3.1 Experimental set-ups and related sample preparation

3.1.1 Binder thermomechanical test

3.1.1.1 Dynamic Shear Rheometer (DSR)

The DSR used in this study is a Modular Compact Rheometer (MCR) 501 by Anton Paar®, provided by Eiffage©. The plate-plate geometry was used, with either an 8mm-diameter or 25mm-diameter configuration.

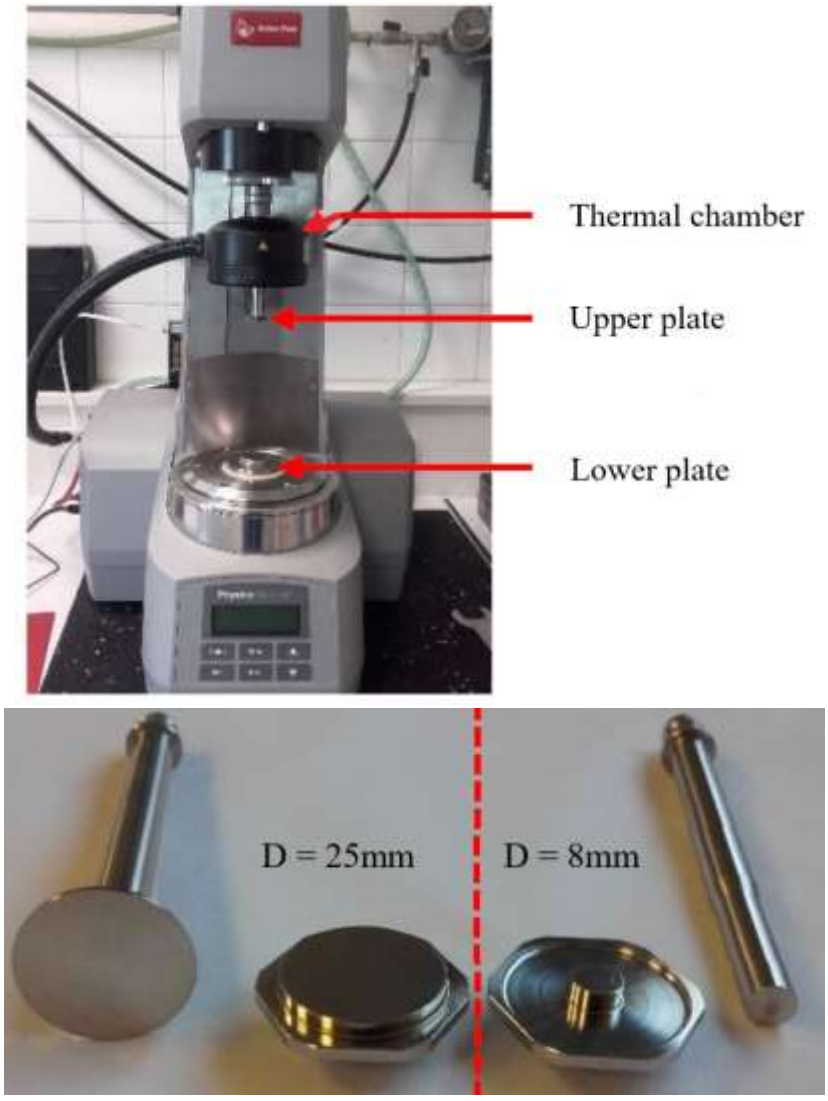

Figure 3-1 *MCR 501 by Anton Paar®, couertesy of Eiffage Company*

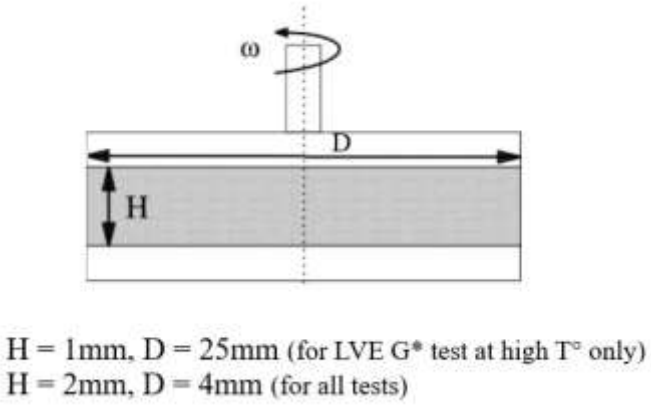

Figure 3-2 *DSR plate-plate specimen geometry*

The specimen preparation was made accordingly to European standards (AFNOR 2012e) in two steps; first, hot bitumen is poured into a silicone moulds to create ready-to-use cylindrical chips. Secondly, these chips are placed on the DSR lower plate and then are heated at 90°C or $T_{RB} + 20°C$. The upper plate is carefully lowered to obtain the desired gaping distance H between the plates with the axial controller. Practically, it is recommended to remove the laterally overflowing bitumen at H + 0.025mm and to keep the residual excess when H is reached, in order to alleviate the risks of stripping due to the thermal contraction of both the axis and the bitumen during cooldown. The usual cooling rate is 2°C/min, and 30 more minutes are necessary to ensure the thermal equilibrium before any test. For almost all results in this thesis, the 8mm-diameter plate geometry was used. The 25mm-diameter plate geometry was only required to measure the low G* values during LVE characterisation tests at high temperature (T ≥ 40°C).

3.1.1.2 Annular Shear Rheometer (ASR)

The Annular Shear Rheometer was developed by the *LGCB-ENTPE*, nowadays known as *LTDS-ENTPE (Laboratoire de Tribologie et Dynamiques des Systèmes – Ecole Nationale des Travaux Publics de l'Etat)* of the University of Lyon, in the 2000s to study the rheology of bituminous binders, from bitumen and mastic (Delaporte 2007). The ASR, described in Figure 3-3, allows applying a homogeneous shear on an annular specimen trapped between metallic cylindrical moulds. For this thesis, the ASR was mounted on a MTS® 50kN servo-hydraulic press. The applied distortion γ is proportional to the relative axial displacement between the internal and the external cylinders, monitored by three MTS extensometers (≈0.2µm precision, which corresponds to ≈2µm/m precision for the distortion in the binder). The shear stress was obtained either via the press 50kN load cell (15N precision), or a much smaller MTS® 200N load cell (0.1N precision) mounted on a by-pass system. The temperature was recorded by four TC SA® thermocouples (0.5mm diameter, 0.15°C precision) plunged into the specimen. The binder, which can flow at high temperature, is kept in place by a thin membrane and a counter-pressure system underneath the specimen. The whole set-up was placed into a Bia Climatic® thermal chamber. ASR specimens require a 4-hour conditioning to reach thermal equilibrium. An exhaustive description of the ASR set-up was made by Delaporte, including essential verifications such as stress/strain homogeneity, thermal equilibrium, potential biases due to inertia forces, membrane stiffness, not centred moulds…etc. (Delaporte 2007).

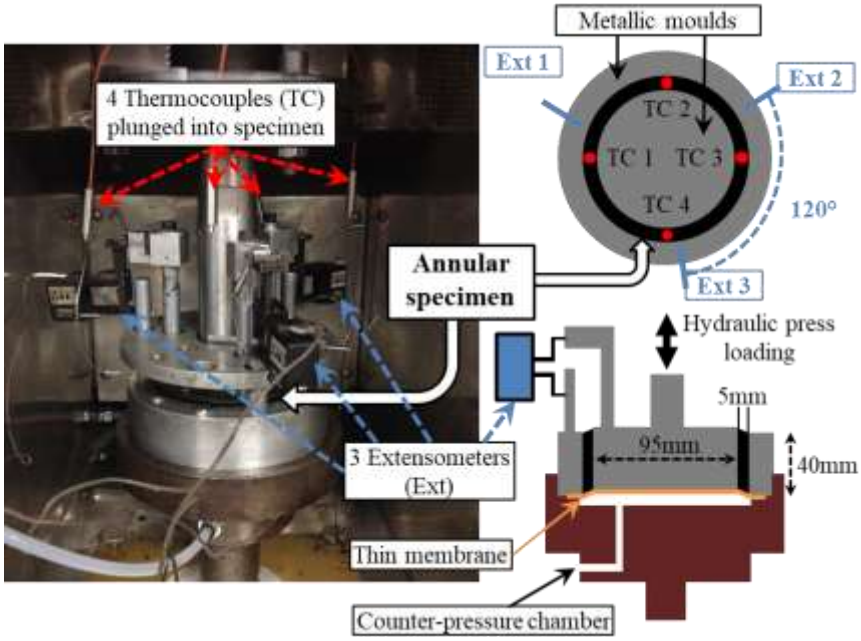

Figure 3-3 *ASR set-up*

Figure 3-4 *Load cells and by-pass system on MTS servo-hydraulic press used with ASR*

The homogeneous stress-strain state in the binder during a shear test with ASR can be expressed

$$\bar{\bar{\sigma}} = \begin{pmatrix} \sigma_{rr} & 0 & \tau \\ 0 & \sigma_{\theta\theta} & 0 \\ \tau & 0 & 0 \end{pmatrix} \quad (3.1)$$

$$\bar{\bar{\varepsilon}} = \begin{pmatrix} 0 & 0 & \gamma/2 \\ 0 & 0 & 0 \\ \gamma/2 & 0 & \varepsilon_{zz} \end{pmatrix} \quad (3.2)$$

, following the coordinate system of Figure 3-5. The shear stress is the load of the axis divided by the average of the inner and outer surface areas of the annular specimen. The distortion is the average of the three extensometers displacements divided by the sample thickness:

$$\tau = \frac{F}{\pi h(R_{int} + R_{ext})} \tag{3.3}$$

$$\gamma = \frac{1}{3}\sum_{i=1}^{3}\gamma_i = \frac{1}{3e}\sum_{i=1}^{3}\Delta h_i \tag{3.4}$$

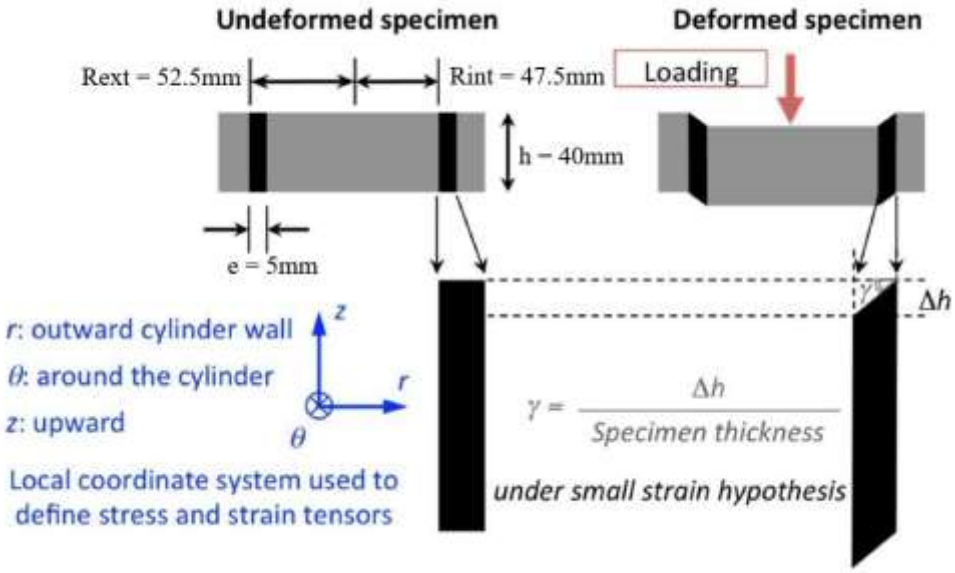

Figure 3-5 *Distortion calculation and coordinate system of a shear test with ASR* (L. Babadopulos 2017)

The ASR sample preparation is illustrated in Figure 3-6. The cylinders were centred and kept together by a metallic centring disc. A plastic film was placed between this disc and the bottom of the mould to avoid bitumen leak. The bitumen was heated at 150°C for 3h, similarly to the standards for laboratory mixing (AFNOR 2017a). The mould was also heated at 150°C, although only between 1 and 2h to avoid deteriorating the plastic film. Before being poured, the bitumen must be usually manually stirred. This step is especially mandatory for polymer-modified bitumen. For mastics, it is better to use a mechanical stirring machine. Eventually, the excess of binder was removed after cooldown and the specimen is kept in a refrigerator at a temperature between 5 to 10°C, at least during one week.

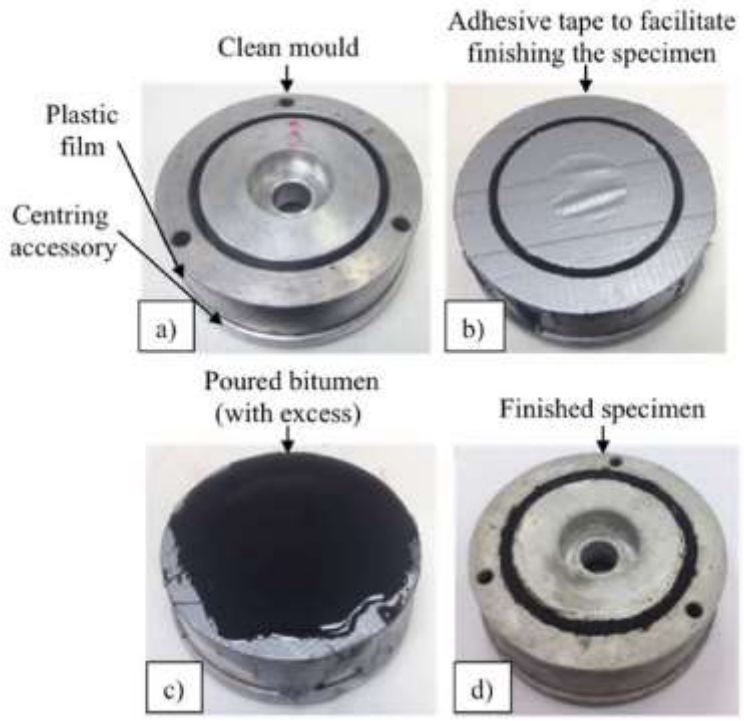

Figure 3-6 *ASR sample preparation* (L. Babadopulos 2017)

3.1.2 Bituminous mixtures test

3.1.2.1 Two-Point Bending test on trapezoidal specimen

The Two-Point Bending (2PB) test on trapezoidal specimen is a standard, inhomogeneous test to characterise thermomechanical performances of bituminous mixtures. The principle is to apply a controlled cyclic displacement at the top of the specimen, whereas the base is fixed. The axial strains and stresses induced by the bending are calculated respectively from the monitored beam top displacement and bending force, using Euler-Bernoulli beam theory. In this work, all 2PB tests were performed with a Vectra® apparatus from Eiffage Company. The complete description of the 2PB apparatus can be found in the Appendix A of the European norm (AFNOR 2012c; 2012d).

Figure 3-7 *Vectra® 2PB apparatus and trapezoidal mixture specimen (height = 250mm), courtesy of Eiffage Company*

The samples were sawn from mixture plates made with a laboratory wheel roller compactor, still following the European norm (AFNOR 2007b).

3.1.2.2 Tension-Compression test on cylindrical specimen

The Tension-Compression (TC) test on cylindrical specimen is a homogeneous axial test, also designed to characterise thermomechanical performances of mixtures. The axial loading was performed with a MTS® servo-hydraulic press. The axial stress was obtained via the MTS® 50kN press load cell (15N precision). The axial strains were measured with three Epsilon® extensometers (Model 3542). It is possible to record radial strains with non-contact sensors, as presented in Figure 3-8 in order to achieve a 3-D characterisation of the material behaviour, although this was not in the scope of this work. The homogeneous stress-strain state in middle of the specimen is therefore written

$$\bar{\bar{\sigma}} = \begin{pmatrix} 0 & 0 & 0 \\ 0 & 0 & 0 \\ 0 & 0 & \sigma \end{pmatrix} \tag{3.5}$$

$$\bar{\bar{\varepsilon}} = \begin{pmatrix} \varepsilon_{rr} & 0 & 0 \\ 0 & \varepsilon_{\theta\theta} & 0 \\ 0 & 0 & \varepsilon \end{pmatrix} \tag{3.6}$$

$$\sigma = \frac{F}{\pi R^2} \tag{3.7}$$

$$\varepsilon = \frac{1}{3}\sum_{i=1}^{3} \varepsilon_i = \frac{1}{3}\sum_{i=1}^{3} \frac{\Delta h_i}{l} \tag{3.8}$$

, with F the applied load, R the radius of the cylindrical specimen, Δh_i the relative displacement measured by the extensometers and l the gauge length of the extensometers.

The surface temperature of the specimen was measured with a TC-SA® PT 100 probe, and the whole set-up was concealed in a Bia Climatic® thermal chamber.

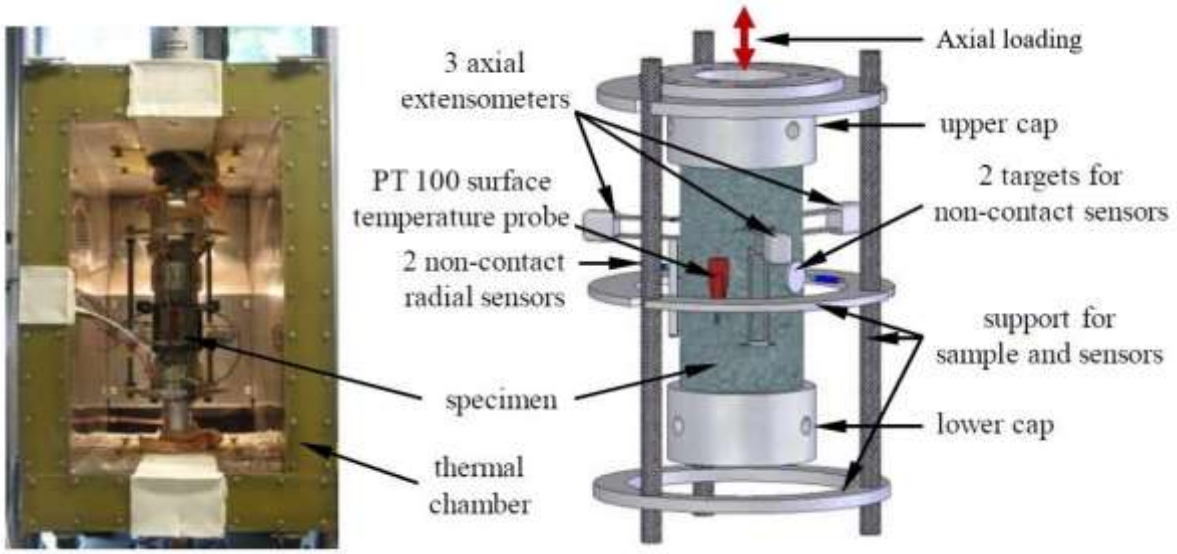

Figure 3-8 *TC on cylindrical specimen set up* (L. Babadopulos 2017)

The cylindrical samples were cored from mixtures plates made with a wheel roller compactor, similarly to the 2PB specimens. The axis of the specimen were parallel to the sweep direction of the compactor wheel (longitudinal), as described in Figure 3-10. As the cut of the specimens requires a lot of cooling water jet, a minimum of two-week delay between the cut and the tests was respected. The samples were mounted on the press axis thanks to metallic caps. The first cap was centred and glued with Araldite® adhesive on a specific centring device, whereas the second one was glued after being mounted on the press, in order to avoid any residual bending stress from misalignment.

Figure 3-9 *Roller compactor, courtesy of Eiffage Company*

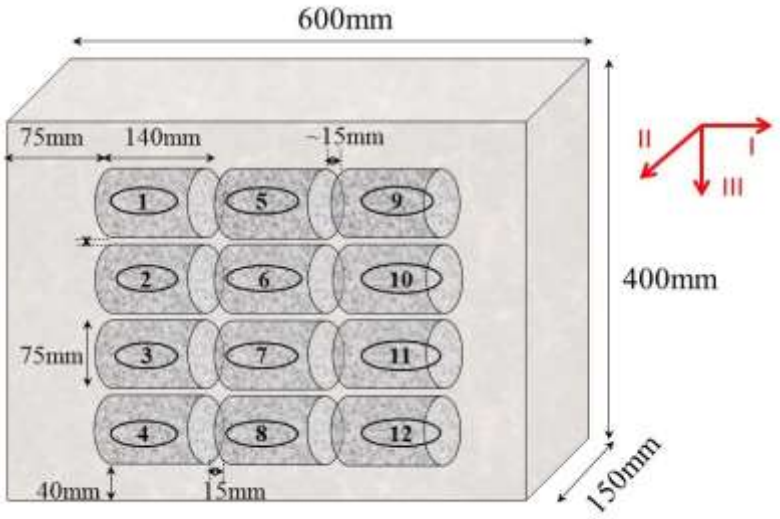

Figure 3-10 *Coring scheme for cylindrical specimen*

3.1.2.3 Indirect Tensile test

The Indirect Tensile (IT) test allows applying tensile stresses by a simple compression on diametric sides of a cylindrical specimen of mixture. This geometry is typically used to determine maximal Indirect Tensile Strength (ITS) of materials during monotonic compression (AFNOR 2018d). The horizontal tensile stresses peak in the vertical diametric plan, and are in practice quasi-homogeneous except near the bearing plates. Nevertheless, they are approximated by the analytical solution of a simplified case (where the compressive load is concentrated on one line) by Hertz (Hertz 1895):

$$\sigma = \frac{P}{\pi D h} \tag{3.9}$$

, with P the applied load, D and h the diameter and the height of the cylinder.

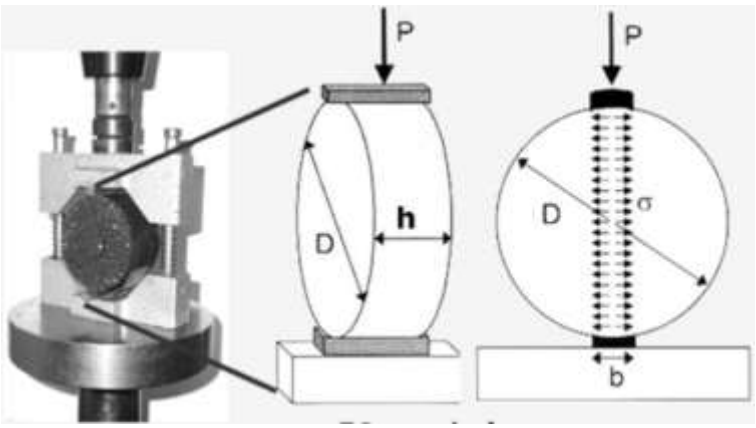

Figure 3-11 *Indirect Tensile test set up* (Grönniger, Wistuba, and Renken 2010)

In this thesis, the IT set-up was used exclusively to perform ITS tests to evaluate the moisture sensitivity of mixtures. Hence, the samples were prepared with the gyratory compactor following the related European standards (AFNOR 2007a; 2018d).

3.1.3 New thermomechanical interface test on bitumen thin film

This section is voluntary kept empty, as the related test was designed during the campaign III of this thesis. The description of this test and the sample preparation are exhaustively covered in Chapter 6

3.1.4 Surface analysis set-ups

3.1.4.1 X-Ray Photoelectron Spectroscopy

X-ray Photoelectron Spectroscopy (XPS) is a surface analysis technique that exploits the photoelectric effect and the Auger effect to identify and quantify elements and even strong chemical bonds (covalent) at the very surface of a given solid (≈10nm depth). The sample is placed in a vacuum chamber ($<10^{-11}$ bar) and bombarded with high energy X-ray photons. Excited surface elements emit core electrons, with a unique kinetic energy depending on the nature of the element, the electronic core layer involved and the potential chemical bonds with neighbour atoms. The electrons create a weak current, which intensity is monitored. Since the conservation of energy implies that the kinetic energy of the emitted photoelectron equals the energy of the absorbed photon *hv*, the sole knowledge of the X-ray frequency is sufficient to identify the original element. A typical XPS spectrum shows various peaks of intensity added to a background (BG) curve, as a function of the binding energy of the photoelectron (in eV). A complete description of the method is available in Moulder et al. (Moulder et al. 1992). In this thesis, a VersaProbe II® spectrometer as well as SmartSoft VP acquisition software, both from ULVAC-PHI©, were used at LTDS. The analysis of the spectra and the determination of the element concentrations were carried out with Multipak® software.

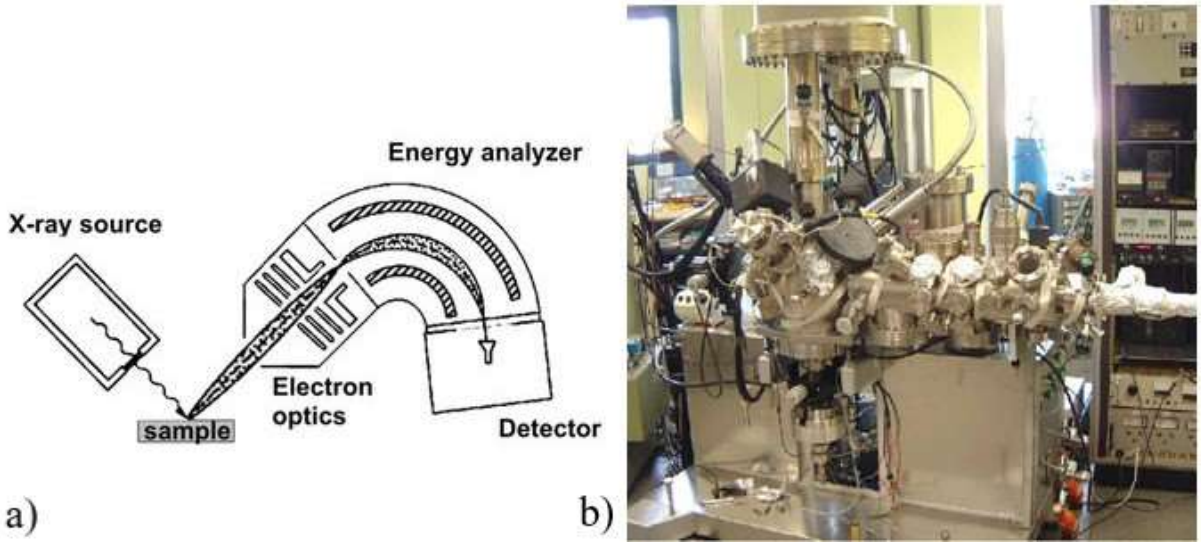

Figure 3-12 *a) Scheme of XPS principle, b) VersaProbe II ® XPS by ULVAC-PHI©*

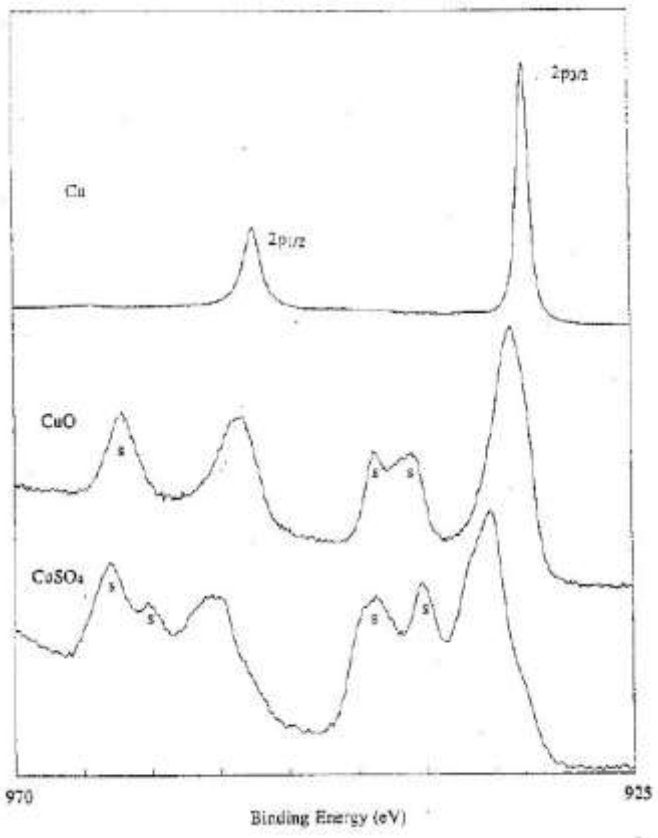

Figure 3-13 *XPS spectra of Cu, CuO and CuSO4* (Moulder et al. 1992)

The preparation of the sample was straightforward: few aggregates of the studied substrate are stuck onto a 4-cm-diameter circular plate. For aggregates larger than 0.5cm, a screw-clamp system is necessary. Although surface cleaning techniques exist, such washing with oxygen peroxide + sulphuric acid solution and/or ultrasonic bath, the tested substrates were directly put on the testing plate. The vacuum degassing could take several hours or even one day before performing the spectra acquisition.

Figure 3-14 *Two road aggregates (D ≈ 1cm) clamped onto the XPS testing plate*

3.1.4.2 Surface free energy and contact angle measurements

The characterisation of surface free energy for road aggregates and bitumen is reviewed in Section 2.4.2.1 In this work, two goniometers, a DSA30® (at LTDS laboratory) and a DSA100® (at Eiffage© laboratory) both by KRUSS© were used for direct contact angle measurement with sessile drop (SD), and for the pendant drop (PD) methods. Both goniometers allow measurement with probe liquids at ambient temperature, whereas only the DSA100® was able to perform measurement with hot bitumen drops, thanks to a regulated heating system. The associated image analysis software by KRUSS© was used.

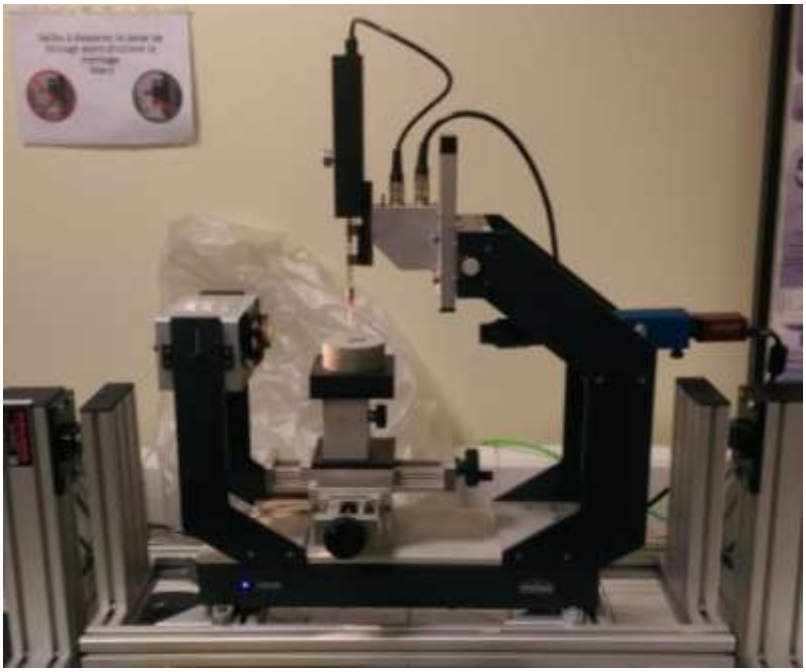

Figure 3-15 *DSA30® goniometer (KRUSS ©) with a cylindrical rock plate sample*

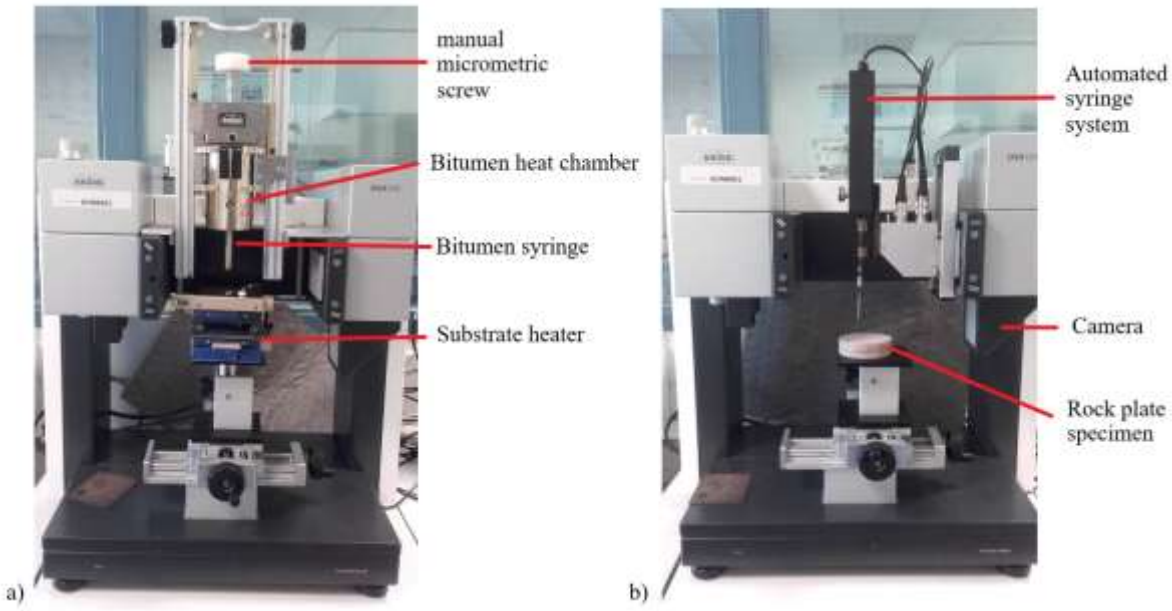

Figure 3-16 *DSA100® goniometer (KRUSS ©) for a) hot bitumen sessile drop configuration, b) regular sessile drop configuration (for probe liquids)*

Only the fabrication of rock plates requires a detailed description, further addressed in the material section 3.2.2No systematic preparatory cleaning procedure was provided for solid substrates, as the influence of such a procedure was part of the study of campaign IV of this thesis (Chapter 7). The samples were simply stored in a dry place at ambient temperature until use. However, they were carefully handled with gloves, by the sides to avoid the slightest surface contamination.

3.2 Materials

3.2.1 Bitumens

Two 50/70 bitumens were used throughout the different campaigns of this thesis, noted “B” and “S”. The associated polymer-modified bitumens (PmB) were respectively noted “Bm” and “Sm”. They were all provided by Eiffage©.

Table 3-1 *Bitumen properties*

Bitumen	Polymer modification	SARA fraction (%)				Colloidal stability index	Penetration grade (10^{-1}mm)	T_{RB} (°C)	Pfeiffer PI	Fraass T (°C)	Elastic recovery (%)
		Saturates	Aromatics	Resins	Asphaltenes						
B	-	9	45	23	24	0.49	54	49.6	-1.13	-	0
Bm	3%, no croslinking	-	-	-	-	-	52	56.4	0.38	-12	43
S	-	4	67	16	14	0.22	61	47.8	-1.32	-	0
Sm	3%, no croslinking	-	-	-	-	-	51	54.8	-0.02	-10	13

3.2.2 Silanes

The main idea of the aggregates surface modification, which is developed in campaign III (Chapter 6), is to either improve or undermine the adhesion between bitumen and aggregate and measure the difference of performances between the respective mixtures. Hence, two different silanes were selected for the chemical surface treatment of substrates.

- One anti-stripping agent, adhesion promoter: n-Octadecyltrimethoxysilane, noted “+”. It is a long carbon chain silane, hydrophobic and lipophilic (good affinity with bitumen is expected).
- One pro-stripping agent, adhesion inhibitor: Nonafluorotriethoxysilane, noted “-”. It is a short fluorinated chain, very hydrophobic and lipophobic (weak affinity with bitumen is expected).

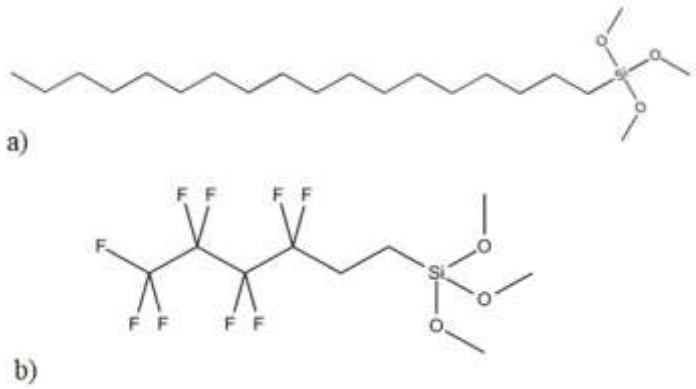

Figure 3-17 *a) anti-stripping silane, b) pro-stripping silane*

3.2.3 Substrates

3.2.3.1 Mineral road aggregates

Crushed mineral aggregates from four rock sources and one reclaimed cement concrete were used. Eiffage© currently employs these materials for road construction in France and provided them.

- "CO": Micro granite porphyry rock from Picampoix quarry (Corbigny, France), the reference substrate. A petrographic study was undertaken for reproducibility purpose, especially regarding the results of surface treatment with silanes in campaign IV (Chapter 7). Two main rock aspects were identified and studied. The first type is composed of 35% phenocrysts (6% quartz, 25% feldspars, 4% Biotite/Chlorite, <1% Amphibole) and 65% microcrystals (58% feldspars, altered in sericite, with mainly 50 to 100µm diameter grains, 6% quartz, <1% biotite/chlorite). It presents a grey colour. The second type is composed of 25% phenocrysts (6% quartz, 15% feldspars, 4% biotite/chlorite) and 75% of microcrystals (54% feldspars, 20% quartz, 1% biotite/chlorite).

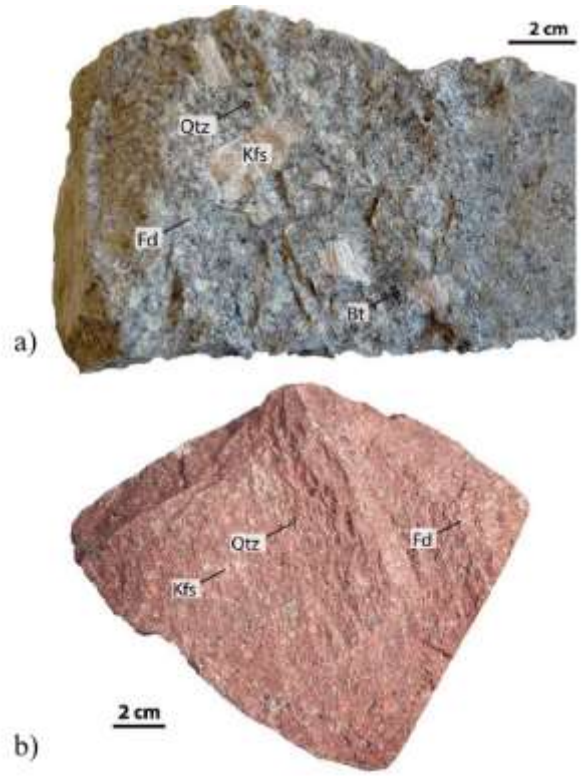

Figure 3-18 *CO rock samples from both main aspects: a) "grey, b) "pink"*

- "BI": Granite rock "BI" from Budillon-Rabatel quarry (Izeaux, France)
- "CR": from Roche Bleues quarry (Frontignan, France)
- "HL": Visean limestone from Haut-Lieu quarry (Haut-Lieu, France)
- "BE" : Reclaimed cement concrete from various origin

3.2.3.2 Rock plates and cylinders

CO rock plates were cut from original Corbigny source rock. First, 8-cm-diameter drill cores were made from quarry boulders. Two types of specimen were cut with diamond saw blade:

- Rock plates: 8x2.5cm high, for surface analysis (Chapter 7), pictured in Figure 3-19
- Rock cylinders: 8x8cm high, for bitumen thin film specimens (Chapter 6)

All samples were resurfaced with a grinding machine to limit surface roughness under 10µm everywhere on both disc surfaces. The roughness was successfully controlled on with a FARO® 3-D arm (5µm precision), pictured in Figure 3-20.

Figure 3-19 *CO cored rock plate and aggregates*

Figure 3-20 *FARO® 3-D arm*

3.2.3.3 Mineral Filler

A limestone filler from Haut-Lieu quarry (Haut-Lieu, France) was used in all tested bituminous mixtures.

3.2.3.4 Glass beads

Spherical glass beads from CVP *Abrasif-Broyage* © were selected as filler for the mastics. There are composed of inert silica (70% SiO_2) and other oxides (13% Na_2O, 7% CaO, 3% MgO, 0.5%Al_2O_3 and 0.2% K_2O). The specific gravity of the glass is 2.46kg/L, for an apparent specific gravity of. 80% of total mass. The filler is made with particles whose diameter is comprised between 40µm and 70µm. Glass beads used for surface analysis in Chapter 7 are noted "G_Agg".

Figure 3-21 *Silica glass beads*

3.2.3.5 Glass plates

Glass plates were Thermo Scientific™ Menzel uncoated microscope slides. They are made of soda-lime glass and present an extremely smooth, ideal surface for surface analysis. The glass plates are referred as “G_P” throughout this work.

Figure 3-22 *Glass plates (Thermo Scientific™ Menzel microscope slides)*

3.2.3.6 Silane-treated substrates

In order to study the bitumen-aggregate adhesion, some substrates were coated with silanes, following an innovative surface modification procedure presented in Chapter 7 Any substrate “X” which underwent silanisation with the anti-stripping silane “+” is labelled “X(+)” or “X[+_Y%]”. The difference between the parenthesis and bracket notations is the parameters of the surface modification procedure, detailed in section 7.2.1. “Y” designates the percentage of silane in solution, which may vary only in the procedure using bracket notations. Similarly, substrates modified with pro-stripping silane are labelled “X(-)” or “X[-_Y%]”. Finally, control substrates that underwent the same surface modification procedure without any silane are noted “X(o)” or “X[o]”. The complete list of silane-treated substrates is available in Section 7.2.2.

3.2.4 Mastics

The mastic plays a crucial role in bituminous mixture performances, as it coats larger aggregates and fills the gap between them. Thermomechanical behaviours (LVE, nonlinearity, fatigue…) and properties (thixotropy, healing capacity…) of mastics are currently being thoroughly studied (L. Babadopulos et al. 2019; Chaturabong and Bahia 2018; Delaporte et al. 2007; Mazzoni et al. 2017; Mazzoni, Virgili, and Canestrari 2019). A contribution to this subject is part of Campaign II (Chapter 5). For that matter, a “model” mastic was tested. It was made out of 60% in volume of pure bitumen B and 40% of glass beads, both presented in previous sections. This mastic was labelled “B_40%”.

Since the filler constitutes the smallest particles of the aggregate skeleton, its specific surface is also the biggest. Hence, the mastic might be the phase in the mixture in which the role of bitumen-aggregate adhesion is exacerbated. Two mastics with silane-treated filler were tested, with the same exact percentage of filler. “B_40%(+)” and “B_40%(-)” respectively refer to the mastics with anti-stripping silane treated beads and with pro-stripping silane treated beads.

Table 3-2 *Tested mastics*

Mastic	Bitumen: B	Filler: Glass beads (D = 40-70µm)	Silane used for filler treatment
B_40%	60%	40%	None
B_40%(+)	60%	40%	Anti-stripping (+)
B_40%(-)	60%	40%	Pro-stripping (-)

3.2.5 Bituminous mixtures

19 different mixtures were tested during this thesis, all presented in Table 3-3. The first 16 mixtures are part of Campaign I, which studies the influence of bitumen aggregates in mixtures performances (Chapter 4), based on four parameters: bitumen type, polymer modification, aggregate type and binder content. The last 3 mixtures were made to study the influence of bitumen-aggregate adhesion in Campaign IV. Their composition is exactly similar as B_CO_5.8, except that the aggregates underwent surface treatment with silanes.

Table 3-3 *Tested mixtures*

Mixture	Bitumen type		Polymer modification		Aggregate type					Binder content		Aggregate surface treated with silanes	
	B	S	Yes	No	CO	BI	CR	HL	Bet	5.8%	4.8%		
B_CO_5.8	X			X	X					X			Campaign I
B_CO_4.8	X			X	X						X		
Bm_CO_5.8	X		X		X					X			
Bm_CO_4.8	X		X		X						X		
S_CO_5.8		X		X	X					X			
S_CO_4.8		X		X	X						X		
Sm_CO_5.8		X	X		X					X			
Sm_CO_4.8		X	X		X						X		
Bm_BI_5.8	X		X			X				X			
Bm_CR_5.8	X		X				X			X			
Bm_HL_5.8	X		X					X		X			
Bm_BE_5.8	X		X						X	X			
S_BI_5.8		X		X		X				X			
S_CR_5.8		X		X			X			X			
S_HL_5.8		X		X				X		X			
S_BE_5.8		X		X					X	X			
B_CO(+)_5.8	X			X	X					X		anti-stripping (+)	Campaign IV
B_CO(-)_5.8	X			X	X					X		pro-stripping (-)	
B_CO(o)_5.8	X			X	X					X		control (o)	

Having a unique grading curve for all tested mixtures with different mineral aggregate sources was a prerequisite of this study to limit bias on test results. Since the Particle Size Distribution (PSD) is *a priori* different for a given aggregate fraction between two aggregate sources, specific compositions were made to approach the reference substrate grading curve (CO) as best as possible. It is worth noticing that the mineral filler content may vary significantly (from 1.4 to 3%), as it served as a variable to adjust the 7.4% passing under 0.063mm sieve (Table 3-4).

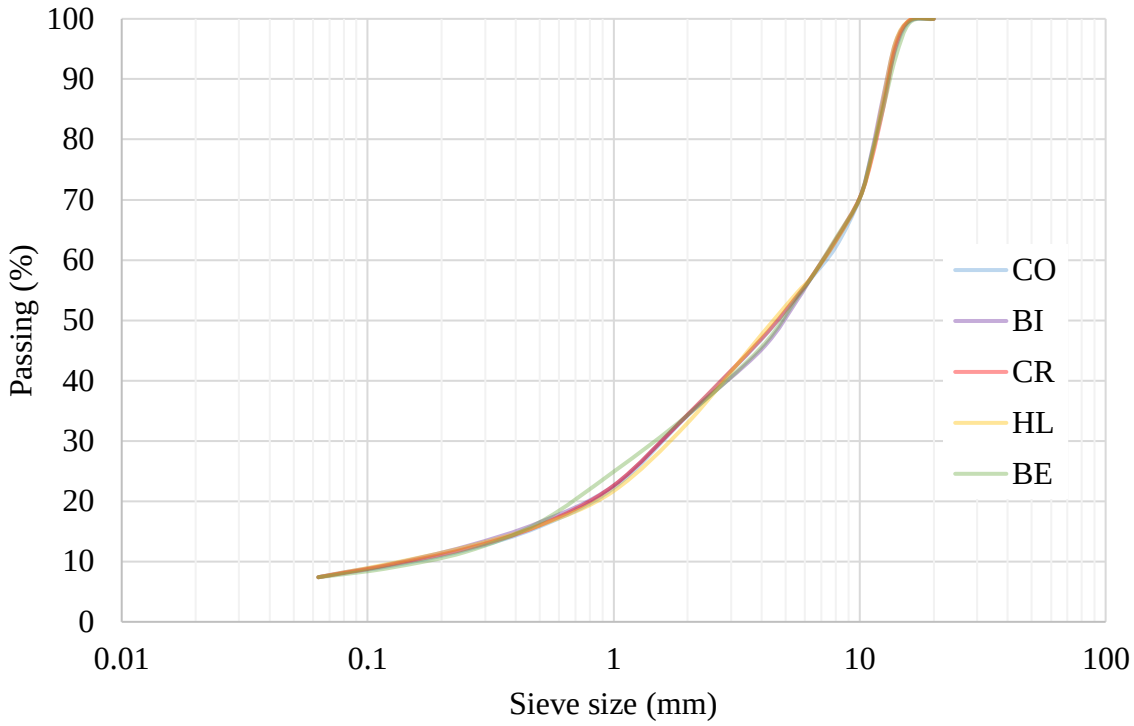

Figure 3-23 *Grading curves*

Table 3-4 *PSD analysis of all aggregate skeleton*

Sieve size (mm)	Passing (%)				
	CO	BI	CR	HL	BE
0.063	7.4	7.4	7.4	7.4	7.4
0.08	8.1	8.2	8.1	8.2	7.9
0.125	9.3	9.6	9.5	9.7	9
0.25	11.9	12.5	12.1	12.4	11.6
0.5	15.8	16.5	16	16	16.5
1	22.2	22.6	22.6	21.7	24.9
2	34.3	34.3	34.4	33	34.3
4	46.9	45.2	47	47.7	45.6
5.6	54.1	53.5	54.2	54.7	53.9
6.3	56.8	56.8	56.9	56.9	56.8
8	62.2	63.2	63.4	63.1	63.6
10	70.2	70.2	70.3	70.2	70.2
11.2	77.3	77.9	76.8	77.2	77.6
12.5	86.4	87.3	85.4	86.9	85.4
14	95	96.1	95.4	96.2	93.6
16	99.6	99.7	99.8	99.8	99.4
20	100	100	100	100	100
	Filler content (% of mixture mass)				
	CO	BI	CR	HL	BE
	3	1.7	2.1	1.4	2.4

3.2.6 Bitumen thin films

The newly developed test on bitumen thin film in Campaign III (Chapter 6) involves specimens where a controlled-thickness film of B bitumen is confined between two cylinders of CO rock (described in section 3.2.3.2). Two film diameters were used: a large diameter (noted "LD") of 8cm, which covers the entire surface of the rock cylinders and a small diameter (noted "SD") between 3 and 4cm. Two film thicknesses were tested: 300 and 100µm. The notation of a specimen is "B_CO_X_Y", with X the thickness of the film in µm and Y indicating the type of diameter used, e.g. "B_CO_300_LD" showed in Figure 3-24.

Figure 3-24 *B_CO_300_LD specimen*

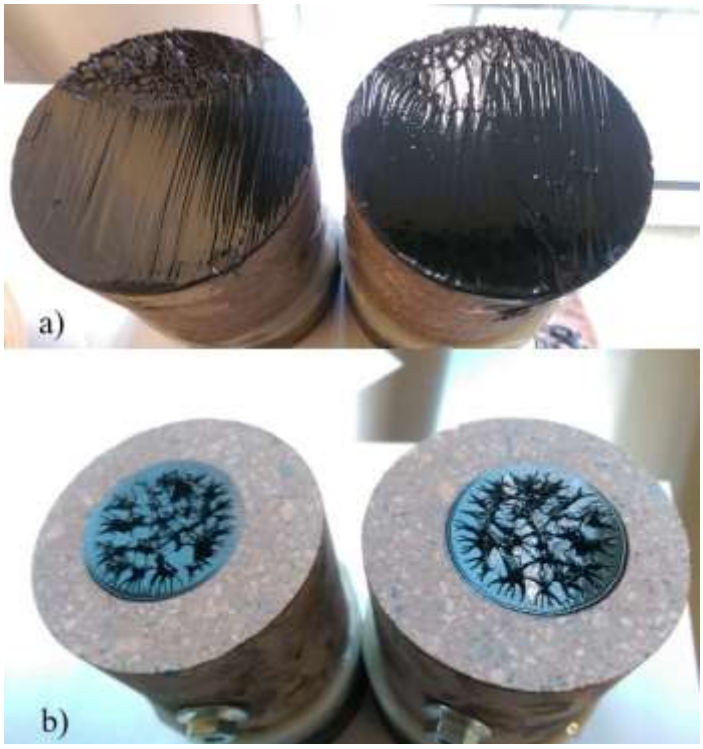

Figure 3-25 *Thin film with a) large diameter (LD), b) small diameter (SD)*

4 Campaign I: Influence of bitumen and aggregate on bituminous mixtures thermomechanical performances

4.1 Objectives

The first campaign of this thesis was designed to investigate the influence of both the bitumen and the aggregates on the thermomechanical performances of bituminous mixtures. In order to achieve this, the campaign was splitted in four research axes:

- Influence of bitumen properties
- Influence of aggregate nature
- Fatigue performances of mixtures and their bitumen
- Predictive equation for mixture fatigue performances

The main objective of these tasks, as far as possible, was to compare each parameter on a quantitative basis without neglecting cross effects, in order to give to paving technologists the less biased tools to predict the critical mixture performances, especially the resistance to fatigue.

For each axis, a detailed description of the test procedures is given before the results display. The materials and test set-ups, however, are not recapped for readability. They are available in Chapter 3.

4.2 Influence of bitumen properties on mixtures performances

In this section, the influence of bitumen properties on mixture performances was investigated according to European standards.

4.2.1 Full factorial 2^3 experimental plan

Eight mixtures share the same aggregate source (CO), as well as a unique grading curve (see the first mixtures of Table 3-3 in section 3.2.5). Three thermomechanical properties were studied:

- Stiffness (AFNOR 2012d). Complex Modulus test was performed on 2PB apparatus with 4 trapezoidal samples per mixture. The average value of norm of complex modulus at 15°C and 10Hz, $|E^*|(15°C/10Hz)$, is a critical variable for French pavement design method. The phase angle φ was also measured.
- Resistance to Fatigue (AFNOR 2012c). The fatigue test was performed on 2PB apparatus at 10°C/ 25Hz with 18 trapezoidal samples per mixture. ε_6 and slope coefficient b and their respective confidence intervals were obtained from Wöhler's curve linear regression (4.1). Estimates a and b of regression parameters $\tilde{A}$ and $\tilde{B}$ were calculated by the least squares method using equation (4.2). The relationship between ε_6, a and b is (4.3). Assuming a normal distribution of error terms $\varkappa_i$, the confidence interval for the b (97.5% confidence) and ε_6 (95% confidence) were delimited by $\Delta b^-, \Delta b^+$ and $\Delta {\varepsilon_6}^-$, $\Delta {\varepsilon_6}^+$ (see Equations (4.4) and (4.5)).

$$\log_{10} N_i = \tilde{A} + \frac{\log_{10} \varepsilon_i}{\tilde{B}} + \varkappa_i \quad , \quad i \in [\![1,18]\!] \tag{4.1}$$

$$\log_{10} N = a + \frac{\log_{10} \varepsilon}{b} \tag{4.2}$$

$$\varepsilon_6 = 10^{(6-a)b} \tag{4.3}$$

$$P\left(b - \Delta b^- < b_{,unknown} < b + \Delta b^+\right) = 97.5\% \tag{4.4}$$

$$P\left(\varepsilon_6 - \Delta {\varepsilon_6}^- < \varepsilon_{6,unknown} < \varepsilon_6 + \Delta {\varepsilon_6}^+\right) = 95\% \tag{4.5}$$

The average norm of initial modulus $|E^*|_{ini}$ and initial loss modulus $E2_{ini}$ (calculated between the 100th and 500th cycles) were measured for all mixtures.

- Water Sensitivity (AFNOR 2018d). The average of maximal indirect tensile stress (ITS) was measured for 3 conditioned and 3 unconditioned samples. The *ITSR* is the ratio of these average maximal stresses.

To obtain the eight different mixtures, three bitumen parameters were combined, with two possible values for each:

- *A*: Bitumen origin, "B" or "S"
- *B*: Polymer modification, pure or modified
- *C*: Binder content, 4.8% or 5.8%

A full factorial experimental plan allows a statistical regression for each response variable, with the evaluation of cross effects between fixed-effect parameters (that are not random variables), as presented in Equation (4.6). *y* is the studied variable, *A* is the parameter accounting for bitumen origin: *A* = -1 for bitumen "B", A = +1 for bitumen "S". *B* characterises bitumen modification: *B* = -1 for pure bitumen, *B* = +1 for polymer modification. *C* = -1 when binder content is 4.8% and *C* = +1 for 5.8%. β_0 represents the average of all *y* values, whereas the other regression coefficients β_X are calculated with Equation (4.7). Therefore, $2\beta_X$ indicates how much a variable changes on average when *X* parameter value changes from -1 to +1.

$$y = \beta_0 + \beta_A A + \beta_B B + \beta_C C + \beta_{AB} AB + \beta_{AC} AC + \beta_{BC} BC + \beta_{ABC} ABC \quad (4.6)$$

$$\beta_X = \frac{\bar{y}|_{X=+1} - \bar{y}|_{X=-1}}{2} \quad (4.7)$$

, with $\bar{y}$ denoting the average of *y*. Four critical response variables were selected: $|E^*|$*(15°C/10Hz)*, ε_6, *b* and *ITSR*.

Regression methods using full factorial plans usually require repetitions for few configurations in order to evaluate the variance due to repeatability. This was not performed in this campaign because it was extremely time-consuming and repeatability of response variables are well known and available in the literature. This is summed up in Table 4-1. Details about regression methods in the analysis of variance (ANOVA) framework can be found in Draper and Smith's work (Draper and Smith 1998).

Table 4-1 *Repeatability of response variables*

Variable		Avg.	95% confidence interval	Source
$\|E^*\|$*(15°C/10Hz)*	MPa	15233	335	NF-EN 12697-26
ε_6	µm/m	n.a.	4.2	NF-EN 12697-24
b	-	n.a.	0.06	NF-EN 12697-24
ITSR	%	n.a n.a.	15* 13.4	NF-EN 12697-12 EAPIC (Somé and Saubot 2015)

*Require further studies according to authors
n.a. = not available

.

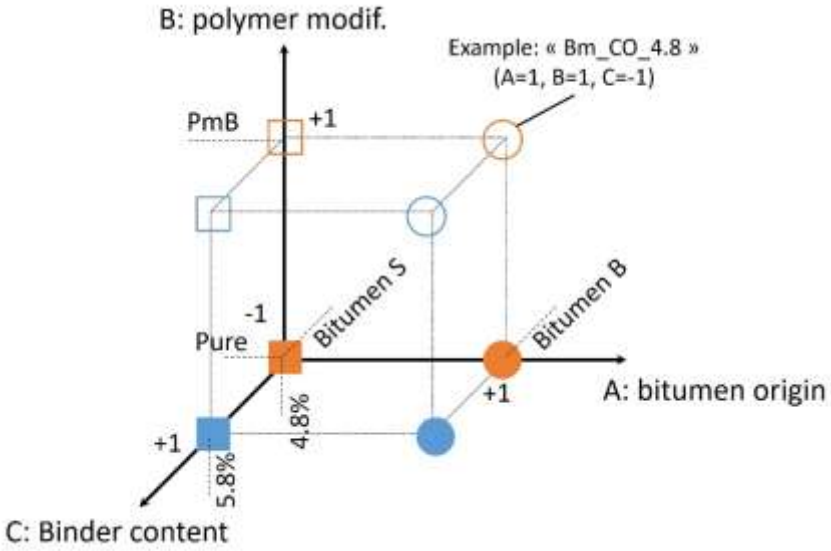

Figure 4-1 *2^3 factorial plan of tested mixtures*

The virtue of factorial plans is to avoid neglecting cross effects and potentially drawing contradictory conclusions on the effect of one specific parameter in two different subcases. Still, it is important to highlight the potential influence of either hidden or neglected factors. In this case, all bias from aggregate skeleton or mix design parameters were minimised using a single grading curve, but the role of air void content *VC* remained one of the biggest concern since it is known to be a major determining factor of thermomechanical performances of bituminous mixtures (see section 2.1.2.4). The impact of void content was therefore thoroughly analysed. VC_{CM}, VC_f and VC_{WS} symbolize the average air void content of respectively complex modulus, fatigue and water sensitivity test specimens.

4.2.2 Results and analysis

All experimental results are displayed in the following Table 4-2 and Figure 4-2.

From a general perspective, void content was completely uncorrelated with complex modulus and fatigue results, as shown respectively in Figure 4-2. a) and c). This might be explained by the fact that the difference between extreme values of VC_{CM} or VC_f between mixtures were successfully contained at 2%. These discrepancies were too small to become a factor of influence, and therefore a bias. Concerning the impact of void content on moisture sensitivity, the specimen fabrication process with the gyratory compactor led to much higher discrepancies than the roller compactor, as usual in practice. However, the correlation between VC_{WS} and *ITSR* was limited, as shown in Figure 4-2. h).

Still regarding general observations, *|E*|(15°C/10Hz)* values, varying from 7756 to 11436 MPa, clearly differed from one mixture to another. These values were quite low considering that mixtures were made with French *EME* mix design. This was due to the lower stiffness of the 50/70 bitumens used in this thesis, instead of the usual 35/50 or 10/20 bitumens generally preferred for this type of pavement mixture. ε_6 values ranged from 79 to 145µm/m, with significant differences between materials. ε_6 exhibited little correlations with $E2_{ini}$ and even *ITSR* (Figure 4-2 f) and g)). On the other hand, the slope coefficient *b* values were all very close to -0.2 (standard value for mixtures in the literature (Di Benedetto and Corté 2005)), except for Bm_CO_5.8 at 0.125, and the wide confidence intervals associated making any analysis unreliable. *ITSR* values ranged from 48 to 82%. Their wide confidence intervals were not measured in this thesis and were taken from the European norm (AFNOR 2018d), although the authors noticed that no consensus exists on the presented values.

Table 4-2 *Result values of thermomechanical tests of mixtures with varying bitumen parameters*

	Complex Modulus 4 samples/mix			**Resistance to fatigue** 18 s./mix						**Water sensitivity** 3 dry + 3 wet s./mix	
	VC_{CM} (%)	$\|E^*\|$ at 15°C /10Hz (MPa)	φ at 15°C /10Hz (°)	VC_f (%)	$\|E^*\|_{ini}$ $E2_{ini}$ (MPa)	ε_6 (µm/m)	$\Delta\varepsilon_6^+$ $\Delta\varepsilon_6^-$ (µm/m)	b	Δb^+ Δb^-	ITSR (%)	VC_{WS} (%)
B_CO_5.8	5.0	7756	20.8	5.1	11631 2968	120	+6.48 -6.15	-0.22	+0.037 -0.055	77	6.4
B_CO_4.8	5.6	9477	18.7	5.7	13236 3031	110	+6.67 -6.29	-0.18	+0.029 -0.043	77	10.3
Bm_CO_5.8	5.0	8752	17.5	5.2	11571 2644	145	+7.54 -7.17	-0.12	+0.022 -0.034	82	5.6
Bm_CO_4.8	6.5	9629	16.1	5.7	13716 2847	120	+7.69 -7.23	-0.19	+0.035 -0.055	81	10.5
S_CO_5.8	5.2	9278	20.9	5.4	13036 2993	83	+5.17 -4.87	-0.23	+0.031 -0.043	66	9.3
S_CO_4.8	6.0	11436	18.1	5.9	15817 3141	79	+6.47 -5.98	-0.21	+0.034 -0.05	48	11.7
Sm_CO_5.8	4.5	9792	18.3	4.4	13701 2833	109	+8.09 -7.53	-0.21	+0.04 -0.064	79	6.8
Sm_CO_4.8	4.6	11418	17.4	4.6	15743 3081	103	+7.84 -7.28	-0.20	+0.034 -0.053	76	10.1

The parametric analysis involved the calculation of regression coefficients β_X (equation (4.7)) for the four response variables. An illustrating example of β_A, β_B and β_C for ε_6 is given in Figure 4-3, , and all regression coefficients are available in Figure 4-4.

Reducing binder content from 5.8% to 4.8% systematically increased |E*| (+17%). Using bitumen S over bitumen B also consistently increased |E*| (+16%). The polymer modification was only a minor factor| (+4%), as well as all the cross effects between parameters (<4%). Mixtures with bitumen B presented much better fatigue performance (average increase of ε_6 by 30µm/m) than ones with bitumen S. The polymer modification also boosted ε_6 (+21µm/m), and increasing binder content from 4.8% to 5.8% slightly improved ε_6 (+11µm/m). The cross effects were very limited in fatigue performances, meaning that the parameters are independent. No clear trend was spotted on slope coefficient *b* (lot of cross effects), all regression coefficients being smaller than confidence intervals anyway. Regarding water sensitivity, choosing bitumen B over S ($2\beta_A$ = +12%) and using polymer modification ($2\beta_B$= +12.5%) were the most influential factors on *ITSR* results. However, the cross effect between those two parameters was important ($2\beta_{AB}$= -8%), which means that using polymer modification after switching from bitumen S to bitumen B will only marginally improve *ITSR* (+4.5%).

Overall, the full factorial plan gives a powerful predictive tool for paving technologists who are looking for optimisation between several performances variables. The ability to create a hierarchy of parameters while evaluating cross effects. This method is obviously limited by the number of required tests, which is a power of two of the number of parameters.

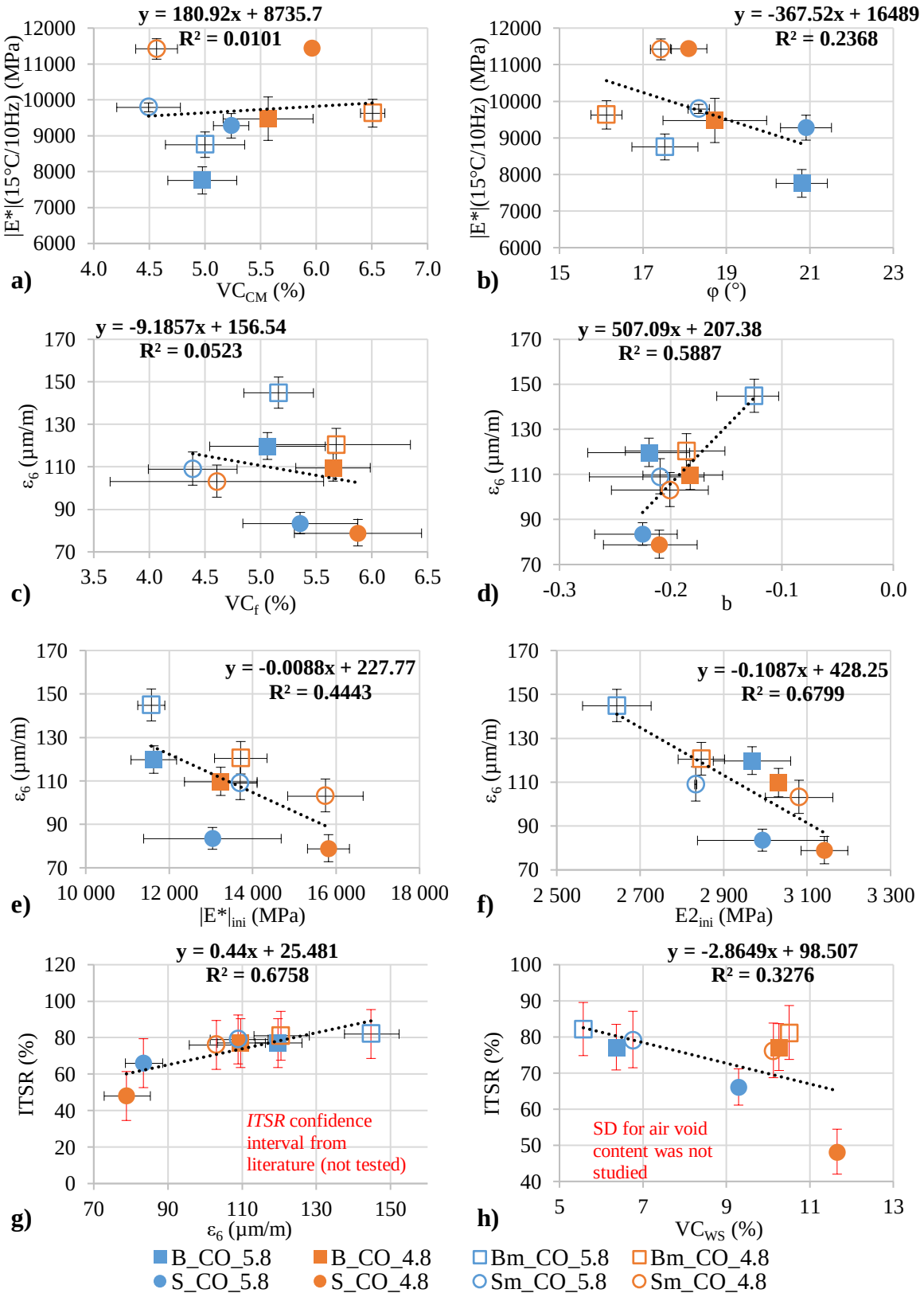

Figure 4-2 *Thermomechanical test results of bituminous mixtures with varying bitumen parameters. Error bars represent confidence intervals for* ε_6 *,b, ITSR, and standard deviation (SD) values for* $|E^*|(15°C/10Hz)$, φ, $E2_{ini}$, $|E^*|_{ini}$, VC_{WS} , VC_f .

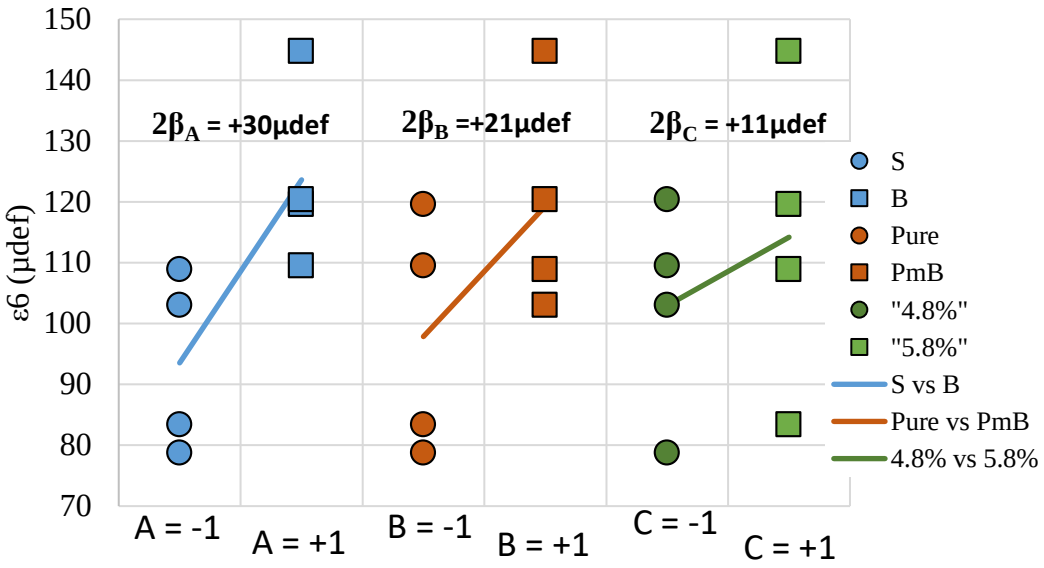

Figure 4-3 *ε6 results and associated regression coefficient β_A, β_B, β_C for varying bitumen parameters*

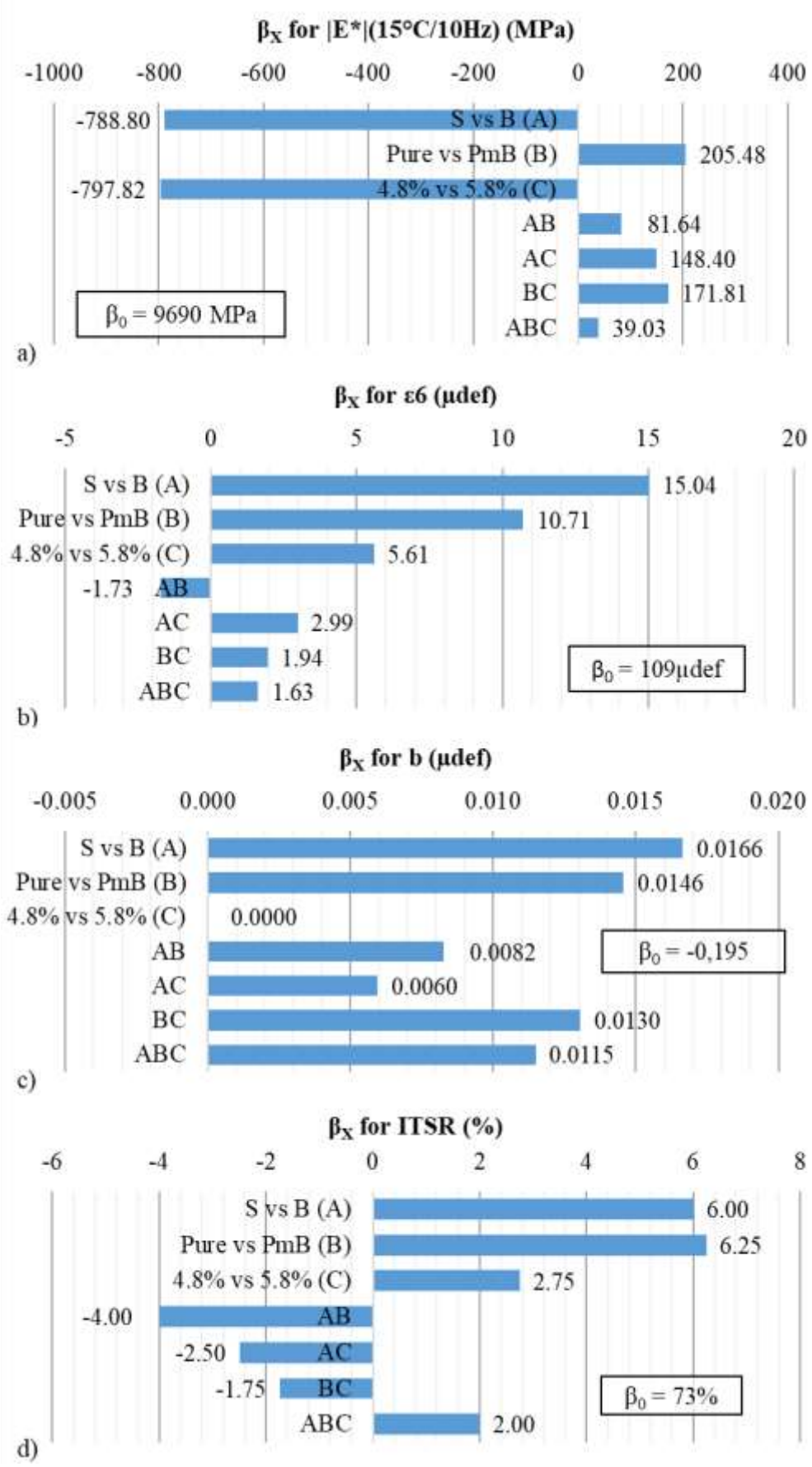

Figure 4-4 *Regression coefficient values for a) |E*|(15°C/10Hz), b) ε_6 , c) slope coefficient b, d) ITSR*

4.3 Influence of aggregate nature on mixtures performances

In this section, the influence of aggregate nature on mixture performances was investigated according to European standards.

4.3.1 Experimental plan

The nature of aggregates, which forms 95% of total mass of mixtures, plays a role in mixtures performances, but this influence can easily be hidden behind stronger determining parameters such as binder or mix design properties (grading curve). In order to address these issues, ten mixtures with the same grading curve (see Figure 3-23) and binder content (5.8%) were tested. Five aggregate sources (CO, BI, CR, HL, BE) and two bitumens (Bm, S) were used. The two bitumens were chosen because of the extreme fatigue performances of their associated mixtures with CO aggregates in the previous study of bitumen properties (Section 4.2). Indeed, their ε_6 values show a 62 µm/m difference (145 vs. 83). The idea was to compare the influence of various aggregates to the full potential of bitumen selection. The approach was different from the previous study on bitumen properties: as too many aggregate parameters (petrography, geometry, porosity…) changed from one source to another, a factorial approach appeared irrelevant. The author opted for a 2x5 scheme with five very different aggregate sources (including original ones such as reclaimed concrete BE), in order to be able to draw qualitative statements.

The very same thermomechanical performances of bituminous mixtures (stiffness, resistance to fatigue and water sensitivity) as in section 4.2.1 were studied with the same standard methods.

4.3.2 Results and analysis

All experimental results are displayed in Table 4-3 and Figure 4-5. The main performances variables (|E*|(15°C/10Hz), ε_6, b, and $ITSR$) are rearranged in Figure 4-6 and a special focus on Wöhler curves is made in Figure 4-7.

Table 4-3 *Result values of thermomechanical tests of mixtures with varying aggregate sources*

	Complex Modulus 4 samples/mix			**Resistance to fatigue** 18 s./mix						**Water sensitivity** 3 dry + 3 wet s./mix	
	VC_{CM} (%)	|E*| at 15°C /10Hz (MPa)	φ at 15°C /10Hz (°)	VC_f (%)	|E*|ini E2ini (MPa)	ε6 (µm/m)	Δε6+ Δε6- (µm/m)	b	Δb+ Δb-	ITSR (%)	VC_{WS} (%)
Bm_CO_5.8	5.0	8752	17.5	5.2	11571 2644	145	+7.54 -7.17	-0.12	+0.022 -0.034	82	5.6
Bm_BI_5.8	5.1	8183	18.4	4.6	11508 2698	142	+14.68 -13.31	-0.18	+0.053 -0.127	92	3.9
Bm_CR_5.8	4.6	8384	17.3	4.4	11923 2914	152	+8.72 -8.25	-0.12	+0.027 -0.048	83	7.2
Bm_HL_5.8	4.3	8246	19.0	4.8	10880 2873	144	+10.44 -9.73	-0.20	+0.046 -0.082	91	2.3
Bm_BE_5.8	4.4	10102	9.8	4.4	11620 1719	138	+11.94 -10.99	-0.14	+0.042 -0.109	77	6.8
Bm_CO_5.8	5.0	8752	17.5	5.2	11571 2644	145	+7.54 -7.17	-0.12	+0.022 -0.034	82	5.6
S_CO_5.8	5.2	9278	20.9	5.4	13036 2993	83	+5.17 -4.87	-0.23	+0.031 -0.043	66	9.3
S_BI_5.8	4.4	9090	20.5	5.0	13414 3082	90	+4.55 -4.33	-0.23	+0.028 -0.037	82	5.1
S_CR_5.8	5.1	9081	21.5	5.0	13409 3220	80	+3.73 -3.57	-0.21	+0.021 -0.026	86	8.3
S_HL_5.8	5.2	8096	24.7	4.9	13331 3302	82	+4.62 -4.37	-0.23	+0.027 -0.036	82	2.2
S_BE_5.8	4.9	11013	11.6	5.1	13790 1969	104	+5.46 -5.18	-0.18	+0.025 -0.035	76	7.7

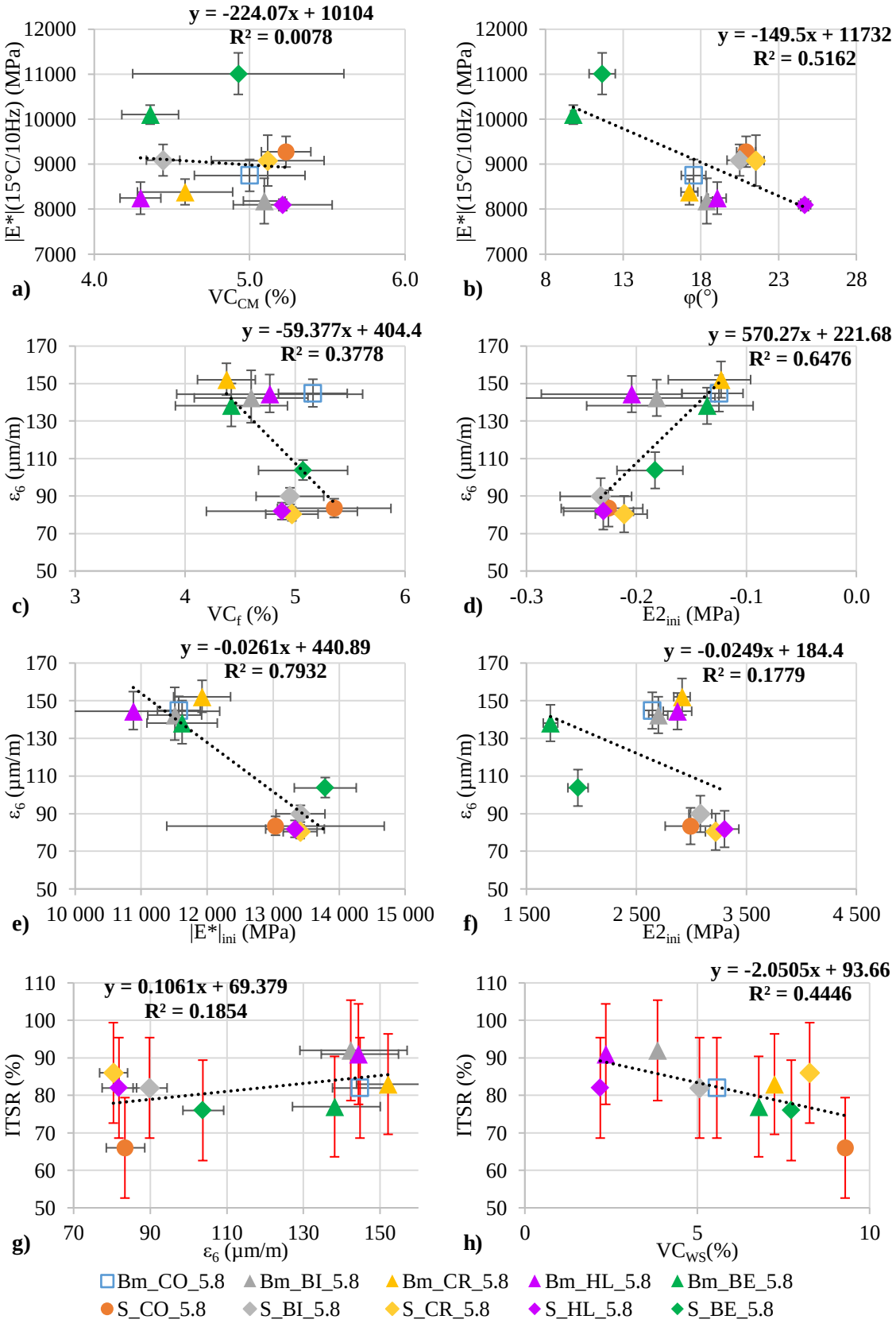

Figure 4-5 *Thermomechanical test results of bituminous mixtures with varying aggregate sources. Error bars represent confidence intervals for ε_6, b, ITSR, and standard deviation (SD) values for $|E^*|$(15°C/10Hz), φ, $E2_{ini}$, $|E^*|_{ini}$, VC_{WS} , VC_f .*

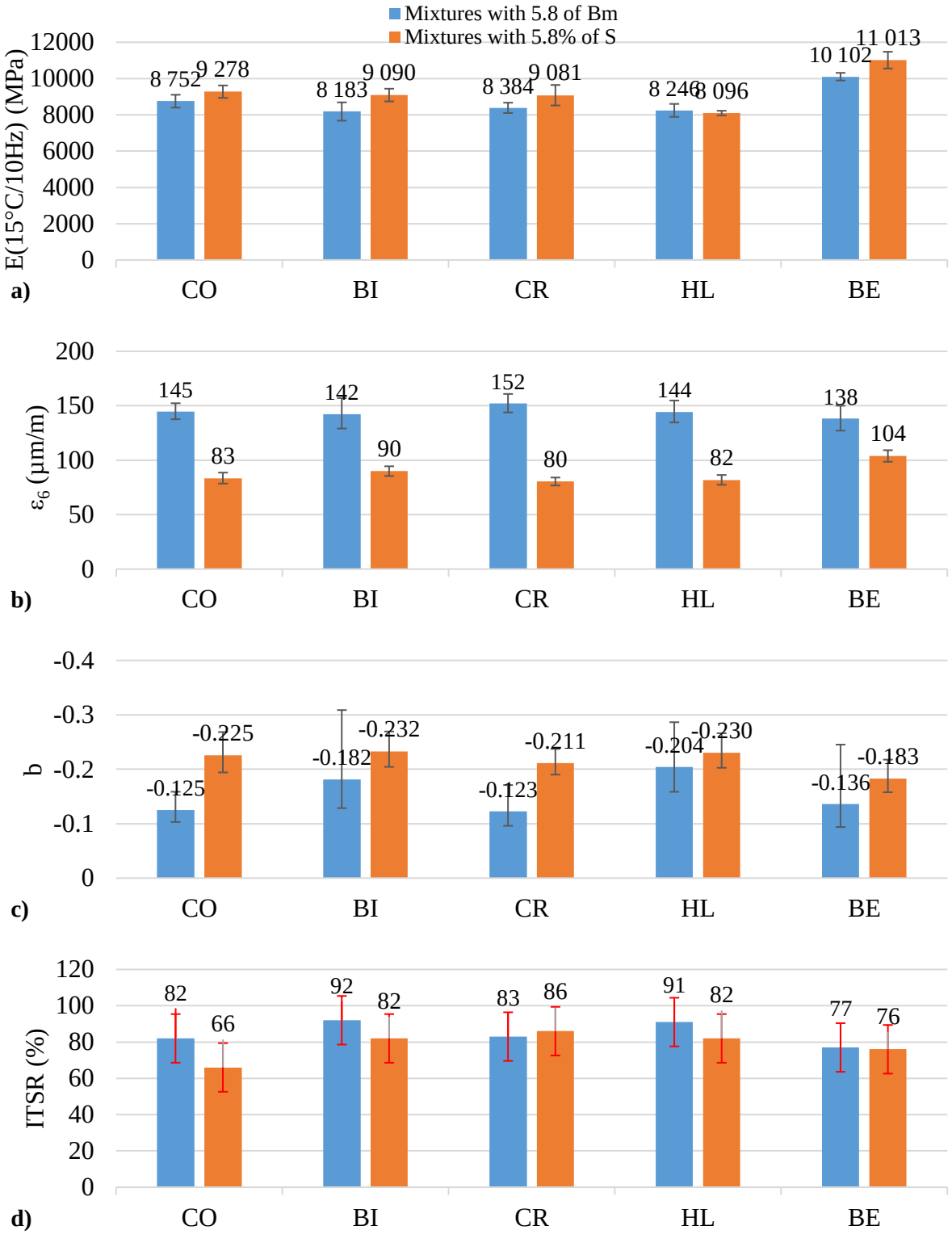

Figure 4-6 *Thermomechanical test results of bituminous mixtures sorted by aggregate sources: a) |E*|(15°C/10Hz), b) ε_6, c) slope coefficient b, d).ITSR. Error bars represent confidence intervals for ε_6 ,b, ITSR, and standard deviation (SD) values for |E*|(15°C/10Hz)*

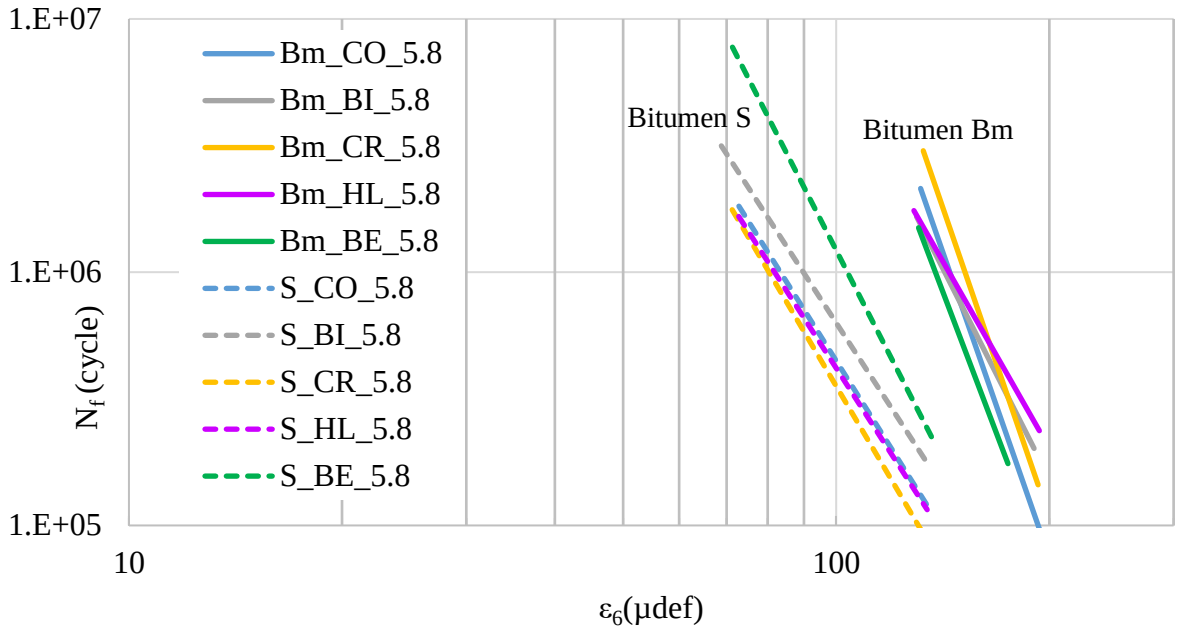

Figure 4-7 *Regression lines of Wöhler curves*

From the general perspective, very similarly to the previous study on bitumen properties, air void content VC_{CM} (stiffness) and VC_f (fatigue) were kept relatively constant between mixtures, with maximal discrepancies of 1%. Therefore, the effect of air voids is minimised. As for the water sensitivity, the air voids values VC_{WS} were much more scattered, introducing a potential bias.

The complex modulus values varied significantly between mixtures with different aggregate sources, from 8096 to 11013 MPa. Mixtures with CO, BI and CR presented very similar results in term of stiffness performances. The HL limestone mixture was the least stiff, whereas the mixture using BE reclaimed concrete aggregates was the stiffest, with a remarkably low phase angle (around 10°) compared to mixtures using all other aggregate sources (around 20°). This could be explained by the fact that reclaimed concrete aggregates possess cementitious parts with high porosity, absorbing more bitumen than other mineral parts during the hot mixing process. For a fixed aggregate source, using bitumen S over Bm almost always mildly increased $|E^*|$*(15°C/10Hz)* (except for HL limestone). Overall, the nature of the aggregate could be more important than the bitumen type for influencing stiffness performances.

In terms of fatigue performances, results showed the opposite: the bitumen type was far more determining than the nature of aggregate. This is clearly illustrated in Figure 4-6.b) and Figure 4-7.Indeed, the average difference of ε_6 between the group of mixtures using bitumen Bm and the one using bitumen S was around 56µm/m. On the other hand, the maximal difference of ε_6 between two mixtures using the same bitumen was "only" 23µm/m (S_CR_5.8 vs. S_BE_5.8). Nevertheless, not only the aggregate nature directly played a minor role on ε_6, but also important cross effect are revealed. The systematic improvement obtained by using bitumen Bm over S is dependent of the aggregate source. The best improvement has been found for CR (+72µm/m), far better than reclaimed concrete BE (+34µm/m). The slope coefficient *b* appeared always smaller for mixtures using bitumen S over Bm, and the results did not show significant trend when comparing aggregate sources.

Regarding water sensitivity, mixtures with bitumen Bm performed overall better (for CO, BI, HL) or the same (CR, BE) as mixtures with S. The nature of the aggregate was influential on *ITSR*, but with significant cross effects. For instance, the difference between S_CO_5.8 and S_CR_5.8 was 20%, but this difference shrinked to 1% when comparing Bm_CO_5.8 to Bm_CR_5.8. The presence of important cross effects between bitumen type and aggregate nature was not surprising, considering that moisture sensitivity is mainly due to the stripping potential of the binder-aggregate interface in presence of water.

4.4 Fatigue performances of mixtures and their bitumens

The fatigue behaviour of bituminous binders are usually less studied than the fatigue performances of bituminous mixtures, since the classical analysis involves time-consuming tests and since the behaviour of mixtures remains the single determining factor of flexible pavement design according to European standards. However, some researches highlighted that good fatigue performances of constituent bitumen could be transferred to the mixture (Hilde Soenen, de La Roche, and Redelius 2003). After establishing fatigue properties of the four bitumens of this campaign with DSR, the relationship between those properties and the fatigue performances of the associated mixtures obtained previously in sections 4.2 and 4.3 are discussed.

4.4.1 Bitumen fatigue performance using DSR

4.4.1.1 Experimental plan

Fatigue tests were performed on four bitumens (B, Bm, S and Sm) with MCR 501 DSR. Ten to thirteen samples per bitumen underwent continuous, strain-controlled cyclic tests with various amplitudes at 10°C and 25Hz. At least three repetitions for three different amplitudes were performed for each bitumen. The shear strain amplitudes (ranging from 0.34% to 1.83%,) were selected for every bitumen to obtain fatigue life surrounding 10^6 cycles, in order to calculate γ_6 accurately. Specimens were noted "X_DSR_Y%_spN", with X the type of bitumen, Y the shear strain amplitude and N the number of the specimen. Three failure criteria were implemented:

- 50% of initial modulus loss criterion $N_{f,\ 50\%}$. This "classical" criterion is arbitrary but widely used, especially in evaluating fatigue performance of mixtures according to European standards. The initial modulus G_{ini} was taken at the 25^{th} cycle.
- Slope change criterion $N_{f,\ slope\ change}$. This criterion is proposed to characterise the failure of DSR samples in parallel plates geometry. Indeed, past results showed that continuous cyclic tests exhibit 3 phases: 1) initial stiffness drop, 2) constant stiffness plateau or very limited stiffness decrease during many cycles, 3) rapid stiffness decrease until complete failure. The last phase has been visually linked to macroscopic crack that initiates at the periphery of the sample and radially expands inwards (H. Soenen and Eckmann 2000). The slope change indicates the tipping point from phase 2 to phase 3, and appears relevant to characterise failure (by loss of sample homogeneity). The tipping point was calculated in $|G^*|$ vs N graph, as the abscissa of the intersect of two tangential lines that fit the phase 2 and phase 3 curves, themselves visually designated.
- Second inflexion point criterion $N_{f,\ inflexion}$. This criterion mimics the one proposed for mixtures by Kim and co-workers (Y.-R. Kim, Little, and Lytton 2003), except that the first inflexion point could be hard to determine due to the stiffness plateau and the biasing effects of steric hardening typically observed in DSR fatigue tests (Planche et al. 2004). For this campaign, the second inflexion point was assumed to be reached after the slope break.

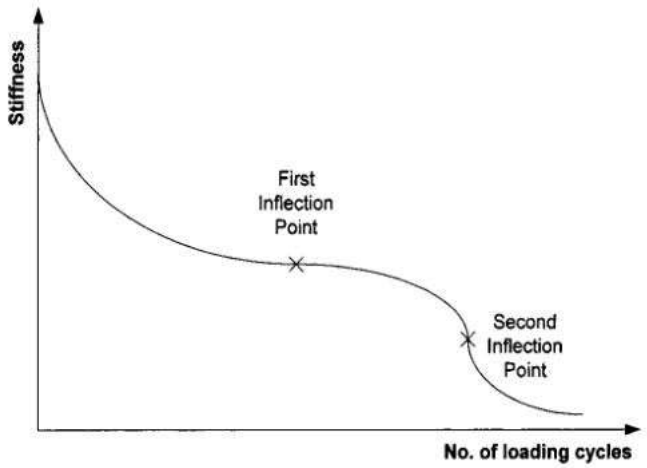

Figure 4-8 *Scheme of first and second inflexion point* (Y.-R. Kim, Little, and Lytton 2003)

In parallel to fatigue tests, discontinuous small amplitude tests at constant temperature (10°C) were performed in order to evaluate the effect of steric hardening on the measurements of complex modulus. This phenomenon is the delayed microstructure rearrangement of bitumen, hours after being cooled down (Planche et al. 2004). The common delay for thermal equilibrium is only around 30min in classical tests with DSR. For these discontinuous tests, after the 30min delay, 30 cycles were applied at 0.02% shear strain amplitude and 25Hz frequency every 4 minutes, at least during 7 hours. Each bitumen (B, Bm, S, Sm) was tested once.

Additionally, a continuous fatigue test at 0.45% shear strain amplitude, 10°C and 25Hz was performed on one bitumen S specimen after 10-hour rest at constant temperature. This rest period was applied directly after the thermal equilibrium. The idea was to compare the result to the fatigue curve in the same conditions but without the preliminary 10-hour rest (both specimens being undamaged nevertheless). Indeed, authors suggested that steric hardening could extend fatigue life at "low" strain amplitudes (Planche et al. 2004). The latter exploratory test was hence proposed as a small contribution to this question.

4.4.1.2 Results and analysis of fatigue tests

All DSR fatigue test results are available in Appendix 1.4. Regarding general observations, the linear regression parameters on Wöhler curves (γ_6, *1/b*) are given in Table 4-4. For reader's sake, detailed results are presented below only for bitumen B, since they proved to be representative of all others. In Figure 4-9, three |G*| curves as a function of cycles are displayed for three different shear strain amplitudes. Additionally, in Figure 4-10, complete Wöhler curves for the three failure criteria are presented.

Generally speaking, the evolution of |G*| as a function of cycles during fatigue tests was in accordance to the previous results in the literature. After an initial modulus drop during the first 1000 cycles (=40s), a stiffness plateau was observed for low strain amplitude tests, with clear modulus increase, probably due to steric hardening (addressed in the following section 4.4.1.3). For higher strain amplitude tests, a slow, linear modulus decrease was obtained instead of the stiffness plateau/increase, as shown in Figure 4-9 a). After this second phase, a systematic slope break marked a rapid change in the specimen behaviour, most likely due to crack initiation in sample periphery, where shear stress and strain peak. The main characteristic of this slope change was that it occurred at sample moduli close or even identical to initial moduli, making impossible the classical interpretation of fatigue damage as a loss of cross section area by homogeneously spread microcracks. The third phase always presented a plummeting modulus until total failure, associated with inwards macro-crack propagation. The crack propagation hypothesis was confirmed a posteriori by visual evaluation of broken samples. The physical mechanism that yields to the macrocrack could not be discussed here, should it come from actual cracking or the continuous rearrangement (debonding and slipping) of the microstructure under shear stress. Some authors tried to mitigate the role of heterogeneity of stress/strain field by testing hollow specimens in parallel plates geometry (Apostolidis et al. 2018). Although they concluded that the hollow geometry allowed a better indication of failure, they did not performed strain-controlled tests to compare to the 3-phase fatigue curve. Additionally, monitoring both the modulus and the crack propagation with rheo-optical testing devices could greatly improve the interpretation of such fatigue behaviour in the future.

The three failure criteria were compared. The second inflexion point was almost always obtained before the point at which the sample exhibits half of the initial stiffness, both points being very close nevertheless. The slope change point was always preceding both previous points. The relative discrepancies of failure points appeared relatively constant between criteria, never exceeding a multiplying factor of two. This is confirmed by the linear regression parameters of bitumens' Wöhler curves in Table 4-4. Indeed, the slope coefficients were almost identical between criteria, indicating that a simple multiplying factor separate fatigue life estimations. This result is illustrated in Figure 4-10 for bitumen B, with almost parallel regression lines. With the previous considerations on the probable simultaneity between the slope change point and the crack initiation in sample's periphery, the slope change criterion appeared as the most reliable criterion. The two others tended to overestimate the sample failure point and therefore overestimate γ_6 too, although they presented the very same slope coefficient *b*.

Notwithstanding slight discrepancies on γ_6 evaluation between failure criteria, the differences between bitumens were clear. Bitumen S showed the worst fatigue performance (average γ_6 = 0.305%), while polymer modified bitumen Bm performed the best (average γ_6 = 0.81%). Polymer modification greatly improved γ_6 results (+63% for bitumen S, + 89% for bitumen B). All slope coefficient *b* were very similar amongst bitumen (around -0.33), except a small difference for Bm (-0.29).

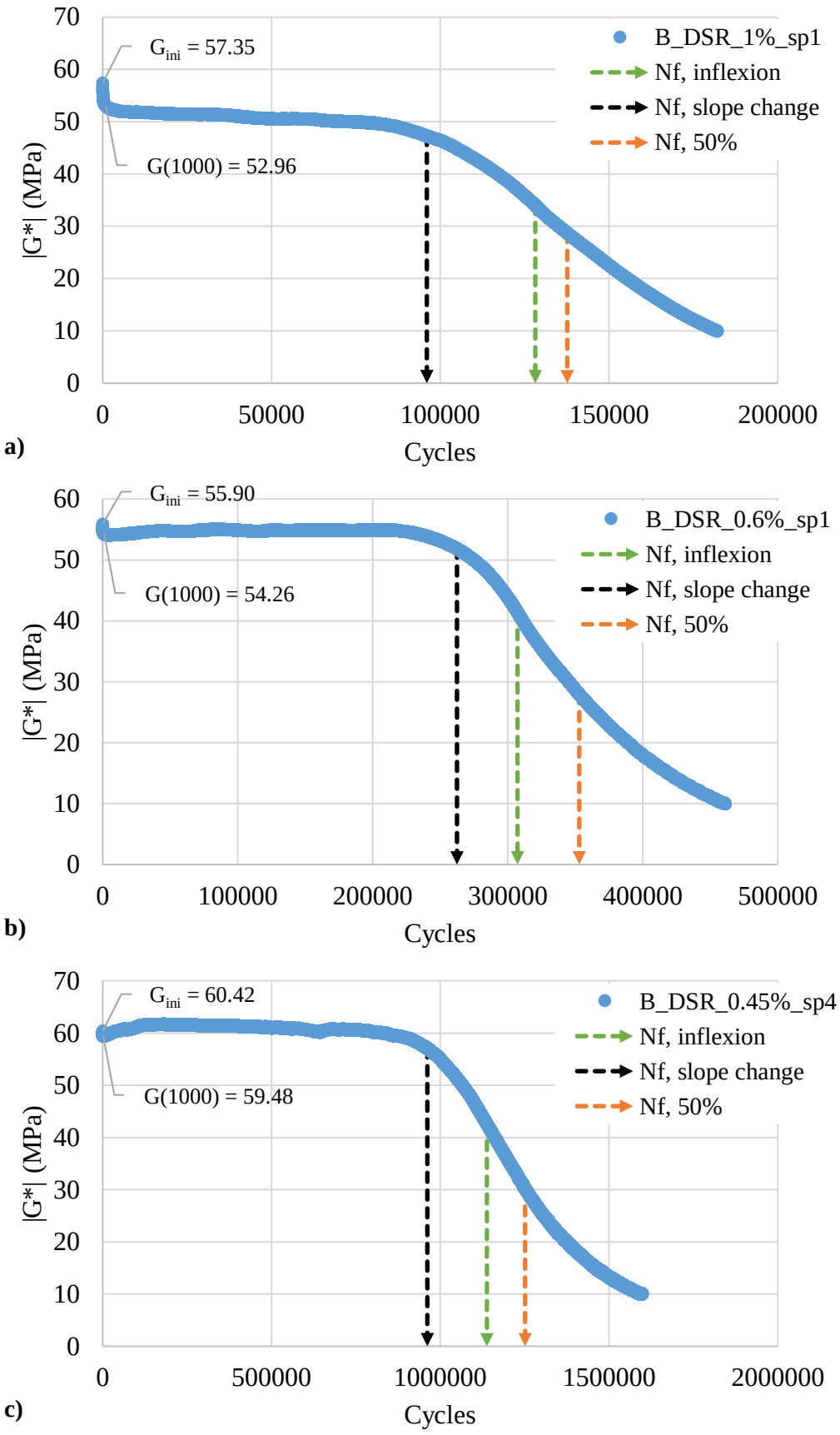

Figure 4-9 |*G**| as a *function of cycles during three fatigue tests on bitumen B at different shear stress amplitudes: a)1%, b) 0.6%, c) 0.45%*

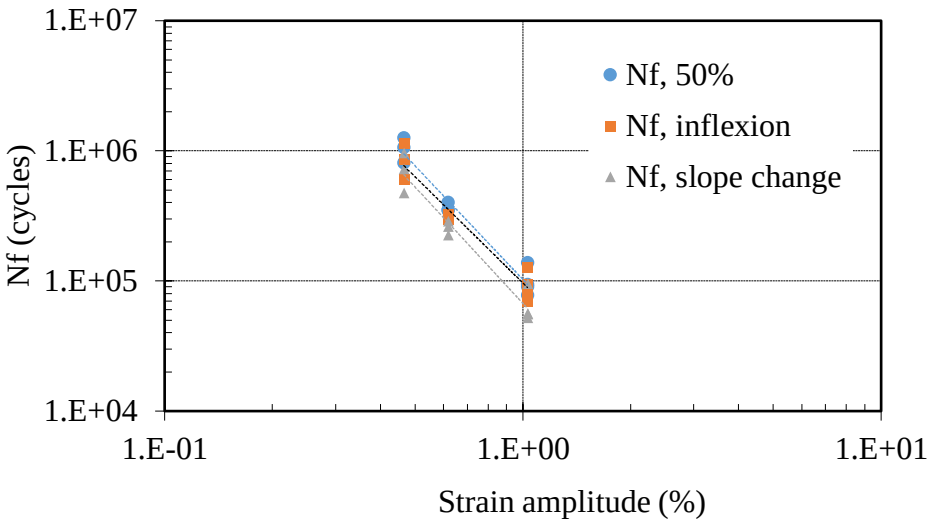

Figure 4-10 *Wöhler curves of bitumen B with three different failure criteria*

Table 4-4 *Linear regression parameters of Wöhler curves obtained with three different failure criteria*

Bitumen	Failure criterion	γ_6 (%)	1/b
B	$N_{f,\ 50\%}$	0.456	-2.90
	$N_{f,\ inflexion}$	0.422	-2.71
	$N_{f,\ slope\ change}$	0.403	-2.97
	avg.	**0.427**	**-2.861**
Bm	$N_{f,\ 50\%}$	0.830	-3.46
	$N_{f,\ inflexion}$	0.815	-3.48
	$N_{f,\ slope\ change}$	0.785	-3.49
	avg.	**0.810**	**-3.474**
S	$N_{f,\ 50\%}$	0.325	-3.12
	$N_{f,\ inflexion}$	0.307	-3.12
	$N_{f,\ slope\ change}$	0.285	-2.95
	avg.	**0.305**	**-3.061**
Sm	$N_{f,\ 50\%}$	0.526	-3.06
	$N_{f,\ inflexion}$	0.496	-2.95
	$N_{f,\ slope\ change}$	0.473	-3.08
	avg.	**0.498**	**-3.027**

The initial loss of modulus during the first 1000 cycles was analysed for all tested specimens. Since the four bitumens did not share the same initial shear moduli G_{ini} (= |G*| at 25th cycle) in the same test conditions, a normalised initial loss of modulus was calculated

$$\frac{\Delta|G^*|}{G_{ini}} = \frac{|G^*|(25^{th}\ cycle) - |G^*|(1000^{th}\ cycle)}{|G^*|(25^{th}\ cycle)} \qquad (4.8)$$

The detailed results are available in Appendix 1.4. An illustrative example is given for bitumen B in Figure 4-11. The initial loss of modulus appeared to be fitting a power function of the shear strain amplitude very well (R^2= 0.99). The power law is simply written

$$\frac{\Delta|G^*|}{G_{ini}} = c(\gamma_0)^p \tag{4.9}$$

,with c and p fitting parameters depending on the material.

The power law regression was performed for all bitumen and results were compiled in Table 4-5. Interestingly, the power coefficient appeared very close to 2 for bitumen B, S and Sm. The associated loss of modulus was limited to less than 10% of initial modulus. This means that the initial loss of modulus was proportional to the dissipated energy, which is itself proportional to the square of the strain amplitude. The average dissipated energy density per cycle, for an equivalent LVE material in parallel-plate geometry, is indeed

$$w_i = \frac{\pi {\gamma_0}^2 |G^*| \sin\varphi}{2} \tag{4.10}$$

The proportionality between the dissipated energy and the initial loss of modulus raised the question of the physical origin of this loss. It has recently been shown that the fully reversible initial stiffness loss in cyclic shear test on binders with ASR was attributed to the combined effects of temperature increase due to energy dissipation and thixotropy (L. F. de A. L. Babadopulos et al. 2019). However, the thermal equilibrium for a given mechanical loading depends on geometrical (sample size), physical (thermal capacity) and environmental properties (thermal chamber efficiency, air convection…). The contributions of reversible phenomena could therefore be different between laboratory set-ups, and obviously in in-situ conditions. Thermomechanical coupling simulations using FEM and rheological models, combined with experimental campaigns with precise monitoring of in-specimen temperature, could pave the way towards a better understanding on phenomena occurring during fatigue (de A. L. Babadopulos, Sauzéat, and Di Benedetto 2017).

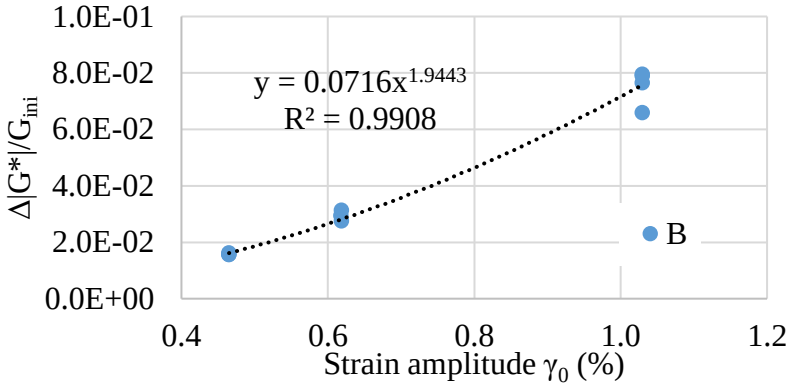

Figure 4-11 *Relative initial modulus loss (4.8) as a function of shear strain amplitude for bitumen B*

Table 4-5 *Power law fitting parameters for initial modulus loss*

Bitumen	c	p	R^2	γ_0 range (%)
B	0.0716	1.94	0.991	0.465 - 1.1
Bm	0.0716	1.63	0.969	0.72 - 1.83
S	0.0821	2.01	0.994	0.34 - 1.03
Sm	0.077	1.85	0.961	0.5 - 1.74

Power law used for initial modulus drop: $\frac{\Delta|G^*|}{G_{ini}} = c(\gamma_0)^p$

4.4.1.3 Quantification of steric hardening of bitumen after specimen cooling

All experimental results regarding steric hardening characterisation are detailed in Appendix 1.3.

In Figure 4-12, an illustrative result of complex modulus (measured periodically at 10°C/25Hz) change of bitumen B during 7-hour rest at constant temperature (10°C) is displayed. Before this rest period, it must be reminded that the bitumen was heated at 90°C during DSR specimen preparation and underwent a 30-min thermal equilibrium (see Section 3.1.1.1) before the complex modulus measurement. The norm of complex modulus increases from 61 to 67.5 MPa at a decreasing rate, whereas the phase angle decreases from 31.6 to 30.3 degrees. This evolution confirms the presence of steric hardening phenomenon previously observed at intermediate temperatures (Planche et al. 2004).

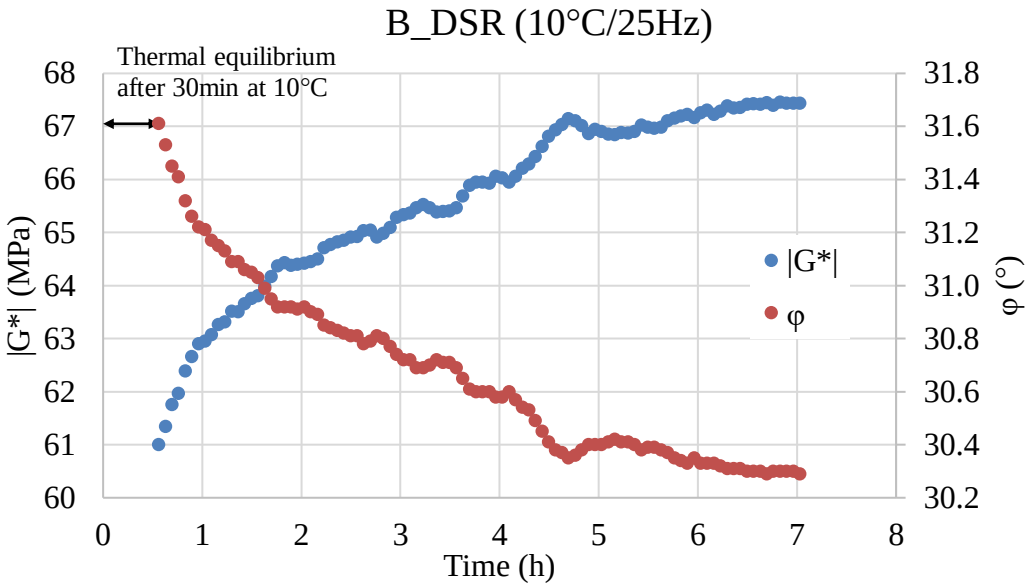

Figure 4-12 *Norm of complex shear modulus and phase angle of bitumen B under constant temperature after specimen setup at 90°C (T=10°C, f= 25Hz)*

Since the role of polymer modification on steric hardening potential is not well documented, the relative evolutions of norm of complex modulus for pure (B, S) and modified (Bm, Sm) were compared in Figure 4-13. The difference of test durations was due to limited DSR availability. All bitumens showed a clear relative modulus increase of at least 9% after 9 hours. It appeared that even for the longest test (18h with Bm), the modulus stabilisation is not achieved, as the rate of increase was still positive. Pure bitumens B and S did behave very similarly, despite having significantly different chemical compositions. The role of polymer modification appeared equivocal, as it reduced the modulus increase with bitumen S, but did not significantly change the behaviour of bitumen B. This suggests that the microstructure rearrangement (i.e. steric hardening) could be partially prevented by the polymer chains. These hypotheses require more tests, such as repeatability and with more materials.

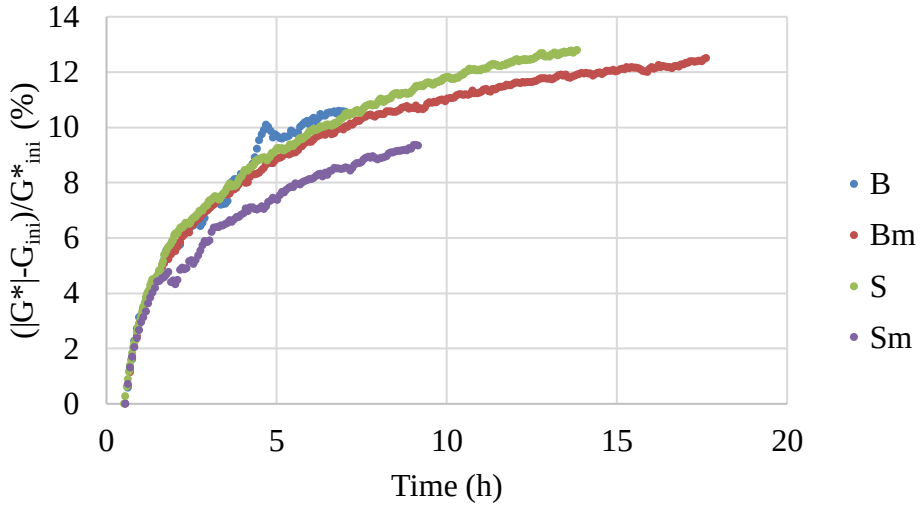

Figure 4-13 *Normalised variations of norm of complex shear modulus under constant temperature after specimen setup at 90°C (T=10°C, f= 25Hz)*

In parallel, an exploratory continuous fatigue test at "low" strain amplitude (0.45%) after a 10-hour rest period at constant temperature (10°C) was performed on S bitumen and the results were compared to the regular fatigue test results (30-minute-rest period only) in Figure 4-14. The biasing effects of steric hardening clearly appeared for the 30-minute-rest specimen. The modulus increase during the first 200000 cycles of testing (5MPa, 6% of initial modulus) was around half of modulus increase obtained by steric hardening during rest periods at constant temperature (Figure 4-13). In phase 2, the 10-hour-rest specimen did not exhibit modulus increase nor a stiffness plateau, but rather a slow linear stiffness decrease. This modulus decrease only appeared for high strain amplitudes in previous fatigue test results, suggesting that the phase 2 was mainly driven by continuous damage. These compared results highlighted the fact that continuous damage is probably occurring, even though heterogeneously, before periphery crack initiation that marks the sample failure. Only a proper fatigue test comparison with different strain amplitudes and sufficient repetitions could conclude on the role of steric hardening on fatigue life. The difference of fatigue life observed in Figure 4-14 could entirely be due to the natural scattering between samples.

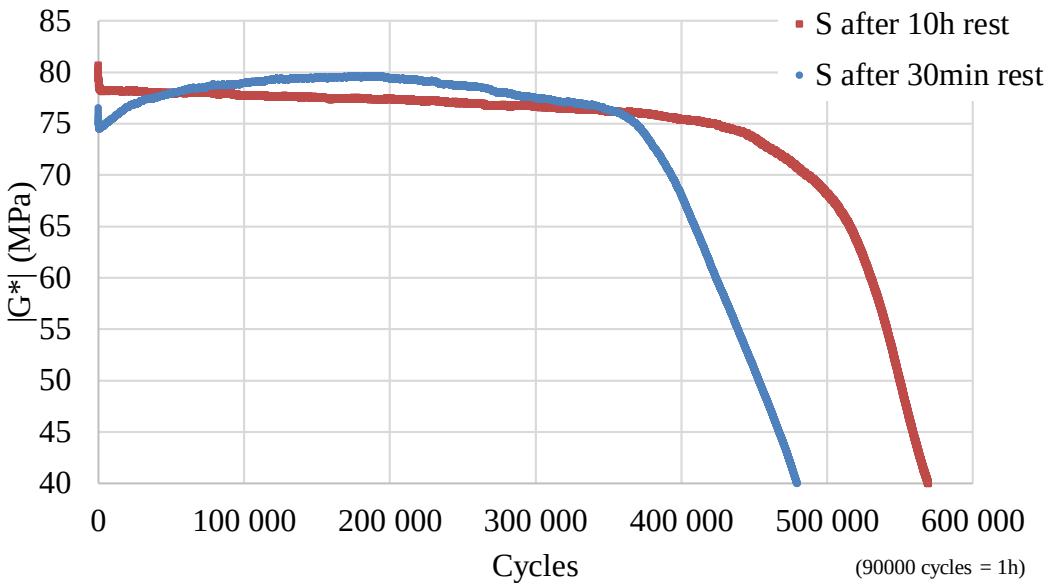

Figure 4-14 *|G*| as a function of cycles for two bitumen S samples with different rest period before fatigue test (30min and 10h) at 0.45% strain amplitude, 10°C and 25Hz*

4.4.2 Comparison of fatigue performances of mixtures and their constituent bitumens

The linear regression parameters of Wöhler curves of mixtures (ε_6, b) obtained with 2-PB fatigue test in sections 4.2 and 4.3 (16 mixtures in total) were plotted as a function of the parameters of their constituent bitumens (γ_6, b) obtained with DSR fatigue test. Both fatigue tests were performed at 10°C/25Hz. The results are given in Figure 4-15 and Figure 4-16. From a general perspective, mixtures' ε_6 appeared to fit reasonably a power function of γ_6, with a power coefficient close to ½ (R^2=0.85). The dispersion could obviously be attributed to the combined influence of bitumen and aggregate on the fatigue performances of mixtures, which was studied in previous sections. From a parametric point of view, the relationship between ε_6 and γ_6 strongly depended on the aggregate nature. Indeed, the power law regression between mixtures with CR aggregates and mixtures with BE aggregates were significantly different although they shared the same bitumens (S and Bm). Nevertheless, the benefits of polymer modification on the resistance to fatigue of bituminous mixtures was found similarly in bitumens performances. This observation is in contradiction with previous work of Soenen et al., where the neat increase of performances observed in PmB were not correlated with better mixtures performances (Soenen, de La Roche, and Redelius 2003). In order to illustrate this statement, the results of Figure 4-15 were displayed again in Figure 4-17, alongside with the results of this previous study. It should be noted that in Soenen and co-workers' paper, the tests were conducted with the same geometries, but at significantly different temperatures (adjusted to obtain the same stiffness between materials) because of the varying penetration grade of the tested bitumens. A single crude oil origin was used to produce the bitumens and a single type of mineral aggregate (microdiorite) was used. A linear relationship between ε_6 and γ_6 was established for pure bitumen only, making results with PmB "oddities". The authors suggested that the polymer chains could be mobilised differently during fatigue tests in bulk bitumen and in mixture. This assumption is directly questioned by the results of this campaign, which clearly suggest a correlation between the increment of fatigue performances of bitumen and mixtures thanks to polymer modification. This affirmation is backed up by results on two bitumens (2 different crude sources) and five very different aggregates sources.

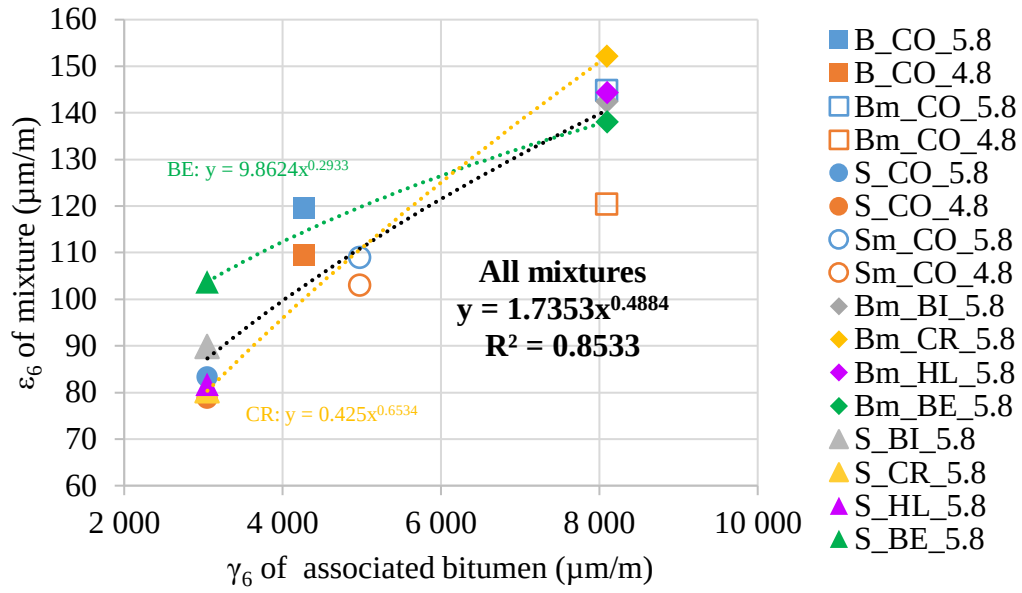

Figure 4-15 *ε_6 of bituminous mixtures as a function of γ_6 of their constituent bitumens*

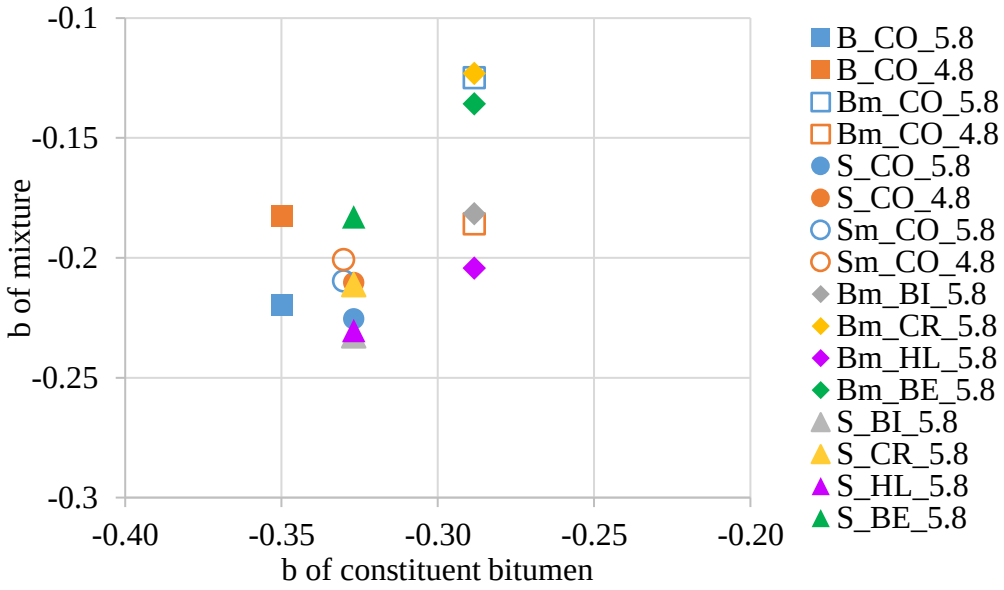

Figure 4-16 *Slope coefficient b of bituminous mixtures as a function of b of their constituent bitumens*

Regarding slope coefficients *b*, the results were consistent across tested materials. Bitumen presented close values centred on -0.33 (from -0.35 to -0.29). Almost all mixtures exhibited close *b* values, this time centred on -0.21 (from -018 to -0.23), to the exception of three mixtures made with Bm bitumen (Bm_CO_5.8, Bm_BE_5.8 and Bm_CR_5.8), whose slope coefficients were particularly high (*b* = -0.13). From a general perspective, it has already been established that the slope coefficients of bituminous mixtures are close to -0.2 (Di Benedetto, Roche, et al. 2004) in standardised conditions. Concerning bitumens, the limited amount of papers dedicated to the classical evaluation of fatigue performance with DSR (H. Soenen and Eckmann 2000; Hilde Soenen, de La Roche, and Redelius 2003) or even METRAVIB® (Vignard et al. 2009), in addition to the current campaign, tends to show that the slope coefficient is closer to -0.3 or -0.35.

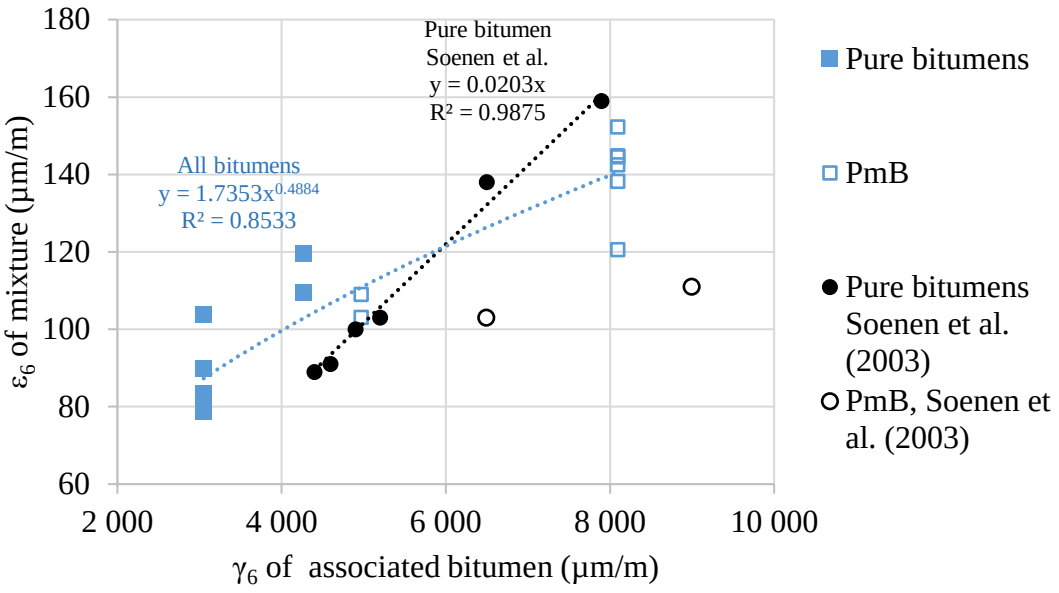

Figure 4-17 *Comparison of ε_6 vs. γ_6 results of Campaign I and previous sources* (Hilde Soenen, de La Roche, and Redelius 2003)

4.5 Predictive equation for mixtures fatigue performances

The classical characterisation of fatigue behaviour of bituminous mixtures is expensive and time-consuming. In the French approach, paving technologists differentiate studies on mixtures in four levels of characterisation:

- Level 1 (mandatory): Compactability with Gyratory press (AFNOR 2007a) and resistance to water (AFNOR 2018d)
- Level 2: Resistance to rutting (AFNOR 2013c)
- Level 3: Rutting + Stiffness (AFNOR 2012d)
- Level 4: Rutting + Stiffness + resistance to fatigue (AFNOR 2012c)

Hence, the characterisation of the resistance to fatigue of mixtures usually implies the realisation of the other tests. Since the fatigue tests are the longest to prepare (18+ trapezoidal samples sawing out of slabs + 2-week curation) and conduct (approx. 2 weeks with a doubled 2PB apparatus), the interest of a reliable, predictive equation of fatigue performance (especially ε_6) is natural among paving technologists.

A predictive equation (4.11) was proposed in this work, with three parameters:

- A: *ITSR* (no unit)
- B: polymer content in bitumen (no unit). PmB possessed 3% of SBS.
- C: $|E^*|$ at 15°C/10Hz (MPa)

These parameters were selected to propose a predictive equation that could be established at level 3 study on mixtures, in order to indicate if a potential fatigue study is worth conducting.

$$\varepsilon_6 = \beta_0 + \beta_A A + \beta_B B + \beta_C C + \beta_{AB} AB + \beta_{AC} AC + \beta_{BC} BC + \beta_{ABC} ABC \qquad (4.11)$$

The predictive equation also had cross parameters, in the same fashion as the regression used in the full factorial plan of Section 4.2. The calculation of the regression coefficient β_X was made by least squares method with Excel® Solver.

The predicted ε_6 values are plotted against the experimental values in Figure 4-18, and the regression coefficients are available in Table 4-6. The agreement between the prediction and the experimental results is fair (R^2=0.63) but the maximum discrepancy equalled 22µdef. This was not surprising considering the complexity behind the fatigue performances (influence of bitumen and aggregate), but this model still catched well the trend over a significant range of ε_6 values, with parameters selected from either material properties (polymer content) or mixtures performances of lower level of study ($|E^*|$ and *ITSR*). Eventually, this model could be fuelled with more classical test results on mixture or even enhanced with new parameters, such as void content, which was not relevant in this study.

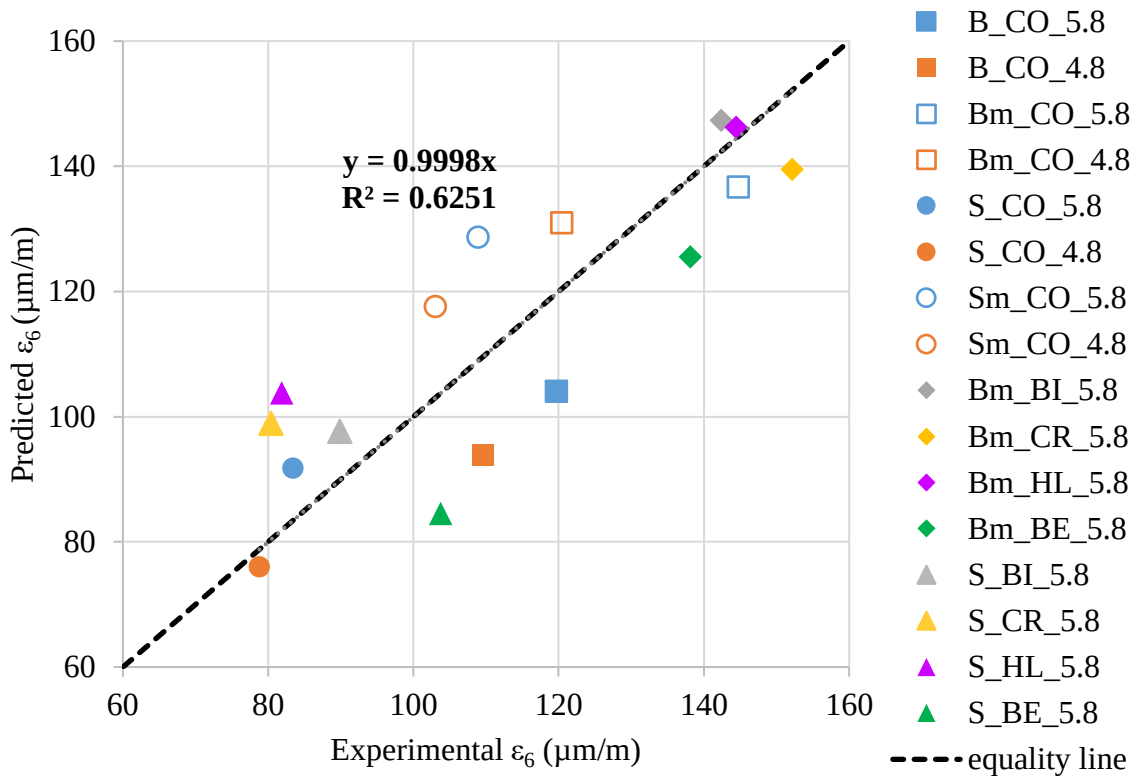

Figure 4-18 *Predicted ε_6 vs. experimental ε_6 of mixtures of campaign I*

Table 4-6 *Regression coefficients used in the prediction of ε_6 (4.11)*

β_0	β_A	β_B	β_C	β_{AB}	β_{AC}	β_{BC}	β_{ABC}
100	65	130	-0.003	1210	-0.004	0	0.015

4.6 Conclusion of Campaign I

This first campaign focused on the influence of bitumen and aggregates on the thermomechanical performances of bituminous mixtures according to the European testing methods.

A full factorial experimental plan was proposed to quantify the influence of the origin of the bitumen, the polymer modification and the binder content on mixtures performances. The results demonstrated that only the origin of the bitumen and the binder content were influential on stiffness, without cross effects. The resistance to fatigue, characterised by ε_6 was strongly determined by the bitumen origin (+30µdef from bitumen S to B), secondly by polymer modification (+20µdef from pure to PmB), and slightly by binder content (+11µdef from 4.8 to 5.8%). Regarding water sensitivity, the two main factors were the bitumen origin (+6% from S to B), the polymer modification (+6% from pure to PmB), but with important cross effects.

The role of the aggregates nature on mixture performances was investigated on 10 different materials (5 aggregates sources for 2 bitumens). The aggregates nature played a significant role on mixture stiffness even with the same recomposed grading curve and the same void content, sometimes greater than bitumen origin or binder content. The impact of aggregates nature on fatigue behaviour was limited, although important cross effects with the constituent bitumen were observed. The nature of aggregates was also a determining factor of water sensitivity, again with important cross effects.

The fatigue performances of the four bitumens of the study were established with DSR fatigue tests. The initial stiffness drop in phase 1 was thoroughly analysed. The relative initial loss of modulus appeared proportional to the dissipated energy by viscous flow. Three failure criteria were implemented, all leading to close results, and clear differences of fatigue life between bitumens. The polymer modification strongly increased the resistance to fatigue (γ_6 increase of +63% for S and +89% for B). The stiffness increase observed in phase 2 at low strain amplitude was attributed to steric hardening, since the material was rapidly cooled down from hot temperature 30 minutes before testing. The quantification of the effects of this phenomenon on complex modulus was achieved with discontinuous sinusoidal test during long rest period at constant temperature. The steric hardening is responsible for relative modulus increase of 9 to 13%, still measureable after 18 hours.

The comparison of fatigue performances of mixtures and their constituent bitumens leads to a reliable power law function between γ_6 and ε_6 with a power coefficient of ½, with non-negligible cross effects with the nature of aggregates. The improvement of resistance to fatigue attributed to polymer modification was found in both bitumens and mixtures, which contradicted previous exploratory results in the literature. The slope coefficient *b* for bitumens were between -0.3 and -0.35. The slope coefficient for the mixtures were closer to -0.2. Overall, the fatigue performances of bitumens appeared strongly linked to fatigue results obtained on mixtures.

Finally, a predictive equation of fatigue performance of mixtures (ε_6) has been proposed, based on one material property (polymer content) and two test performances (|E*| at 15°C/10Hz and *ITSR*). A fair agreement between the prediction and the experimental values was obtained. This predictive tool could be adjusted with more test results or even enhanced with new parameters.

5 Campaign II: Behaviours of bitumens and mastic made with glass beads

5.1 Objectives

The second campaign of this thesis focused on the characterisation of the behaviour of pure bitumens, PmB and one bituminous mastic made with glass beads :

- in the linear viscoelastic (LVE) domain
- during cyclic loading and rest periods (LRP)

The first objective behind the characterisation of LVE behaviour of bituminous binders was to study the influence of the polymer modification and the relationship between the glass-bead mastic and its constituent bitumen, with the help of 2S2P1D rheological model (Olard and Di Benedetto 2003). The second objective was to compare the complex modulus test results of all bitumens between the Annular Shear Rheometer (ASR) and the classical Dynamic Shear Rheometer (DSR).

The study of bituminous binders submitted to LRP has proven to be crucial to allow the separation and the quantification of the reversible (self-heating, nonlinearity and thixotropy) and irreversible (damage) phenomena occurring in bituminous materials that undergo repeated loading cycles (Shan et al. 2010; 2011; Q. T. Nguyen 2011; Salvatore Mangiafico 2014; L. F. de A. L. Babadopulos et al. 2019). Additionally, the healing potential of bituminous binders directly challenges the reversibility of damage over long rest periods. Hence, the main objective of this work on LRP was to separate and quantify the role of each phenomenon including healing during loading and particularly long rest periods, with a variety of binders and different loading amplitudes.

5.2 Linear viscoelastic behaviour

This section is dedicated to the characterisation of the LVE behaviour of bitumens and one mastic made with glass beads using results from complex shear modulus tests.

5.2.1 Complex shear modulus tests

Two pure bitumens (B and S) and their associated PmB (Bm and Sm) were tested. Additionally, the glass-bead mastic “B_40%”, made of 60% (in volume) of bitumen B and 40% of silica glass beads of homogeneous size (c.f. materials section 3.2), was characterised. The general term “binder” will designate either the bitumen or the glass-bead mastic in the rest of this work.

All binders were tested with the Annular Shear Rheometer (ASR). The procedure of complex shear modulus test with ASR, described in Figure 5-1, consisted of frequency sweep tests from 10 to 0.01Hz at seven different temperatures from -15°C (or -10°C) to 60°C. For each temperature, a 4-hour rest was imposed before the frequency sweep test, which ensured thermal equilibrium (Delaporte 2007; L. Babadopulos 2017). It should be noted that a preliminary frequency sweep test at 10°C is performed before starting the actual complex modulus test from the lowest temperature (-15°C or -10°C). This was added to validate the sample integrity after passing the lowest temperature by comparing the results to the second passage at 10°C. Previous work indeed showed the potential stripping of binder from the cylindrical metallic moulds of ASR due to discrepancies of thermal contraction (Orozco 2016). All specimens tested with ASR were noted “X_ASR_spY”, with X designating the material name and Y the specimen number. The complex modulus test was performed only once per material, except for bitumen B (B_ASR_sp1 and B_ASR_sp5). Indeed, the potential discrepancies due to repeatability with this apparatus have already been studied, and represent only few percent in relative change of $|G^*|$ (less than 8%) and few tenth of degrees variations on phase angle (less than 0.5) (Delaporte 2007).

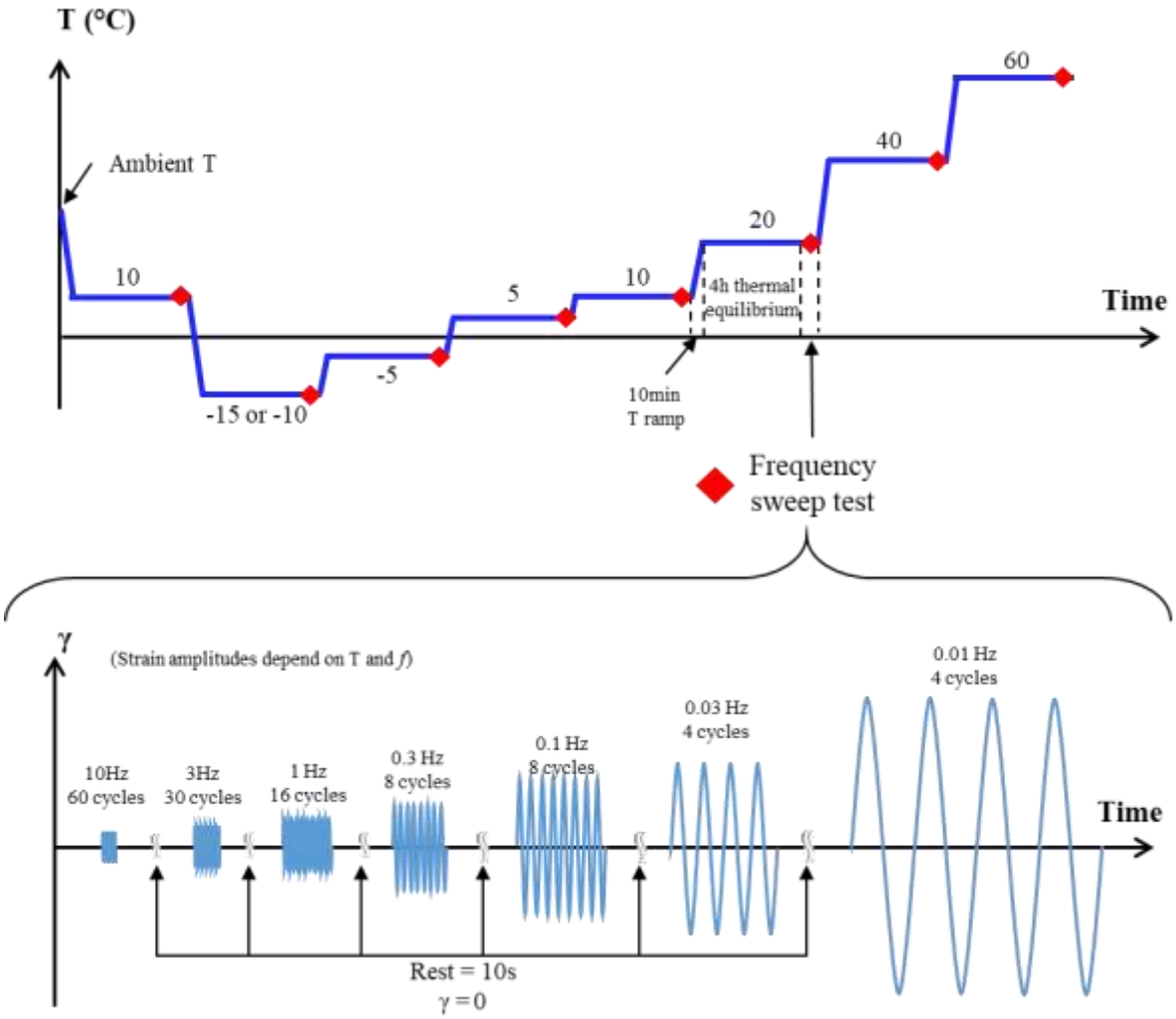

Figure 5-1 *Scheme of the thermomechanical loading applied during complex shear modulus test using ASR*

All bitumens were also tested with the DSR with the parallel plates (PP) geometry. The complex modulus test consisted of two series of frequency sweep tests for each bitumen, schematised in Figure 5-2. The first one used 8mm diameter plates for low temperatures ranging from -20°C to 40°C. The second one used 25mm diameter plates for high temperatures ranging from 30°C to 70°C. In both cases, the bitumen chip samples were preliminary mounted on the plates at 90°C (see section 3.1.1.1). Frequency sweep tests from 10 to 0.01Hz were applied at a constant shear strain amplitude of 0.1% (=1000µm/m) for each isotherms after a 30-minute rest to obtain thermal equilibrium. Although steric hardening effects on the modulus could be important for the first isotherm (after a quick cooling from 90°C) as it has been proven in Chapter 4, these effects were neglected in the analysis of results. Indeed, the potential discrepancy on the complex modulus value (about 10% in first approximation) was negligible compared to the scale amplitude of modulus measures (at least 5 decades). All bitumens were tested only once with DSR and were noted “X_DSR”, with X designating the bitumen name.

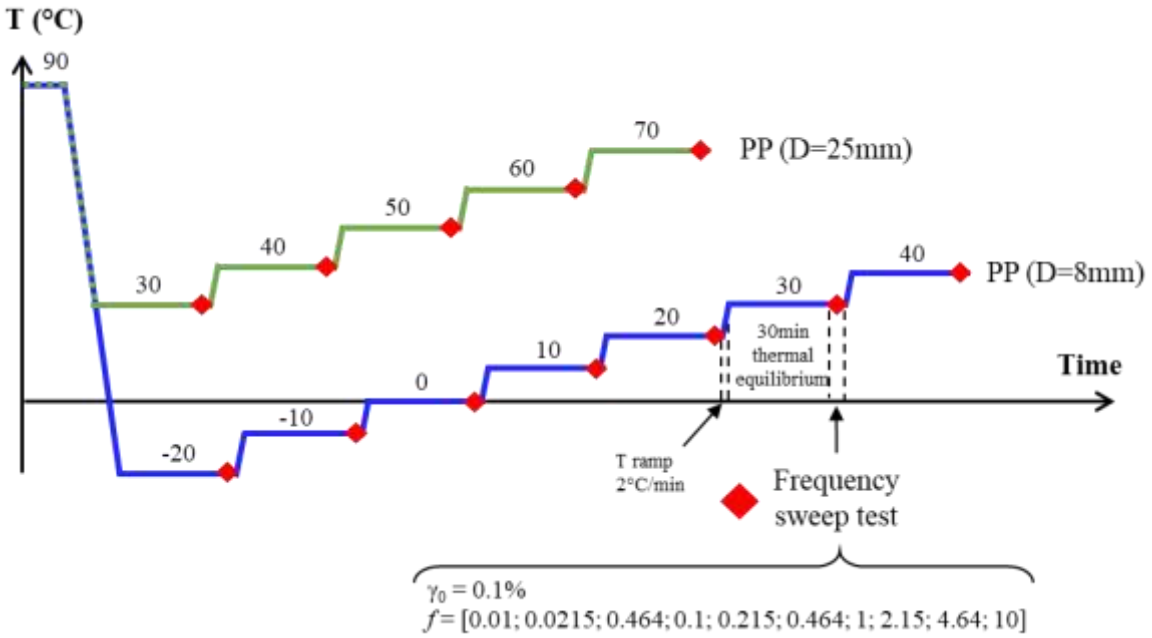

Figure 5-2 *Scheme of the procedure for the complex shear modulus test using DSR with parallel plate (PP)*

5.2.2 Results and analysis

All results of complex shear modulus tests on binders are available in Appendices 1.1.1.

5.2.2.1 Bitumens

Regarding complex modulus tests results on bitumen, the first step of analysis was the comparison between DSR and ASR results. An example of complete ASR and DSR results and their associated 2S2P1D models for bitumen B is given in Figure 5-3. At intermediate temperatures (0°C < T < 40°C), the values of complex shear modulus were always very close. For instance, for bitumen B at 10°C, the maximal relative difference was 12% of norm of complex modulus and 1° of phase angle for all tested frequencies, even if the complex modulus dramatically changed as a function of the frequency (|G*| = 45MPa at 10Hz against |G*|=1MPa at 0.01Hz). These very consistent results between ASR and DSR test set-ups were also checked at high temperatures (>40°C), although the ASR started exhibiting some limitations around 60°C, especially on phase angle evaluation, due to very low stress signals. However, at low temperatures (<0°C), DSR values of |G*|were always smaller than ASR values. The asymptotic glassy moduli G_0 were significantly lower (from 20 to 50% depending on the bitumen) when predicted with DSR results than when predicted with ASR results. Similar discrepancies were found by previous studies that compared DSR to Metravib® test results (Salvatore Mangiafico 2014). In this work, the ASR prediction should be preferred, since it corresponded very well with the literature, with a G_0 value around 1GPa (Read and Whiteoak 2003). Hence, it is possible that there was a flaw in DSR measurements, possibly due to bitumen stripping from the plates or another phenomenon that reduces the apparent cross sectional area of the sample. This hypothesis would imply that the related loss of modulus would only depend on the temperature and not the frequency, creating “steps” in the complex modulus curves in complex planes (loss of TTSP), as it is shown for ASR test results in Figure 5-3 a). In fact, the DSR results formed a unique curve without clear step between the lowest temperatures (0, -10, -20°C). This observation challenged the initial stripping hypothesis. Another possibility for the underestimation of the glassy modulus was the deformation of the torsion shaft that could lead to an overestimation of the actual shear strain in the sample. This potential bias is obviously not possible with the ASR set-up thanks to the extensometers that allows a direct measure of shear strains (see Section 3.1.1.2).

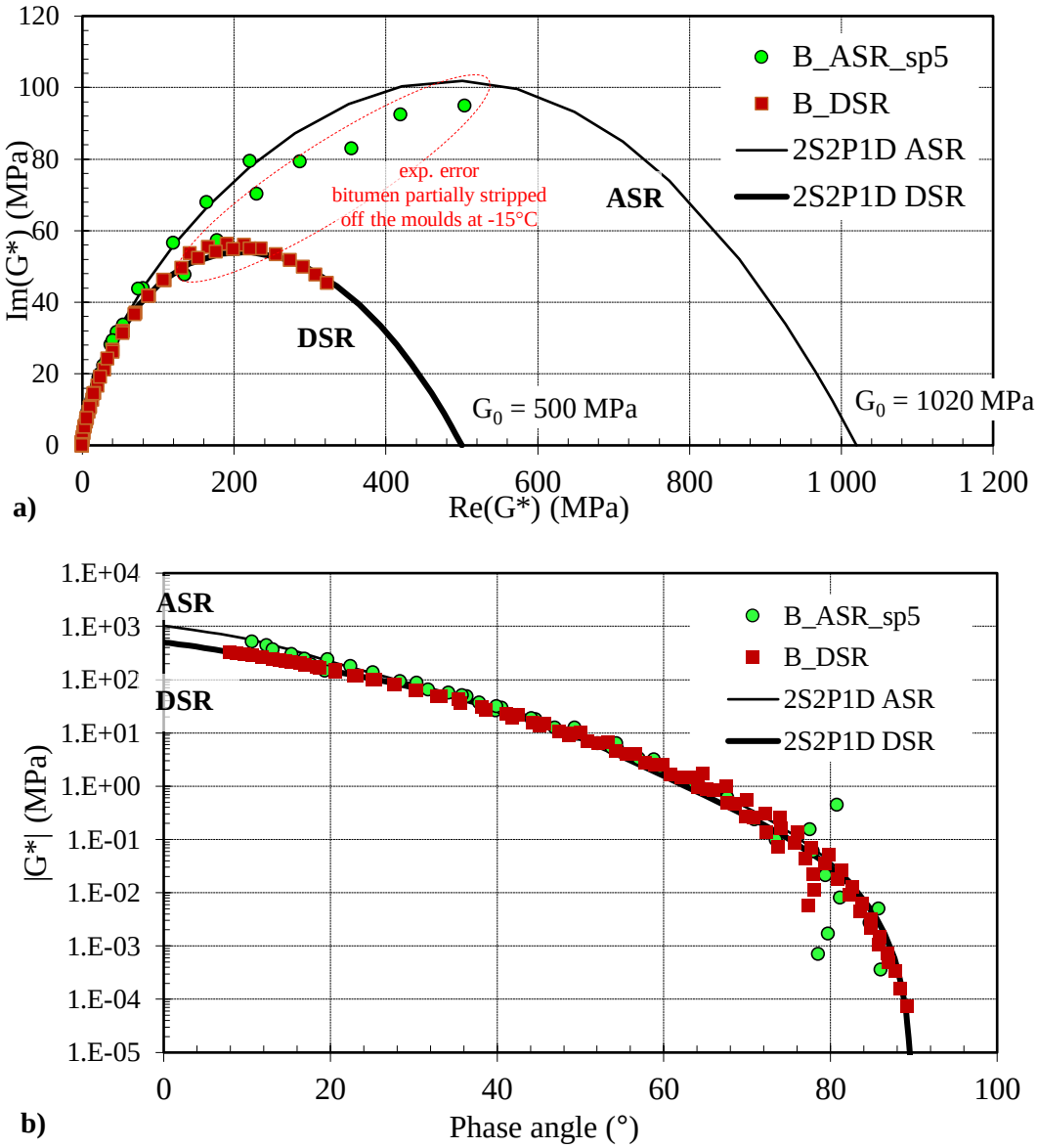

Figure 5-3 C*omplex shear modulus test results and associated 2S2P1D models of bitumen B, obtained with ASR and DSR in: a) Cole-Cole plot, b) Black diagram*

In the light of the previous observations, combined ASR and DSR complex modulus tests results were built with ASR results at low temperatures (usually $T \leq 20$°C) and DSR at high temperatures (usually $T \geq 10$°C), with overlapping isotherms at least over a 10°C range at intermediate temperatures. For the purpose of brevity, only the combined ASR + DSR results of bitumen B are fully displayed in Figure 5-4 and Figure 5-5. In this figures, isotherms and master curves (T_{ref} = 15°C) of |G*| and φ are represented. The complex modulus results in Cole-Cole plot and Black diagram, as well as the WLF law for the shift factors a_T and 2S2P1D model for the LVE behaviour are also plotted. Finally, the master curves and normalised complex shear modulus were added. This normalised modulus is defined as

$$G^*_{norm} = \frac{G^* - G_{00}}{G_0 - G_{00}} \tag{5.1}$$

For other bitumens, please refer to Appendices 1.1.1. The transition from ASR to DSR results were systematically seamless. Eventually, all combined ASR + DSR results provided accurate measurements of the norm of complex modulus over 7 decades (from 2×10^{-5} to 5×10^{2} MPa).

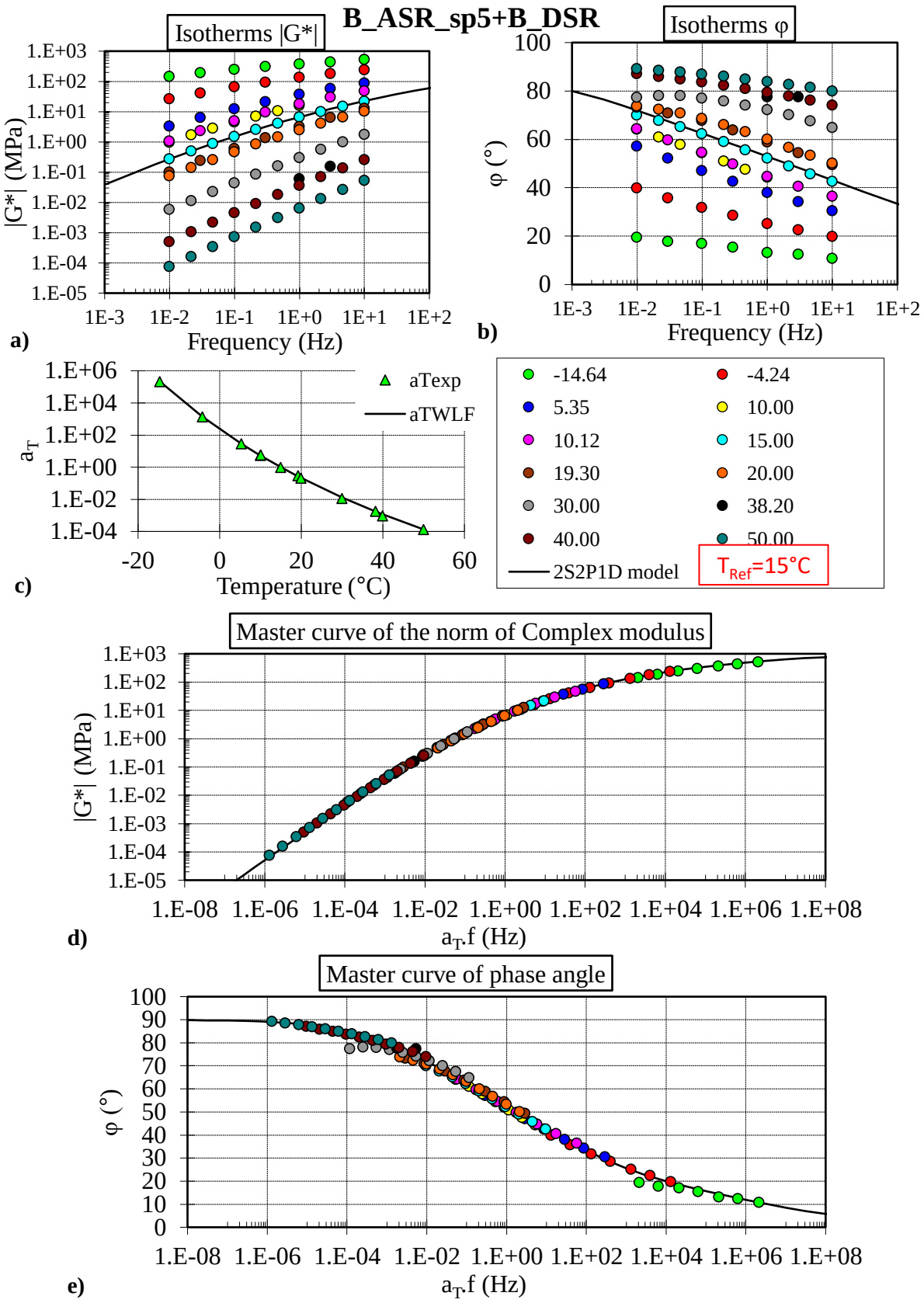

Figure 5-4 *Combined results of complex shear modulus tests with ASR and DSR for bitumen B: a) Isotherms of |G*|, b) isotherms of phase angle, c) shift factors a_T, as a function of temperature d) master curve of |G*|, e) master curve of phase angle. T_{ref} = 15°C*

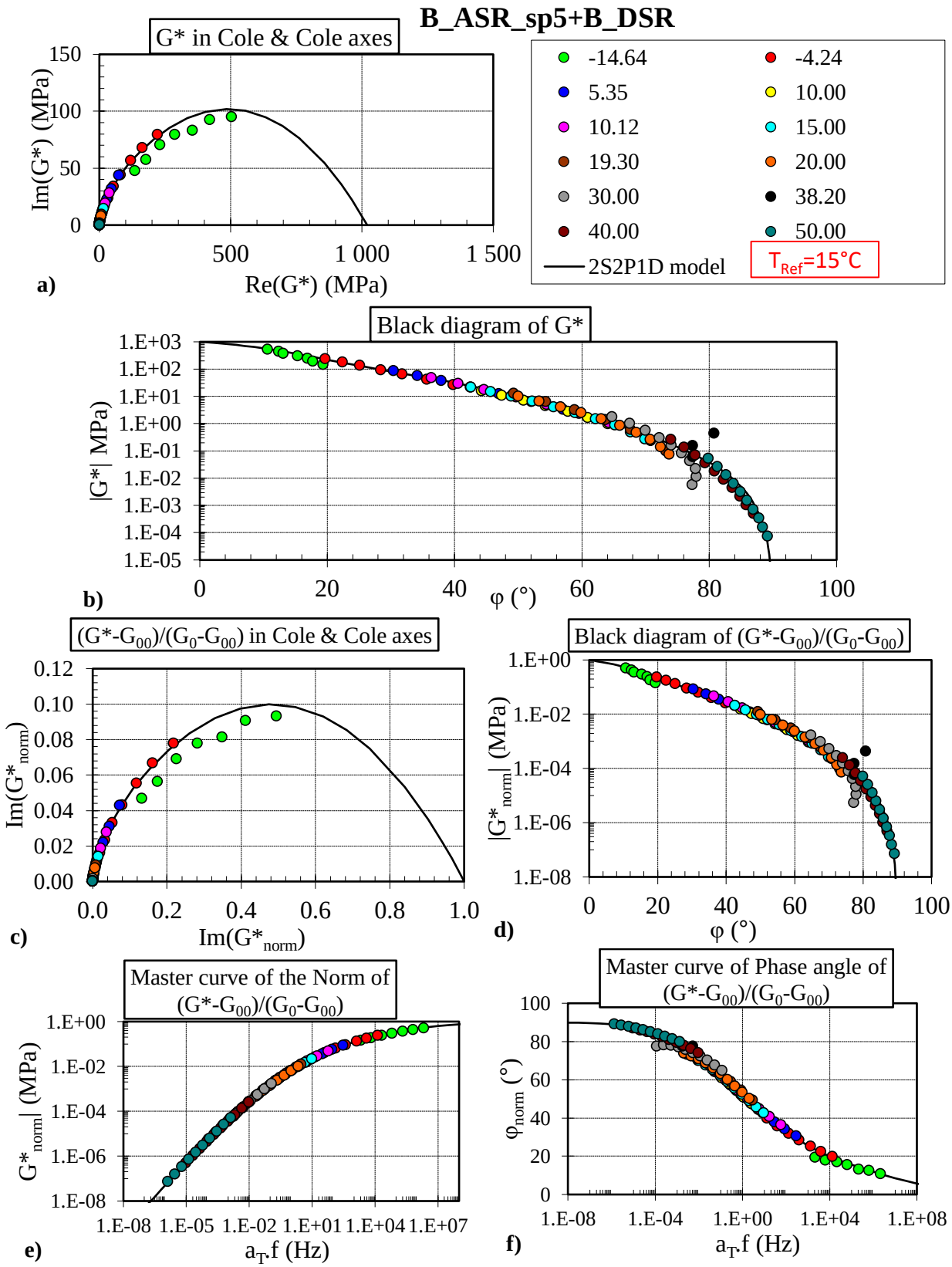

Figure 5-5 *Combined results of complex shear modulus tests with ASR and DSR for bitumen B: a) G* in Cole-Cole plot, b) G* in Black diagram, c) G*$_{norm}$ in Cole-Cole plot, d) G*$_{norm}$ in Black diagram, e) master curve of |G*$_{norm}$|, f) master curve of phase angle of G*$_{norm}$. T_{ref} = 15°C.*

From a general perspective, the Time-Temperature Superposition Principle (TTSP) was verified for all four bitumens. An example of master curves of norm of complex modulus and phase angle (T_{ref} = 15°C) is available in Figure 5-4 d) and e). Moreover, the WLF equation (see Section 2.3.2.2.4) modelled correctly the shift factors, as shown in Figure 5-6. All WLF parameters values are listed in Table 5-1. The bitumens B and S exhibited different a_T, with B being slightly more thermo-sensitive than S. The polymer modification of both bitumens, however, almost did not modify their respective shift factors.

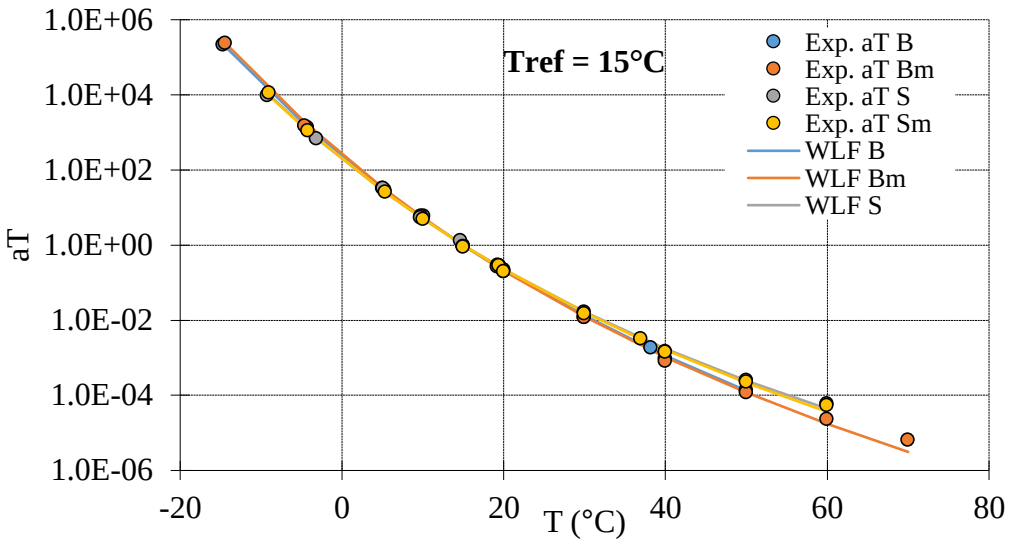

Figure 5-6 *Experimental shift factors and associated WLF law of bitumens at T_{ref} = 15°C, based on combined ASR + DSR results*

Table 5-1 *2S2P1D constants and WLF parameters of bitumens results obtained with ASR, DSR and combined ASR+DSR results*

		2S2P1D constants							WLF parameters		
		G_{00} (MPa)	**G_0 (MPa)**	**k** -	**h** -	**δ** -	**τ_0 (s)**	**β** -	**T_{ref} (°C)**	**C_1** -	**C_2 (°C)**
ASR	B_ASR_sp1	0	1020	0.25	0.62	5.0	1.04E-04	100	15	20.4	151.5
	B_ASR_sp5	0	1020	0.25	0.62	5.0	9.75E-05	100	15	20.4	151.5
	Bm_ASR_sp2	0.0006	1000	0.23	0.58	5.4	8.01E-05	280	15	24.9	177.4
	S_ASR_sp2	0	1000	0.24	0.55	2.2	7.40E-05	60	15	20.4	151.8
	Sm_ASR_sp1	0.0005	890	0.22	0.57	3.0	1.08E-04	50	15	13.1	101.8
DSR	B_DSR	0	500	0.24	0.60	2.7	1.80E-04	110	15	28.0	203.3
	Bm_DSR	8E-05	800	0.15	0.47	2.0	1.20E-05	1000	15	21.2	158.1
	S_DSR	0	700	0.23	0.57	2.0	1.20E-04	40	15	17.8	136.7
	Sm_DSR	3E-05	580	0.23	0.57	2.2	2.00E-04	40	15	17.8	136.7
ASR + DSR	B_ASR_sp5+DSR	0	1020	0.25	0.62	5.0	8.08E-05	100	15	18.6	133.3
	Bm_ASR_sp2+DSR	5E-05	1000	0.24	0.63	5.8	1.03E-04	400	15	18.7	131.6
	S_ASR_sp2+DSR	0	1000	0.24	0.55	2.2	6.53E-05	60	15	16.0	120.1
	Sm_ASR_sp1+DSR	3E-05	860	0.23	0.61	3.0	1.24E-04	100	15	16.9	125.9

The 2S2P1D model, described in Section 2.3.2.4.3, was used to model the LVE behaviour of bitumens. The 2S2P1D calibration constants are listed in Table 5-1, alongside with the WLF parameters. The glassy shear moduli were comprised between 860 and 1020 MPa. The polymer modification altered significantly the value of G_0 only for bitumen S (from 1000 to 860 MPa). Polymer-modified bitumens Bm and Sm also exhibited static moduli (respectively 5×10^{-5} and 3×10^{-5}), whereas pure bitumen tended to be purely viscous at high temperature and low frequency. The static moduli of PmBs were expected because of the elastic skeleton created by the polymer chain network. Although the WLF parameters were very similar between pure bitumens and their respective polymer modified versions, some 2S2P1D constants were quite different after polymer modification. For instance, h = 0.55 for bitumen S and 0.61 for Sm, and δ and β varied in both B and S cases. On the other hand, h did not change much between B (0.62) and Bm (0.63), and k seemed to be almost constant around 0.24 for all four tested bitumens.

Overall, the fitting of 2S2P1D model was excellent for pure bitumens, for instance with less than 10% error on bitumen B over ten decades of equivalent frequency (from 10^{-5} to 10^{5}Hz for T_{ref} = 15°C). Nevertheless, the model started to falter for the phase angle prediction of PmBs at low equivalent frequencies, as this could be observed in the master curves of norm of complex shear modulus and phase angle in Figure 5-7. As for the existence of static modulus for PmB, the polymer chain network influenced the phase angle value at these low equivalent frequencies. In order to tackle these prediction discrepancies specific to PmBs, it would be possible to add a third parabolic element to the existing 2S2P1D. This was not done here, because of the lack of different materials (only 2 couples of bitumens with the same penetration grade) and the expected improvement on the prediction, which did not justify increasing the complexity of a 9-parameters model (7 2S2P1D constants + 2 WLF parameters).

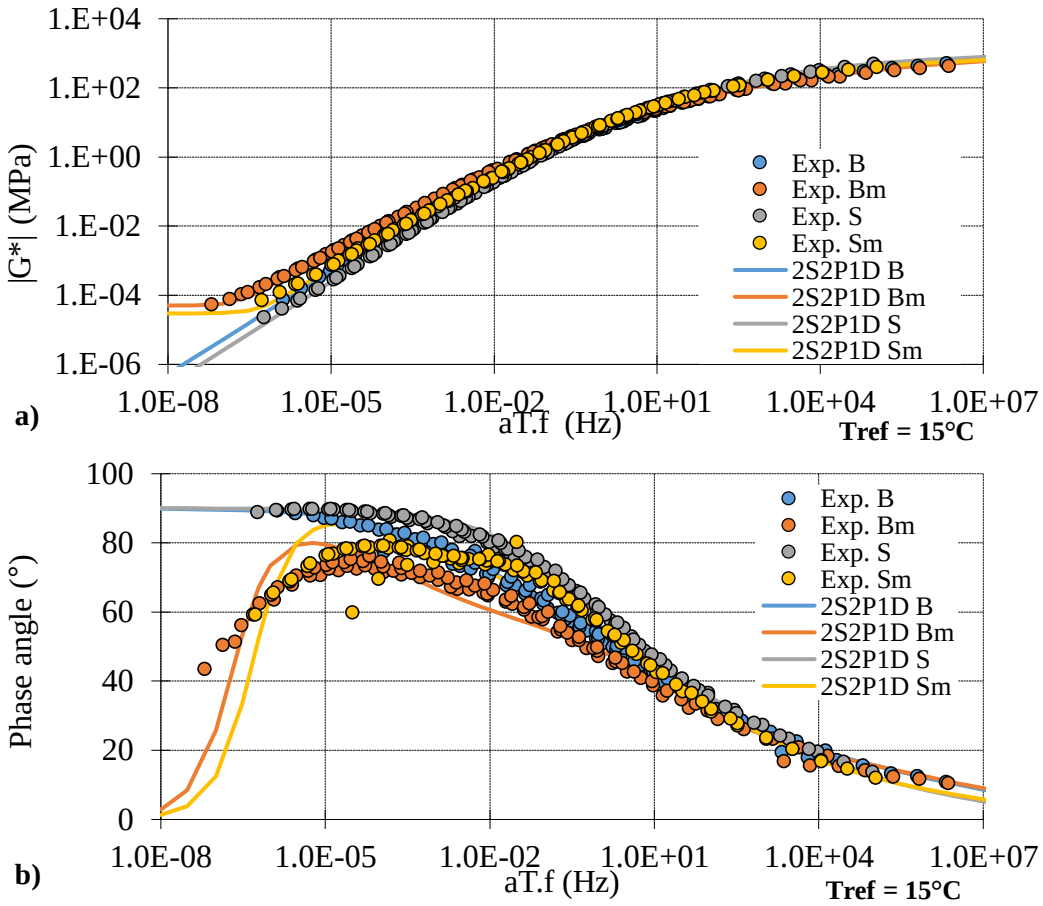

Figure 5-7 *Master curves of complex shear modulus of bitumens and their associated 2S2P1D models at T_{ref} = 15°C: a) Norm of complex modulus, b) phase angle*

5.2.2.2 Mastic made with glass beads

The shear complex modulus test results on mastic B_40% are presented in Figure 5-8 and Figure 5-9. The WLF parameters, alongside with the 2S2P1D constants used to model the LVE behaviour of the mastic are available in Table 5-2. In this table, the model parameters of the constituent bitumen B, previously introduced in section 5.2.2.1, are also presented for comparison purpose. Moreover, the normalised complex shear moduli of both mastic and bitumen are presented together in Figure 5-10.

Just as for the bitumens, the mastic validated the TTSP. The WLF equation provided a satisfying model of shift factors, and the 2S2P1D model suited well the experimental results. The mastic B_40% shared the same shift factors with its constituent bitumen B. This suggests that the time and temperature dependency of LVE behaviour of mastic is fully inherited from its bitumen. This conclusion has already been reached for other bitumen/mastic couples studied with ASR (Delaporte et al. 2007; L. Babadopulos 2017). Four 2S2P1D constants were shared (k, h, δ, β). The glassy modulus of mastic was significantly higher than its corresponding bitumen G_0 (4GPa vs. 1GPa). In opposite to the null static modulus of bitumen B, the mastic B_40% had a G_{00} of 300 Pa. This suggested that the glass beads create a rigid skeleton at high equivalent temperatures. This configuration is not obvious in the first place. In the ideal case of a perfectly dispersed spherical beads of homogeneous size, the percentage of filler to obtain grain-to-grain contact in a bitumen matrix need to be at least 52%. In this study case, the filler only formed 40% of the total volume, so that only a part of the beads could form a rigid skeleton. In addition to the asymptotic moduli, B_40% and B differed only on the temperature-related constant τ_0 of the 2S2P1D model. This implied that their normalised shear complex modulus must share the same curve in Black diagram, as confirmed in Figure 5-10. In conclusion, the mastic with 40% of glass beads inherited the LVE properties of its constituent bitumen.

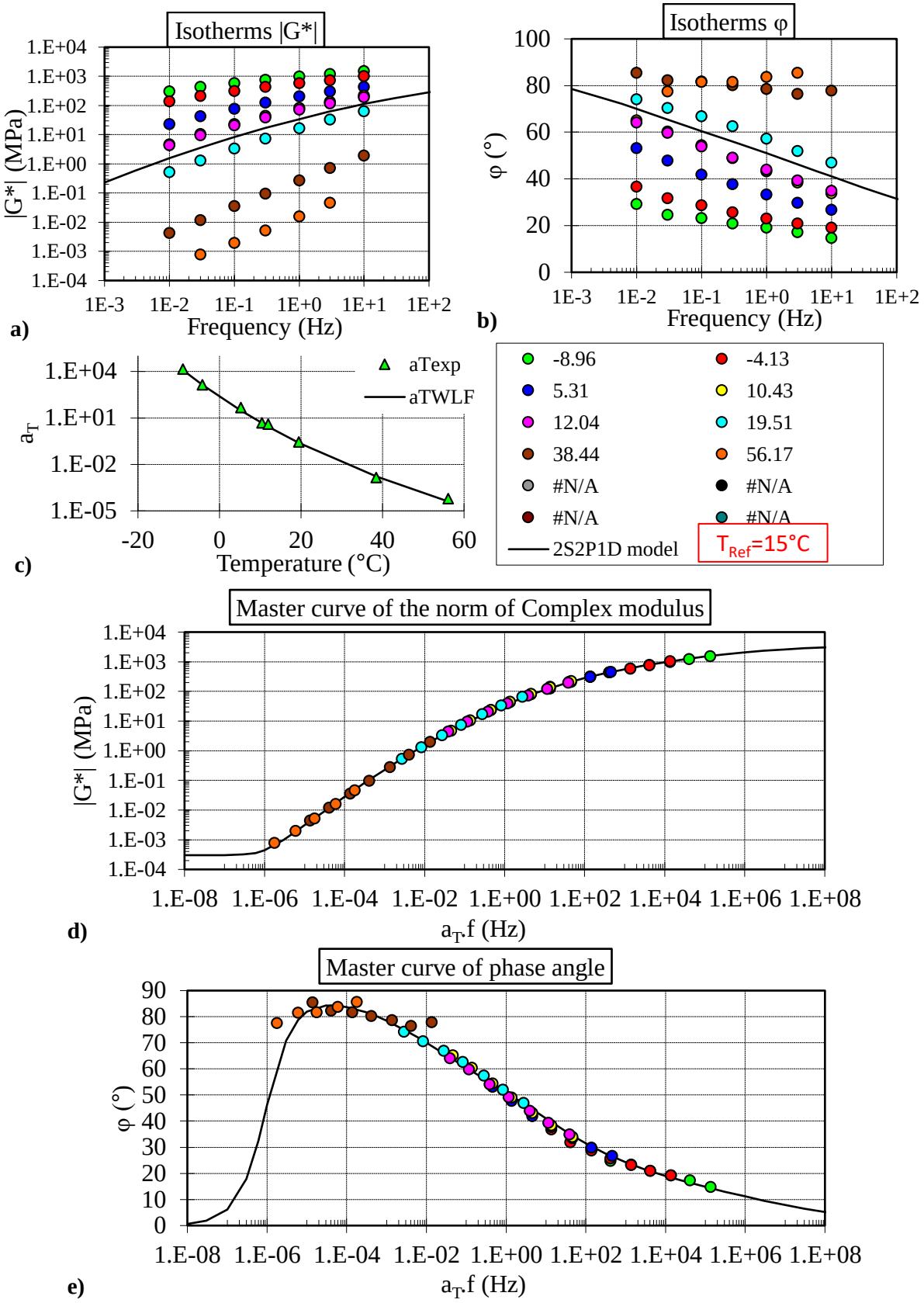

Figure 5-8 *Combined results of complex shear modulus tests with ASR for mastic B_40%_ASR_sp1: a) Isotherms of |G*|, b) isotherms of phase angle, c) shift factors a_T, as a function of temperature d) master curve of |G*|, e) master curve of phase angle. T_{ref} = 15°C*

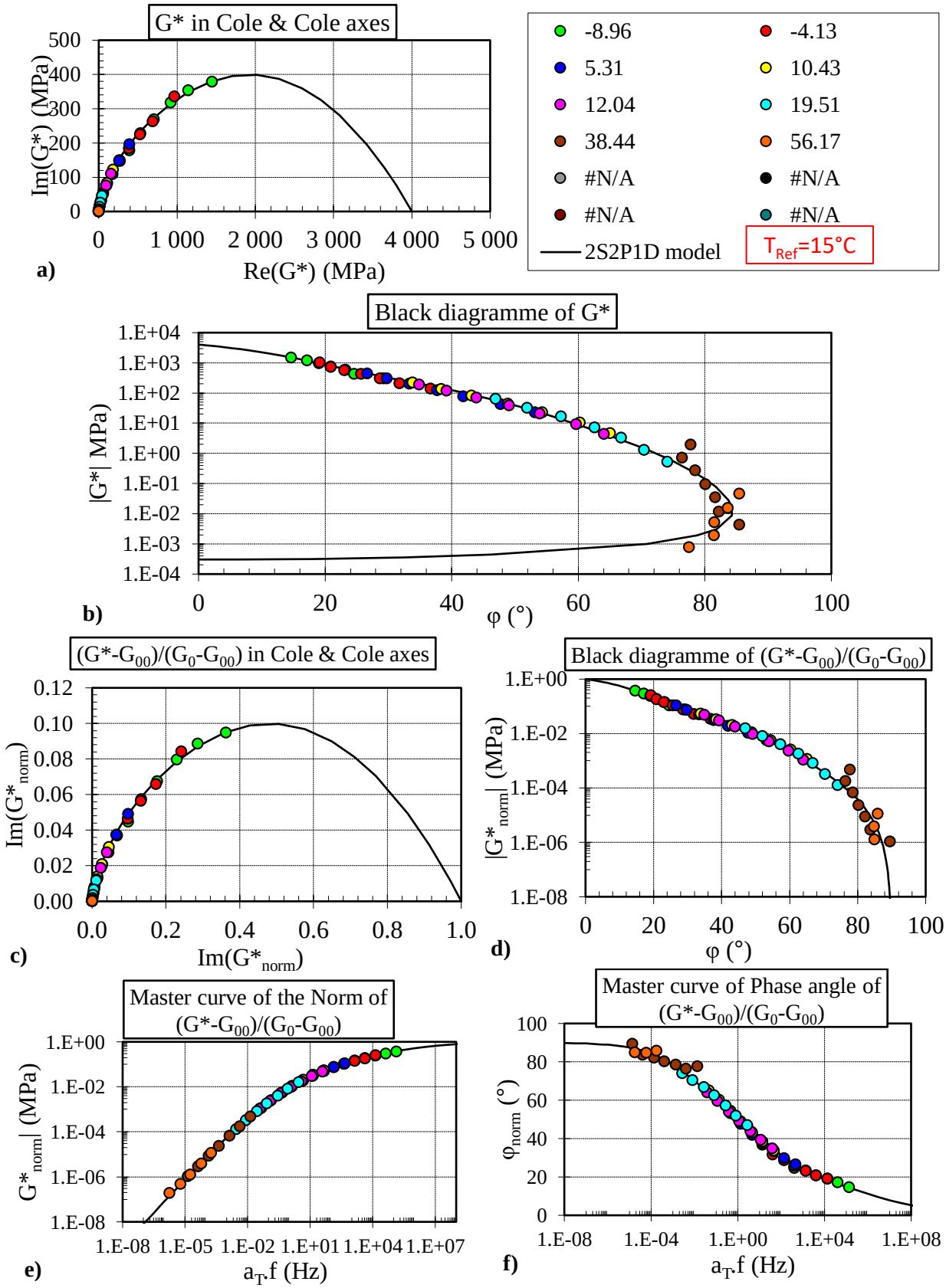

Figure 5-9 *Combined results of complex shear modulus tests with ASR for mastic B_40%_ASR_sp1: a) G* in Cole-Cole plot, b) G* in Black diagram, c) G^*_{norm} in Cole-Cole plot, d) G^*_{norm} in Black diagram, e) master curve of $|G^*_{norm}|$, f) master curve of phase angle of G^*_{norm}. T_{ref} = 15°C*

Table 5-2 *2S2P1D constants and WLF parameters of mastic and its constituent bitumen*

	2S2P1D constants							WLF parameters		
	G_{00} (MPa)	G_0 (MPa)	k -	h -	δ -	τ_0 (s)	β -	T_{ref} (°C)	C_1 -	C_2 (°C)
Constituent bitumen B_ASR_sp5+DSR	0	1020	0.25	0.62	5.0	8.08E-05	100	15	18.6	133.3
Mastic B_40%_ASR_sp1	0.0003	4000	0.25	0.62	5.0	1.31E-04	100	15	18.6	133.3

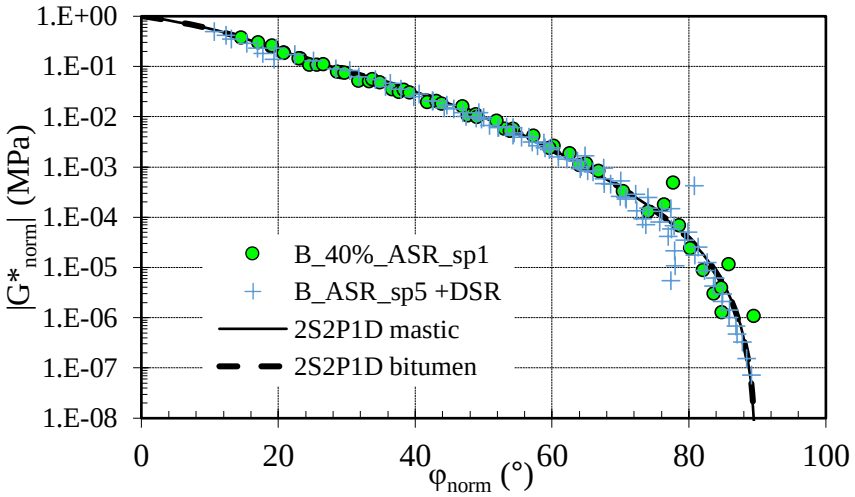

Figure 5-10 *Normalised complex shear modulus of mastic B_40% and its constituent bitumen B in Black diagram. 2S2P1D models of both binders are added.*

5.3 Behaviour during cyclic Loading and Rest Periods test

In this section, the behaviour of binders during cyclic Loading and Rest Periods (LRP) test was studied with the ASR, following the ENTPE approach described in Section 2.3.4.6.2.

5.3.1 Experimental plan

5.3.1.1 Loading and Rest Period test

All four bitumens (B, Bm, S, Sm) and the glass beads mastic (B_40%) of Campaign II underwent LRP tests with the ASR. All specimens were stored in refrigerator at 5°C between fabrication and testing. This should prevent biasing effects from steric hardening (in opposite to DSR specimens that were rapidly cooled).

The LRP test was composed of three loops, themselves composed of one loading period and one rest period. The loading periods were continuous, sinusoidal and controlled at a constant shear strain amplitude at 10Hz. During rest periods, a null average distortion was imposed. However, discontinuous complex modulus measurements at low strain amplitudes (in the LVE domain of the tested binder, under 1000µm/m) were performed from time to time during rest periods to monitor the stiffness recovery. For each recorded "rest point", only 30 cycles at 10Hz were applied. Approximately 50 rest points were distributed logarithmically during each rest periods. For the whole duration of the LRP test, the thermal chamber temperature was kept constant at 10°C. The full description of the LRP test designed for this thesis is given in Figure 5-11. It involved 3 loops, each of them constituted of one loading and one rest period.

- Loop 1: The 1st loading (noted L1) was run until half of the initial modulus $|G^*_{ini}|$ is reached. The 1st rest period (R1) lasted 120h.
- Loop 2: The 2nd loading (L2) lasted 10000 cycles, regardless of the strain amplitude or the modulus evolution. The 2nd rest period (R2) lasted 24h. This second loop was applied to check if the behaviour resistance to loading and the recovery capacity were altered after loop 1.
- Loop 3: The 3rd loading (L3) was run until the failure of the sample, that marked the end of the LRP test.

For each binder, at least two LRP tests were performed, one with "high" loading strain amplitude, the other with "low" loading strain amplitude. Since the complex moduli at 10°C/10Hz were different between binders, these loading amplitudes were individually calculated to obtain the same initial dissipated energy per cycle, using Equation (2.44). Therefore, the low and high loading amplitudes for bitumens corresponded respectively to initial dissipated energies of 2.3kJ/m^3/cycle and 10kJ/m^3/cycle. For the mastic B_40%, the strain amplitudes corresponded to initial dissipated energies of 3.8 kJ/m^3/cycle and 8kJ/m^3/cycle. This difference for the mastic compared to the bitumens was due to the ASR load cell limitations at high loading amplitude and the too long fatigue life at low strain amplitude. All loading strain amplitudes are summed up in Table 5-3.

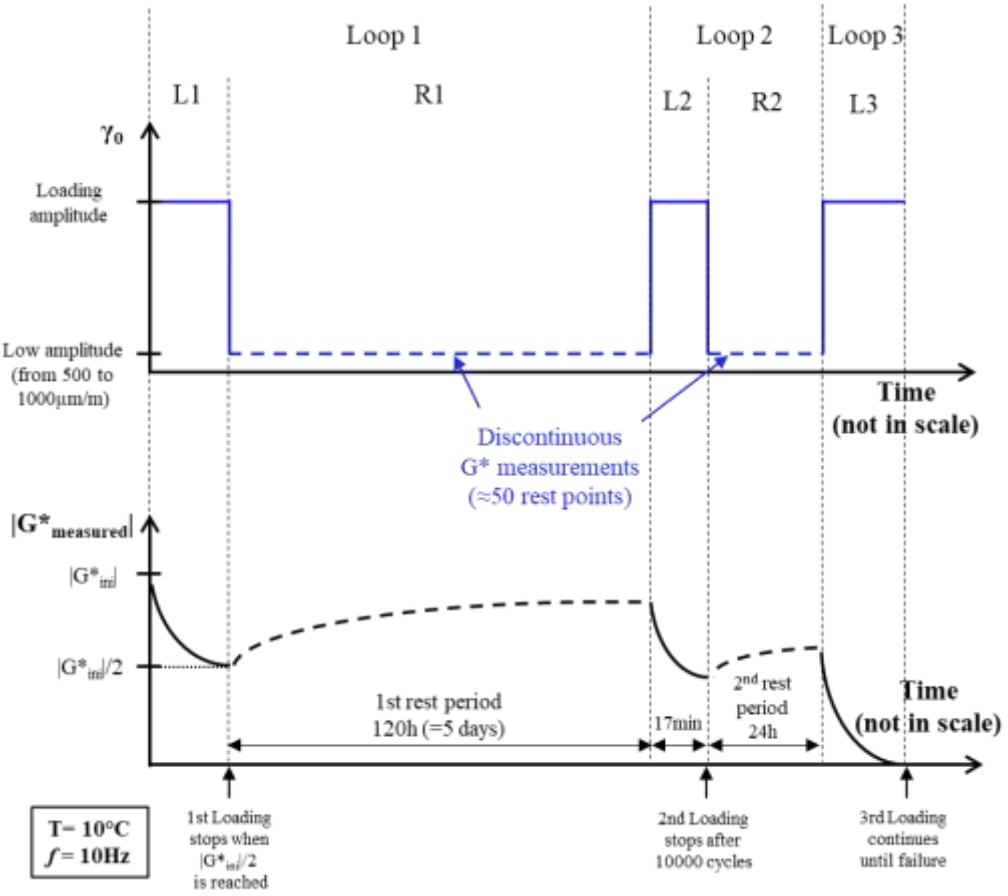

Figure 5-11 *Scheme of LRP test procedure*

Table 5-3 *Loading shear strain amplitudes of LRP tests on binders*

		dissipated energy per cycle (KJ/m3)				
		38	10	8	3.8	2.3
Mat.	Specimen	Associated γ_0 (µm/m)				
B	B_ASR_sp6		10700			
	B_ASR_sp7					5350
Bm	Bm_ASR_sp2		10800			
	Bm_ASR_sp3					5200
	Bm_ASR_sp4	21700				
S	S_ASR_sp5		9000			
	S_ASR_sp6					4320
Sm	Sm_ASR_sp2		9180			
	Sm_ASR_sp3 (failed)					4400
	Sm_ASR_sp4				5620	
B_40%	B_40%_ASR_sp5			4350		
	B_40%_ASR_sp6				3000	
		"very high" strain amplitude	"high" strain amplitude		"low" strain amplitude	

5.3.1.2 Preliminary strain amplitude sweep test

Nonlinearity in bitumen has been identified as a biasing effect on the equivalent modulus during continuous fatigue or LRP tests (Q. T. Nguyen 2011; Van Rompu et al. 2012; S. Mangiafico et al. 2015; L. F. de A. L. Babadopulos et al. 2019). A preliminary strain amplitude sweep (SAS) test is necessary to quantify the nonlinearity, at least at the beginning of LRP test when the specimen is still intact. In this study, a SAS test preceded each LRP test, introduced this in the previous Section 5.3.1.1. Controlled strain amplitude loading cycles were imposed at 10°C and 10Hz. Five shear strain amplitudes (noted $\gamma_{0,1}$, $\gamma_{0,2}$, $\gamma_{0,3}$, $\gamma_{0,4}$ and $\gamma_{0,5}$) were applied, by decreasing value order. The value of the amplitudes depended on the tested material, but $\gamma_{0,2}$ was always taken equal to the loading amplitude of the following LRP test, and $\gamma_{0,5}$ equalled the strain amplitude of the brief complex modulus evaluation at rest points of LRP tests, which was between 500 and 1000µm/m. The SAS loading were rather short (30 cycles per amplitude), and rest periods (from 5 to 30 min) were imposed between consecutive amplitudes, as reversible phenomena such as self-heating can occur even during these short loadings with high strain amplitude (L. F. de A. L. Babadopulos et al. 2019).

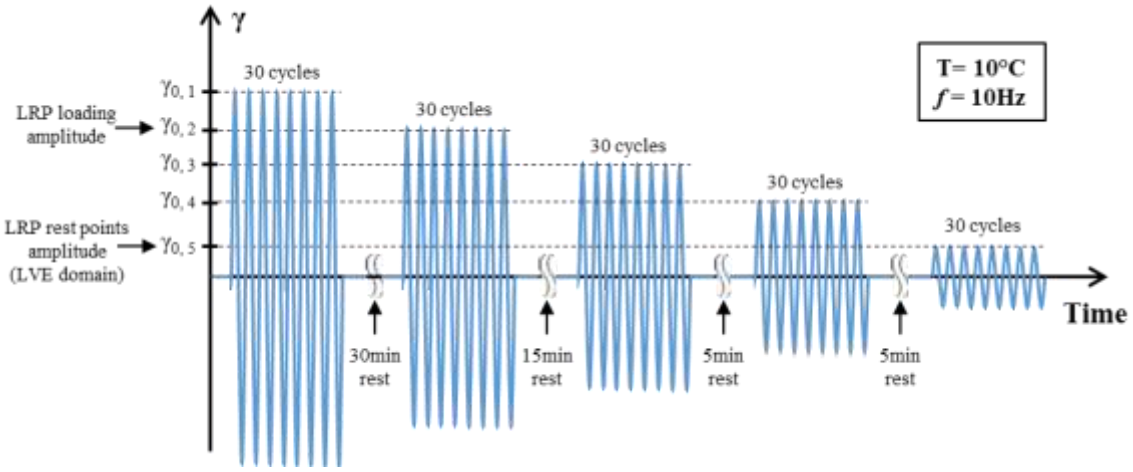

Figure 5-12 *Scheme of preliminary SAS test before LRP*

5.3.2 Results and analysis

5.3.2.1 Evolution of equivalent modulus and in-specimen temperature during LRP test

In this section, the experimental results of LRP tests are introduced with one representative case: a test on bitumen B (B_ASR_sp6) at high loading amplitude (γ_0 = 10700µm/m). The complete results for the ten other tested specimen are available in Appendices 1.5.

Regarding terminology, $G^*_{measured}$ stood for the equivalent complex shear modulus measured at high amplitude during loading period (Li) and for the complex shear modulus measured at low amplitude during the rest periods (Ri).The notion of equivalent modulus is discussed in Section 2.3.3.2. G^*_{ini} designated the initial complex shear modulus in the LVE domain, obtained with the preliminary SAS test (detailed in Section 5.3.2.25.3.1.2), right before the start of the first loading L1. Moreover, the distinction between the total number of applied loading cycles throughout the successive LRP loops (regardless of the rest periods) and the relative number of applied cycles for a given loop required clarification; they were respectively labelled “cumulated cycles” and “loop cycles”. Similarly, the “loop rest time” designated the elapsed rest time relative to each rest period.

The evolution of equivalent modulus, phase angle and in-specimen temperature of B_ASR_sp6 during the LRP test at high loading amplitude (10700µm/m) is displayed in Figure 5-13. For readability, Figure 5-13 a) and b) focuses on loadings, whereas Figure 5-13 c) and d) focuses on rest periods. The initial modulus and the initial specimen temperature are also represented. Moreover, the complete evolution of the equivalent complex modulus during LRP was plotted in Black space in Figure 5-14, where loading cycles (3^{rd}, 30^{th}, 100^{th}, 1000^{th}…etc) and rest points (measured after 0, 1, 5, 30, 240min…) are highlighted. In this graph, the 2S2P1D model of bitumen B, introduced in Section 5.2.2.1, was added.

A systematic discrepancy between the initial modulus G^*_{ini} (measured in LVE domain) and the equivalent modulus $G^*_{measured}$ at the beginning of the first loading L1 (measured at high strain amplitude) was observed for all binders, confirming the existence of nonlinearity effects on the equivalent modulus. These effects, such as the "nonlinearity gap" illustrated in Figure 5-14, and their correction for LRP test analysis are further discussed in the next Section 5.3.2.2.

Considering the first loading L1, the norm of equivalent modulus halved after approximately 25000 cycles, while the phase angle increased from 37 to 43.5° (Figure 5-13 a)). In the meantime, the average in-specimen temperature soared (+3.5°C, Figure 5-13 b)). During the following rest period (R1), the norm of equivalent modulus quickly recovered at 95% of its initial value in the first 4 hours of rest. However, the total recovery took 4 to 5 days, obviously at a much lower rate. Interestingly, the total recovery of the phase angle was fast, after only 4 hours (Figure 5-13 c)). The initial thermal equilibrium was also reached after this delay (Figure 5-13 d)). This observation suggested that the recovery during rest could be separated in two distinct phases: a first rapid modulus and phase angle recovery that lasted 4 hours, at least partially due to the specimen cooling to the thermal chamber temperature, and a second slower modulus recovery at initial phase angle and constant in-specimen temperature. The last phase corresponded well to the effect of a healing-type phenomenon, with a material at thermodynamic equilibrium but with a structural reconstruction, where microcracks are slowly closing up over days. All these trends on the evolution of equivalent modulus were observed for the four bitumens (B, Bm, S, Sm) and the glass-bead mastic (B_40%) during the first loop of LRP tests at high loading amplitude (see respectively Appendices 1.5.1.1, 1.5.2.1, 1.5.3.1, 1.5.4.1 and 1.5.5.2). For LRP test at low loading amplitude, however, even if the thermal equilibrium is reached after 4 hours, the initial modulus was not always totally recovered (for instance S_ASR_sp6, appendix 1.5.3.3 and B_40%_ASR_sp6, appendix 1.5.5.1). This was probably because reversible phenomena (nonlinearity, self-heating and thixotropy) are less prominent compared to actual damage at lower loading amplitude.

In Figure 5-13 a), the equivalent modulus showed a different path (i.e. rate of change) during the second loading L2, as compared to L1, although the initial values were equal. If this observation is true for B and B_40% at high loading amplitude (Appendices 1.5.1.1 and 1.5.3.1), it was not the case for PmB Bm and Sm (Appendices 1.5.2.1 and 1.5.4.1), where L1 and L2 modulus curves coincided. For bitumen S (Appendix 1.5.3.1), the equivalent modulus curves shared the same rate of change, but not the same starting point, as the initial modulus was not totally recovered after R1. Before commenting further on these different results, it is very important to highlight the potential biasing effects of reversible phenomena, i.e. nonlinearity, self-heating and thixotropy.

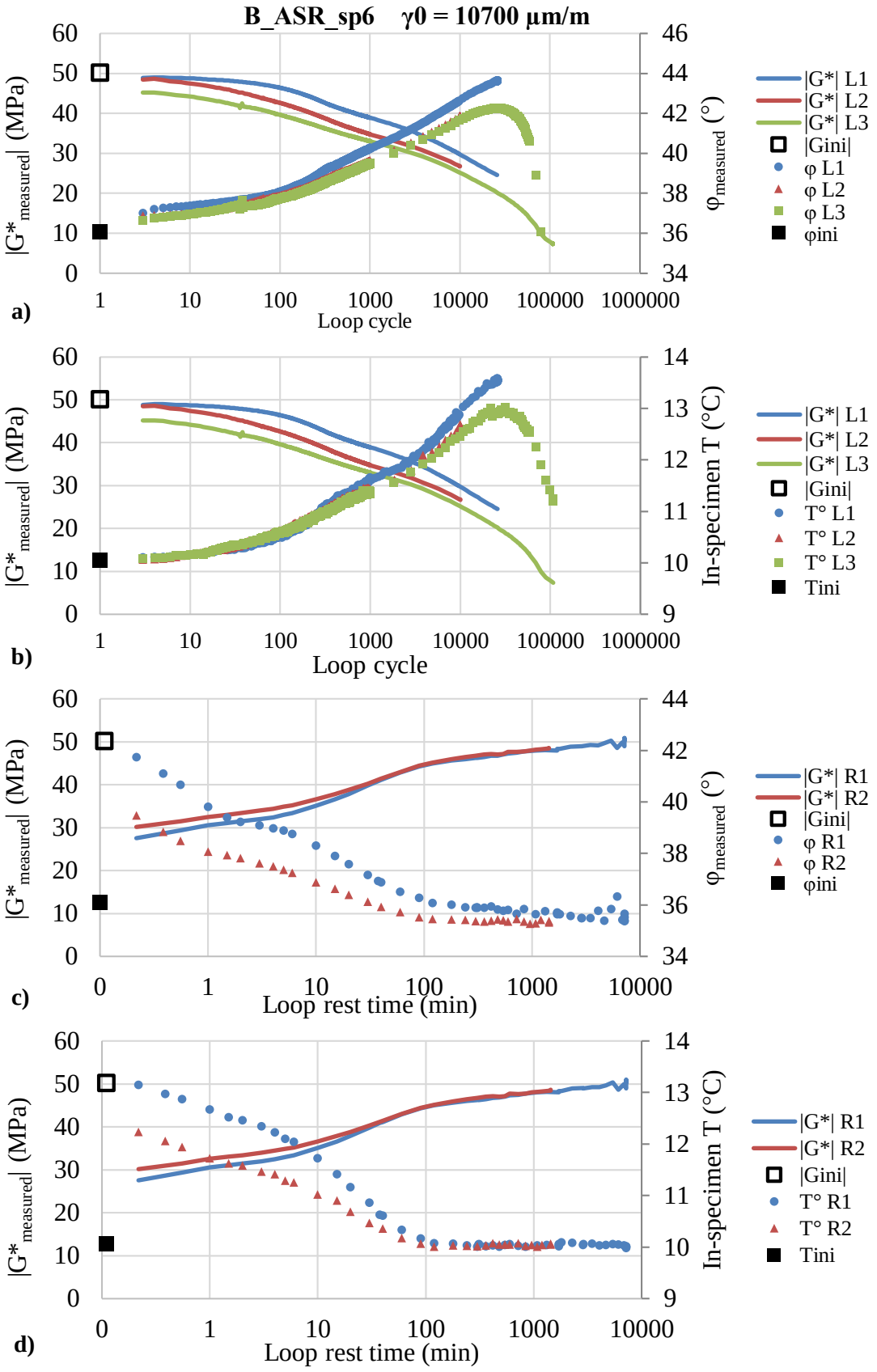

Figure 5-13 *LRP test results of B_ASR_sp6 at high loading amplitude (10700µm/m): a) $|G^*_{measured}|$ and $\varphi_{measured}$ vs. loop cycle, b) $|G^*_{measured}|$ and in-specimen temperature vs. loop cycle, c) $G^*_{measured}|$ and $\varphi_{measured}$ vs. loop rest time, d) $|G^*_{measured}|$ and in-specimen temperature vs. loop rest time*

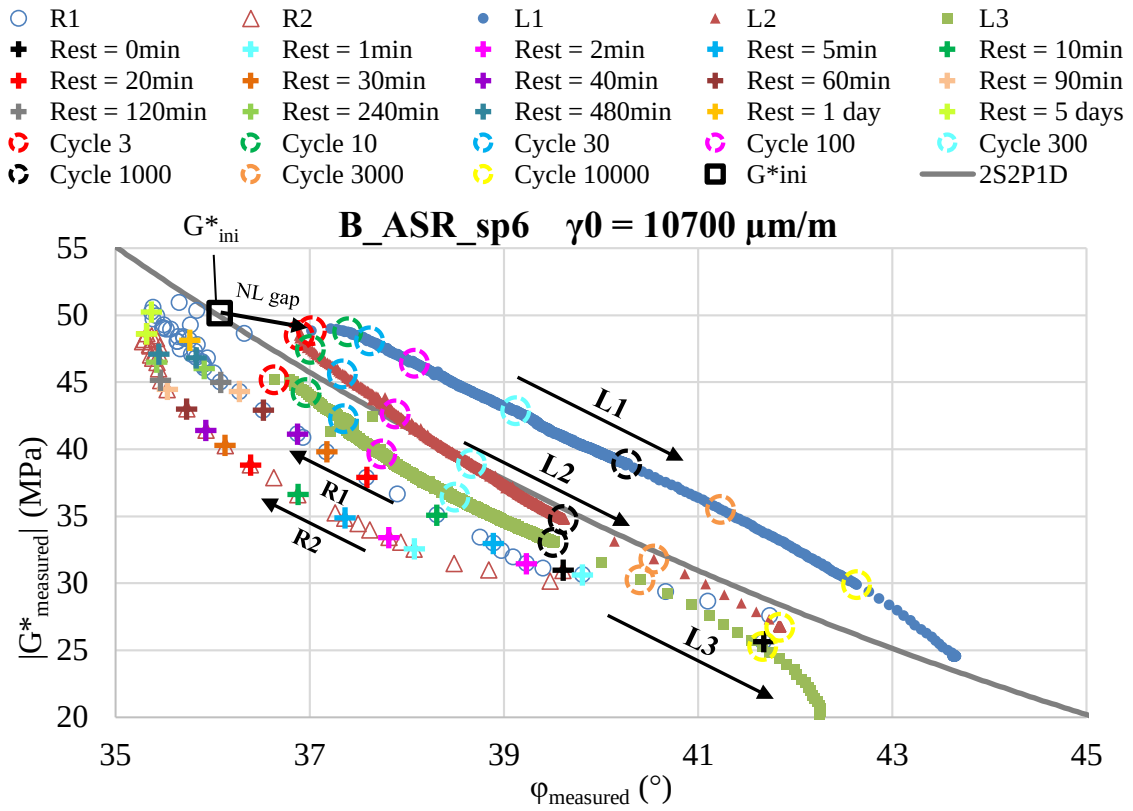

Figure 5-14 *Black diagram of equivalent modulus during LRP test of bitumen B at high loading strain amplitude (10700µm/m)*

One of the potential bias on the analysis of the LRP test results is the precision of the applied strain amplitude, for two reasons: the instantaneous nonlinearity effects and the delayed reversible phenomena (self-heating and thixotropy). Indeed, two loading periods would be comparable if the material underwent the same loading history or even the same strain amplitude at any point. Hence, the quality of strain amplitude applied by the press controller was verified for B_ASR_sp6 and displayed in Figure 5-15. The strain amplitude varied a lot at the beginning of each loading. In fact, the PID algorithm for the controller required regular manual corrections, since there was no compensator able to follow up with the rapid change of stiffness of the sample. That explained why the loading periods might possess different strain history during the first 100 or 200 cycles. The effects of nonlinearity could significantly differ at this stage. The quantification and correction of these effects is discussed in the next Section 5.3.2.2

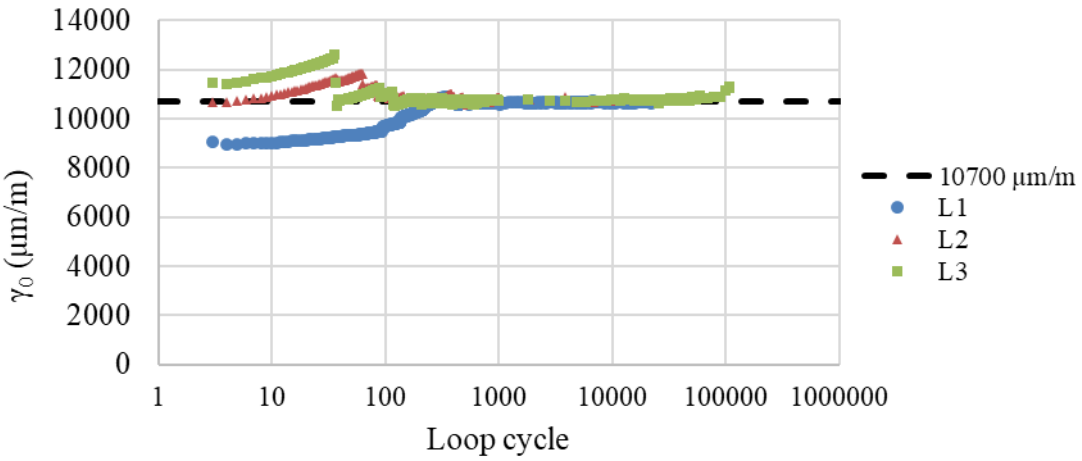

Figure 5-15 *Measured shear strain amplitude during loading periods of B_ASR_sp6*

The effects of self-heating and cooling on the equivalent modulus during respectively loading and rest periods was obviously a bias in the analysis of LRP results, especially at the beginning of loadings. The average in-specimen-temperature was recorded with four high precision thermocouples. In order to validate the quality of the measurement, the recorded temperature increase $\Delta T_{measured}$ was compared to the temperature increase $\Delta T_{dissipated}$ that would be obtained by the total conversion of the dissipated energy into heat in the adiabatic case, with a specific heat capacity of bitumen of 1770J/kg/°C (Read and Whiteoak 2003). The same value was arbitrarily kept for the mastic. An example of temperature increases (B_ASR_sp6, high loading amplitude) is given in Figure 5-16. $\Delta T_{dissipated}$ was systematically tangential to the $\Delta T_{measured}$ at the beginning of the loading, which validated the quality of the measurement. The specimen, in contact with the metallic moulds and the thermal chamber air at 10°C, appeared exchanging heat after few dozens of cycle (= few seconds). Fundamentally, there is a limitation to the in-specimen temperature control; Indeed the heat exchange depends on the exchange surface area, whereas self-heating is occurring in the bulk of the binder. The discrepancies of temperature increase between loops were due to different strain amplitudes at the beginning of the loading periods (see Figure 5-15). Secondly, the different rates of modulus loss between loops might also produce these discrepancies. The quantification and correction of self-heating effects is discussed in Section 5.3.2.1.

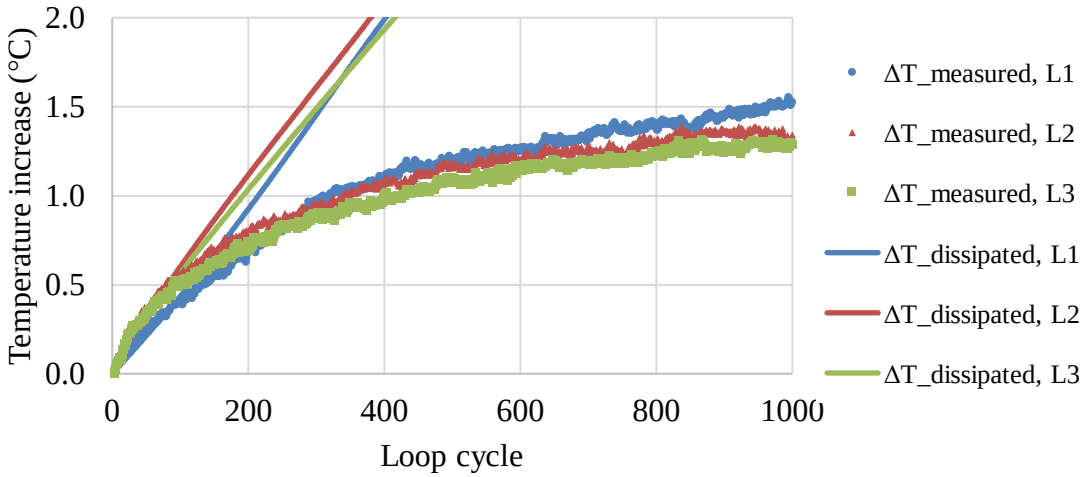

Figure 5-16 *Temperature increases during loadings of B_ASR_sp6 at high loading strain amplitude (10700µm/m), measured from thermocouples and calculated from viscous energy dissipation*

From a general perspective, the comparison of equivalent modulus evolution between successive loops (either loading or rest periods) was not deemed relevant before the correction of the effects of nonlinearity and self-heating due to energy dissipation. Hopefully, the elimination of these two biasing effects could help characterising and quantifying clearly thixotropy, damage and healing. This is addressed in the following sections.

In the meantime, the samples failures were examined after the continuous fatigue loading L3. An illustrative example is given in Figure 5-17, for Bm_ASR_sp2 after high loading amplitude LRP test. Overall, a macrocrack was visible along most of the annular specimens, at either the upper part or the bottom part of the sample. This indicated the preceding existence of microcraks. Unfortunately, it was not possible to verify the presence of the macrocrack across the whole height of the annular specimen.

Figure 5-17 *Bottom part of Bm_ASR_sp2 sample after LRP test at high loading amplitude (10800µm/m)*

5.3.2.2 Quantification and correction of nonlinearity effects

The strain amplitude dependency of the equivalent modulus of binders was evaluated with the SAS test at 10°C/10Hz (described in section 5.3.1.2) that preceded each LRP test. The SAS test results of bitumen B and of mastic B_40% are displayed in Figure 5-18. The corresponding samples B_ASR_sp6 and B_40%_ASR_sp6 were both submitted to high loading amplitude LRP test (respectively 10700 and 4350µm/m), with overall comparable initial dissipated energy (10 and 8 kJ/m^3/cycle). All other SAS test results are available in Appendix 1.2.2.

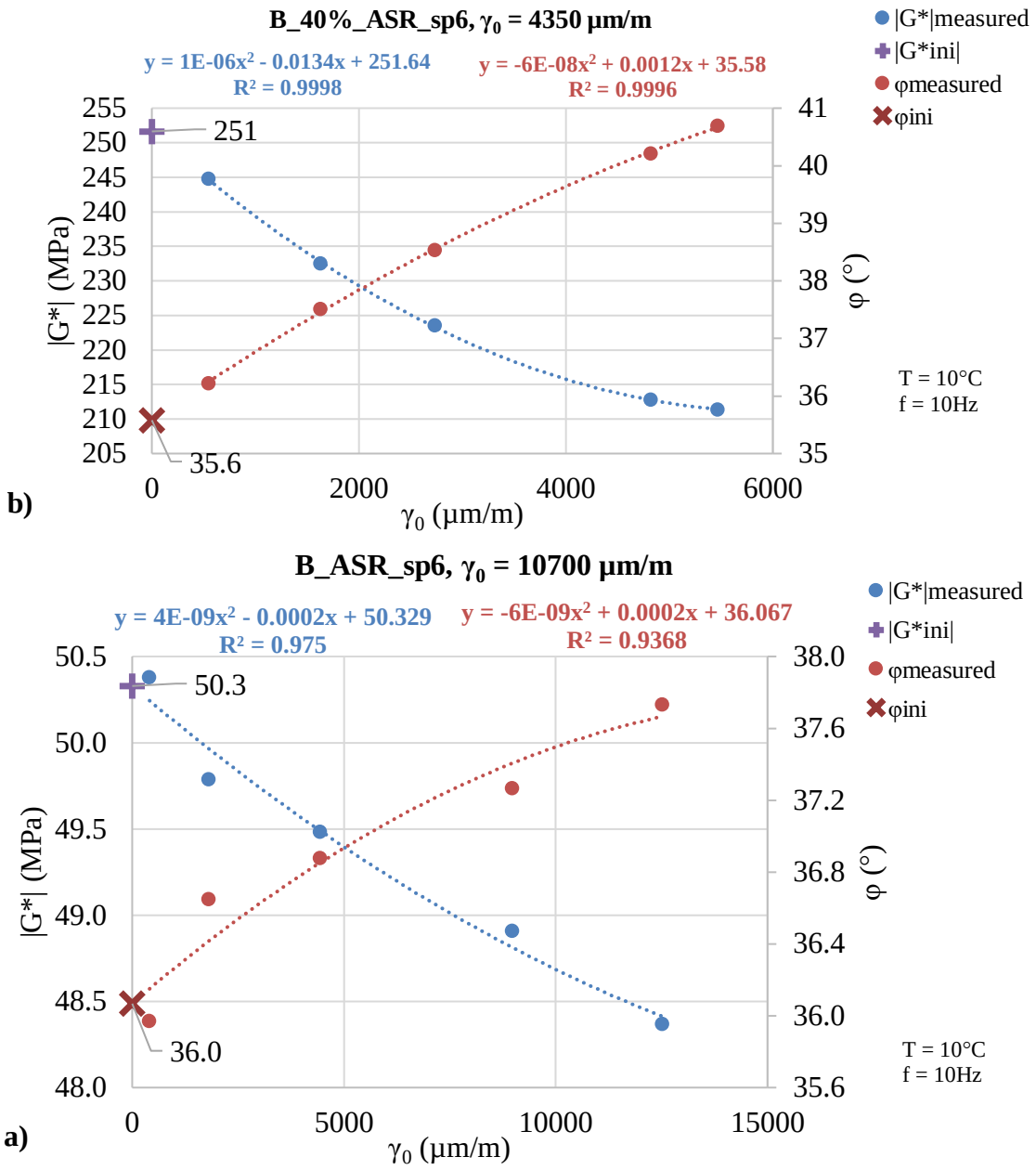

Figure 5-18 *Equivalent complex shear modulus as a function of shear strain amplitude obtained with SAS test at 10°C/10Hz for: a) bitumen B (B_ASR_sp6), b) mastic B_40% (B_40%_ASR_sp6)*

All bitumens and the glass-bead mastic showed a strain dependency of norm of equivalent modulus and phase angle, which could be well modelled by parabolic functions. That led to the definition of the nonlinear complex modulus $G^*_{NL}(\gamma_0)$ in Equations (5.2) and (5.3). The simulated complex modulus in LVE domain was therefore obtained for the asymptotic case where the strain amplitude is null (i.e. $G^*_{NL}(0)$). This value was taken as the initial modulus G^*_{ini} of LRP test (Equation (5.4)). For bitumens, the calculated G^*_{ini} was almost identical to the measured equivalent modulus at the lowest amplitude of the SAS test ($\gamma_{0,5}$ = 500 or 1000 µm/m). This is illustrated for bitumen B in Figure 5-18 a). For the mastic B_40%, however, there was a clear discrepancy between the measurement at $\gamma_{0,5}$ = 500 and the calculated G^*_{ini} of about 3% in norm of complex modulus and 0.8° in phase angle (Figure 5-18 b)). Moreover, the conventional LVE limit, i.e. the strain amplitude at which the norm of the equivalent modulus represents 95% of the LVE complex modulus (which corresponded to G^*_{ini} in this work), was not reached for all bitumens, except for Bm_ASR_sp4, the only specimen tested at very high amplitudes (LVE limit obtained at ≈16000µm/m). The LVE limit of the mastic B_40% was reached at γ0 = 1000µm/m, hence 16 times smaller than the bitumen LVE limit. This ratio was due to the glass particles inclusion, which locally caused great concentrations of stresses and strains in the bitumen matrix, exacerbating locally nonlinearity effects. This ratio of bitumen/mastic LVE limits of 16 obtained with 40% of silica beads was interesting; Recent studies with the same mastic but with only 30% of glass beads, that also underwent SAS tests with ASR at 10°C/10Hz, showed a LVE limits ratio between 2.3 to 2.8 (L. Babadopulos et al. 2019). The filler concentration in mastics seems to be critical for LVE limits, and generally speaking for nonlinear behaviour.

$$|G^*_{NL}|(\gamma_0) = a{\gamma_0}^2 + b\gamma_0 + c \tag{5.2}$$

$$\varphi_{NL}(\gamma_0) = a'{\gamma_0}^2 + b'\gamma_0 + c' \tag{5.3}$$

$$G^*_{ini} = G^*_{NL}(0) = c \tag{5.4}$$

The nonlinear complex modulus equations (5.2) and (5.3), found for each binder, allowed proposing a correction model for the effects of nonlinearity on the equivalent modulus during LRP tests. The equivalent modulus corrected from nonlinearity (NL) effects was noted $G^*_{NL-corrected}$ and was calculated with Equations (5.5 and (5.6. A complex correction factor $k^*_{NL}(\gamma_0)$ was applied to the equivalent modulus measured at a given amplitude γ_0. This factor was the ratio of the initial complex modulus G^*_{ini} and the calculated nonlinear modulus $G^*_{NL}(\gamma_0)$. This correction model corresponds to a fixed multiplication of the norm and a fixed addition of phase angle to the measured modulus. The correction was the same whatever the state of the tested material (self-heated, damaged,…etc.). Nevertheless, this correction could be considered valid as a first approximation at the beginning of loading periods, since the material was at SAS tests temperature (10°C), and was either intact or rested with close-to-initial stiffness.

$$\frac{G^*_{NL-corrected}(\gamma_0)}{G^*_{measured}} = \frac{G^*_{NL}(0)}{G^*_{NL}(\gamma_0)} = \frac{G^*_{ini}}{G^*_{NL}(\gamma_0)} = k^*_{NL}(\gamma_0) \tag{5.5}$$

$$G^*_{NL-corrected}(\gamma_0) = k^*_{NL}(\gamma_0) \times G^*_{measured} \tag{5.6}$$

The LRP results corrected from nonlinearity effects are all available in Appendix 1.5. An example of equivalent modulus corrected from nonlinearity effects is displayed in Figure 5-19; $G^*_{NL-corrected}$ of bitumen B at high loading amplitude (B_ASR_sp6) is plotted in Black diagram. The original uncorrected results are available in Figure 5-14 for comparison. The "nonlinearity gap" between G^*_{ini} and the 3rd cycle values of L1 was successfully erased by the NL correction.

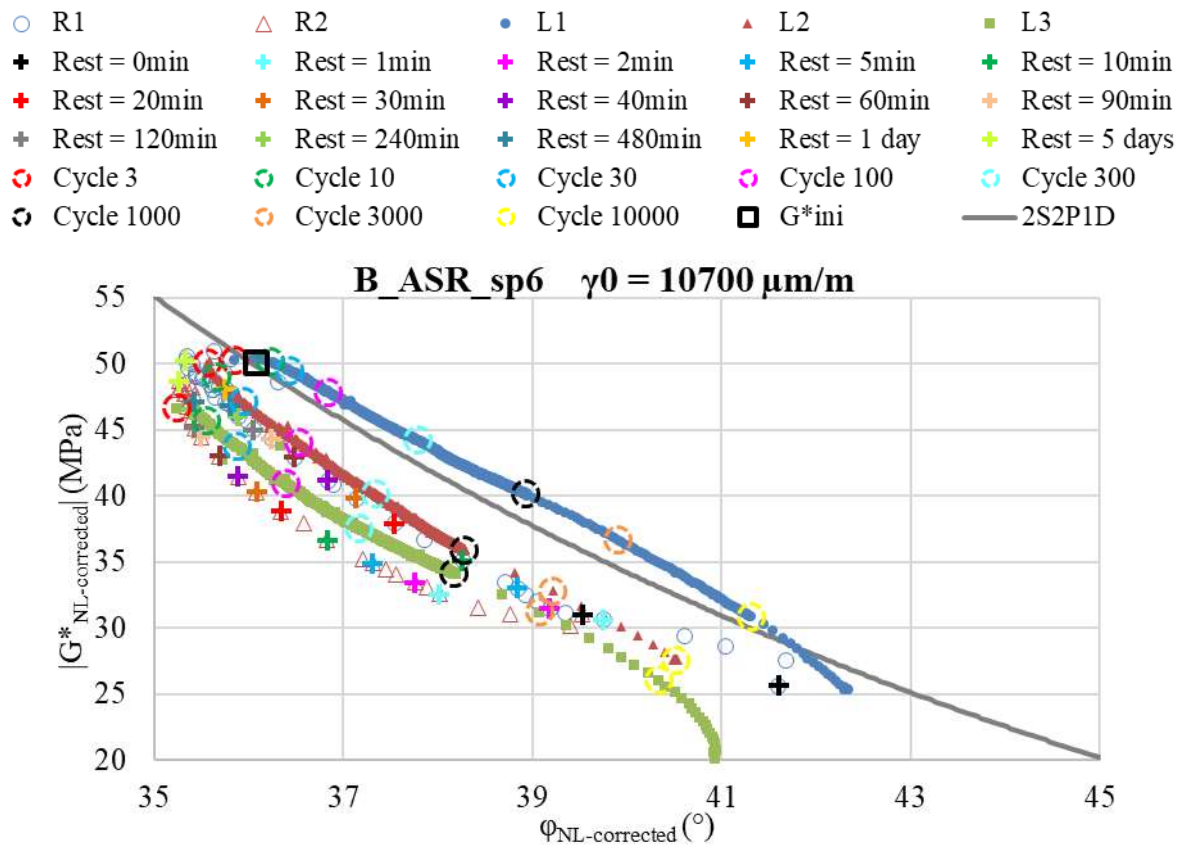

Figure 5-19 *Black diagram of equivalent modulus corrected from nonlinearity effects during LRP test of bitumen B at high loading strain amplitude (10700µm/m)*

5.3.2.3 Quantification and correction of the effects of self-heating due to energy dissipation

In the same fashion as the correction of nonlinearity effects, a correction model of the effects of self-heating due to viscous dissipation is proposed in this section. As seen previously in Section 5.3.2.1, the temperature in the binder soared during loading phases (few degrees at high loading amplitude). The "temperature correction" was made using the temperature dependence of complex modulus of binder, already studied and modelled with the 2S2P1D model in Section 5.2. The equivalent modulus corrected from the internal variations of temperature was noted $G^*_{T-corrected}$ and was calculated with Equations (5.7) and (5.8). A complex correction factor $k^*_T(T, T_{ini})$ was applied to the equivalent modulus measured, with T the in-specimen temperature and T_{ini} the initial equilibrium temperature (10°C in this study) at which the equivalent modulus is corrected. This factor was the ratio of the modelled complex moduli at T_{ini} ($G^*_{2S2P1D}(T_{ini})$) and T ($G^*_{2S2P1D}(T)$), as expressed in Equations (5.7) and (5.8). Just as for the nonlinearity, this correction model corresponded to a fixed multiplication of the norm and a fixed addition of phase angle to the measured modulus, regardless of the state of the tested material (thixotropic breakdown, damaged,…etc.). From a physical point of view, the damage, understood as homogeneously spread microcracks in the specimen structure, did not show specific reason to modify the temperature dependence of the tested material itself. Regarding potential thixotropy, this was much more unclear, since the diminution of apparent stiffness it usually causes is due to microstructural breakdown at a molecular level, very similarly to what a temperature increase would induce. If previous work clearly differentiated both phenomena (e.g. their induced equivalent modulus changes in complex plane do not share the same directions) (L. F. de A. L. Babadopulos et al. 2019), cross effects have never been studied before. This blind-spot on the relationship between thixotropy and temperature effects was not studied because of its complexity, which would require to precisely control the temperature of the specimen despite varying level of loadings and heat flows form energy dissipation.

$$\frac{G^*_{T-corrected}(T,T_{ini})}{G^*_{measured}} = \frac{G^*_{2S2P1D}(T_{ini})}{G^*_{2S2P1D}(T)} = k^*_T(T,T_{ini}) \qquad (5.7)$$

$$G^*_{T-corrected}(T,T_{ini}) = k^*_T(T,T_{ini}) \times G^*_{measured} \qquad (5.8)$$

The LRP results corrected from self-heating effects are all available in Appendix 1.5. An example of corrected equivalent modulus is displayed in Figure 5-20Figure 5-19; $G^*_{T-corrected}$ of bitumen B at high loading amplitude (B_ASR_sp6) is plotted in Black diagram. The original uncorrected results and the corrected results for nonlinearity effects are available respectively in Figure 5-14 and Figure 5-19 for comparison.

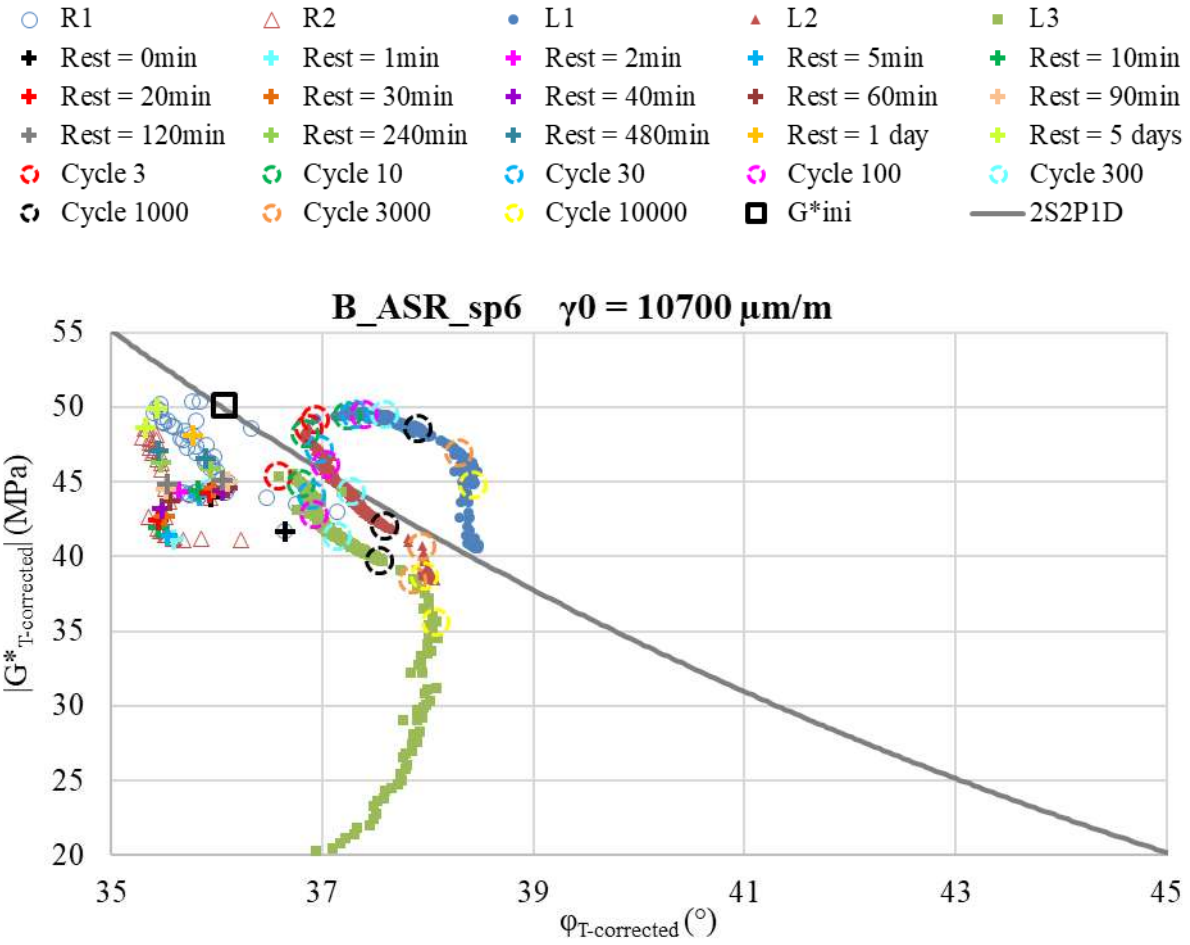

Figure 5-20 *Black diagram of equivalent modulus corrected from temperature effects during LRP test of bitumen B at high loading strain amplitude (10700µm/m)*

The LRP results corrected from temperature effects let appear the other phenomena responsible for modulus loss and recovery, which were thoroughly discussed in the following section 5.3.2.4.

5.3.2.4 Evaluation of thixotropy breakdown and build-up, damage and healing

The objective of this section is to compare the behaviour of the equivalent complex modulus of binders through the successive LRP loops (loading + rest periods), with the correction of the biasing effects from nonlinearity and self-heating, introduced in the previous Sections 5.3.2.2 and 5.3.2.3. In doing so, it is possible to evaluate clearly the role of other reversible phenomena (thixotropic breakdown and its associated build-up), damage and potentially healing phenomenon.

The equivalent modulus corrected from temperature and nonlinearity effects (noted $G^*_{T,NL-corrected}$) is expressed as:

$$G^*_{T,NL-corrected}(T, T_{ini}, \gamma_0) = k^*_T(T, T_{ini}) k^*_{NL}(\gamma_0) \times G^*_{measured} \qquad (5.9)$$

The corrected LRP results at high loading amplitude and of bitumen B and bitumen S are displayed in Figure 5-21. For other binders and/or loading amplitude, see Appendix 1.5. By looking at the first loop (L1 + R1) across all LRP tests on bitumens at high and low loading amplitudes (further noted "HA" and "LA" for readability), four phases were distinguished:

- A quick phase angle increase (≈1° at LA and ≈2° at HA) accompanied by a slight modulus decrease (2 to 5% of $|G^*_{ini}|$, only visible at HA) was observed over a characteristic number of loading cycles $N_{characteristic}$ at the very beginning of L1. For pure bitumens, $N_{characteristic}$ = 1000 cycles, and for PmB, $N_{characteristic}$= 10000 cycles. This rapid change in material behaviour is attributed to thixotropic breakdown.
- Following the thixotropic breakdown during L1, a slower phase of modulus decrease (≈15% of $|G^*_{ini}|$ at HA, ≈30% at LA) at constant phase angle was observed over a characteristic number of loading cycles $N_{characteristic}$ comprised between 10^5 and 10^6 cycles for all bitumens. It was identified as the real fatigue damage, because it corresponded well to what is expected from homogeneously spread microcracks. The part of half of the initial modulus loss during L1 that was attributed to damage significantly diminished for increasing amplitude. This was obviously due to the limitations of the effects of reversible phenomena (self-heating, nonlinearity and thixotropy) on the equivalent modulus at lower loading amplitudes, and confirmed that generally, in presence of such phenomena, the sole measurement of the stiffness is not sufficient to evaluate the actual damage of the specimen.
- At the beginning of the rest period R1, a relatively quick phase angle decrease (≈1 or 2° at HA and 1° or less at LA) accompanied by a slight modulus increase (≈5%) was observed. The exact evaluation of the recovered modulus right after the loading was difficult because of the potential errors of the temperature and nonlinearity corrections (Equation (5.9)) when the material is heated and mechanically agitated. Nevertheless, this phase systematically appeared and its characteristic time $t_{characteristic}$ varied between bitumens (1min for B and 20min for S, Sm and Bm). This recovery phase was attributed to a delayed thixotropic build-up.
- Following the thixotropic build-up, a slow recovery of modulus at constant phase angle was observed, until the initial modulus was reached at the end of R1. The amount of recovered modulus was always more or less equal to the modulus loss due to damage, with a characteristic time of 5 days. This strongly suggested that this recovery could be the fingerprints of a healing phenomenon.

The illustration of these four phases, associated with four distinct phenomena (respectively thixotropic breakdown, damage, thixotropic build-up and healing) is given in Figure 5-21. The principal argument in favour of this phenomenological decomposition, which is still a subject of debate in the literature on the fatigue testing of bituminous material, was the important discrepancies of: 1/ characteristic time or loading cycle, 2/ directions of equivalent modulus in complex plane induced by the phenomena.

In Figure 5-21 a), the evolution of $G^*_{T,NL-corrected}$ of bitumen B during loading L2 appeared very different from L1; the modulus loss during the first 1000 cycles was significantly greater during L2, making the distinction of the thixotropic breakdown and the damage phase less clear. However, this was not the case for bitumen S (Figure 5-21 b)), where $G^*_{T,NL-corrected}$ evolution during L1 and L2 was very similar in Black diagram (same direction, with clear thixotropic breakdown and damage phases). This difference in behaviour after the first loop of LRP test was further studied for all binders at both high and low loading amplitudes, with the graphs representing the evolution of $|G^*_{T,NL-corrected}|$, normalised by initial modulus G_{ini}, as a function of the cumulated number of applied cycles in Figure 5-22 (B, Bm and S) and Figure 5-23 (Sm and B_40%).

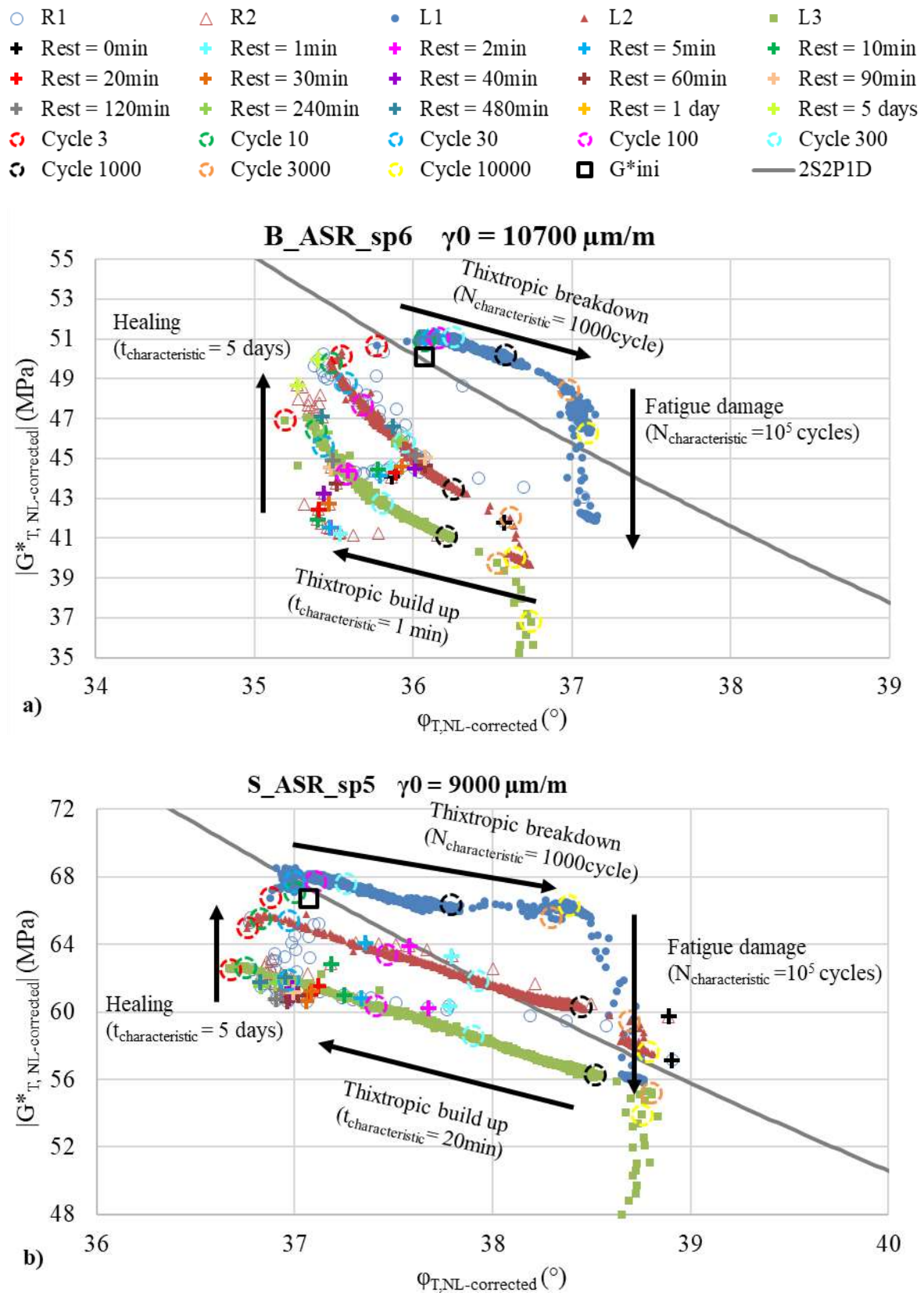

Figure 5-21 *Black diagram of equivalent modulus corrected from both temperature and nonlinearity effects during LRP test of: a) bitumen B at high loading strain amplitude (10700µm/m), b) bitumen S at high loading strain amplitude (9000µm/m)*

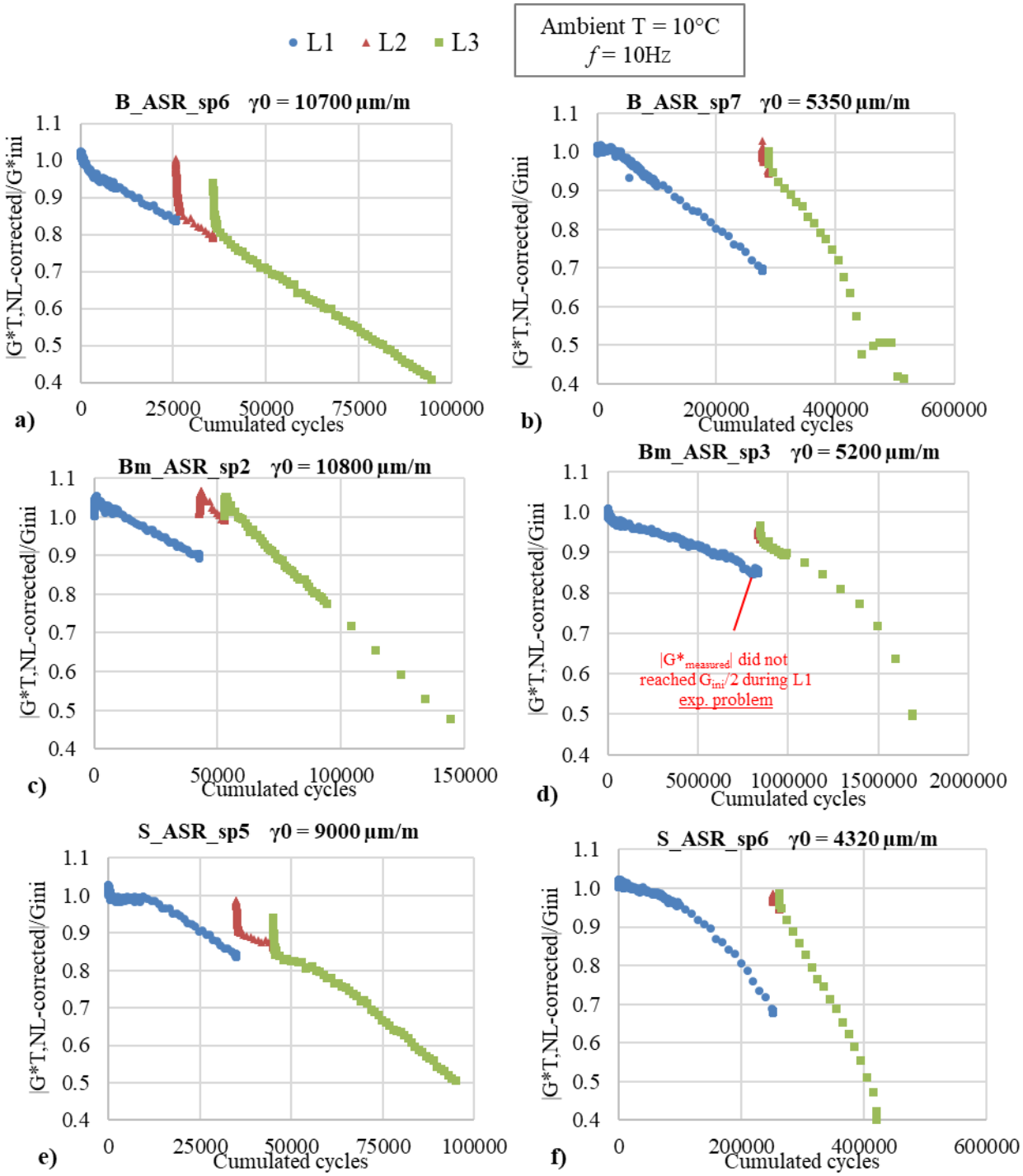

Figure 5-22 *Normalised norm of equivalent complex shear modulus corrected from temperature and nonlinearity effects as a function of cumulated cycles for: a) B_ASR_sp6, HA (10700µm/m), b) B_ASR_sp7, LA (5350µm/m), c) Bm_ASR_sp2, HA (10800µm/m), d) Bm_ASR_sp3, LA (5200µm/m), e) S_ASR_sp5, HA (9000µm/m), f) S_ASR_sp6, LA (4350µm/m)*

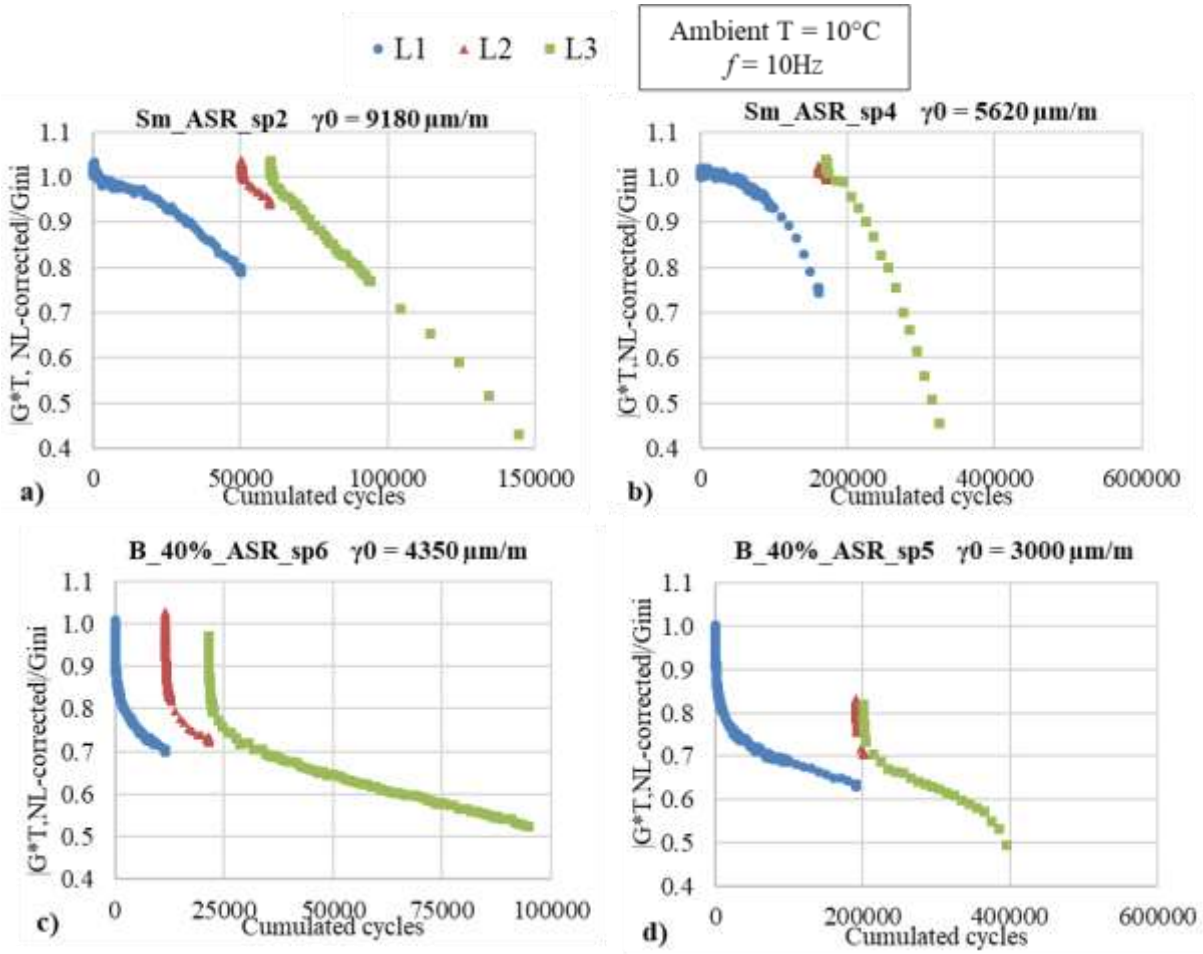

Figure 5-23 *Normalised norm of equivalent complex shear modulus corrected from temperature and nonlinearity effects as a function of cumulated cycles for: a) Sm_ASR_sp2, HA (9180µm/m), b) Sm_ASR_sp4, LA (5620µm/m), c) B_40%_ASR_sp6, HA (4350µm/m), d) B_40%_ASR_sp5, LA (3000µm/m)*

The curves of norm of equivalent modulus corrected from temperature and nonlinearity biasing effects exhibited mostly the evolution of damage in the different samples. Indeed, as previously seen, the rapid thixotropic breakdown played a minor role on the norm of $G^*_{T,NL-corrected}$ (from 1% to 5% of initial modulus), that was concentrated in the first 1000 or 10000 cycles of loading periods. All binders presented portions of curve with steady rate of damage. The best example was bitumen B at both HA and LA in Figure 5-22 a) and b). A linear damage over respectively 15 and 30% of the initial modulus was obtained during L1. The following loading L2 and L3 were significantly different, despite the fact that the sample was completely healed after R1. The damage rate was extremely high in the first 1000 cycles, and stayed higher than the damage rate of L1 afterwards. This proved that the complete recovery of stiffness attributed to healing was not synonym of the recovery of the initial material integrity. Therefore, the resistance to fatigue damage of bituminous binders is a function of the loading history (including rest), and not simply of the measured stiffness at a given point. From a microstructural point of view, one hypothesis could be that the microcracks induced during L1 were naturally "stitched" in the bulk of the bitumen by molecular agitation, so that they could sustain low amplitude loading during rest, but would be quickly reopen if high amplitude loading is applied. This hypothesis could not be tested during this thesis, but this might be possible using rheo-optical techniques or indirectly by monitoring other physical properties of the binder, such as the dielectric constant, that might be affected by the presence of microcraks.

Some limitations of the correction method for self-heating and nonlinearity effects are exposed in the Figure 5-22 and Figure 5-23. In Figure 5-22 c), the modified bitumen Bm presented norms of corrected modulus higher than the initial modulus at the very beginning of L1. This was due to two factors: first, the measurement of the in-specimen temperature increase, that surpassed during a hundred cycles the calculated temperature increase by energy dissipation (see appendix 1.5.2.1). This biased measurement was probably due to local thermal effects on thermocouples when the temperature changed rapidly. Secondly, the nonlinearity effects on equivalent modulus are known to be temperature-dependent for bituminous binders, as they decrease when temperature increases for a fixed strain amplitude (L. Babadopulos et al. 2019). The nonlinearity correction might have been a little bit "too strong" in some cases, although the error represented only few % of modulus change for bitumens.

5.4 Conclusion of Campaign II

The linear viscoelastic behaviour (LVE) and the behaviour during load and rest periods (LRP) at 10°C/10Hz were studied for various bituminous binders: two pure bitumens (B, S), two PmB (Bm, Sm) and one mastic made with glass beads (B_40%).

Regarding the LVE characterisation of bitumens, the unification of complex shear modulus results with ASR and DSR allowed to make up for the systematic underestimation of glassy modulus with sole DSR results. The TTSP was valid for all bitumens, and the shift factors were modelled by WLF equation. The polymer modification did not alter the WLF parameters. Additionally, the 2S2P1D model was used to simulate the LVE behaviour. The model was overall very good, but lacked precision for the phase angle of PmB at high equivalent frequency. The PmBs exhibited an asymptotic static modulus at low equivalent frequency, whereas the pure bitumens tended to be purely viscous.

The LVE behaviour of the glass-bead mastic was studied with ASR. The mastic shared the same shift factors and the WLF parameters with its constituent bitumen B, as well as four of the seven 2S2P1D constants (k, h, δ, β). The asymptotic moduli G_{00} and G_0, and the temperature-related constant τ_0 were different. The mastic inherited some of the LVE properties of the bitumen. These results confirm previous observations from our laboratory team.

LRP tests were performed at high and low loading amplitude (HA and LA) for each binder. The loss of half of the initial modulus during the first loading period L1 was systematically recovered after 5 days of rest. A nonlinearity gap was observed between the initial modulus (LVE domain) and the apparent modulus during the first loading cycles. The temperature increase due to self-heating from viscous energy dissipation went up to 3.5°C at HA.

A preliminary strain amplitude sweep (SAS) test quantified the nonlinearity effects on the equivalent modulus. These effect corresponded up to 5% decrease of norm of equivalent modulus and up to 2° increase phase angle for bitumen, and seem more important for mastics. Parabolic functions were successfully used to simulate the strain amplitude dependence of norm and phase angle of the equivalent modulus in first approximation. Based on these functions, a model of equivalent modulus corrected from nonlinearity effect was proposed. Similarly, a model of equivalent modulus corrected from self-heating based on the 2S2P1D model and the in-specimen temperature, was also proposed.

The combination of the correction of temperature and non-linearity effects on the equivalent modulus during LRP loops allowed identifying four distinct phases, with different characteristic time and effects on the modulus : 1/ Thixotropic breakdown, occurring fast at the beginning of loading periods (about 1000 cycles), 2/ fatigue damage corresponding to a slow decrease of modulus at constant phase angle (mainly between 10^5 to 10^6cycles), 3/ thixotropic build-up, occurring fast at the beginning of rest periods (between 1 to 20min), 4/ healing characterised by a slow recovery of modulus at constant phase angle (5 days). The amplitude of thixotropy effects and other reversible phenomena, were strongly dependent of the loading amplitude. Their influence on the modulus was very limited at LA. The analysis of the corrected modulus as a function of cumulated cycles showed that binders often exhibit linear damage per cycle over considerable portions of modulus loss. Additionally, after the first loading and rest period, the material initial integrity, understood as its resistance to damage, was never totally recovered, even if the initial modulus was recovered. Hence, the rate of damage seemed dependent on the loading history (which includes rest periods) of the material, and not on the modulus value at a given point in time.

6 Campaign III: New interface test on bitumen thin film and first results

6.1 Objectives

The third campaign of this thesis focused on the development on a new interface test on bitumen thin film trapped between two rock cylinders for two main objectives: the LVE characterisation of bitumen confined in a thin film geometry, and the testing of an ideal, homogeneous bitumen/aggregate interface. This study comprised several steps:

- Description of the new thin film test set-up and its instrumentation. The main objective of the set-up was to be able to measure precisely the axial stress and strains in a film of only few hundred micrometres in thickness and few centimetres in radius, in order to measure the apparent axial modulus of the confined bitumen.
- Description of the fabrication of the thin film specimen, which involved the critical stage of creating a homogeneous bitumen film with a precise thickness between two bulky cylinders of rock.
- Search for an analytical solution for the stress and strain tensors in the rock and bitumen phases of the thin film specimen submitted to uniaxial tension-compression. Previous studies on the Poker chip geometry (Lindsey et al. 1963; Sultana, Bhasin, and Liechti 2014) proposed a solution for rigid caps and a film aspect ratio (the thickness divided by the diameter) of 1/20.
- Simulation with finite element (FE) method of the thin film specimen submitted to uniaxial loading, in order to compare it with the analytical solution
- Experimental characterisation of LVE behaviour of the thin film specimen made with bitumen B, in order to study the relationship of the apparent modulus with the already known LVE bulk characteristics of the bitumen (e.g. shear complex modulus from Campaign II).
- Experimental pull-off tests of thin film specimen, to explore the possibility of studying either the cohesive failure of the bitumen and/or the adhesive failure of a plane and smooth bitumen/aggregate interface.

6.2 Description of the thin film test set-up

The thin film test was performed on an INSTRON® hydraulic press, equipped with a 25kN load cell (see Figure 6-1). The thin film specimen, as described in material Section 3.2.6, was composed of a bitumen film trapped between two rock cylinders. The bitumen film thickness, noted *e*, ranged between 100 and 300µm for this campaign. The whole sample preparation is detailed in the next Section 6.3. The axial strains in the rock and in the bitumen were measured with a system of two pairs of extensometers with different gauge lengths:

- 2 long INSTRON® extensometers (“L1” and “L2”), placed diametrically opposite to each other. The long gauge length, noted *L*, measured 9cm.
- 2 short INSTRON® extensometers (“S1” and “S2”), also placed diametrically opposite to each other. The short gauge length, noted *l*, measured 1cm.

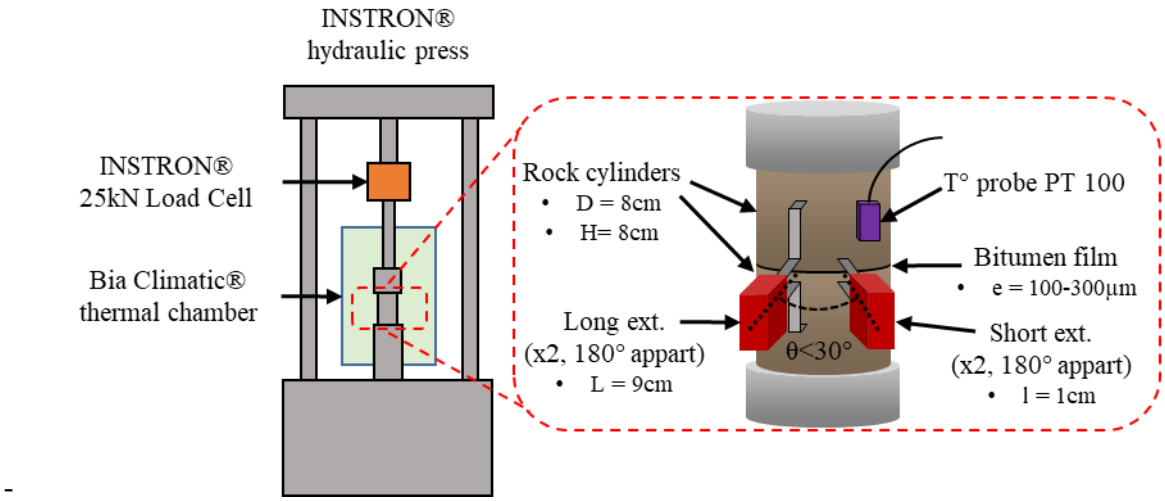

Figure 6-1 *Scheme of thin film test set-up*

Assuming the homogeneity of deformation in both the rock and the bitumen phases, the axial strains ε_R and ε_B could be calculated from the difference of recorded displacements between the short and long extensometers (illustrated in Figure 6-2):

$$\varepsilon_{rock} = \frac{d_L - d_S}{L - l} \tag{6.1}$$

$$\varepsilon_{film} = \frac{d_S - \varepsilon_{rock}(l - e)}{e} \tag{6.2}$$

, where d_L, d_S were the average displacement of long and short extensometer pairs (set at 0µm when no loading is applied).

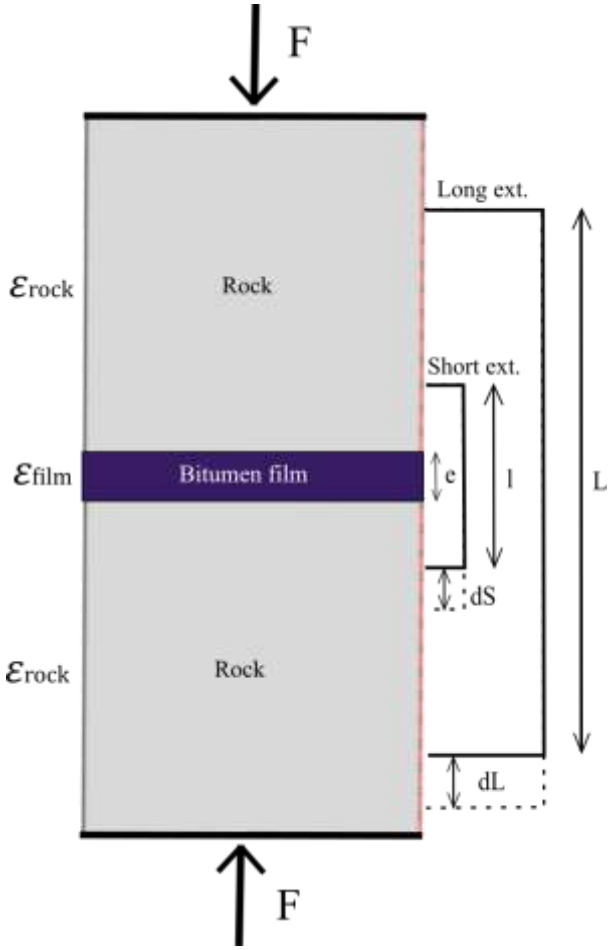

Figure 6-2 *Scheme of the combination of short and long extensometers on bitumen thin film specimen*

Additionally, the axial stresses was simply related to the axial load *F* applied along the press axis, measured in the load cell and the cross-sectional surface area:

$$\sigma_{rock} = \frac{4F}{\pi D_{rock}^2} \tag{6.3}$$

$$\sigma_{film} = \frac{4F}{\pi D_{film}^2} \tag{6.4}$$

, with D_R and D_B the diameters of the rock cylinder and the bitumen thin film. This distinction was useful in the "small diameter" (SD) version of the thin film (see section 3.2.6), which concentrated the stresses on a smaller area. The rock cylinder diameter, however, always measured 8cm.

The knowledge of axial strains and stresses was sufficient to determine the apparent stiffness of both rock and bitumen film phases

$$E_{rock} = \frac{\sigma_{rock}}{\varepsilon_{rock}} = \frac{4F(L-l)}{\pi D_{rock}^2 (d_L - d_S)} \tag{6.5}$$

$$E_{film} = \frac{\sigma_{film}}{\varepsilon_{film}} = \frac{4Fe}{\pi D_{film}^2 \left(d_S - \varepsilon_R (l-e)\right)} \tag{6.6}$$

This technique has been used for the thermomechanical characterisation of interface between bituminous layers (Freire et al. 2018). This is important to notice that the apparent stiffness E_B of the film was not *a priori* the uniaxial modulus of the constituent material, i.e. Young's modulus E in isotropic linear elasticity (ILE), or the complex modulus E^* in the isotropic linear viscoelastic (ILVE) case. Indeed, only the calculation of the stress and strain distribution in ILE (or ILVE) in the film, taking into account the potential deformation of the cylinders and all necessary boundary conditions, could establish the relationship between the apparent stiffness and the material's property. This was addressed in Section 6.4.

The test temperature was imposed via a Bia Climatic® thermal chamber. The surface temperature was monitored with a TCSA© PT100 probe put on the rock. Since the specimen had approximately the same dimensions as a classical cylindrical specimen of bituminous mixture for tension-compression tests, a minimum of 4-hour rest was imposed to obtain thermal equilibrium for each test temperature.

6.3 Procedures for specimen preparation and preservation during test

The specimen preparation was separated in two main steps:

- Fabrication
- Setup on the hydraulic press

The fabrication of the thin film specimen is illustrated in Figure 6-3. The first step was to prepare the spacing tool that ensure precisely the thickness of the bitumen film. In order to do so, high precision metallic foils of the desired thickness were cut in strips (20mm long by 2-3mm width). Then, they were carefully polished on every edge, since the cutting generally leaves micrometric flaws. Three of them were taped to an annular piece of cardboard (internal diameter 9cm, external diameter 12cm), at 120° from each other. The foil strips were placed towards the centre of the cardboard piece, so that they would touch the edge of the rock cylinder (over 2mm), just as presented in Figure 6-3 1/. After the spacer preparation, two nuts were glued at half of the height of each top and bottom cylinders, diametrically opposed. Before furnace heating, the bottom cylinder was protected from bitumen stains with tape. The cylinders and the bitumen were heated at 150°C for 3h. The bitumen was then poured directly on the bottom cylinder. The top cylinder was placed manually, a critical phase during which the annular cardboard might be hit, and the top cylinder could also slide (Figure 6-3 4/). However, once the exceeding bitumen has flowed out, at the point which the spacer was in contact with the rock cylinders, the specimen was very stable. The two cylinders were aligned manually with a metallic ruler while the bitumen was still very hot. Finally, after the specimen cooldown at 5°C (conservation temperature), the protection tape was removed and the compression springs (Figure 6-3 6/) were screwed onto the nuts, so that the specimen would be kept in compression at all time.

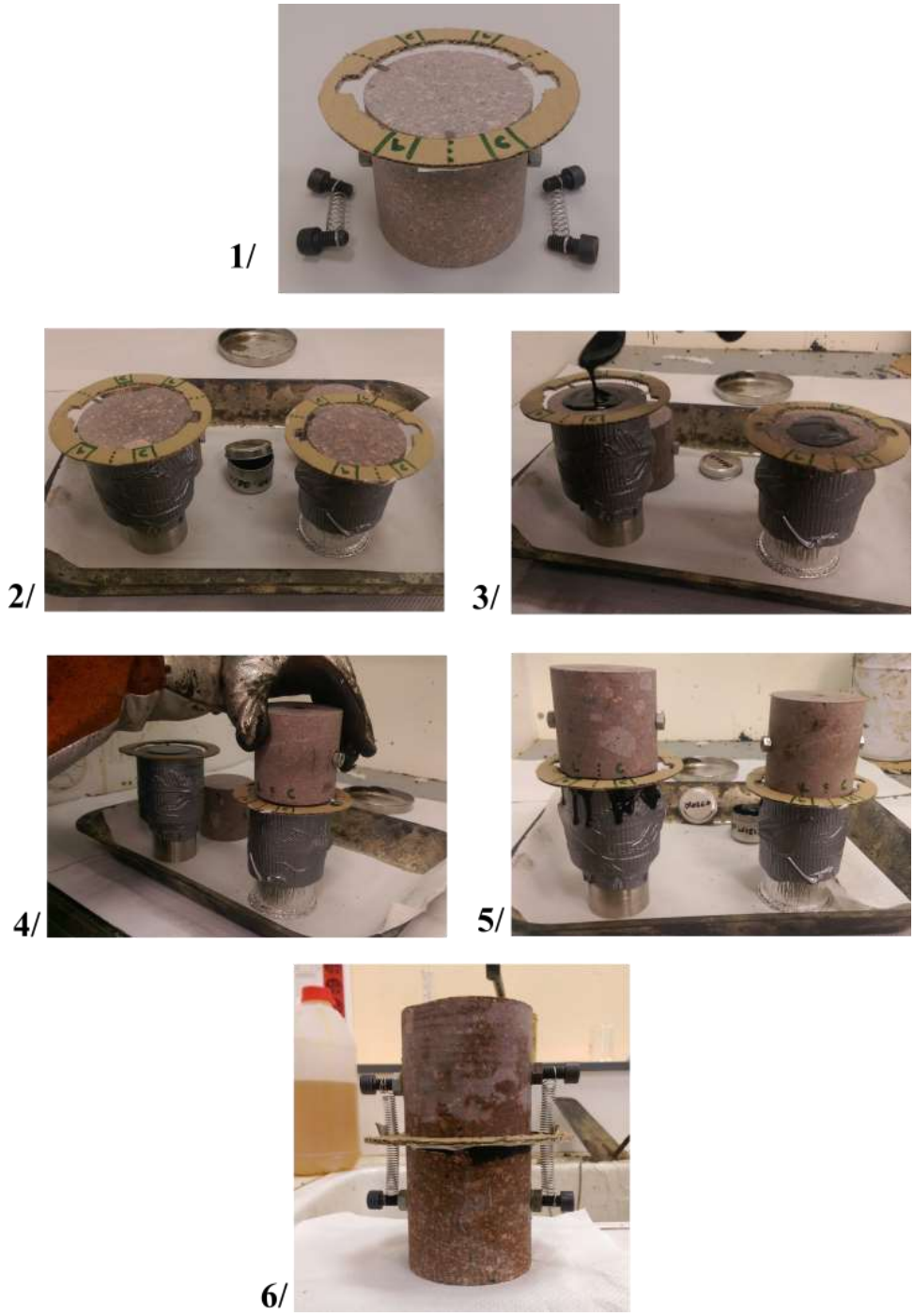

Figure 6-3 *Fabrication of specimen for thin film test*

The setup on the hydraulic press was quite standard (Figure 6-4). The specimen was glued to a first metallic cap with Araldite® glue, using an adequate work bench. The first cap was mounted on the upper axis of the hydraulic press. The second cap was fixed onto the lower axis, and then glued to the bottom rock cylinder. This process of gluing the second cap with the specimen already mounted on the press limited the bending stresses from misalignment and angular discrepancies in the whole axis. The whole axis was kept under a small compression of 0.030 kN. The three metallic foil strips ensured the integrity of the bitumen film. At this stage, the compression springs could be removed. This cleared the space for the two extensometers pairs (the gauge knives were glued on the rock cylinders) and the PT 100 temperature probe.

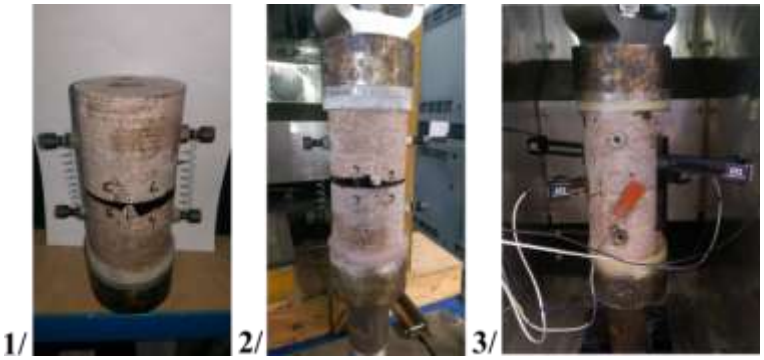

Figure 6-4 *Setup on the hydraulic press and instrumentation of the thin film specimen*

It was crucial to preserve the film integrity during tests with varying temperature. Indeed, a change in temperature induce thermal dilatation/contraction in all parts of the setup (metallic axis, rock cylinders, bitumen film…etc.). To relieve the system from thermal stress, the axis was kept under a small compression of 0.030 kN until the thermal equilibrium. Before any test different from monotonic tensile test (e.g. a cyclic frequency sweep test), the metallic foil strip had to be removed at constant press axis displacement. This operation was critical, since it required to open the thermal chamber for few seconds. Afterwards, the displacement value of all extensometers were reset to 0µm in the press controller. The tests were usually strain-controlled, by the average value of the short extensometers, to avoid the thin film destruction. The test ended by a return to the initial displacement. If the test continued with other temperatures, the metallic foil strips were inserted back in the specimen and the whole axis was put back under small compression until the next thermal equilibrium. Overall, the spacing system using high precision metallic foil strips has proven to be very useful for specimen fabrication and preservation during test. Thin films with a homogenous thickness of 100 to 300µm were produced. With perfectly flat caps, perhaps metallic ones, one could even create films with thickness of few dozens of micrometres.

6.4 Analytical solution of stress and strain distribution in a isotropic linear elastic (ILE) or viscoelastic (ILVE) thin film specimen

For homogeneous materials or assemblies of piecewise homogeneous materials such as the thin film geometry, the correspondence principle states that the linear viscoelastic (LVE) formulation of a mechanical problem in the transformed Laplace-Carson domain is homologous to its linear elastic (LE) formulation in time domain (R. M. Christensen 1982). The following analysis was expressed in the elastic version for its simplicity. Furthermore, both rock and bitumen materials were assumed isotropic. After a recap of the existing similar solutions, this section focused on the study of analytical solution of stress and strain distribution in the thin film specimen under uniaxial compression, for isotropic linear elasticity (ILE). The isotropic linear viscoelastic (ILVE) case was not expressed, since it can directly be obtained from the correspondence principle.

6.4.1 Previous solution for the Poker-chip geometry with rigid caps and finite aspect ratio under axial tension

An analytical solution for the Poker-chip geometry, previously introduced in the literature review Section 2.4.2.2 (coordinate system are displayed in Figure 2-61), has been formulated in the case of imposed axial strain ε_{zz} on the film of finite aspect ratio (Lindsey et al. 1963). Completely rigid caps replaced the rock cylinders in this study. The solution was expressed:

$$\frac{\sigma_{rr}}{E\varepsilon_{zz}} = \frac{\sigma_{\theta\theta}}{E\varepsilon_{zz}} = \frac{1-\upsilon}{(1+\upsilon)(1-2\upsilon)}\left[1 - \frac{I_0\left(r\sqrt{3(1-2\upsilon)}\right)}{I_0\left(a\sqrt{3(1-2\upsilon)}\right)}\right] \quad (6.7)$$

$$\frac{\sigma_{zz}}{E\varepsilon_{zz}} = \frac{\sigma_{rr}}{E\varepsilon_{zz}} + \frac{\upsilon}{(1+\upsilon)}\left[1 - \frac{I_0\left(r\sqrt{3(1-2\upsilon)}\right)}{2I_0\left(a\sqrt{3(1-2\upsilon)}\right)}\right] \quad (6.8)$$

$$\frac{\sigma_{rz}}{E\varepsilon_{zz}} = \frac{3\upsilon}{(1+\upsilon)\sqrt{3(1-2\upsilon)}}\left[\frac{I_1\left(r\sqrt{3(1-2\upsilon)}\right)}{I_0\left(a\sqrt{3(1-2\upsilon)}\right)}\right] z \quad (6.9)$$

, with E the Young's modulus, υ the Poisson's ratio, r the radial position, z the axial position, a the radius of the poker-chip specimen and also the aspect ratio (the specimen thickness equalled 1), I_0 and I_1 the modified Bessel function of the first kind (respectively of order 0 and 1). With relatively small aspect ratios (around 20) and near-incompressibility conditions for the film ($\upsilon > 0.49$), the solution was far from homogeneous (depended on r). With increasing aspect ratio and/or lowering the Poisson's ratio, however, the equations suggested that the varying part of the stress and strain tensors (with the Bessel function) could be concentrated near the periphery of the film, if $(I_0\left(r\sqrt{3(1-2\upsilon)}\right) \ll I_0\left(a\sqrt{3(1-2\upsilon)}\right)$, leaving most of the specimen in homogeneous oedometric conditions.

6.4.2 Solution for the thin film specimen with infinite aspect ratio and non-rigid rock cylinder

In this section, the deformability of both the rock phase and the bitumen film specimen was taken into account. The Young's modulus and the Poisson's ratio of the ILE rock were noted E_R and υ_R. Similarly, the "bitumen" film (here also considered ILE material) parameters were noted E_B and υ_B. The mathematical solution to the Poker-chip geometry with non-rigid plates was deemed intractable by the authors of the solution with rigid plate (Lindsey et al. 1963), presented in the previous section. Nevertheless, they proved the possibility of having homogeneous stress and strain distribution almost everywhere, except at the periphery of the sample. Therefore, a critical assumption was made, in order to greatly simplify the problem with non-rigid rock: Only the homogeneous part of the specimen was studied; The side effects were neglected and the boundary conditions applied at the infinite. Consequently, the specimen was considered as an infinite slab of bitumen trapped in two semi-infinite spaces of rock. Since the thickness of the film e was finite, the aspect ratio appeared infinite. The homogeneity hypothesis was further tested with Finite Element (FE) simulations in section 6.5.

Two loading cases were considered.

- Loading case 1 (Figure 6-5): axial compression in oedometric conditions (no radial strains) for both phases. The imposed axial stress (in z direction) was noted σ. The stress and strain tensors in both phases were:

$$\bar{\bar{\sigma}}_R = \begin{pmatrix} \sigma_{rr,R} & 0 & 0 \\ 0 & \sigma_{\theta\theta,R} & 0 \\ 0 & 0 & \sigma \end{pmatrix}, \ \bar{\bar{\varepsilon}}_R = \begin{pmatrix} 0 & 0 & 0 \\ 0 & 0 & 0 \\ 0 & 0 & \varepsilon_{zz,R} \end{pmatrix} \quad (6.10)$$

$$\bar{\bar{\sigma}}_B = \begin{pmatrix} \sigma_{rr,B} & 0 & 0 \\ 0 & \sigma_{\theta\theta,B} & 0 \\ 0 & 0 & \sigma \end{pmatrix}, \ \bar{\bar{\varepsilon}}_B = \begin{pmatrix} 0 & 0 & 0 \\ 0 & 0 & 0 \\ 0 & 0 & \varepsilon_{zz,B} \end{pmatrix} \quad (6.11)$$

The generalised Hooke's law (ILE materials) applied to the tensors (6.10) and (6.11) yielded

$$\bar{\bar{\sigma}}_R = \begin{pmatrix} \frac{\upsilon_R}{1-\upsilon_R}\sigma & 0 & 0 \\ 0 & \frac{\upsilon_R}{1-\upsilon_R}\sigma & 0 \\ 0 & 0 & \sigma \end{pmatrix}, \bar{\bar{\varepsilon}}_R = \begin{pmatrix} 0 & 0 & 0 \\ 0 & 0 & 0 \\ 0 & 0 & \frac{\sigma}{E_{oedo,R}} \end{pmatrix} \quad (6.12)$$

$$\bar{\bar{\sigma}}_B = \begin{pmatrix} \frac{\upsilon_B}{1-\upsilon_B}\sigma & 0 & 0 \\ 0 & \frac{\upsilon_B}{1-\upsilon_B}\sigma & 0 \\ 0 & 0 & \sigma \end{pmatrix}, \bar{\bar{\varepsilon}}_B = \begin{pmatrix} 0 & 0 & 0 \\ 0 & 0 & 0 \\ 0 & 0 & \frac{\sigma}{E_{oedo,B}} \end{pmatrix} \quad (6.13)$$

,with the definition of the oedometric modulus E_{oedo}, also found as *M*, P-wave modulus, or constrained modulus in the literature:

$$E_{oedo} = \frac{E(1-\upsilon)}{(1+\upsilon)(1-2\upsilon)} \quad (6.14)$$

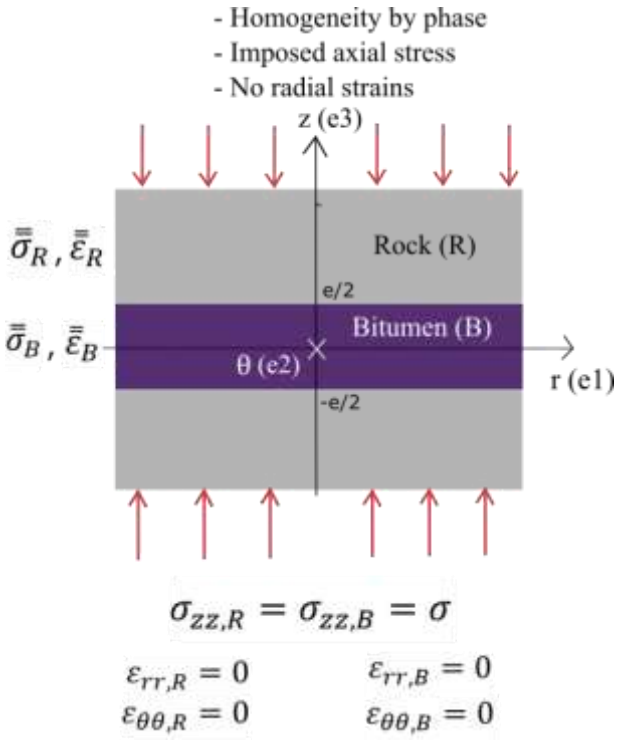

Figure 6-5 *Scheme of loading type 1: oedometric compression*

- Loading case 2 (Figure 6-6): Imposed radial stress in the rock, equal to the opposite of the radial stresses obtained from loading type 1.Additionnaly, the axial stresses were null, and the radial strains were equal between both phases.

$$\bar{\bar{\sigma}}_R = \begin{pmatrix} \frac{-\upsilon_R}{1-\upsilon_R}\sigma & 0 & 0 \\ 0 & \frac{-\upsilon_R}{1-\upsilon_R}\sigma & 0 \\ 0 & 0 & 0 \end{pmatrix}, \bar{\bar{\varepsilon}}_R = \begin{pmatrix} \varepsilon_{rr,R} & 0 & 0 \\ 0 & \varepsilon_{\theta\theta,R} & 0 \\ 0 & 0 & \varepsilon_{zz,R} \end{pmatrix} \quad (6.15)$$

$$\bar{\bar{\sigma}}_B = \begin{pmatrix} \sigma_{rr,B} & 0 & 0 \\ 0 & \sigma_{\theta\theta,B} & 0 \\ 0 & 0 & 0 \end{pmatrix}, \bar{\bar{\varepsilon}}_B = \begin{pmatrix} \varepsilon_{rr,R} & 0 & 0 \\ 0 & \varepsilon_{\theta\theta,R} & 0 \\ 0 & 0 & \varepsilon_{zz,B} \end{pmatrix} \quad (6.16)$$

After calculation using the generalised Hooke's law:

$$\bar{\bar{\sigma}}_R = \begin{pmatrix} \frac{-\upsilon_R}{1-\upsilon_R}\sigma & 0 & 0 \\ 0 & \frac{-\upsilon_R}{1-\upsilon_R}\sigma & 0 \\ 0 & 0 & 0 \end{pmatrix}, \bar{\bar{\varepsilon}}_R = \begin{pmatrix} \frac{-\upsilon_R}{E_R}\sigma & 0 & 0 \\ 0 & \frac{-\upsilon_R}{E_R}\sigma & 0 \\ 0 & 0 & \frac{2{\upsilon_R}^2}{E_R(1-\upsilon_R)}\sigma \end{pmatrix} \quad (6.17)$$

$$\bar{\bar{\sigma}}_B = \begin{pmatrix} -\frac{E_B}{E_R}\frac{\upsilon_R}{(1-\upsilon_B)}\sigma & 0 & 0 \\ 0 & -\frac{E_B}{E_R}\frac{\upsilon_R}{(1-\upsilon_B)}\sigma & 0 \\ 0 & 0 & 0 \end{pmatrix}, \bar{\bar{\varepsilon}}_B = \begin{pmatrix} \frac{-\upsilon_R}{E_R}\sigma & 0 & 0 \\ 0 & \frac{-\upsilon_R}{E_R}\sigma & 0 \\ 0 & 0 & \frac{2\upsilon_B}{1-\upsilon_B}\frac{\upsilon_R}{E_R}\sigma \end{pmatrix} \quad (6.18)$$

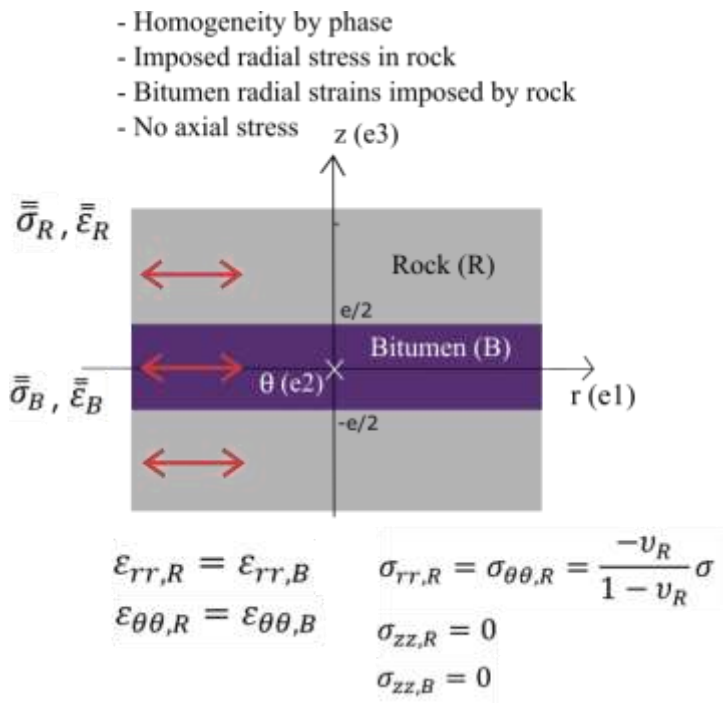

Figure 6-6 *Scheme of loading case 2: radial stress imposed in the rock and equality of radial strains*

According to the superposition principle, the solution to the superposition of the two loading cases was the sum of the solutions to each loading case. When combined, the stress and strain state in both phases was:

$$\bar{\bar{\sigma}}_R = \sigma \begin{pmatrix} 0 & 0 & 0 \\ 0 & 0 & 0 \\ 0 & 0 & 1 \end{pmatrix},\ \bar{\bar{\varepsilon}}_R = \sigma \begin{pmatrix} \frac{-\upsilon_R}{E_R} & 0 & 0 \\ 0 & \frac{-\upsilon_R}{E_R} & 0 \\ 0 & 0 & \frac{1}{E_R} \end{pmatrix} \tag{6.19}$$

$$\bar{\bar{\sigma}}_B = \sigma \begin{pmatrix} \frac{E_B}{1-\upsilon_B}\left(\frac{\upsilon_B}{E_B} - \frac{\upsilon_R}{E_R}\right) & 0 & 0 \\ 0 & \frac{E_B}{1-\upsilon_B}\left(\frac{\upsilon_B}{E_B} - \frac{\upsilon_R}{E_R}\right) & 0 \\ 0 & 0 & 1 \end{pmatrix}$$

$$\bar{\bar{\varepsilon}}_B = \sigma \begin{pmatrix} \frac{-\upsilon_R}{E_R} & 0 & 0 \\ 0 & \frac{-\upsilon_R}{E_R} & 0 \\ 0 & 0 & \frac{1}{E_{oedo,B}} + \frac{2\upsilon_B\upsilon_R}{E_R(1-\upsilon_B)} \end{pmatrix} \tag{6.20}$$

The radial stresses were voluntary nullified in the rock phase, which behaved overall like in a classical uniaxial compression. This hypothesis was made to satisfy the real boundary condition of no confinement pressure at the specimen periphery($\sigma_{rr} = 0$) that happened during the real thin film test. This leaved a radial pressure in the bitumen of $\sigma_{rr,B} = \frac{E_B}{1-\upsilon_B}\left(\frac{\upsilon_B}{E_B} - \frac{\upsilon_R}{E_R}\right)$, which was impossible at the film periphery, but could hopefully be neglected.

The theoretical modulus of the film, as the ratio of the axial stress σ and the axial strain was

$$E_{theo} = \frac{(1-\upsilon_B)E_R E_{oedo,B}}{E_R(1-\upsilon_B) + 2\upsilon_B\upsilon_R E_{oedo,B}} \tag{6.21}$$

6.5 Finite element simulation of ILE thin film test

In this section, a FE model of the thin film specimen was tested.

6.5.1 FE model description

A 2D axisymmetric model of the thin film specimen was created with COMSOL® (Figure 6-7). The dimensions of the rock cylinders was the same as the real ones (D=80mm, H=80mm). The thickness of the film was adjusted to satisfy the different tested aspect ratios. The bottom part of the sample was restrained in displacement, and the tension-compression was simulated by imposing a vertical displacement at the top of the specimen. The extensometers were also simulated; A1 and A2 represented the contact points of the gauge knives of the short extensometer, and B1 and B2 of the long extensometers. Exactly as for the real thin film test set-up in equation (6.6), the apparent simulated modulus of the bitumen film was calculated as:

$$E_{simul} = \frac{e\overline{\sigma}}{\left(d_S - \frac{d_L - d_S}{L - l}(l - e)\right)} \tag{6.22}$$

,with $\overline{\sigma}$ the numerical average axial stress, calculated at the central cross section of the bitumen film.

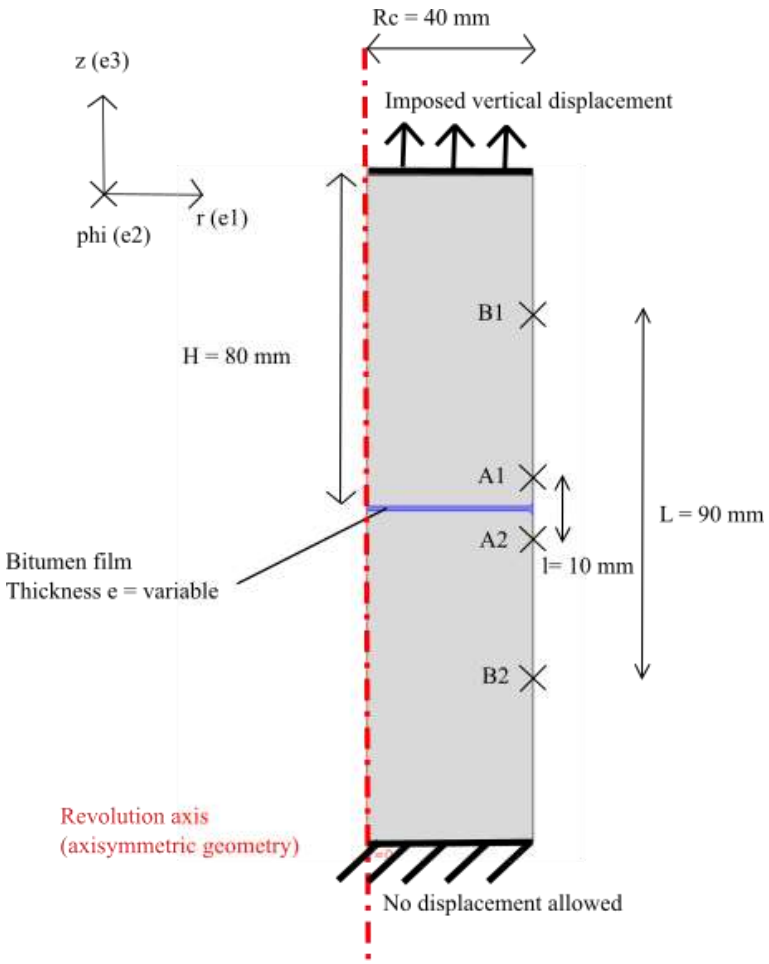

Figure 6-7 *FE model of the thin film specimen*

6.5.2 Example of stress and strain distribution for E_b =122MPa , υ_b, = 0.35, E_R = 50 GPa, υ_R = 0.3

The FE simulation of the thin film specimen was run for a "standard" set of parameters, for both phases:

- E_b =122MPa, υ_b, = 0.35. The Young's modulus for the bitumen in the film corresponded to a shear modulus G_b of 45MPa, which equalled the norm of complex shear modulus obtained for bitumen B at 10°C/10Hz in Campaign II. The value of its Poisson's ratio was arbitrary.
- E_R = 50 GPa, υ_R = 0.3. The modulus of the rock was obtained by both experimental compression and wave propagation tests, and the Poisson's ratio was arbitrary, in the classical range of granite rocks (Stowe 1969).

The film thickness was 300µm and the aspect ratio $e/D \approx 1/267$. The vertical displacement imposed at the top of the specimen equalled +5µm (tension).

The results of strain and stress tensor terms rr, θθ, zz and rz are displayed respectively in Figure 6-8 to Figure 6-11, in the central part around the film.

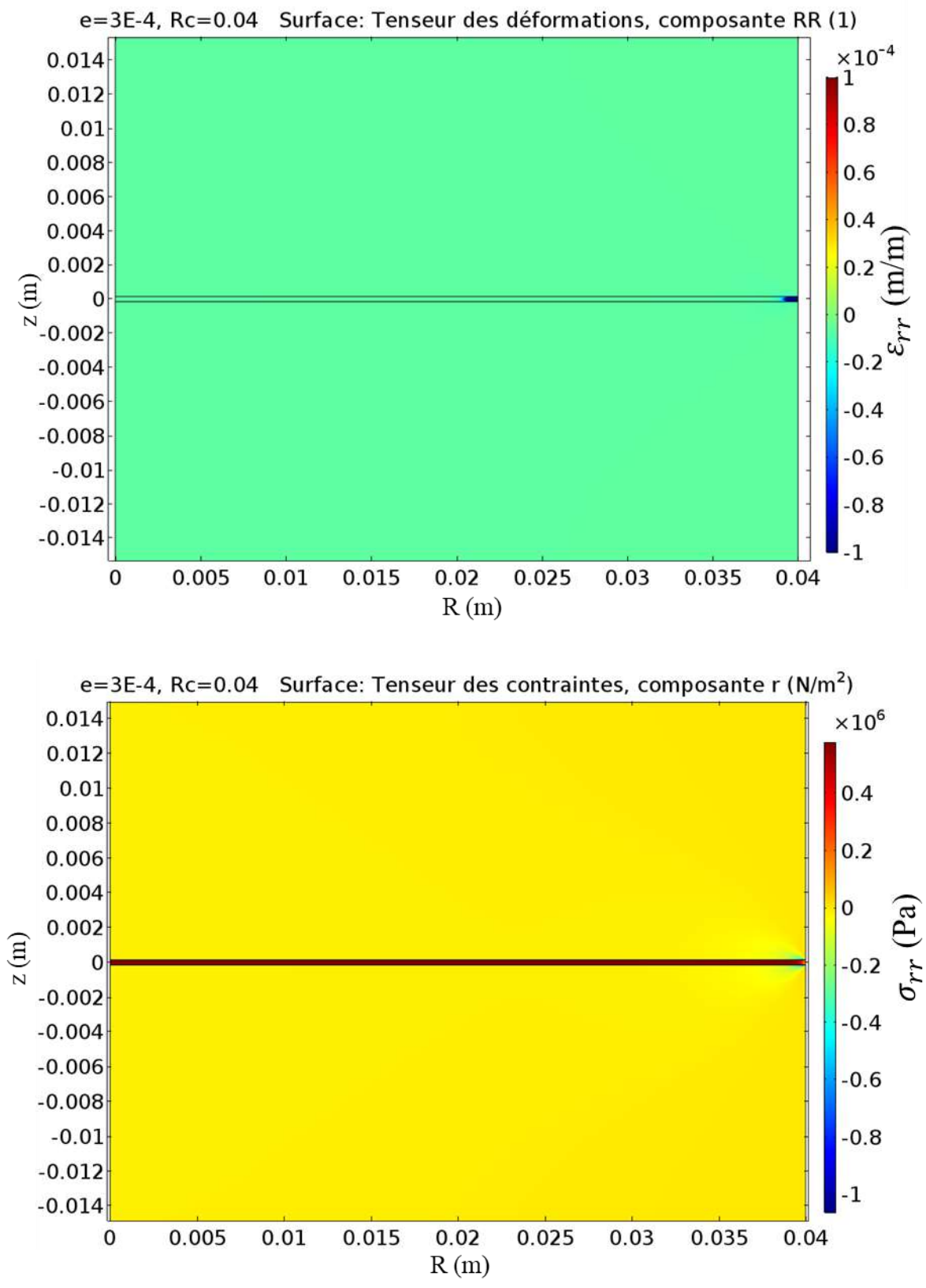

Figure 6-8 *Distribution of strain and stress tensor terms rr in the central part around the film*

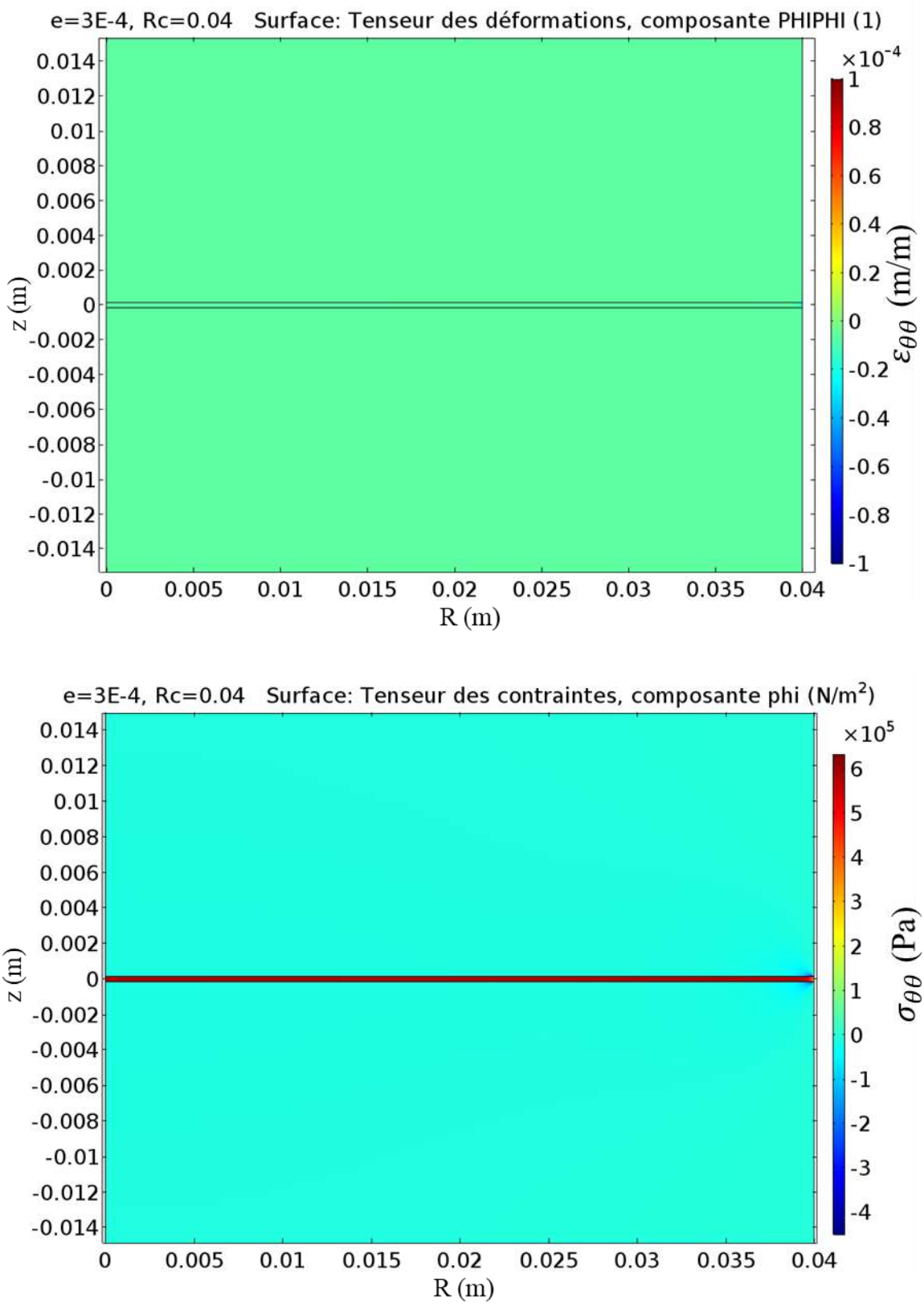

Figure 6-9 *Distribution of strain and stress tensor terms θθ in the central part around the film*

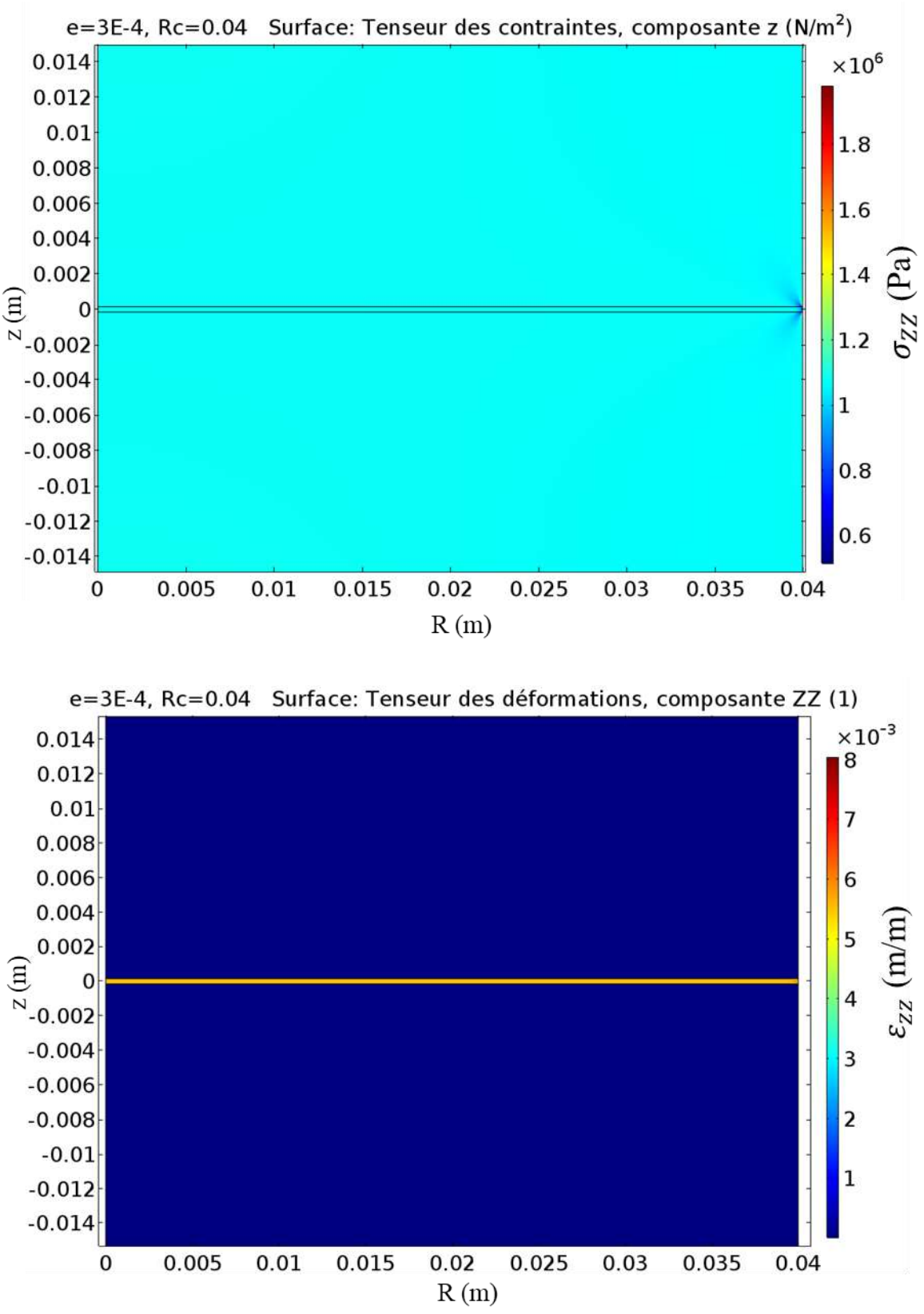

Figure 6-10 *Distribution of strain and stress tensor terms zz in the central part around the film*

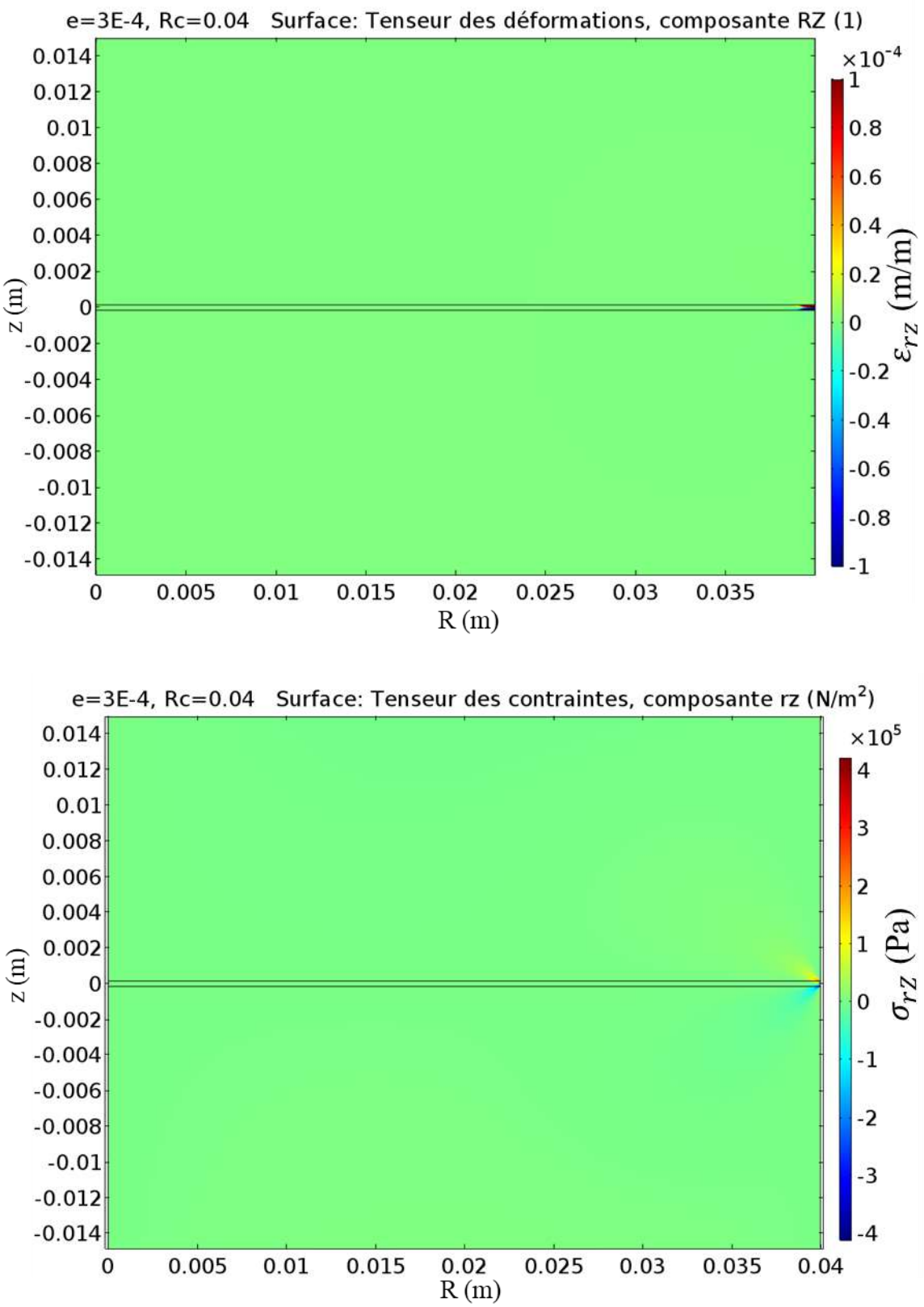

Figure 6-11 *Distribution of strain and stress tensor terms rz in the central part around the film*

From a general perspective, the results clearly showed an homogeneous state of stress and strain of both the bitumen and the rock phases, except in the vicinity of the periphery of the bitumen film. In Figure 6-10, the axial stresses σ_{zz} equalled 1.07MPa almost everywhere which was the average value $\overline{\sigma}$, calculated for the whole bitumen section at z = 0. Additionally, the axial strains for both phases $\varepsilon_{zz,\,B}$ and $\varepsilon_{zz,\,R}$ were also constant, equalling respectively 5.5×10^{-3} and 2.1×10^{-5}. In rr-direction (Figure 6-8), the rock presented negligible radial stress $\sigma_{rr,\,R}$ (from -0.014 to 0 MPa) compare the axial one $\sigma_{zz,R}$ (1.07MPa), suggesting that the rock was overall behaving like in a uniaxial test, and therefore that the radial strains in both phases $\varepsilon_{rr} = 6.5 \times 10^{-6}$ were imposed by the rock deformation. Moreover, the ratio between the average axial stress $\overline{\sigma}$ and the average axial strain $\varepsilon_{zz,\,B}$ taken in the homogeneous part of the bitumen film equalled 1.9×10^{2}MPa, which was very close to the value of $E_{oedo,\,B}$ (=1.94 MPa). In conclusion, the assumptions of strain and stress homogeneity and null radial stress in the rock phase, made in the analytical approach in Section 6.4.2, were validated in first approximation for a "standard" set of parameters, where the rock was much stiffer than the bitumen and where the aspect ratio was quite small (1/267).

Since side effects were observed, the accordance between the axial strains simulated by the extensometers $\varepsilon_{zz,\,simul}$ and the local axial strains in the central section of the film $\varepsilon_{zz,\,local}$ was of utmost importance for the validity of the thin film test. The ratio of $\varepsilon_{zz,\,local}$ and $\varepsilon_{zz,\,simul}$ as a function of the radial position is displayed in Figure 6-12. The predicted strains by the simulated extensometers matched at max. 1% error the local strain values over 98.5% of the radius of the film. The right measure of the homogeneous axial strain state by the extensometers was obtained with the standard set of parameters. Consequently, the simulated modulus E_{simul}, defined in Equation (6.22), corresponded well to the film axial stiffness (in this case the oedometric modulus of the bitumen).

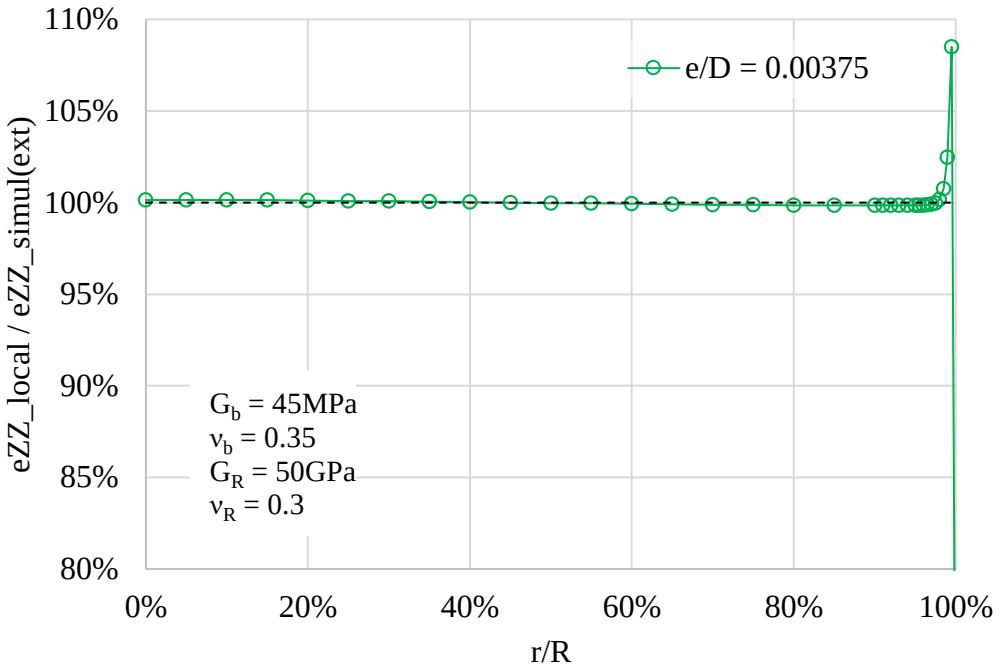

Figure 6-12 $\varepsilon_{zz,\,local}$/ $\varepsilon_{zz,\,simul}$ as a function or the relative radial position for the standard set of parameters

6.5.3 Influence of bitumen parameters and specimen aspect ratio on the simulated modulus

The validity of the analytical solution depended on the parameters of the thin film specimen. In this section, a parametric study compared the theoretical modulus E_{theo} (Equation (6.21)) and the simulated modulus E_{simul} (Equation (6.22)), with varying bitumen shear modulus G_b = [0.02 ; 4 ; 45 ; 1000] (MPa), bitumen Poisson's ratio υ_b = [0.35 ; 0.40 ; 0.45; 0.47 ; 0.49]. The associated names were written "GX_ υY", with X the value of the shear modulus and Y the value of the Poisson's ratio (e.g. "G1000_υ0.45") Moreover, the tested aspect ratio logarithmically scaled from 1/2667 to 2.5. The simulation results are displayed in Figure 6-13. In this figure, the normalised simulated modulus $(E_{simul} - E_b) / (E_{theo} - E_b)$ is represented for all sets of parameters. A value close to 1 equated to a good agreement between the simulation and the analytical solution. A value close to 0 would mean that the simulated modulus and the Young's modulus of the bitumen phase were the same.

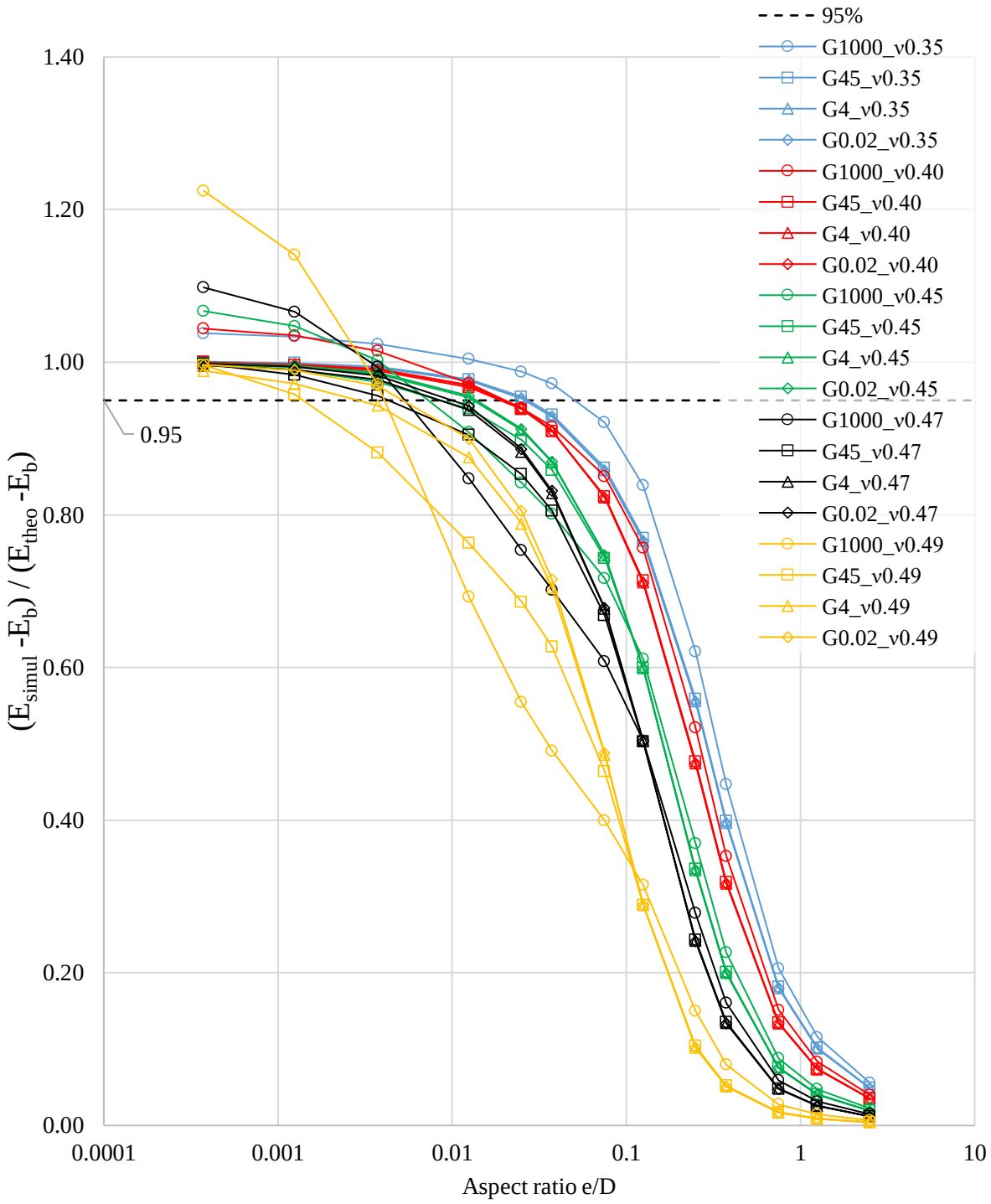

Figure 6-13 *Normalised simulated modulus as a function of aspect ratio, with varying bitumen parameters.*

The first observation in Figure 6-13 was the systematic discrepancies between the analytical prediction and the simulation obtained with high modulus bitumen (G_b = 1000MPa, which corresponded to the glassy modulus of bitumen B from Campaign II). At this point, the difference of stiffness between the rock and the bitumen phase might compromise the homogeneity by inducing non-negligible radial stress in the rock. With less stiff bitumen phase (G_b<45MPa), all simulations lead to the analytical solution, provided a small enough aspect ratio (less that 5% difference between E_{simul}-E_b and E_{theo}-E_b under 1/800 aspect ratio). The aspect ratio required to obtain this good agreement could be reduced to 1/266 for υ_b<0.47 and even 1/80 for υ_b<0.45. As the bitumen became more incompressible (with higher oedometric modulus), the aspect ratio required to obtain a good fit increased. For all sets of parameters, the simulated modulus tended to the Young's modulus of the bitumen for aspect ratio around 2.5.

6.6 Experimental characterisation of LVE behaviour of bitumen thin film

6.6.1 Experimental plan

Three samples of 300µm-thick film were tested. Two samples had a large-diameter bitumen film of 80mm ("B_CO_300_LD_sp1" and "B_CO_300_LD_sp2"), which ensured an aspect ratio of 1/267. The third sample had a small-diameter bitumen film of 3.7cm ("B_CO_300_SD_sp1"), for a respective aspect ratio of 1/123. The complex modulus tests on the bitumen thin film consisted of frequency sweep test at different intermediate temperatures. The tested frequencies were 0.01, 0.03, 0.1, 0.3, 1 and 3Hz. The test temperatures of specimen B_CO_300_LD_sp1 were 40, 35, 25 and 15°C, whereas the specimens B_CO_300_LD_sp2 and B_CO_300_SD_sp1 were tested at 50, 40 and 30°C. The loading was controlled by the average displacement d_S of the short extensometers (S1 and S2, see Figure 6-2). The standard applied amplitude was 1µm, which equated to a maximum of 0.33% of axial strain in the film. However, for high equivalent frequencies, the amplitude was lowered to 0.5µm to preserve the sample, since tensile stresses could break the rock cylinders. On the other hand, at high equivalent frequencies, the amplitude needed amplification up to 5µm (which corresponded to a 1.7% of axial strain in the film) due to very weak load cell signals. Additionally, the hydraulic press was equipped with a torsion controller, that allowed maintaining a null angular rotation and monitoring the torque (z axis) during the complex modulus tests.

Regarding analysis, two ways of calculating the apparent axial strains in the film were implemented:

- The first one was by dividing the average displacement of the short extensometers, neglecting the part of measured displacement due the deformation of rock cylinders

$$\varepsilon_{film1} = \frac{d_S}{e} \tag{6.23}$$

- The second one is the classical analysis proposed in Equation (6.1) and (6.2), illustrated in Figure 6-2. The part of apparent axial strain due to the rock deformation was deduced.

$$\varepsilon_{film2} = \varepsilon_{film} = \frac{d_S - \varepsilon_R(l-e)}{e} \tag{6.24}$$

$$\varepsilon_{Rock} = \frac{d_L - d_S}{L - l} \tag{6.25}$$

The associated modulus were noted E^*_{film1}, E^*_{film2} and E_{rock}, and simply obtained by dividing the stress by the apparent axial strains. The direct comparison between E^*_{film1} and E^*_{film2} allowed a clear evaluation of the bias due to the rock deformation.

6.6.2 Results and analysis

All complex modulus test results on bitumen thin film are detailed in Appendix 3.1. In this manuscript, the measured extensometer displacements, the calculated strains in the rock and the bitumen phases, the axial load and torque were compared for one small-diameter film (B_CO_300_SD_sp1) and one large-diameter film (B_CO_300_LD_sp2). Figure 6-14 and Figure 6-15 comprised the results for B_CO_300_SD_sp1 at respectively 50°C/0.1Hz and 30°C/3Hz. Similarly, Figure 6-16 and Figure 6-17 focused on the results of B_CO_300_LD_sp2 at respectively 50°C/0.1Hz and 30°C/3Hz. These two particular temperature and frequency conditions, 50°C/0.1Hz and 30°C/3Hz, were chosen as they presented the extreme behaviours obtained with this complex modulus test. The results of B_CO_300_LD_sp1 were not presented here, since one of the long extensometers had bad signal issues.

For the small-diameter specimen B_CO_300_SD_sp1, whether at 50°C/0.1Hz (in Figure 6-14 a) and b)) or at 30°C/3Hz (in Figure 6-15 a) and b)), the measured displacement between the long and the short extensometers was identical for both diametrically opposed pairs. However, if the S1 and L1 (first pair, depicted in blue dots) always shared the same values, just as S2 and L2 (second pair, depicted in red dots) did, the measure between the two pairs was not always equal. Indeed, at 30°C/3 Hz, the second pair was in phase opposition (+/-180°) with the first pair and had a significantly different amplitude, meaning that the specimen experienced flexion in addition to axial tension-compression at 1kN load amplitude. At 50°C/0.1 Hz, no flexion was observed, because of the very small axial effort in the axis (0.015kN amplitude). Theoretically, the presence of flexural strains in the bitumen film were not a problem for the analysis of the apparent axial modulus, if the average displacement signals d_S and d_L were used to measure axial strains. Since the discrepancy between the sinusoidal fits of the short and the long extensometers was always under the precision of the sensors (<0.1µm), the axial strain in the rock phase was not even measurable. Consequently, the calculated deformations ε_{film1} and ε_{film2} always appeared equal for the whole temperature and frequency range tested on B_CO_300_SD_sp1, as suggested in Figure 6-14 c) and Figure 6-15 c). Additionally, the average axial strains in the bitumen thin film were much greater (>3000µm/m) than the potential axial strains in the rock (<1µm/m). Eventually, the rock cylinders could be considered as rigid bodies for this small-diameter specimen, and the apparent axial modulus could be identified as the oedometric modulus of the bitumen. This was addressed further in this section.

The displacement signals obtained with the large-diameter specimen B_CO_300_LD_sp2 were significantly different from the ones obtained with small-diameter specimen B_CO_300_SD_sp1 previously discussed. At 50°C/0.1Hz, the short extensometers (Figure 6-14 a)) presented a greater displacement amplitude than the long extensometers (Figure 6-14 b)), respectively 3.0µm against 2.3µm. This surprising result exposed an experimental flaw of the thin film test, only seen with large-diameter specimens. Two potential explanations for these unexpected discrepancies were proposed:

- The axial load along the axis induced a torque with the screw thread of one of the centred screws that linked the parts of the set-up together. Evidence of such a torque was indeed recorded by the press controller, as shown in Figure 6-16 d). The torque have caused the film specimen to flow under shear stress in θz-direction.
- If the plane of the bitumen thin film was not exactly perpendicular to the press axis, the projection of axial load onto the rθ-plane of the film could have been non-null, resulting in small shear stresses in the rz-direction. This could be tested with radial displacement measurement in future studies.

In both cases, the shear modulus was expected to be very small compared to the apparent axial modulus of the film (which should coincide with the oedometric modulus of the bitumen). Hence, even if the potential shear stresses were themselves small compared to the axial ones, the resulting shear strains could still be important. The biasing effect of an undesired displacement of the extensometers knives in rθ-plane on the their axial displacement would be magnified for the smaller gauge lengths, which could explain the fact that the amplitudes of the short extensometers were greater than the amplitudes of the long extensometers. This situation lead to flawed measurement of the axial strains in both bitumen and rock phases (i.e. negative rock modulus), that discarded the large-diameter specimen for further analysis.

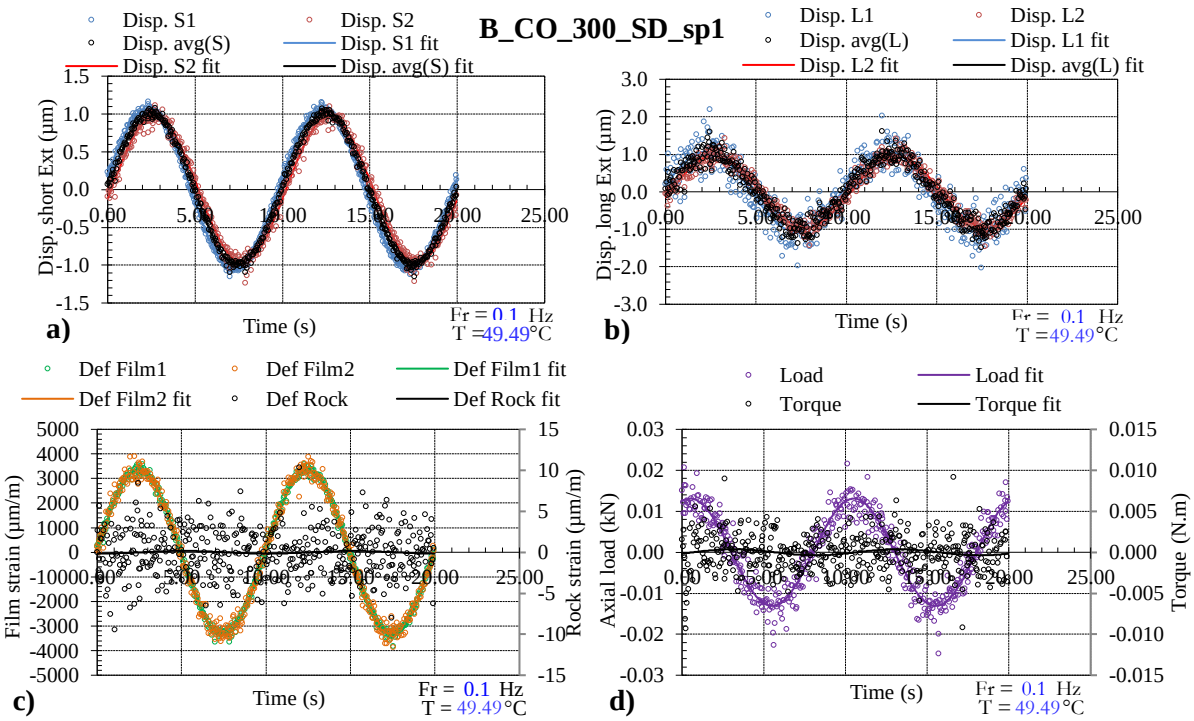

Figure 6-14 *Complex modulus tests results of B_CO_300_SD_sp1 at 50°C and 0.1Hz: a) displacement measured by small extensometers, b) displacement measured by long extensometers, c) calculated strains in film and rock phases, d) axial load and torque, all as a function of time*

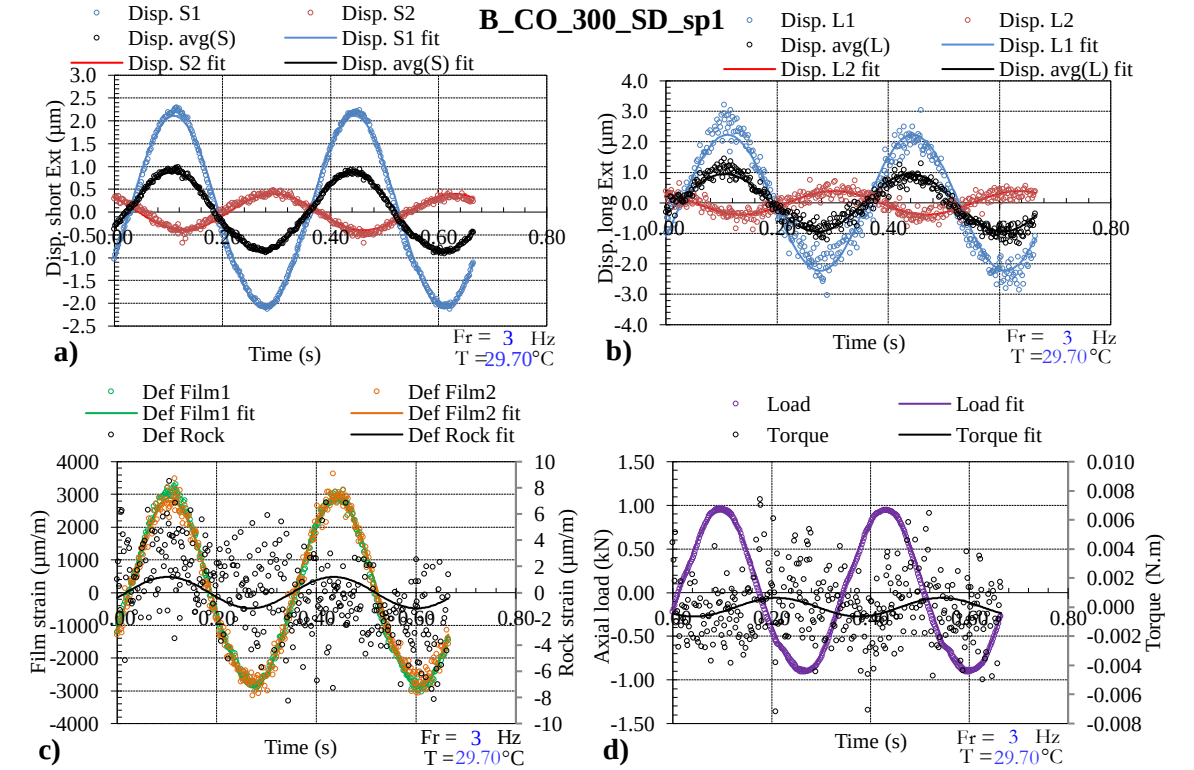

Figure 6-15 *Complex modulus tests results of B_CO_300_SD_sp1 at 30°C and 3Hz: a) displacement measured by small extensometers, b) displacement measured by long extensometers, c) calculated strains in film and rock phases, d) axial load and torque, all as a function of time*

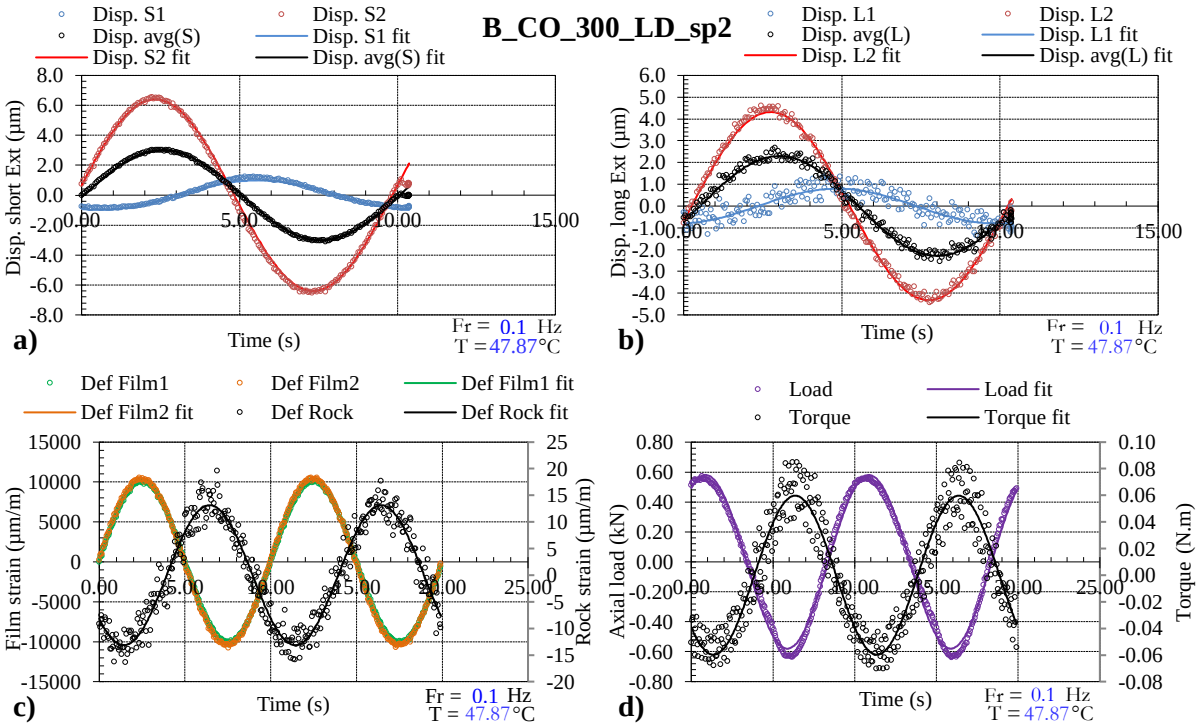

Figure 6-16 *Complex modulus tests results of B_CO_300_LD_sp2 at 50°C and 0.1Hz: a) displacement measured by small extensometers, b) displacement measured by long extensometers, c) calculated strains in film and rock phases, d) axial load and torque, all as a function of time*

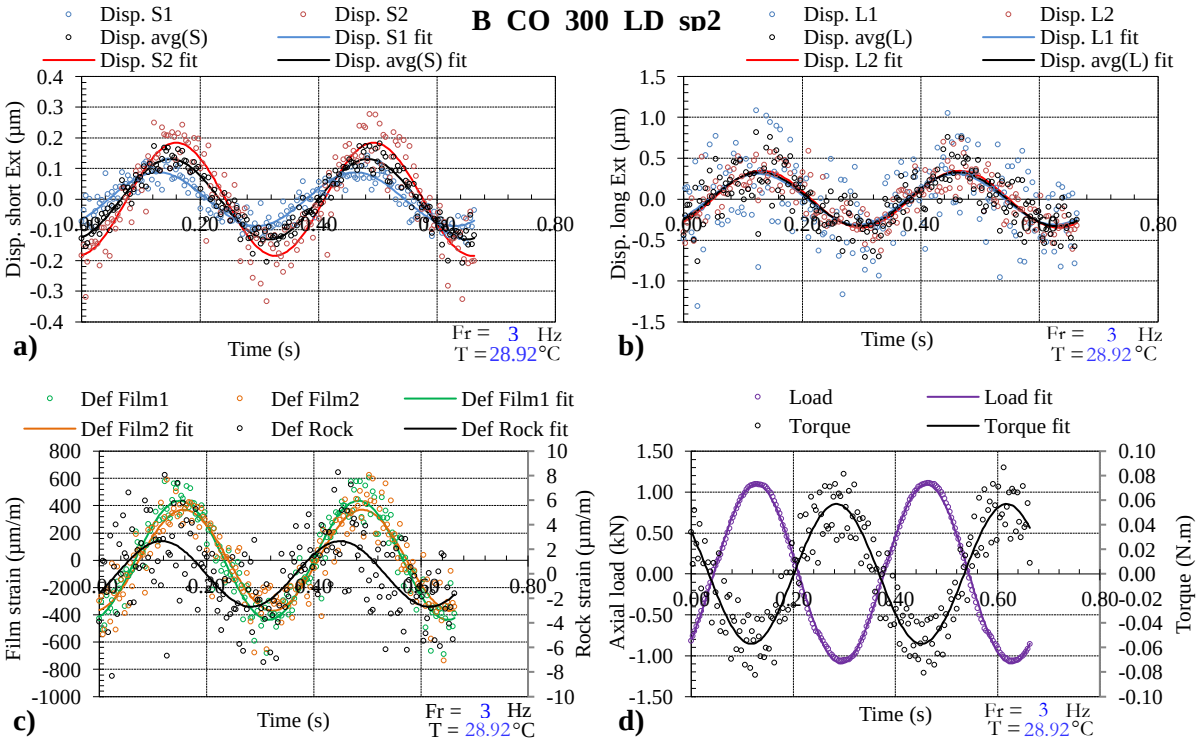

Figure 6-17 *Complex modulus tests results of B_CO_300_LD_sp2 at 30°C and 3Hz: a) displacement measured by small extensometers, b) displacement measured by long extensometers, c) calculated strains in film and rock phases, d) axial load and torque, all as a function of time*

The complex modulus test results of the small-diameter specimen B_CO_300_SD_sp1 did not present *a priori* experimental flaws observed with large-diameter specimens. The displacement amplitudes and phase angle for all temperature and frequencies are listed in Table 6-1. The isotherms of norm and phase angle of the different moduli E^*_{film1}, E^*_{film2} and E_{rock} are displayed for all tested temperatures and frequencies in Figure 6-18.

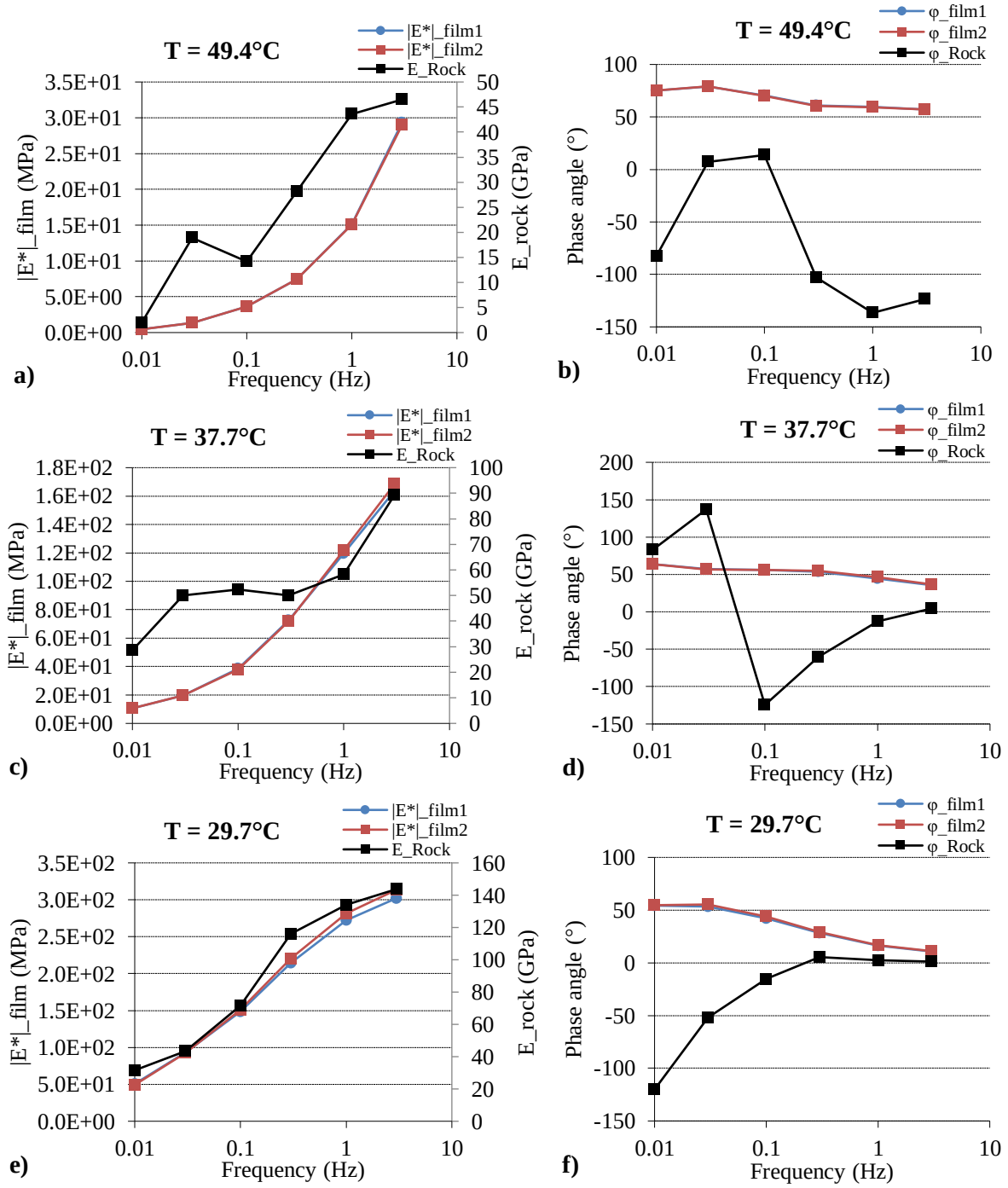

Figure 6-18 *Complex axial moduli of rock and bitumen film obtained with B_CO_300_SD_sp1: a) Norm at 49.4°C, b) Phase angle at 49.4°C, c) Norm at 37.7°C, d) Phase angle at 37.7°C, e) Norm at 29.7°C, f) Phase angle at 29.7°C*

Table 6-1 *Amplitude and phase angle of displacement signals obtained during the complex modulus test on B_CO_300_SD_sp1*

B_CO_300_SD_sp1

	Temerature (°C)	49.4						39.7						29.7					
	Frequency (Hz)	0.01	0.03	0.1	0.3	1	3	0.01	0.03	0.1	0.3	1	3	0.01	0.03	0.1	0.3	1	3
Disp. amplitude (μm)	S1	1.00	1.01	1.06	1.20	1.52	2.13	1.29	1.71	2.28	2.71	3.02	3.21	2.50	2.81	2.88	2.55	2.28	2.07
	S2	1.01	1.00	0.96	0.89	0.77	0.75	0.88	0.71	0.63	0.75	1.00	1.09	0.62	0.79	0.91	0.71	0.49	0.38
	Avg. Small Ext	1.00	1.00	1.00	1.00	1.01	1.06	1.00	1.01	1.01	1.00	1.01	1.07	1.00	1.01	0.99	0.94	0.91	0.86
	L1	1.00	1.03	1.08	1.20	1.54	2.19	1.33	1.78	2.50	3.06	3.31	3.39	2.71	3.04	3.24	2.86	2.47	2.21
	L2	0.98	0.99	0.95	0.87	0.78	0.83	0.91	0.81	0.93	1.14	1.18	1.14	1.01	1.06	1.18	0.91	0.56	0.38
	Avg. Long Ext	0.99	1.01	1.00	0.99	0.99	1.03	1.02	1.01	0.97	0.98	1.07	1.15	0.93	0.99	1.05	1.01	0.99	0.94
	In 1cm length of 50GPa rock cylinder (calculated)	0.00	0.00	0.00	0.00	0.00	0.00	0.00	0.00	0.01	0.01	0.02	0.02	0.01	0.01	0.02	0.03	0.04	0.04
Phase angle (°)	S1	74.1	76.0	62.5	47.2	40.5	37.0	45.5	37.2	40.6	46.7	45.0	40.3	44.3	50.7	44.9	34.4	21.7	15.1
	S2	75.9	82.0	78.8	79.2	99.5	137.2	91.1	112.5	162.9	88.8	225.6	229.2	190.3	223.9	231.3	230.2	221.9	215.2
	Avg. Small Ext	75.0	79.0	70.2	60.8	59.5	57.2	63.8	57.3	55.9	53.3	44.7	35.8	54.3	53.3	42.0	28.5	16.3	10.8
	L1	73.9	75.0	62.4	46.5	38.6	34.8	44.4	34.8	36.5	43.3	43.1	39.8	40.1	46.9	43.4	35.3	22.5	15.5
	L2	75.6	82.3	80.0	81.3	105.2	145.1	93.7	119.8	172.3	212.2	228.0	232.8	194.0	225.4	233.8	235.0	229.5	224.5
	Avg. Long Ext	74.8	78.6	70.7	61.1	59.8	57.1	64.1	58.3	55.9	49.7	40.3	33.4	53.8	47.7	37.6	26.7	15.1	9.9

From Table 6-1, the phase lag between the displacement signals between extensometer pairs (S1 vs. S2, or L1 vs. L2) was for some temperature and frequency points no equal to 0 or 180° (which were expected in pure TC or mixed TC and flexion). It appeared that there was a transition between the low equivalent frequencies that showed pure TC and the high equivalent frequencies that showed mixed TC and flexion, with increasing phase lag between the first and the second pair of extensometer. This was not clearly understood from an experimental standpoint, but nevertheless it questioned at least the values of the phase angle obtained from the average signals. The amplitude of the apparent axial strains should also be affected by this experimental artefact, but it was not considered important in comparison with the time and temperature dependency of the apparent axial modulus (3 orders of magnitude of variation in this study). Moreover, extreme points such as 50°C/0.1Hz and 30°C/3Hz did not show this phase lag between extensometer pairs. For large-diameter specimen B_CO_300_LD_sp1, this experimental artefact was not observed at all.

From a general perspective, the discrepancies between E^*_{film1} and E^*_{film2} (respectively represented by blue dots and red dots in Figure 6-18) were negligible for all temperatures and frequencies, confirming the previous observations made on displacement signals of extensometers. The strains in the rock were genuinely not measurable, which lead to unrealistic modulus values E_{rock}, and even non-null phase angle values. In Table 6-1, the expected displacement amplitude of 1cm length (gauge length of the short extensometers) of a rock phase with a standard 50GPa modulus was always under 0.05µm considering the measured axial effort and the cylinder diameter, whereas the precision of the extensometers was limited at 0.1µm. *In fine,* the rock could be considered rigid. The apparent axial modulus was *a* priori associated with the oedometric modulus of the bitumen, since no radial strain was imposed by the rock.

The apparent axial modulus of the film E^*_{film1} was further analysed in Figure 6-19, where its shift factors are displayed, alongside with its master curves of norm and phase angle, and its representation in complex planes (Cole-Cole plot and Black diagram). In addition to the experimental results, the WLF fitted equation and the 2S2P1D model of the shear complex modulus G* of the constituent bitumen B, obtained from campaign II (Figure 5-4 and Figure 5-5), is displayed. Although the TTSP seemed valid for the E^*_{film1}, the shift factor differed from the ones obtained for G*. This could be due to different shift factors between the shear modulus and the Poisson's ratio in the studied range of temperature and frequency. For much lower temperature (below 0°C), previous studies showed that the same shift factors for LVE behaviour of bitumen were shared between G^* and E^* (Delaporte 2007). The norm of apparent axial modulus of the film was much higher than the norm of complex shear modulus. The master curve of the ratio of the norms of these moduli $|E^*_{film1}|/|G^*_{ASR+DSR}|$ was built and is presented in Figure 6-20. The ratio varied between 250 at high equivalent frequencies and 32000 at low equivalent frequencies. This was due to the time and temperature dependency of the Poisson's ratio of the bitumen, who is known to become incompressible at high temperature. Based on the assumption that the bitumen phase was in oedometric conditions and that the Poisson's ratio was a real number (which assumed that the oedometric and the shear moduli shared the same phase angle), it was possible to estimate the value of the Poisson's ratio using Equation (6.26).

$$\upsilon = \frac{|G^*| - |E^*_{oedo}|}{|G^*| - 2|E^*_{oedo}|} \tag{6.26}$$

Based on this equation (6.26), the master curve of Poisson's ratio of the bitumen B was built in Figure 6-21. All values of υ were superior to 0.498, and the bitumen appeared to approach near-incompressibility (up to 0.49998) at high equivalent temperature. The number of significant figures for the Poisson's ratio was at least equal to the number of orders of magnitude separating the shear modulus and the oedometric modulus. For instance, with a 1/10000 ratio between the shear and oedometric moduli, a relative error of 100% on the oedometric modulus evaluation would only change the Poisson's ratio from 0.49997 to 0.49998. This level of precision is obviously impossible with other 3D characterisation techniques that compares axial and radial strains by direct measurements under a uniaxial load. Additionally, the thin film geometry with sufficient aspect ratio and rigid caps allowed obtaining oedometric conditions (as shown by the FE study in Section 6.5), without a conventional triaxial system with lateral confining pressure.

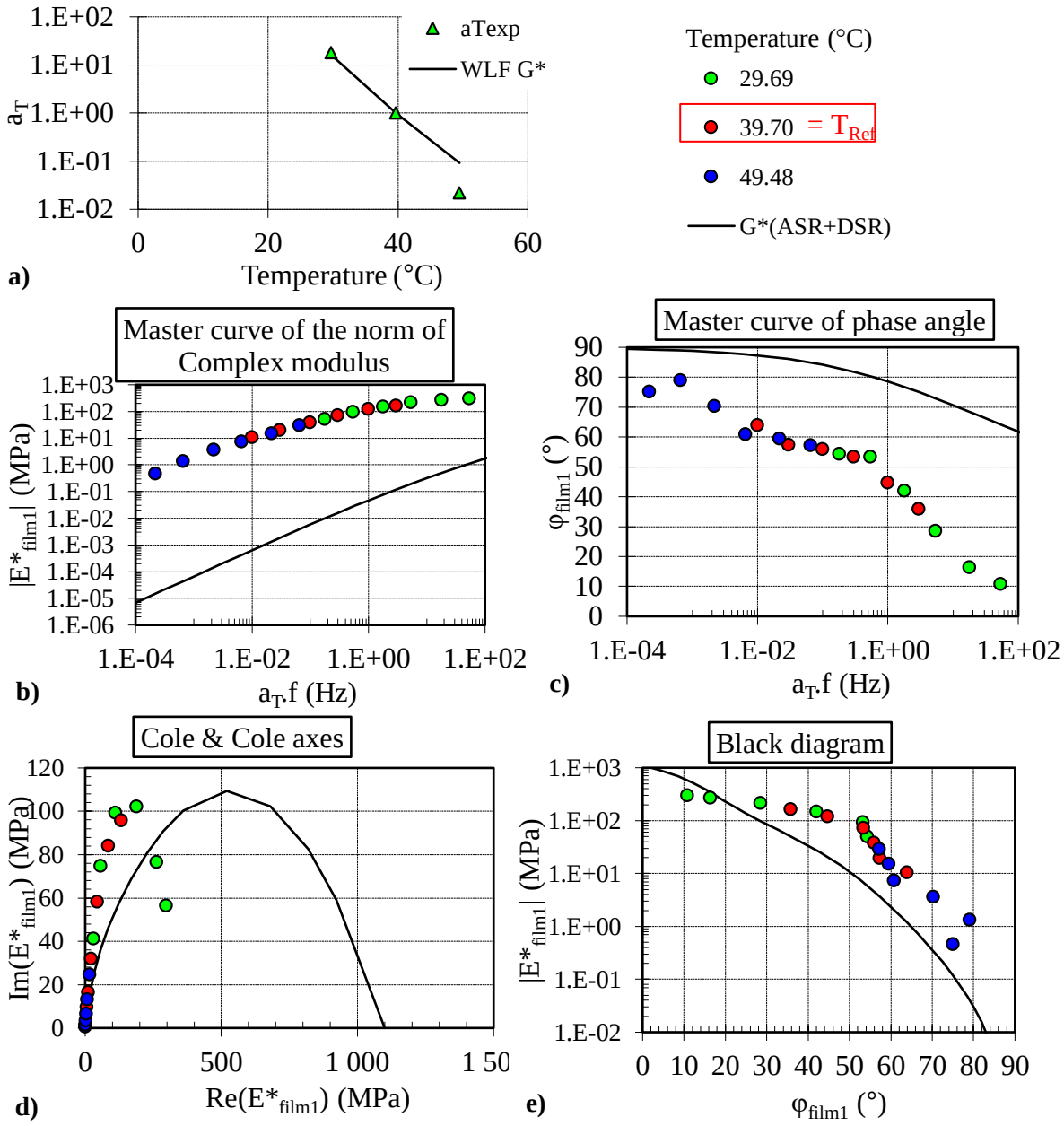

Figure 6-19 *Complex modulus test results of B_CO_300_SD_sp1, compared with 2S2P1D model of the shear complex modulus G* of bitumen B obtained by ASR + DSR in campaign II (see Table 5-1) : a) Shift factors, b)Master curve of norm of complex modulus, c) master curve of phase angle, d) Cole-Cole plot, e) Black diagram*

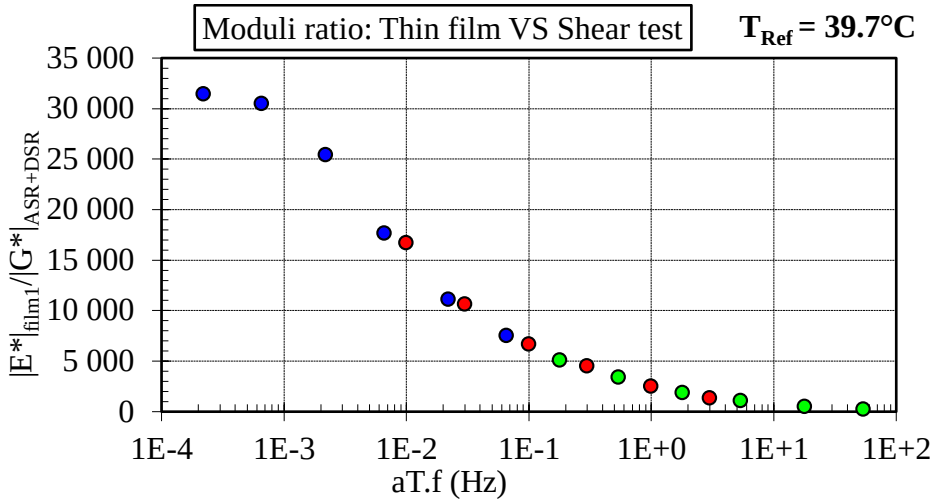

Figure 6-20 *Master curve of the ratio of the norm of thin film complex modulus of B_CO_300_SD_sp1 and shear complex modulus of the bitumen B modelled by 2S2P1D*

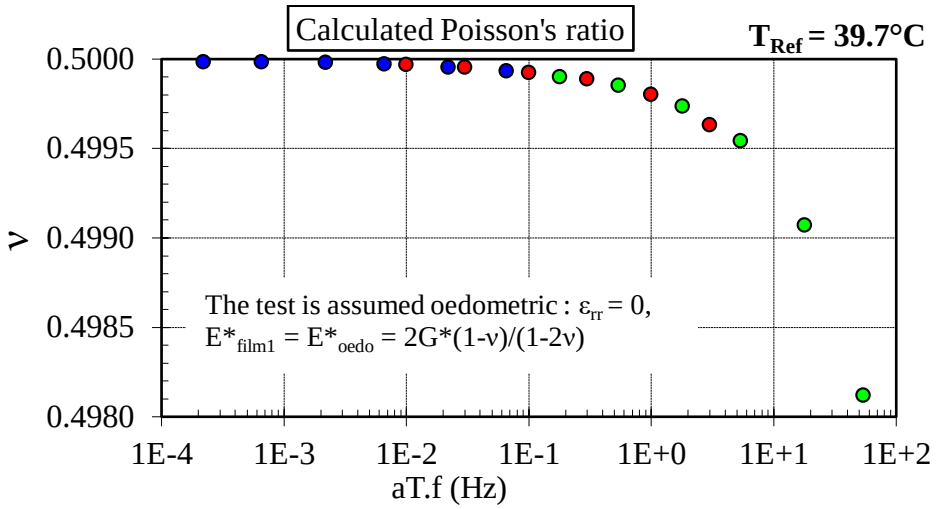

Figure 6-21 *Master curve of the Poisson's ratio of bitumen B*

This study of the LVE behaviour of a confined bitumen thin film between rock cylinders leads to the estimation of the complex oedometric modulus. When combined with complex shear modulus test results, it was proved to be very useful to calculate near-incompressibility Poisson's ratio of bitumen. However, the calculation of the average axial strains in the film with the two extensometers pairs was challenged by experimental difficulties. In particular, the fragility of the rock cylinders limited the stress range and therefore the possibility to test lower temperature. In the future, studies with large-diameter, metallic cylinders could yield to a wider range of apparent axial modulus. Moreover, the potential relative lateral displacement of the cylinders could be measured by non-contact sensors. Eventually, repetition should also be studied.

6.7 Pull-off test of bitumen thin film at constant strain rate

In this section, some exploratory pull-off tests on bitumen thin film specimens were performed.

6.7.1 Experimental plan

This exploratory study was limited to six specimens; the sample preparation procedure, discussed in Section 6.3, was indeed time consuming. Two specimens with large-diameter (LD) film (B_CO_300_LD_sp1 and B_CO_300_LD_sp2), and four specimens with small-diameter (SD) film (B_CO_300_SD_sp1, B_CO_300_SD_sp1, B_CO_300_SD_sp3 B_CO_100_SD_sp1) were tested. Three SD samples had a 300-thick bitumen film, and one had a 100µm-thick film. The pull-off tests were controlled at constant strain rate in the bitumen film, by imposing a displacement ramp on the average of the short extensometers. The targeted strain rate was 0.0028 s^{-1}. All tests were carried out at 30°C.

6.7.2 Results and analysis

For the four small-diameter film specimens, the displacement of the two pairs of short and long extensometers, as well as the recorded axial stress, were displayed as a function of time in Figure 6-22. The recorded stress was rigorously an apparent stress during the test: the ratio between the axial load and the surface area of the bitumen film. Unfortunately, the experimental results of the pull-off test of the large-diameter specimen could not be exploited, since the rock cylinders did not sustain the corresponding axial stresses. Indeed, the rock cylinders, cored in boulders, presented particularly fragile regions. Pictures of failure profiles are shown in Figure 6-23. From the axial stress curves and the failure profiles, the tensile strength (i.e. the peak value of the recorded stress) and the failure type are listed alongside with the tests conditions in Table 6-2 for all tested specimen. Two experimental flaws were reported:

- The specimen B_CO_100_SD_sp1 was tested at a strain rate of 0.00055 s^{-1}, five times less than expected, due to a command error.
- The specimen B_CO_300_SD_sp1 underwent an unrecorded compression during thermal conditioning before being submitted to tension

From a general perspective, the displacement curves obtained by the pairs of short and long extensometers showed that flexion could take place at the beginning of the pull-off tests. In Figure 6-22 b), the first extensometer pair (S1 and L1) of B_CO_300_SD_sp1 was in extension, whereas the second one (S2 and L2) was in contraction during the first 10 seconds of the tension test, way after the peak force in the sample (at 2s). The maximal displacement gap between the extensometers pairs increased up to 20µm. Afterwards, the gap diminished to a steady value of 4µm, while the effort on the sample decreased. This phase was attributed to a progressive failure of the sample, which released overall efforts and consequently reduced the discrepancies induced by flexion, to eventually almost recover the initial displacement gap. The other thin film samples of 300-µm thickness (Figure 6-22 c) and d)), which failed under significantly less maximal efforts, did not exhibit much flexion. For all four specimens, the effort decreased continuously as the film was further stretched. No abrupt failure was observed, as the stresses were relaxed by the viscous flow of the bitumen in strain-controlled mode.

a)

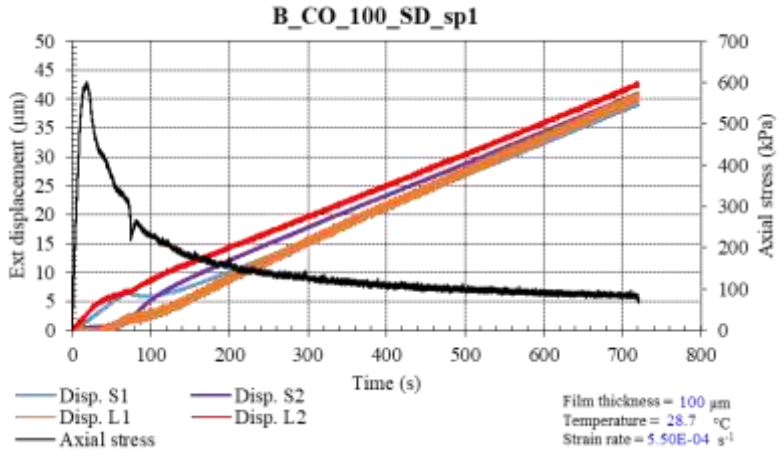

b)

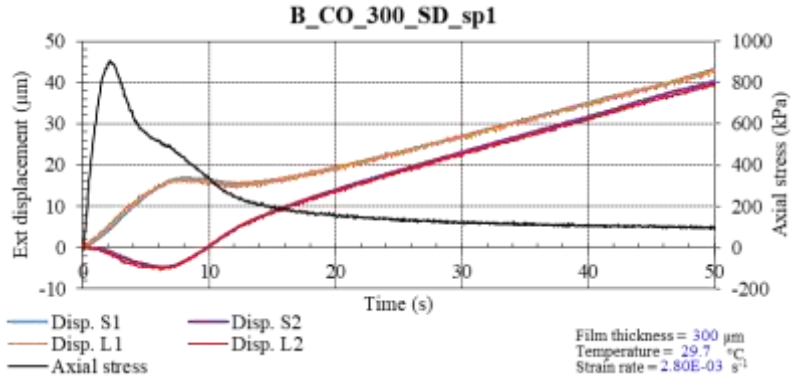

c)

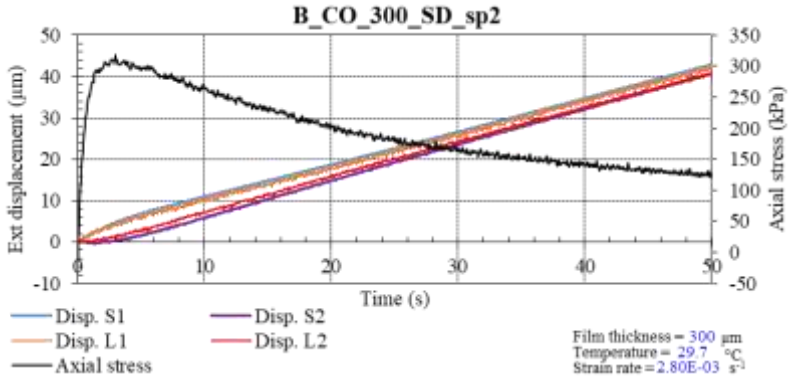

d)

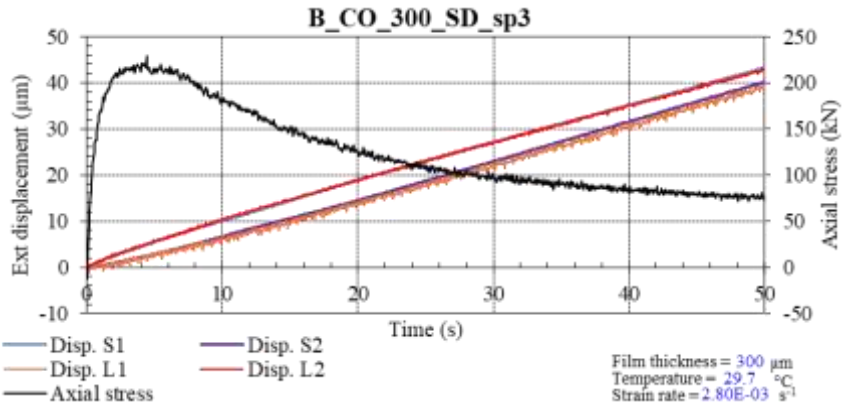

Figure 6-22 *Extensometers displacement and axial stress during tension tests for a)B_CO_100_SD_sp1, b) B_CO_300_SD_sp1, c) B_CO_300_SD_sp2, d) B_CO_300_SD_sp3*

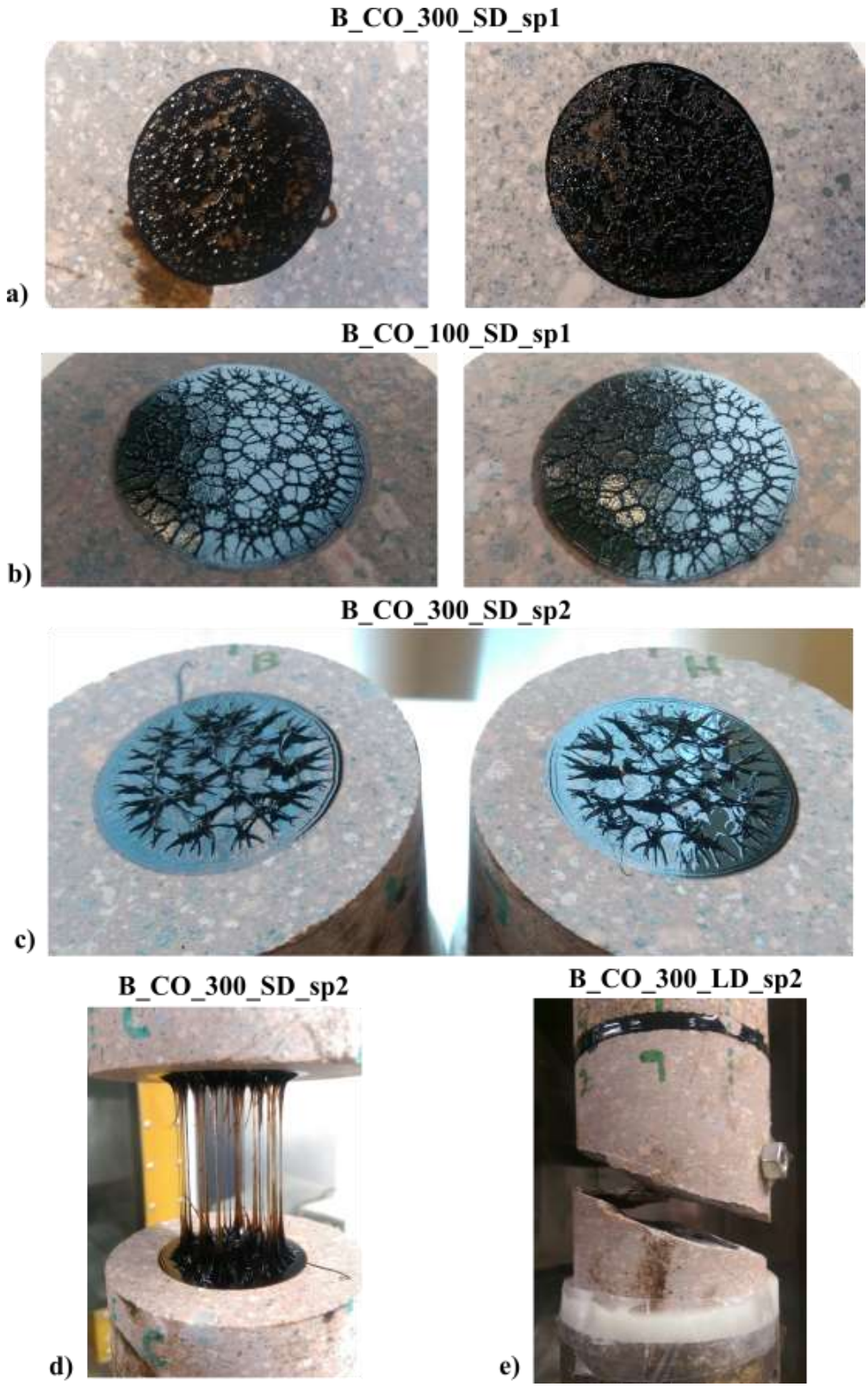

Figure 6-23 *Tension failure profile for a) B_CO_300_SD_sp1, b) B_CO_100_SD_sp1, c) B_CO_300_SD_sp2. d) Remnant of bitumen filaments at the end of the tension test on B_CO_300_SD_sp2. e) Tension failure of rock in large-diameter film geometry B_CO_300_LD_sp2*

Table 6-2 *Recap of tensile strength, failure type and tension test conditions*

Thin film specimen	Thickness (µm)	Temperature (°C)	Strain rate (s-1)	Tensile strength (kPa)	Failure type
B_CO_100_SD_sp1	100	28.7	5.50E-04*	603	Cohesive
B_CO_300_SD_sp1	300*	29.7	2.80E-03	906	Adhesive + cohesive
B_CO_300_SD_sp2	300	29.7	2.80E-03	319	Cohesive
B_CO_300_SD_sp3	300	29.7	2.80E-03	230	Cohesive
B_CO_300_LD_sp1	300	16.0	2.80E-03	-	in rock
B_CO_300_LD_sp2	300	30.0	2.80E-03	-	in rock

* Accidental compression before stripping, deformation not recorded
** five time less strain rate as expected (command error)

In term of failure type, two cases were observed. With B_CO_300_SD_sp2, B_CO_300_SD_sp3 and B_CO_100_SD_sp1, a purely cohesive failure was obtained (example of failure profile in Figure 6-23 b) and c)). For the sample B_CO_300_SD_sp1, which underwent accidental compression before the tension test, a mix of cohesive and adhesive failure was obtained. In the cohesive failure parts, the profiles presented the evidence of former cavitation and void growth. As the voids grew, the resisting bitumen between seemed to flow in "curtain" shape around the voids, as the bitumen pattern left in Figure 6-23 b) suggested. At this point, homogeneity of the film was lost. The further elongation of these bitumen curtain lead to the "filament" structure (Figure 6-23 d)), where all voids were connected. At this point, the resisting effort was too weak to be measured and the extensometers had already been removed, since they could not bear more than 1000µm opening. The size of the grown voids seemed related to the thickness (or potentially its aspect ratio) of the thin film.

Regarding tensile strength of SD samples in Table 6-2, B_CO_300_SD_sp2 and B_CO_300_SD_sp3 were comparable (329 and 230 kPa, cohesive failure). These values were rather small compared to cohesive strength values obtained with classical stress-controlled pull-off test at nearly the same temperature (Canestrari et al. 2010), of about an order of magnitude. The failure mechanism appeared very different, since the failure is always abrupt in monotonic stress-controlled tests, and the bitumen film does not evolve into the filament structure previously described in the previous paragraph. Additionally, for B_CO_300_SD_sp1, which experienced accidental compression before stripping, the tensile stress was much more important (906kPa), with a hybrid failure (adhesive + cohesive). This tensile strength was comparable to the classical values for hybrid failure (same order of magnitude), suggesting that the adhesive tensile strength did not depend on the loading mode.

Eventually, this short exploratory research demonstrated the potential to realise pull-off tests on thin films of the desired thickness with a precise strain-controlled mode and the means to evaluate potential flexion in the sample thanks to the extensometers pairs.

6.8 Conclusion of Campaign III

This third campaign focused on the development of a new interface test on a thin film of bitumen trapped between two rock cylinders. A system of two pairs of one short extensometer and one long extensometer was used to measure the average axial strains in both the rock and the bitumen phases.

The fabrication procedure of the sample has been presented. The thickness homogeneity was insured by precise spacers made with metallic foil strips.

An analytical solution for the strain and stress tensors in both the rock and the bitumen phases has been presented, in a homogeneous case that neglected the side effects at the periphery of the bitumen film. The axial strains in the film were due to two contributing factor: the oedometric compression of the bitumen and the radial strains imposed by the rock deformation.

In order to validate the analytical solution, a finite element simulation of the thin film test was made with COMSOL® software. The homogeneity hypothesis was confirmed for a realistic set of parameters for the rock and the bitumen. Furthermore, the system of short and long extensometers at the periphery of the rock cylinder was simulated, so that the apparent axial modulus could be calculated. A parametric study on the influence of the Young's modulus, the Poisson's ratio and the aspect ratio of the bitumen film was run to compare the simulated apparent modulus and the theoretical modulus predicted by the analytical solution. For aspect ratios under 1/250, the prediction was very satisfactory for a large range of modulus and Poisson's ratio.

The LVE characterisation of the thin film specimen was performed with complex modulus tests at relatively high temperatures (30°C to 50°C), because of the limitations on the tensile stress amplitude due to the fragility of the rock. The TTSP was validated for the apparent axial modulus of the thin film, although the shift factors appeared different from the ones obtained for the complex shear modulus test results (ASR and DSR from Campaign II). Since the apparent strains in the rock phase were negligible for the small-diameter thin film specimen (B_CO_300_SD_sp1), the bitumen phase was considered in purely oedometric conditions, and the apparent axial modulus was associated with the oedometric modulus of the bitumen B. The several orders of magnitude separating $|E^*_{oedo}|$ and $|G^*|$ indicated that the bitumen was almost incompressible, especially at low equivalent frequency. The associated Poisson's ratio values were comprised between 0.498 and 0.49998. Eventually, the thin film geometry proved its great potential to evaluate the bitumen behaviour in confined conditions, without a conventional triaxial test set-up with lateral confinement pressure. However, some experimental issues remained without clear explanation. Furthermore, the range of test conditions should be extended (temperature, strain or stress amplitude…), especially at lower temperature with metallic caps instead of rock cylinders for the LVE characterisation of the bitumen thin film. Repeatability should also be further studied.

Finally, few exploratory pull-off tests at constant strain rate (0.00028 s^{-1}) at 30°C were performed on thin film specimens. The large-diameter specimens failed in the rock phase due to local fragile regions in the rock cylinders. For some small-diameter specimens, flexion strains due to specimen misalignment with the press axis (one part of the film was in compression) at the beginning of the test was observed with the extensometer pairs. Two failure types were obtained: a purely cohesive failure, with relatively low maximal tensile strength and a hybrid adhesive + cohesive failure with tensile strength comparable to classical results with pull-off tests (stress controlled). Although this exploratory study clearly lacked specimen repetition due to the time-consuming sample preparation procedure, the thin film geometry proved to be a good way to develop precisely strain-controlled pull-off tests with parallel plates and monitor potential flexion strains during the tests, which are very rarely studied.

7 Campaign IV: Influence of aggregate surface treatment with silanes on mastic and mixture thermomechanical performances

7.1 Objectives

The fourth and final campaign of this thesis investigated the influence of aggregate surface treatment with silanes on the thermomechanical performances of bituminous mastics and bituminous mixtures. The overarching objective of this chapter was to elaborate a method to test the influence of bitumen-aggregate adhesion without modifying the constituent materials and the mix design parameters.

The strategy was therefore to modify only the surface of the aggregates at the molecular scale by coating silanes with specific properties. A new silanisation procedure was proposed to create silane-treated substrates. Two different silanes were selected: an adhesion promoter and an adhesion inhibitor, in order to exacerbate the role of modified bitumen-aggregate interface in mastic and mixture performances.

Then, a surface analysis campaign was run to study the effectiveness of the silanisation procedure with two approaches: the direct observation of the silane molecules at the substrate surface and the comparison of the physicochemical properties of the silane-treated and the control substrates.

Finally, the influence of the silane treatment of the aggregates surface on the thermomechanical performances of the bituminous mastics and mixtures was tested. For mastics, the LVE behaviour and the behaviour during Loading and Rest Periods (LRP) were studied. For mixtures, the LVE behaviour, the resistance to fatigue, the stiffness at 15°C/10Hz and the water sensitivity were studied.

7.2 Substrates with silane-treated surface and control substrates

The principle of silanisation, i.e. the coating of the surface of a substrate with silane molecules, was described in Section 2.4.5. This section focused on the description of the silanisation procedure and on the recap of the materials treated with anti-stripping and pro-stripping silane agents, as well as the control materials tested in Campaign IV.

7.2.1 New silanisation procedure

The procedure of silanisation of rock and glass substrates was based on a hydroalcoholic solution of 95% ethanol (≥99.99% purity, from Atlantic Labo©), 4.6% distilled water and 0.4% acetic acid (80% concentration from Atlantic Labo©). The ethanol served as solvent for the silanes used in this study (presented in Section 3.2.2). The water was necessary to activate the silanes and the substrate surface, i.e. creating the silanol groups that will eventually form as siloxane bond. The acetic acid was added as a catalyst for the silanisation reaction (DeMonredon-Senani 2004). Throughout this thesis, two slightly different procedures were proposed:

- Type 1: the procedure for samples that were tested to verify the effectiveness of the silanisation with surface analysis techniques, namely the X-ray Photoelectron Spectroscopy and the contact angle method (addressed in Section 7.3). The sample substrates were plunged into a beaker full of hydroalcoholic solution. The silanes were then added at the desired concentration. The reaction was enhanced by automated stirring during 1 hour at ambient temperature. Afterwards, the substrates were filtered and rinsed successively with water and ethanol, with three repetitions. Finally, the samples were dried at 70°C during 4 hours. The procedure is schematised in Figure 7-1.

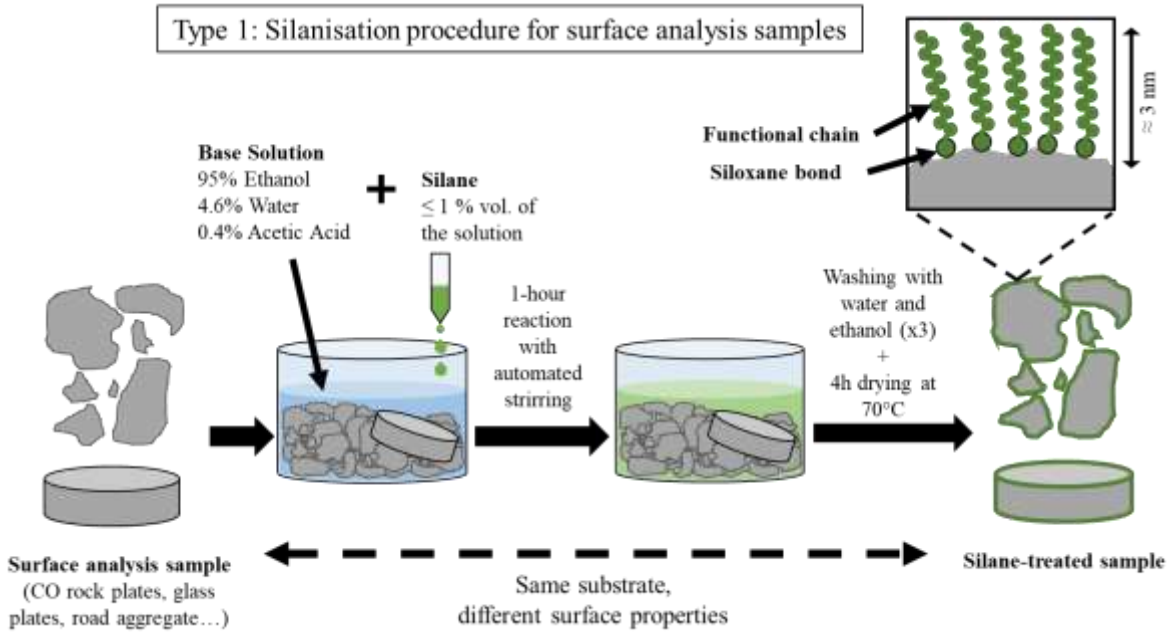

Figure 7-1 *Scheme of the silanisation procedure (type 1) for surface analysis samples*

- Type 2: the procedure for aggregates, filler and glass beads that were used to produce the bituminous mastics and mixtures further studied, respectively in Sections 7.4 and 7.5. This procedure differed from the previous "type 1", in the way that it was specifically designed to avoid filtering. This could have altered the grading curves of the separate aggregates fractions that were silanised in different trays. Indeed, the main objective of this campaign was to be able to compare the performances of mixtures with the very same composition but with different binder/aggregate affinity. In order to do so, the aggregates were immerged in trays of hydroalcoholic solution containing 0.2% of silane (as presented in Figure 7-2). During three hours, the aggregates were manually stirred from time to time. Then, the solution was evaporated by placing the trays on hot plates. After total evaporation, the aggregates were dried at 110°C during 24h, before being used for mixture (or mastic) fabrication. The procedure is schematised in Figure 7-3.

Figure 7-2 *Trays of CO aggregates and HL filler during the evaporation phase of the silanisation procedure*

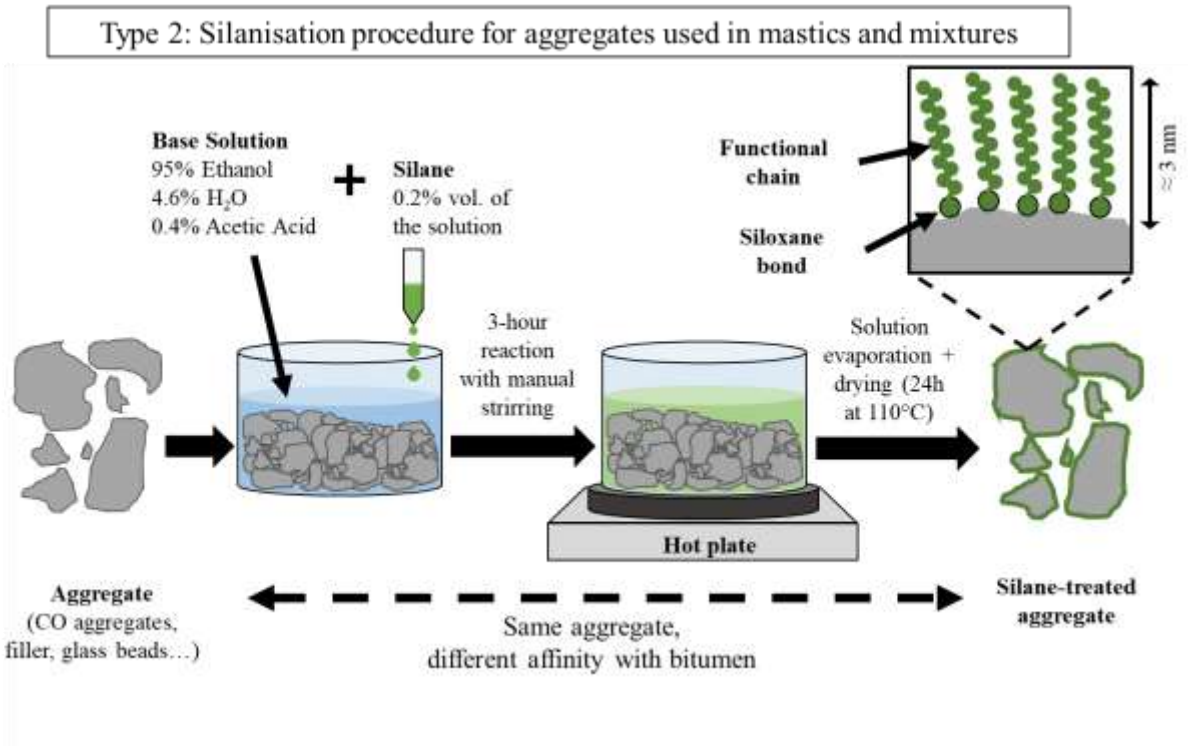

Figure 7-3 *Scheme of the silanisation procedure (type 2) for aggregates used in mastics and mixtures*

Regarding safety precaution for both types of silanisation procedure, it is recommended to always wear glasses, gloves and a mask. The silanes are reactive to water and can be harmful to any tissue (skin, eye, mouth, lungs...), and the acetic acid can also irritate. Moreover, the ethanol solution was inflammable, and should be kept away from any flame. Electric hot plates were preferred for the evaporation phase, that was performed either under extractor hood or outdoor.

7.2.2 Materials treated with anti-stripping and pro-stripping silane agents and control materials of Campaign IV

All silane-treated and control materials are listed in Table 7-1. The original substrates in this section are presented in Section Substrates3.2.3The Corbigny rock aggregates and plates were labelled “CO_Agg” and “CO_P”, and the glass beads and plates were noted “”G_Agg” and G_P”. The notation for anti-stripping (adhesion promoter) and pro-stripping (adhesion inhibitor) silane treatments was respectively “+” and “-“. The label for control substrates that underwent the silanisation procedure without silanes was “o”. Control substrates that did not went through the silanisation procedure did not have a supplementary label. Two categories of substrate were identified, corresponding to the two types of silanisation procedure presented in Section 7.2.1: The substrate samples used for surface analysis techniques in Section 7.3 and the aggregates used in bituminous materials that underwent thermomechanical tests in Sections 0 and 7.5. The associated notation for the surface analysis samples was “[X_Y%]”, with X the label of the silane and Y the percentage of the silane in the solution. Similarly, the notation for the aggregates used in bituminous materials were noted “(X)”, with X the label of the silane (always at 0.2% concentration).

Regarding only the surface analysis samples, two experimental sessions were performed, detailed in Section 7.3. The first session (completed in 2017) comprised XPS and contact angle method with substrate samples treated with different silane concentrations, whereas the second session (completed in 2018) focused on contact angle method with fixed silane concentrations. All the samples from each session are identified in Table 7-1.

Table 7-1 *Silane-treated and control materials used in Campaign IV*

			Corbigny microgranite rock (CO)		Glass (G)		Anti-stripping silane with carbon chain (+), [+]	Pro-stripping silane with fluorinated chain (-), [-]	Control substrate with silanisation procedure (o), [o]	Control substrate without silanisation procedure
			Aggregate (Agg)	Cored plate (P)	Silica beads, D=40-70µm (Agg)	Glass plate (P)				
Samples for surface analysis	1st session (2017)	XPS	CO_Agg[o]	X					X	X
			CO_Agg[+_1%]	X			1%			
			CO_Agg[-_0.2%]	X				0.2%		
			G_Agg		X					
			G_Agg[+_1%]		X		1%			
			G_Agg[-_0.2%]		X			0.2%		
		Contact angle method	CO_P	X					X	X
			CO_P[+_1%]	X			1%			
			CO_P[-_0.2%]	X				0.2%		
			G_P			X				
			G_P[o]			X			X	
			G_P[-_0.2%]			X		0.2%		
			G_P[-_2%]			X		2%		
	2nd session (2018)	Contact angle method	CO_P	X					X	X
			CO_P[o]	X					X	
			CO_P[+_0.2%]	X			0.2%			
			CO_P[-_0.2%]	X				0.2%		
			G_P[o]			X			X	
			G_P[+_0.2%]			X	0.2%			
			G_P[-_0.2%]			X		0.2%		
Bituminous materials with silane treated aggregates	Mixtures 5.8% B 91.2% CO 3% HL filler		B_CO_5.8 (Campaign I)	X						X
			B_CO(o)_5.8	X					X	
			B_CO(+)_5.8	X			0.2%			
			B_CO(-)_5.8	X				0.2%		
	Mastics 60% B 40% beads		B_40% (Campaign II)		X					X
			B_40%(+)		X		0.2%			
			B_40%(-)		X			0.2%		

7.3 Surface analysis and physicochemical properties of silane-treated substrates

This section focused on the characterisation of silane-treated substrates with two approaches:

- A surface analysis approach with the XPS, to study the atomic composition of the silane-treated and control substrates (both CO rock and glass) at a molecular scale (≤10 nanometres)
- A physicochemical approach with the contact angle method, to compare the substrates affinity with probe liquid (and potentially establish the surface energy components of substrates) and with hot bitumen

7.3.1 Surface analysis using X-ray Photoelectron Spectroscopy

The XPS principle, test set-up and sample preparation are described in Section 3.1.4.1. The studied substrates are listed in Table 7-1. It comprised three samples for each CO rock and glass aggregates: one with anti-stripping silane treatment (long carbon chain, promoter of adhesion with bitumen), one with pro-stripping silane treatment (short fluorinated chain, inhibitor of adhesion with bitumen), and one control sample. The XPS spectra of CO rock and glass aggregates were obtained with an Al X-ray source and are displayed in Figure 7-4 and Figure 7-5. In those diagrams, the intensity (i.e. the number of electron emitted per second) was represented as a function of the binding energy. Peaks of intensity were associated with atomic elements and their related electron subshell (Moulder et al. 1992). The relative concentration of elements was deduced from the surface areas between intensity peaks and the local background (BG) curves for a given spectrum. Since, the intensity scale is not relevant neither to compare peaks in one spectrum, nor to compare spectra, it has been modified for readability between samples.

Regarding CO aggregates (Figure 7-4), standard elements for mineral were identified (Si, O, C, C in carbonate form, Mg, Al…). The spectrum of the carbon chain treated aggregates CO_Agg[+_1%] did not exhibit much peak differences from the control sample CO_Agg[o] spectrum. On the other hand, the spectrum of the aggregatestreated with fluorinated chain silanes presented an important peak at 684eV, attributed to the presence of fluorine atoms (F1s). Since fluorine is particularly visible through XPS and completely absent for CO_Agg[o] and CO_Agg[+_1%], this peak was the evidence for a proper surface coating with silane. Moreover, the XPS requires extremely low pressure conditions (10^{-12} bar), which should cause the desorption of the least. The observed elements at the surface of the substrate were most likely strongly bonded (e.g. covalent bond).

Similarly, the glass beads (Figure 7-5) exhibited the expected elements (Si, O, Na, Mg), listed by the commercial provider. The relative size of the carbon peak C1s and the oxygen peak O1s was clearly different between the spectra of the control sample (G_Agg) and of the sample treated with carbon chain silanes (G_Agg[+_1%]), suggesting an effective silane coating. Moreover, the fluorine atoms were remarkably visible on the glass beads treated with fluorinated chain silanes G_Agg[-_0.2%]. An interesting phenomenon was observed near the carbon peak C1s; While G_Agg and G_Agg[+_1%] samples showed a single peak at 282 eV, characteristic of the C1s, the sample G_Agg[-_0.2%] with fluorinated chain showed a double peak, at 282 and 291 eV. The second peak at 291 is due to the binding energy shift in the electron subshell 1s caused by the covalent bond of the carbon atom to two fluorine atoms (“C-F2”), which was characteristic of the fluorinated chain silane (Figure 3-17 b)). This double peak was less obvious with the CO aggregates, since another peak due to mineral carbonates (CO3) was also present near 290 eV.

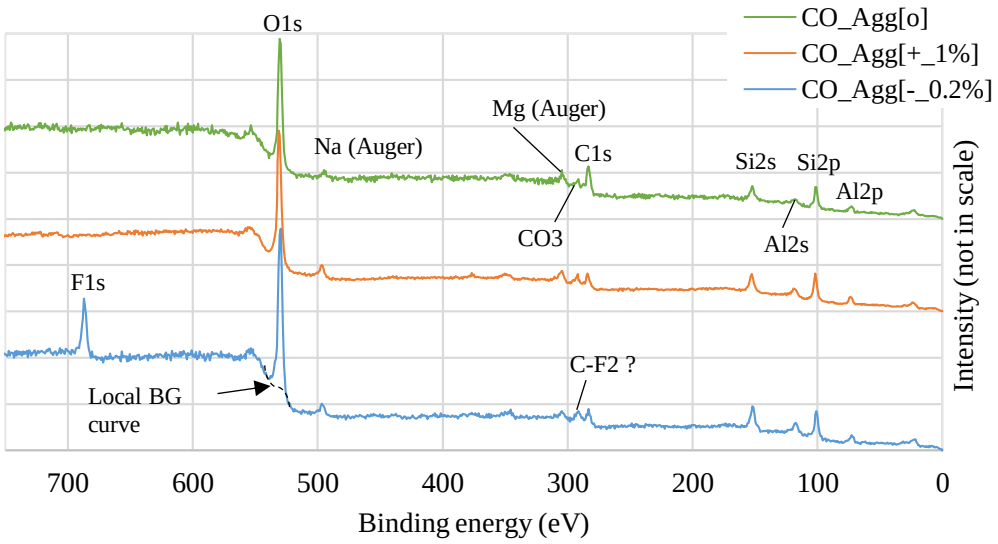

Figure 7-4 *XPS spectra of CO_Agg[o], CO_Agg[+_1%] and CO_Agg[-_0.2%]*

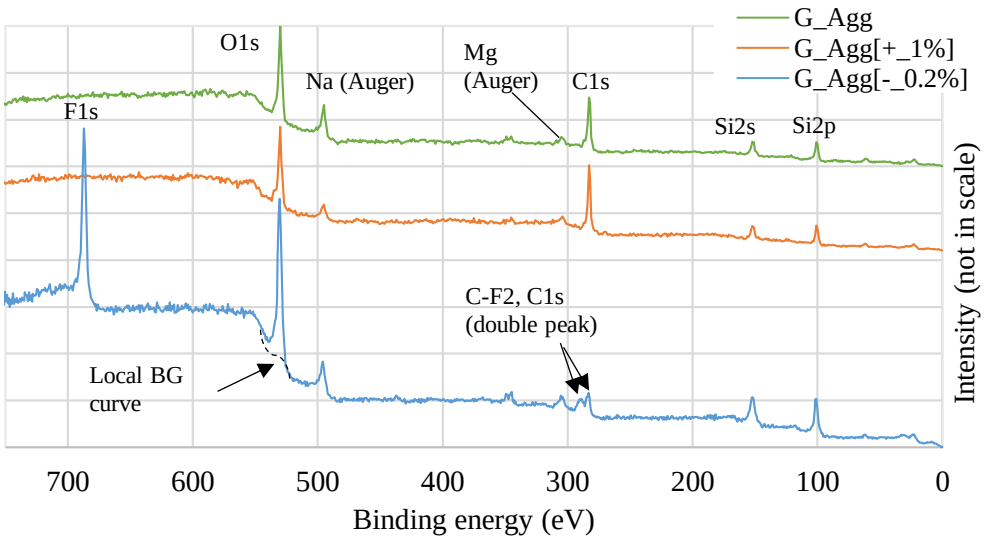

Figure 7-5 *XPS spectra of G_Agg[o], G_Agg[+_1%] and G_Agg[-_0.2%]*

It was possible to estimate the relative atomic concentration of the main elements by comparing the surface area of their related peaks (Moulder et al. 1992). This method allows obtaining average concentrations over 10-nm depth. The results are presented in Table 7-2, where the relative concentration of carbon, oxygen, fluorine and silicon were calculated. This confirmed the lack of discrepancies between CO_Agg[+_1%] and CO_Agg[o], the noticeable increase in carbon content between G_Agg[+_1%] and G_Agg (from 44 to 53%), and the clear presence of fluorine with both rock and glass aggregates treated with fluorinated silanes (13% and 29%). These results could not be extended to more samples or better quantitative analysis, because of the availability (and expensive cost) of the XPS device.

Table 7-2 *Relative concentration of the main elements at the surface of substrates (depth = 10nm)*

	Relative concentration calculated from peak intensity			
	C1s	O1s	F1s	Si2p
CO_Agg[o]	13%	72%	no peak	14%
CO_Agg[-_0.2%]	6%	66%	13%	15%
CO_Agg[+_1%]	14%	69%	no peak	16%
G_Agg	44%	41%	no peak	15%
G_Agg[-_0.2%]	20%	38%	29%	13%
G_Agg[+_1%]	53%	35%	no peak	13%

Overall, the surface analysis with XPS validated the silanisation procedure for the glass and the CO rock substrates, at least on a qualitative basis. The atomic concentration estimation could be a great control tool to improve the coating performances of silanisation procedure on a quantitative basis.

7.3.2 Characterisation of physicochemical properties using contact angle method

The contact angle method is described in Section 2.4.2.1.1. The tested substrates are listed in Table 7-1. The characterisation of physicochemical properties of silane-treated substrates involved two types of tests with contact angle method:

- The classical characterisation with sessile drop of different probe liquids
- The affinity with sessile drop of hot bitumen, only for CO rock plates

The tests with probe liquids were regrouped in two experimental sessions. During the first experimental sessions (completed in 2017), various concentrations of silane in hydroalcoholic solution was used and a sample repetition was made for the control rock plate CO_P. For all sample of the first session, five measurements of contact angle with water were performed at ambient temperature. During the second experimental session, the silane concentration for silanisation procedure was set to 0.2%, since it was the value retained for the fabrication of bituminous materials with silane-treated aggregates (studied in Sections 0 and 7.5). The contact angle study was extended to four probe liquids (water, ethylene glycol, glycerol and diiodomethane).

The contact angle tests of silane-treated and control substrates with hot bitumen was made with two pure (B ans S) and two polymer modified (Bm and Sm) bitumens, described in section 3.2.1. The wetting test temperature was imposed at 130°C, by a thermal chamber adapted to the goniometer (Figure 3-16).

7.3.2.1 Contact angle with probe liquids and surface tension components of substrates

The results of the first experimental session of contact angle tests with water sessile drop on silane-treated and control substrates are displayed in Figure 7-6.

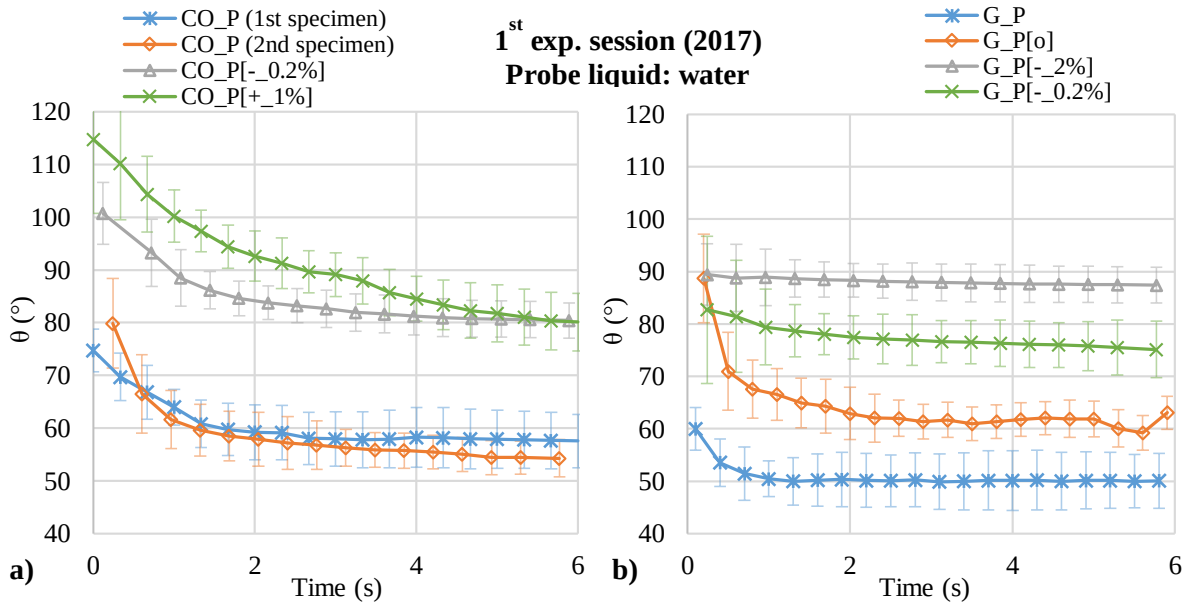

Figure 7-6 *Average and standard deviation of contact angle values of sessile drop of water on substrates as a function of time.(1st experimental session) a) Corbigny rock and b) glass*

For all cases of Figure 7-6, the contact angle values appeared stabilised after 5 seconds, and therefore comparable. The two control rock plates CO_P yielded the same results (≈55°). The silanised rock plates showed an increased hydrophobicity (+20°), just as expected from the non-polar silane molecules. Regarding the glass plates, the control sample G_P behaved differently from the control sample that underwent the silanisation procedure without silanes G_P[o]. The chemicals at the surface were modified by the silanisation solution (possible presence of ethanol itself). The silane surface treatment yielded also an increase in hydrophobicity for both anti-stripping and pro-stripping agents (respectively (+25° and +35°).

The results of the second experimental session of contact angle tests with four probe liquids are displayed in Table 7-3. Alongside with the average and the standard deviation of the contact angle values, the polar and dispersive parts of the surface energy of all tested substrates were calculate using the Owens-Wendt equation (2.108). γ_S^p and γ_S^d were obtained by minimizing the error with the four liquids by least squares. This equation considered that the vapour pressure π_e of the generalised Owens-Wendt model (2.111) was negligible for the study substrates, which was unusual for mineral aggregates (Bhasin 2006) with potentially high surface energies. This assumption was challenged in Section 7.3.2.2.

From Table 7-3, the control substrates yielded similar results as the first experimental session with water sessile drop. The trend of hydrophobicity increase of substrates with both anti-stripping and pro-stripping agents was again observed, although the contact angle values were not identical, especially for the glass plates, where the contact angle increase was limited. For example from G_P[o] to G_P[-_0.2%], an increase of +12° was obtained during the second experimental session, versus +25° in the first one. The discrepancies could be explained by repeatability of reproducibility issues (indeed, different glass and CO rock substrates lots, as well as different silane lots were used between the two experimental sessions. The measurements could also vary because of the various duration between the drying process and the contact angle tests with unmonitored sample conservation conditions.

Table 7-3 *Contact angle values with probe liquids and surface energy components of the substrates of the 2nd experimental session*

		2nd exp. Session (2018): 4 probe liquids										
		Contact angle θ (°)								**Surface free energy** Owens-Wendt theory (mJ/m²)		
		Water		Ethylene Glycol		Glycerol		Diiodomethane		γ_S	γ_S^p	γ_S^d
		Avg.	SD	Avg.	SD	Avg.	SD	Avg.	SD			
Glass	G_P[o]	49.6	2.5	36.1	1.7	57.4	2.4	50.4	1.0	46.5	20.6	25.8
	G_P[+_0.2%]	56.5	1.3	38.4	1.1	69.3	1.3	53.6	0.7	41.2	16.9	24.2
	G_P[-_0.2%]	61.2	3.0	49.2	1.0	77.5	1.6	56.5	0.9	36.3	14.7	21.5
CO Rock	CO_P	41.2	1.7	16.8	1.2	39.8	1.6	41.6	1.4	54.9	23.5	31.4
	CO_P[o]	40.9	2.4	-	-	36.1	1.8	41.5	2.1	58.9	23.4	35.5
	CO_P[+_0.2%]	47.8	2.0	25.4	1.8	-	-	38.6	0.7	53.7	19.3	34.4
	CO_P[-_0.2%]	68.9	1.9	38.3	1.1	-	-	54.0	1.5	41.0	10.5	30.5

Nevertheless, the surface energy components of the substrates, calculated with the four probe liquids during the 2nd experimental session, indicated a reduction of the polar part due to the presence of the silanes. The best illustration was given by the clear discrepancy between the polar components of the fluorinated silane-treated glass plate G_P[-_0.2%] and its associated control plates G_P[o] and G_P (10.5 vs. 23.5mJ/m²). It should be underlined that the absolute values of the surface energy components of mineral substrates were probably biased by the inability to properly measure the vapour pressure π_e, and should only be taken as qualitative indicators of change of surface properties due to silanisation.

7.3.2.2 Substrate affinity with bitumen sessile drop

The CO rock plates of the second experimental session were also used to characterise the effect of silane surface treatment of the wetting of hot bitumen drop at 130°C. All contact angle values of bitumen Bm (3 repetitions for each plate) are display in Figure 7-7. After 30 seconds, the contact angle seemed stabilised. Hence, the average contact angle value measured at 30s for each couple of bitumen and rock plates were compared in Figure 7-8. There was not sensible discrepancies due to bitumen type, or polymer modification, for a fixed substrate. However, the silane surface treatment appeared as a huge factor on the contact angle for fixed bitumen. Indeed, the control rock plates CO_P[o] had an average contact angle of 19°. The rock plates treated with anti-stripping silane (carbon chain) CO_P[+_0.2%] exhibited approximately the same value (21°), whereas the rock plates with pro-stripping silane (fluorinated chain) CO_P[-_0.2%] presented a much more repellent behaviour towards bitumen, materialised by a wetting angle of 70°. The silane modification appeared to have fundamentally altered the bitumen-aggregate interface. The lipophobic fluorinated molecules at the surface of the rock plates strongly modified the physicochemical properties of the substrate. The explanation for the absence of visible change of bitumen affinity between CO_P[o] and CO_P[+_0.2%] might be due to chemical pollution of the control sample that underwent the silanisation procedure (possible presence of ethanol), or simply the weak effect of the carbon-chain silanes on the overall behaviour.

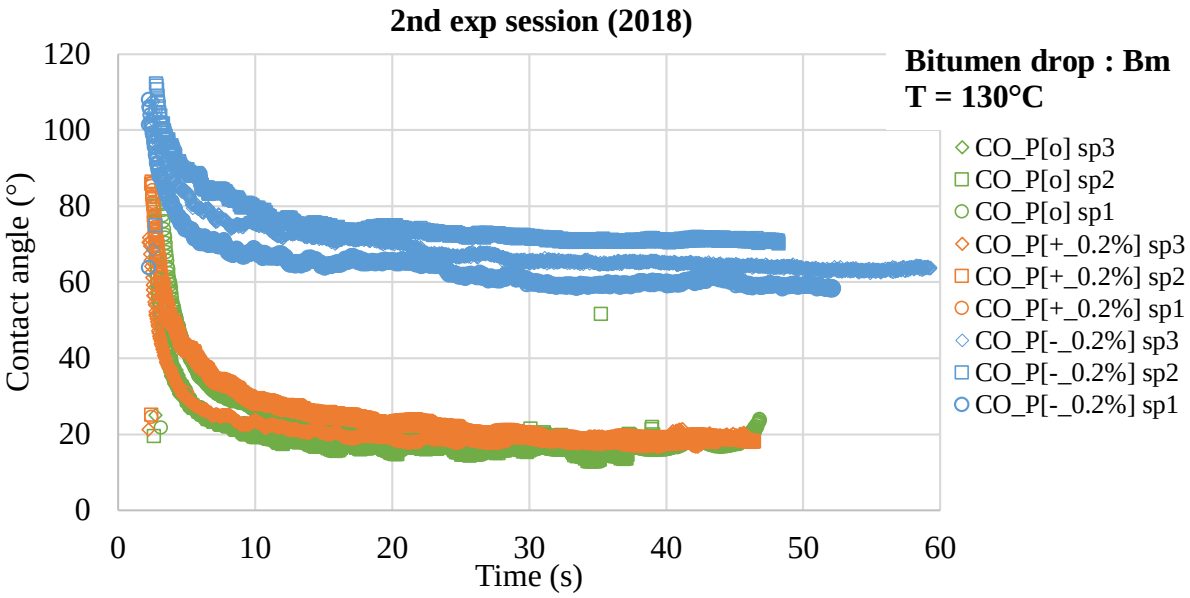

Figure 7-7 *Contact angle of hot drops of bitumen Bm with treated and control substrates*

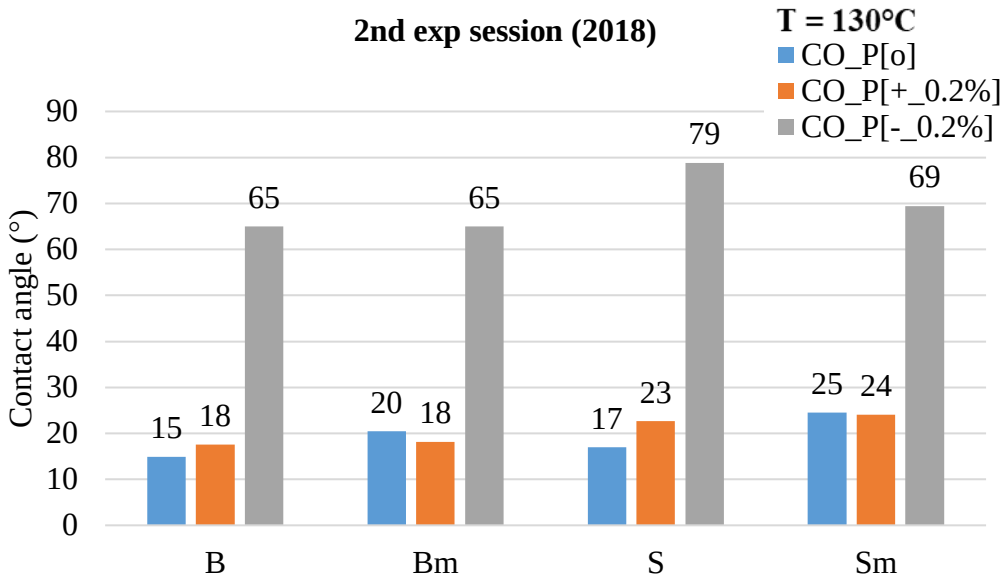

Figure 7-8 *Average contact angle of hot drops of bitumen with treated and control substrates (measured 30s after the drop deposit)*

The surface free energy components for the four bitumens B, Bm, S, Sm were provided by Eiffage© and are displayed in Table 7-4. Since the surface free energy components of the CO rock were known, the additional knowledge of the components for the bitumens allowed the use the Owens-Wendt model to predict the contact angle values and compare it with experimental results of Figure 7-8. This comparison is also displayed in Table 7-4. The Owens-Wendt theory predicted complete wetting of the bitumen on all the rock plates ($\cos\theta>1$), which was not was the experimental tests yielded at all. Only the discrepancies between the rock plate treated with fluorinated chain silanes CO_P[-_0.2%] and the others samples were correlated from the prediction to the experimental results. The fact that theoretical prediction was very poor could be explained by the neglected biasing effect of the equilibrium pressure π_e, which might be predominant as the CO rock could be a high surface energy substrate. The acquisition of π_e required at least a Universal Sorption Device (described in Section 2.4.2.1.3), that was not available during this thesis. Secondly, the surface free energy components of the rock plates were acquired at ambient temperature, which differed from the high temperature set for the contact angle tests with hot bitumens. Overall, the contact angle method appeared to be a remarkable tool to verify the change of physicochemical properties of substrates treated with silanes, although the quantitative and predictive approach based on work of adhesion theory that was supposed to measure the affinity with bitumen completely lacked precision to be relevant.

Table 7-4 *Surface free energy values and comparison between predicted and measured contact angle of bitumens*

	Surface free energy (mJ/m²)			Owens-Wendt prediction $2\frac{\sqrt{\gamma_S^p\gamma_L^p}+\sqrt{\gamma_S^d\gamma_L^d}}{\gamma_L}-1=\cos\theta$			Experimental value at 130°C cos(θ)		
Bitumen	γ_L^p	γ_L^d	γ_L	CO_P[o]	CO_P[+_0.2%]	CO_P[-_0.2%]	CO_P[o]	CO_P[+_0.2%]	CO_P[-_0.2%]
B	7.3	22.1	29.5	1.78	1.68	1.36	0.97	0.95	0.42
Bm	9.8	18.0	27.8	1.89	1.78	1.42	0.94	0.95	0.42
S	8.5	18.7	27.3	1.91	1.80	1.45	0.96	0.92	0.19
Sm	11.2	15.9	27.1	1.94	1.81	1.43	0.91	0.91	0.35

7.4 Thermomechanical behaviours of mastics with silane-treated glass beads

This section focused on the comparison of thermomechanical behaviour between mastics with glass beads treated with silanes and a control mastic. Two types of thermomechanical behaviours were studied:

- linear viscoelastic (LVE) behaviour
- behaviour during Load and Rest Periods (LRP)

All tests were performed on the ASR (description in Section 3.1.1.2).The three tested mastics are listed in Table 7-1. They were composed of 60% bitumen B and 40% of glass beads in volume (description in section 3.2.4). The mastic with anti-stripping silane treatment was noted “B_40%(+)”. The mastic with pro-stripping silane treatment was noted “B_40%(-)”. Finally, the control mastic was labelled “B_40%”

7.4.1 LVE behaviour

The LVE characterisation of mastics consisted in complex shear modulus tests, performed in Campaign II, and fully described in Section 5.2.1 (schematised in Figure 5-1).

The detailed results of complex modulus test on mastics are available in Appendix 1.1.2. The experimental results of the control mastic B_40% were presented in Section 5.2.2.2, also as part of Campaign II. From a more general perspective, all mastics respected the TTSP; the experimental shift factors a_T and their associated WLF models are displayed as functions of temperatures in Figure 7-9. The master curves of norm of shear complex modulus and phase angle are presented respectively in Figure 7-10 a) and b). Additionally, the normalised complex shear moduli G^*_{norm} in Black diagram and Cole-Cole plane were plotted in Figure 7-13Figure 7-11 a) and b). In both Figures Figure 7-10 and Figure 7-11, the 2S2P1D models of all mastics were added to experimental data. The 2S2P1D constants of the mastics and their constituent bitumen are listed in Table 7-5, alongside with the WLF parameters.

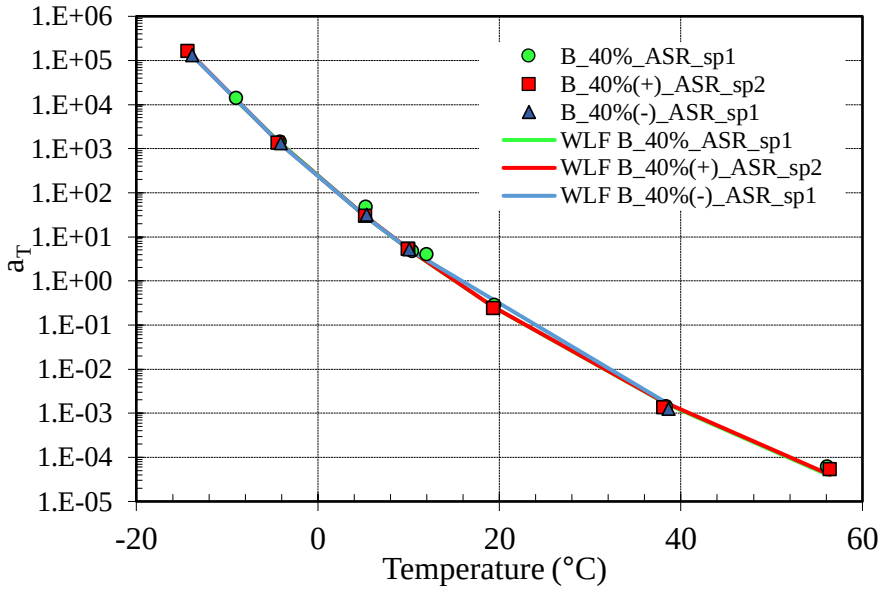

Figure 7-9 *Experimental and modelled shift factors of mastic with silane-treated glass beads (B_40%(+)_ASR_sp2 and B_40%(-)_ASR_sp1) and control mastic (B_40%_ASR_sp1), as a function of temperature*

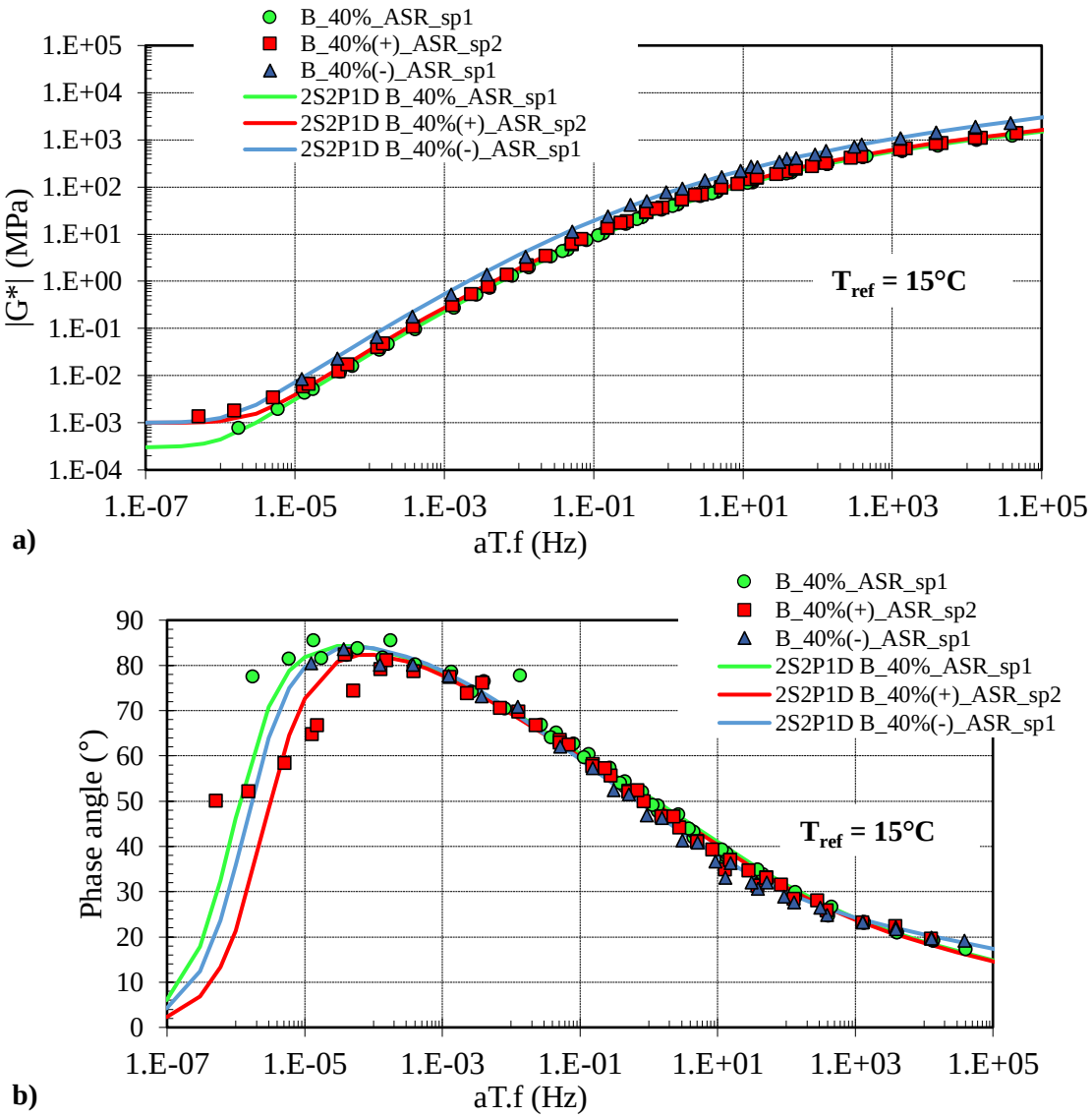

Figure 7-10 *Master curves of complex shear modulus of mastic with silane-treated glass beads (B_40%(+)_ASR_sp2 and B_40%(-)_ASR_sp1) and control mastic (B_40%_ASR_sp1): a) norm of complex modulus, b) phase angle. 2D2P1D models were added for each mastic.*

All mastics shared the same shift factors and the same WLF parameters consequently. The surface treatment of glass beads with silanes did not seem to alter the temperature dependence of the complex shear modulus of mastics. Moreover, the master curves of B_40%(+)_ASR_sp2 (with anti-stripping silane) and B_40%_ASR_sp1 (control) were almost identical, expect a mild divergence at the highest temperature (≈57°C). It should be noted that at such temperature, the limits of resolution of the ASR are challenged, since the load cell signal amplitude was close to the noise amplitude. The mastic with glass beads treated with pro-stripping silane B_40%(-)_ASR_sp1 appeared consistently stiffer than the other mastics at intermediate and high equivalent frequencies, where the ASR precision is unequivocal. The modulus value was approximately twice the values of the others mastics B_40%(+)_ASR_sp2 and B_40%_ASR_sp1. It was suspected that an issue on glass bead concentration had happened during the corresponding mastic fabrication. Indeed, B_40%(-)_ASR_sp1 behaved like a control mastic with higher filler particle concentration, with only a different asymptotic moduli. The sole modification of the bitumen-beads interface by pro-stripping silane to explain these moduli discrepancies were not deemed rational, because it targeted the binder-aggregate adhesion and not the binder compliance. Moreover, both pro-stripping and anti-stripping silane had very limited influence on the modulus of the mixtures with treated aggregates (addressed in Section 7.5).

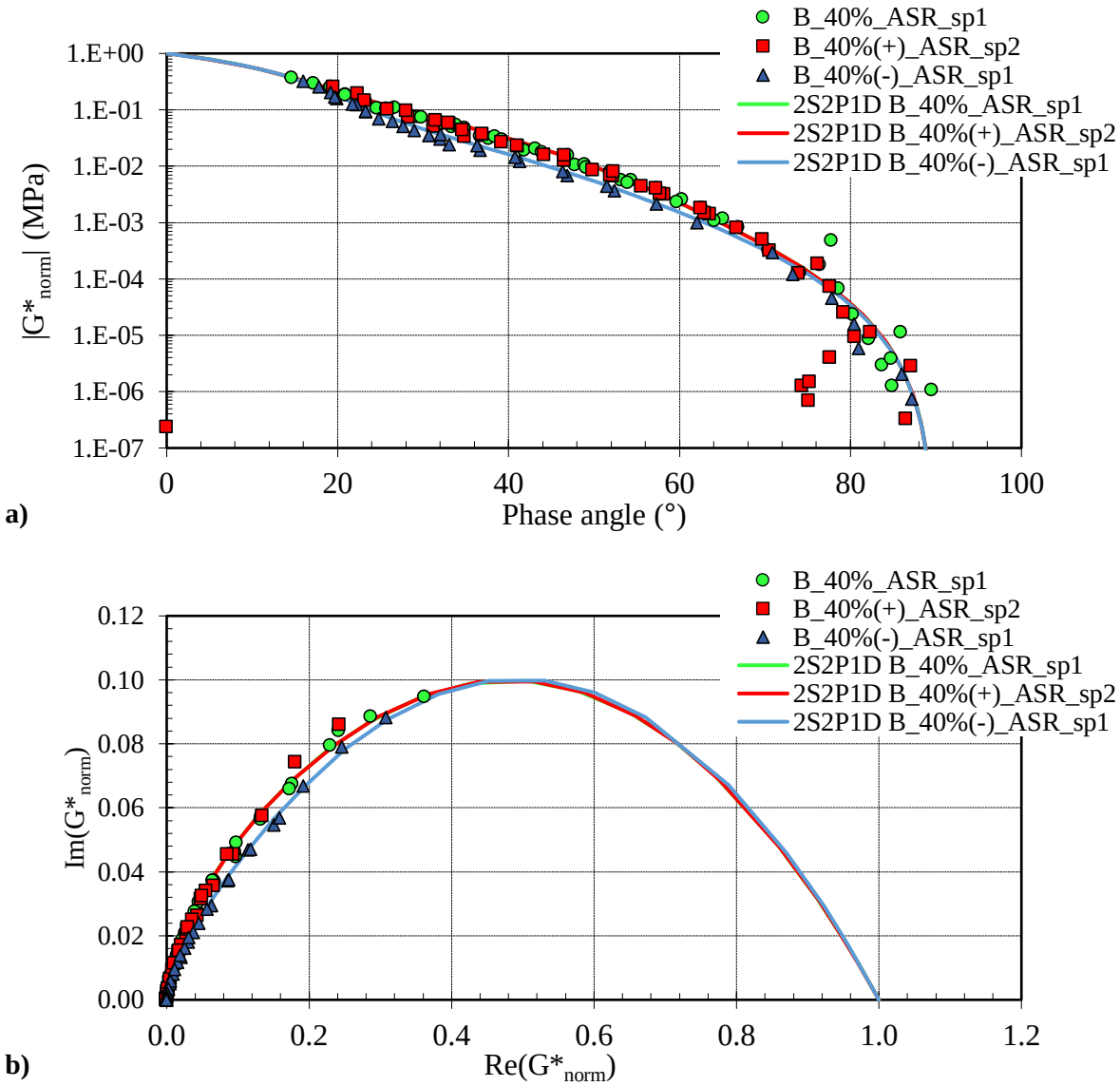

Figure 7-11 *Normalised complex shear modulus of mastics with silane-treated glass beads (B_40%(+)_ASR_sp2 and B_40%(-)_ASR_sp1) and control mastic (B_40%_ASR_sp1): a) in Black diagram, b) in Cole-Cole plot. 2D2P1D models were added for each mastic.*

Table 7-5 *2S2P1D constants and WLF parameters of mastics with silane-treated glass beads (B_40%(+)_ASR_sp2 and B_40%(-)_ASR_sp1), control mastic (B_40%_ASR_sp1) and constituent bitumen (B)*

	2S2P1D constants							WLF parameters		
	G_{00} (MPa)	G_0 (MPa)	k -	h -	δ -	τ_0 (s)	β -	T_{ref} (°C)	C_1 -	C_2 (°C)
B_ASR_sp5+DSR	0	1020	0.25	0.62	5.0	8.08E-05	100	15	18.6	133.3
B_40%_ASR_sp1	0.0003	4000	0.25	0.62	5.0	1.31E-04	100	15	18.6	133.3
B_40%(+)_ASR_sp2	0.001	4200	0.25	0.62	5.0	1.54E-04	100	15	18.6	133.3
B_40%(-)_ASR_sp1*	0.001	11300	0.25	0.62	8.0	1.06E-04	100	15	18.6	133.3

* The real % of glass beads was uncertain

Regarding 2S2P1D models, the mastics B_40%(+)_ASR_sp2 and B_40%_ASR_sp1 shared 4 constants with their constituent bitumen B (*k, h, δ, β*). Their glassy modulus G_0 were also very close (4200 and 4000 MPa). The mastic with glass beads treated with pro-stripping silane also shared only 3 constants (*k, h, β*) with other mastics. The probable overconcentration of glass beads in B_40%(-)_ASR_sp1 provided a G_0 of 11.3 GPa, almost three times the glassy moduli of the other mastics. A sensible influence of pro-stripping silane on the LVE behaviour did not appear plausible with regards of the shared 2S2P1D constants, inherited from the bitumen.

Overall, this study strengthened the idea that the effect of bitumen-beads interface modification with the silanisation had little if no effect on the LVE behaviour of mastics, which derived from the LVE behaviour of the constituent bitumen and the mix design parameters (e.g. glass bead concentration)

7.4.2 Behaviour during LRP

The Load and Rest Period test was already performed on binders with ASR in Campaign II, and fully described in Section 5.3.1 (schematised in Figure 5-11). The high and low loading amplitudes (noted HA and LA) for mastics with silane-treated beads and the control mastic are listed in Table 7-6.

All detailed LRP test results on mastics are available in Appendix 1.5, and the results of the control mastic B_40% were thoroughly presented in Section 5.3.2. The very same analysis process as in Campaign II was implemented to evaluate the role of the silane treatment of glass bead on the behaviour during LRP; the effects of temperature variations due to energy dissipation during loading periods, as well as the nonlinearity effects on the equivalent modulus were corrected according to Equation (5.9). The equivalent modulus corrected from temperature and nonlinearity effects $G^*_{T,NL\text{-}corrected}$ of all mastics at low loading amplitude are displayed in Figure 7-12. The norm of normalised equivalent modulus corrected from temperature and nonlinearity effects, noted $|G^*_{T,NL\text{-}corrected}|/G_{ini}$ was plotted against the cumulated number of loading cycles in Figure 7-13.

Table 7-6 *Loading shear strain amplitudes of LRP tests on mastic with silane-treated glass beads (B_40%(+) and B_40%(-)) and on control mastic B_40%*

		dissipated energy per cycle (KJ/m3)	
		8	3.8
Mastic	Specimen	Associated γ_0 (µm/m)	
B_40%	B_40%_ASR_sp5	4350	
	B_40%_ASR_sp6		3000
B_40%(+)	B_40%(+)_ASR_sp1	4300	
	B_40%(-)_ASR_sp3		2970
B_40%(-)	B_40%_ASR_sp3*****	3000	
	B_40%_ASR_sp4*****		2000

*** The real % of glass beads was uncertain**

In Figure 7-12, the mastic with glass beads treated with pro-stripping silane B_40%(-)_ASR_sp4 presented a particularly high initial modulus, twice the value of the moduli of the other mastics B_40%(+)_ASR_sp3 and B_40%_ASR_sp5. This echoed the observations made during for the LVE behaviour characterisation in Section 7.4.1; the glass bead concentration in specimens of mastic B_40%(-) was probably higher than 40% due to an error during mastic fabrication, leading to higher stiffness. As the loading amplitudes of each specimen were calculated to correspond to a common initial dissipated energy per cycle (3.8kJ/m^3 for LA, 8kJ/m^3 for HA), the loading amplitudes applied to B_40%(-) specimens were sensibly lower. The relevance of comparing this mastic to the others in order to study the sole influence of the bitumen-beads adhesion when it was undermined by pro-stripping silane appeared limited. However, the mastic with glass beads treated with anti-stripping silane was legitimately comparable to the control mastic.

From a general perspective on the evolution of $G^*_{T,NL\text{-}corrected}$ of mastics during loading periods, dramatic decrease of norm of modulus and increase of phase angle were observed during the first 10000th cycles. Afterward, the phase angle appeared stable, whereas the norm of modulus continued to decrease. These two distinct phases corresponded very well to what was obtained for bitumens in Campaign II (Section 5.3.2), and were attributed respectively to thixotropic breakdown and damage (microcracks). During rest periods, a continuous recovery of phase angle and norm of modulus was observed, This observation differed from the LRP results of bitumens, where two distinct recovery phase were distinguished: a first rapid recovery of norm of modulus and phase angle decrease, followed by a slow recovery of norm of modulus at constant phase angle. These two stages were attributed respectively to thixotropic build up and healing. In the case of mastics, it seemed that the two stages were cofounded. Indeed, in a composite material such as the glass beads mastics, the location of microcracks whether in the bitumen phase (matrix) or in the glass beads (inclusions), and possibly at the interface bitumen-bead interface, influences the norm and phase angle of the equivalent modulus of the mastic (homogenised at the macroscopic scale).

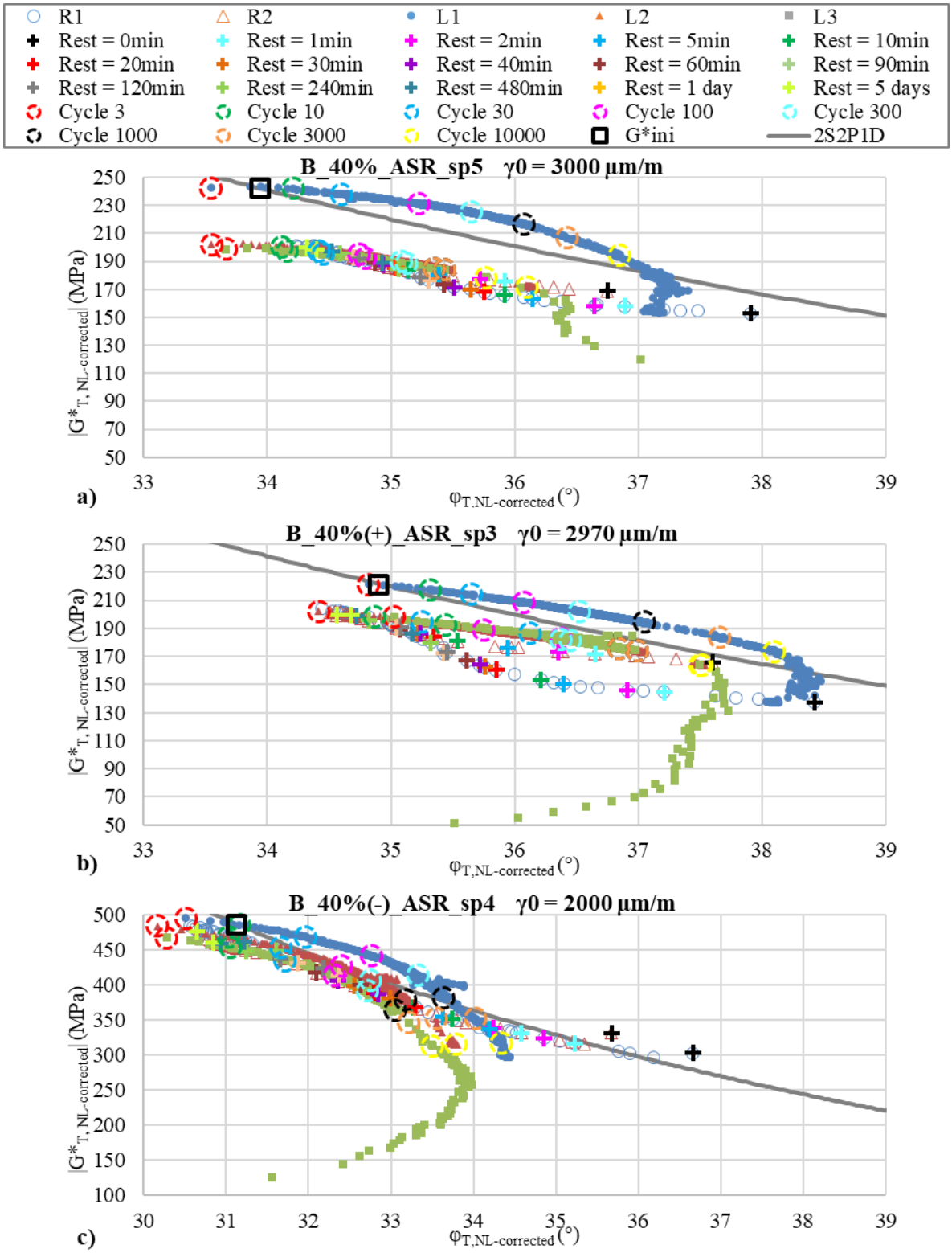

Figure 7-12 *Black diagram of equivalent shear modulus corrected from temperature and nonlinearity effects during LRP test at low loading amplitude for: a) control mastic B_40%, b) mastic with glass beads treated with anti-stripping silane B_40(+), c) mastic with glass beads treated with pro-stripping silane B_40%(-). Initial moduli G*$_{ini}$ and 2S2P1D models were added for each mastic.*

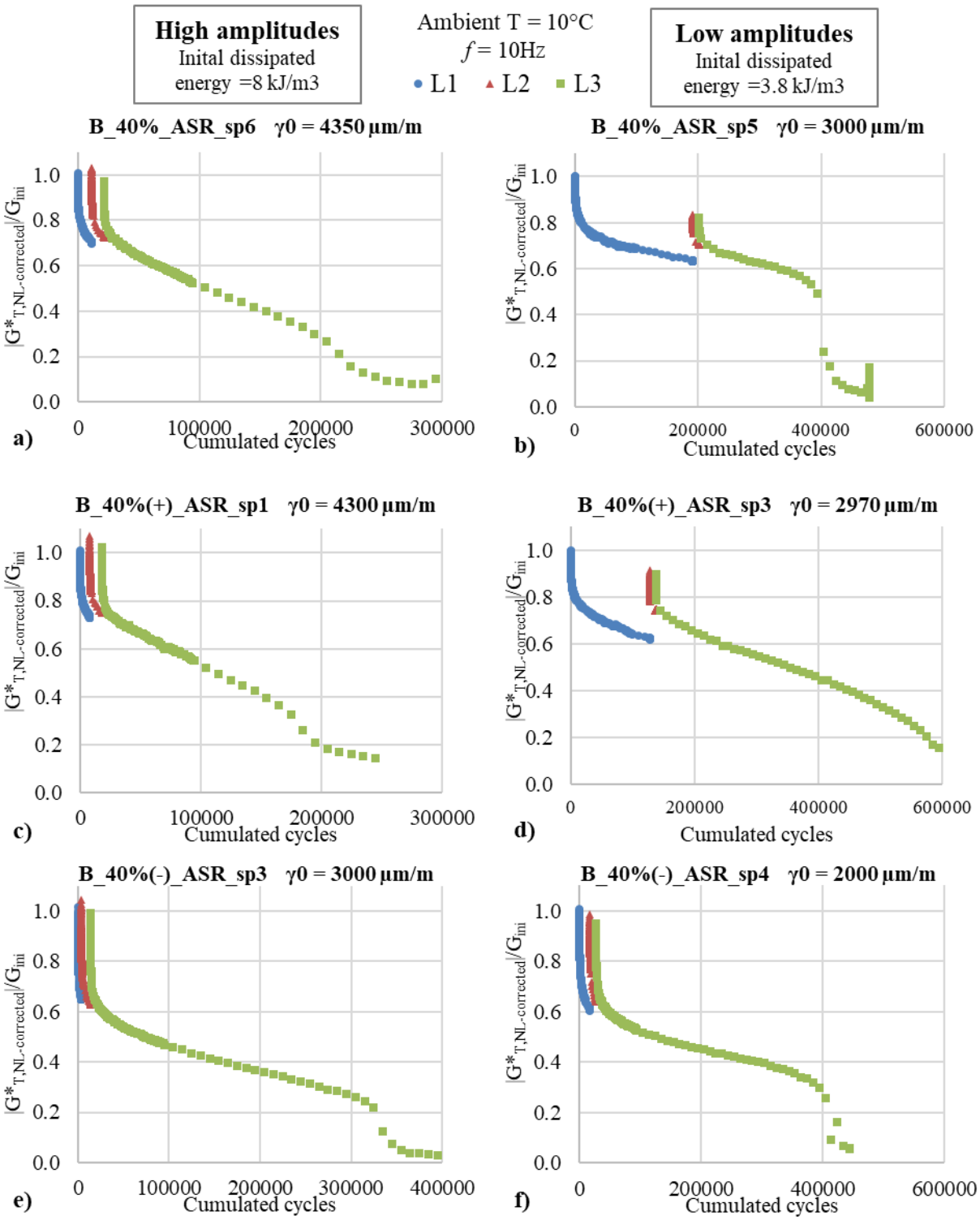

Figure 7-13 *Normalised norm of equivalent complex shear modulus corrected from temperature and nonlinearity effects as a function of cumulated cycles: a) B_40%_ASR_sp6, HA (4350µm/m), b) B_40%_ASR_sp5, LA (3000µm/m), c) B_40%(+)_ASR_sp1, HA (4300µm/m), d) B_40%(+)_ASR_sp3, LA (2970µm/m), e) B_40%(-)_ASR_sp3, HA (3000µm/m), f) B_40%(-)_ASR_sp4, LA (2000µm/m)*

The normalised equivalent modulus corrected from temperature and nonlinearity effects as a function of the cumulated loading cycles (Figure 7-13) allowed to evaluate the recovery capacity and the damage rate of mastics. At high loading amplitude (HA), the modulus loss during the first loadings L1 and L2 was completely recovered during the respective rest periods R1 and R2. This was the case for all studied mastics B_40%_ASR_sp6, B_40%(+)_ASR_sp1 and B_40%(-)_ASR_sp3, where the effects of reversible phenomena were predominant. At low loading amplitude (LA), however, the first loading L1 was clearly different from the following loadings, and the initial moduli of B_40%_ASR_sp5 (Figure 7-13 d)) and B_40%(+)_ASR_sp3 (Figure 7-13 f)) were not completely recovered after R1 (only up to 90 and 85%). Moreover, a damage phase at constant rate was observed during L1 for those two mastics. For the mastic with glass bead treated with pro-stripping silane, at low loading amplitude (B_40%(-)_ASR_sp4, Figure 7-13 f)), the reversible phenomena appeared still predominant.

Overall, the glass bead treatment with anti-stripping silane did not seem to have a sensible effect on the behaviour during LRP tests. Unfortunately, the influence of the surface treatment with pro-stripping silane could not be tested due to probable wrong glass bead concentration in the corresponding mastic. The role of bitumen-aggregate adhesion should be first studied in shorter, simpler thermomechanical tests than LRP test.

7.5 Thermomechanical performances of mixtures with silane-treated aggregates

This section investigated the thermomechanical performances between bituminous mixtures with silane-treated aggregates and control mixtures. The thermomechanical performances of bituminous mixtures were sorted into two sub-sections:

- LVE behaviour
- Resistance to fatigue, stiffness at 15°C/10Hz and water sensitivity

The bituminous mixtures with silane-treated aggregates and the control mixtures are listed in Table 7-1. All mixtures shared the same bitumen (B), the same binder content (5.8%), the same grading curve (CO, Figure 3-23). The mixtures with aggregates treated with anti-stripping silane were noted B_CO(+)_5.8. Similarly, the mixtures with aggregates treated with pro-stripping silane were noted B_CO(-)_5.8. The control mixture with aggregates that underwent the silanisation procedure without silanes was labelled B_CO(o)_5.8, whereas the control mixture with original CO aggregates was labelled B_CO_5.8.

7.5.1 LVE behaviour

The characterisation of the LVE behaviour of the bituminous mixtures consisted of uniaxial complex modulus tests. The set-up of the tension-compression (TC) test on cylindrical specimen is described in Section 3.1.2.2. The complex modulus test consisted of frequency sweep tests (0.01, 0.03, 0.1, 0.3, 1, 3 and 10 Hz) conducted at different temperatures (-25, -15, -5, 5, 15, 25, and 35°C), schematised in Figure 7-14. The loading amplitude was imposed at 50µm/m, which was below the commonly accepted LVE limit of 100µm/m for mixtures (G. D. Airey, Rahimzadeh, and Collop 2003).

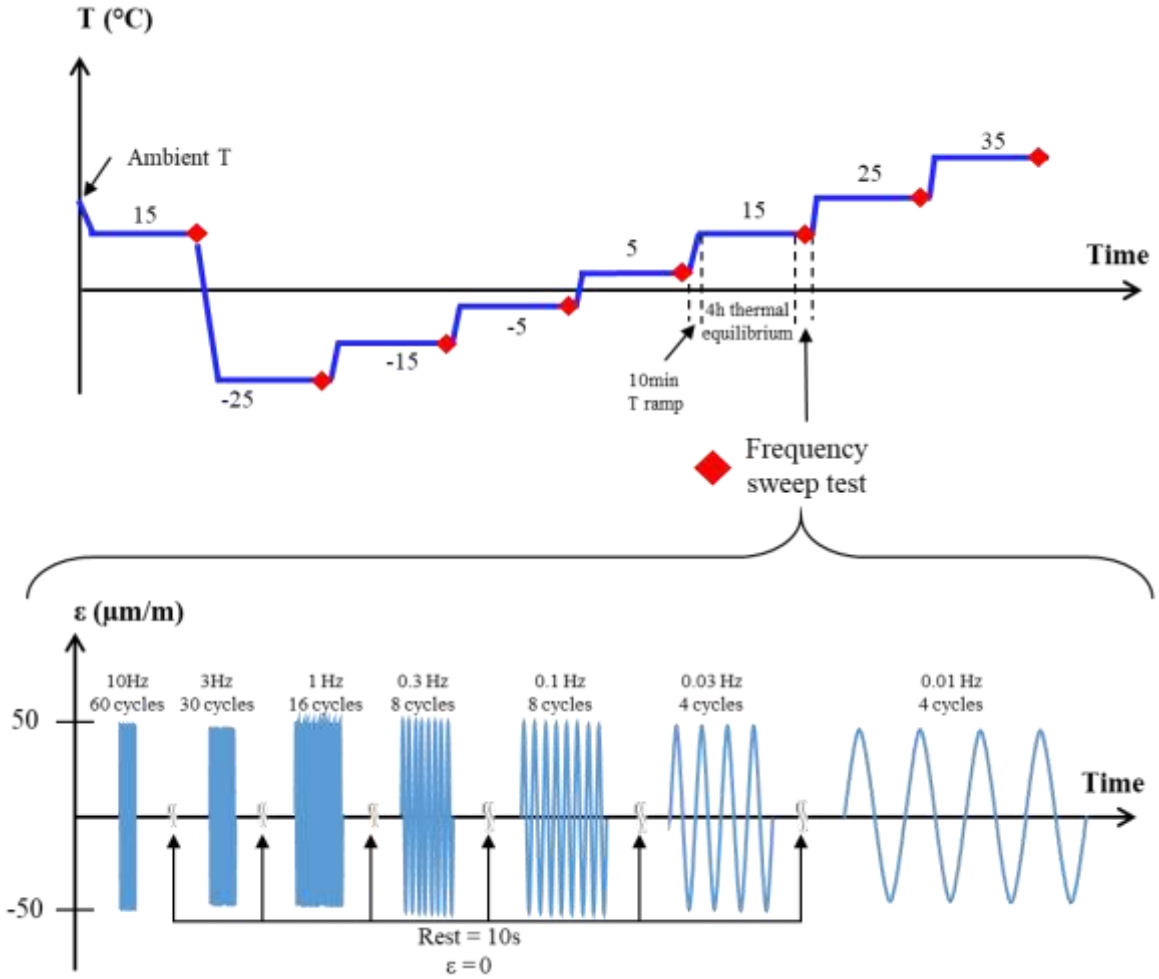

Figure 7-14 *Scheme of complex modulus tests of bituminous mixtures with TC on cylindrical specimen*

The detailed results of complex modulus tests on bituminous mixtures is available in Appendix 2.1.2. All mixtures respected the TTSP; the experimental shift factors a_T and their associated WLF models for the are displayed as functions of temperature in Figure 7-15. The master curves of norm of complex modulus and phase angle are plotted in Figure 7-16 a) and b). Additionally, the normalised complex modulus in Cole-Cole plot and Black diagram is represented in Figure 7-17 a) and b). The 2S2P1D models of all mixtures were added to experimental data. The 2S2P1D constants of bituminous mixtures are listed in Table 7-7, alongside with their WLF parameters.

The mixtures with silane-treated aggregates shared almost the same shift factors as the control mixture, and the same WLF parameters consequently. As for the mastics, the silane treatment of aggregates seemed to have little or no effect on the temperature dependence of the complex modulus of mixtures. Mixtures with silane-treated aggregates and control mixtures shared the same normalised complex modulus curves in complex representations (Figure 7-17). The master curves of norm of complex modulus (Figure 7-16 a)) showed that the asymptotic moduli E_0 and E_{00} were very close. In fact, the discrepancies of the glassy and the static moduli between the mixtures with silane-treated aggregates and the control mixtures could not be distinguished from the repetition scattering observed between the specimens of control mixtures (B_CO_58_sp11 vs B_CO_5.8_sp12). Regarding 2S2P1D models (see Table 7-7), all mixtures shared four constants (k, h, δ, β). The E_0 values varied between 31800 and 33000 MPa, and E_{00} values varied between 20 and 45MPa. The constant accounting form the temperature dependence of the complex modulus in 2S2P1D model τ_0 presented little discrepancies between the mixtures specimens with silane-treated aggregates (0.0015 and 0.0016 s) and the control mixture specimens (0.0022 and 0.0035s). This was the only sensible effect of the silane treatment on the LVE behaviour of bituminous mixture, but it was still very limited nevertheless.

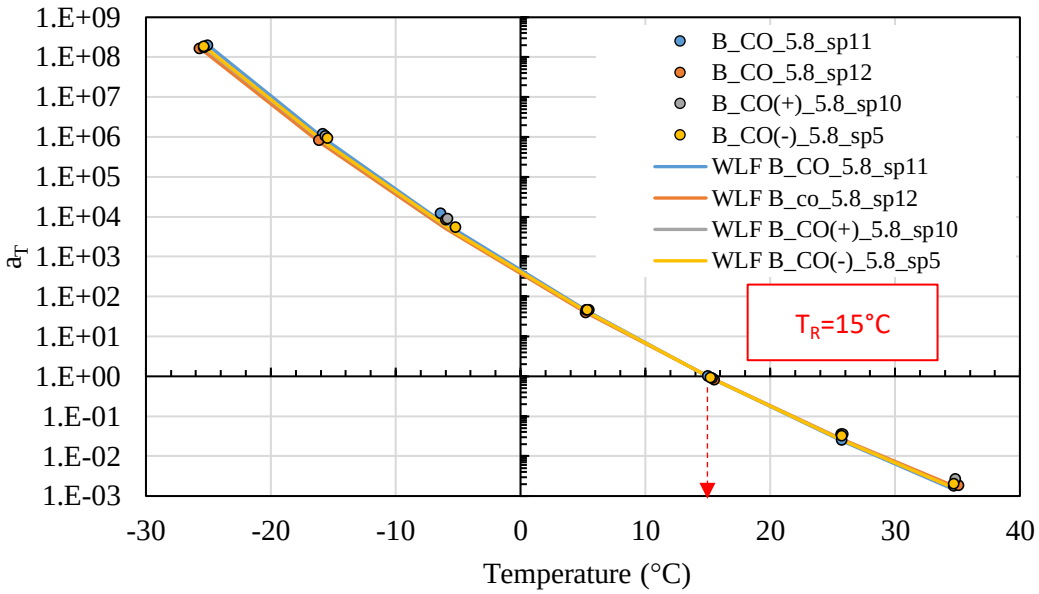

Figure 7-15 *Shift factors of mixtures with silane-treated aggregates (B_CO_5.8(+)_sp10 and B_CO_5.8(-)_sp5) and control mixtures (B_CO_5.8_sp11 and B_CO_5.8_sp12). WLF models were added for each mixture.*

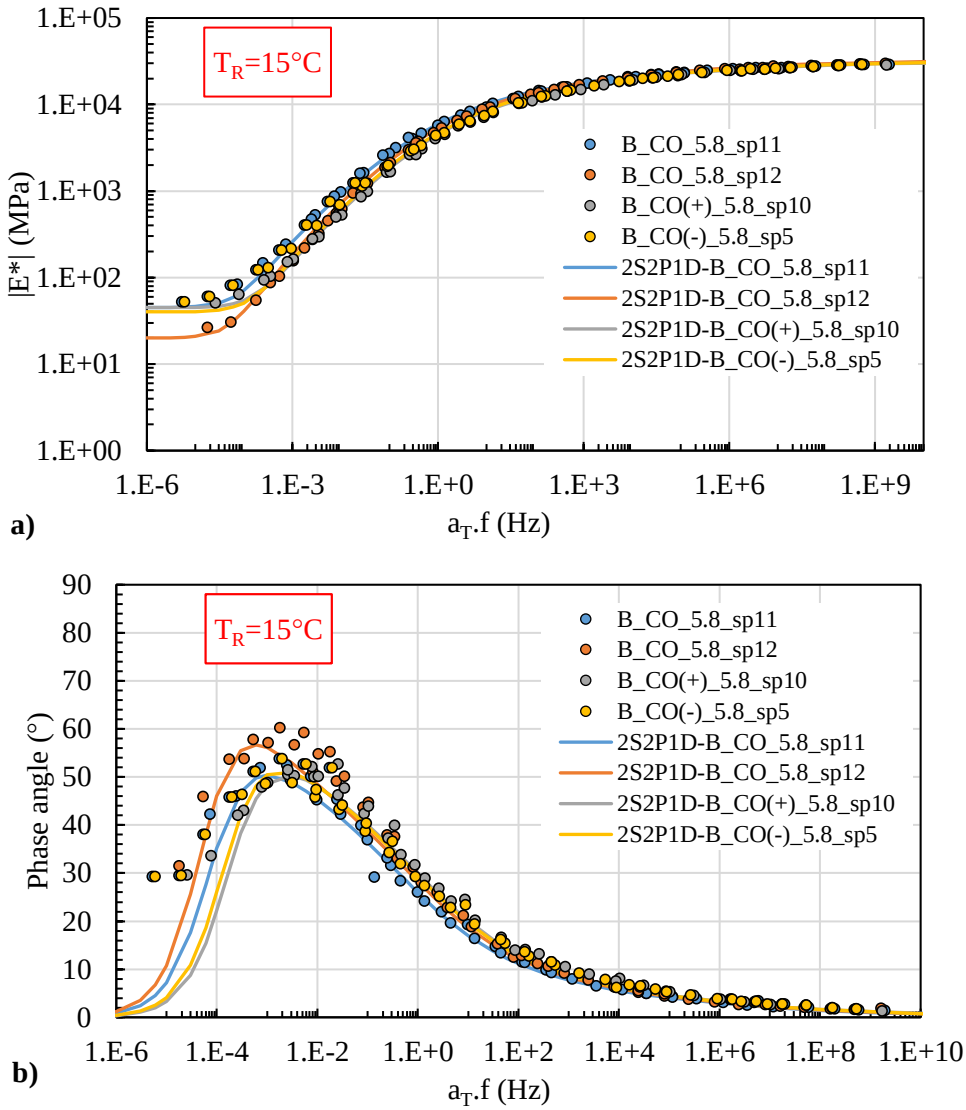

Figure 7-16 *Master curves of complex modulus of mixtures with silane-treated aggregates (B_CO_5.8(+)_sp10 and B_CO_5.8(-)_sp5) and control mixtures (B_CO_5.8_sp11 and B_CO_5.8_sp12): a) norm of complex modulus, b) phase angle. 2D2P1D models were added for each mixture.*

Overall, the complex modulus tests results showed that the influence of surface modification of CO aggregates with anti-stripping and pro-stripping silanes on the LVE behaviour of bituminous mixtures was very limited and possibly negligible. As for the LVE characterisation of mastics (in Section 7.4.1), the LVE behaviour of mixtures appeared primarily determined by its components and its mix design parameters rather than by the properties of its bitumen-aggregate interface.

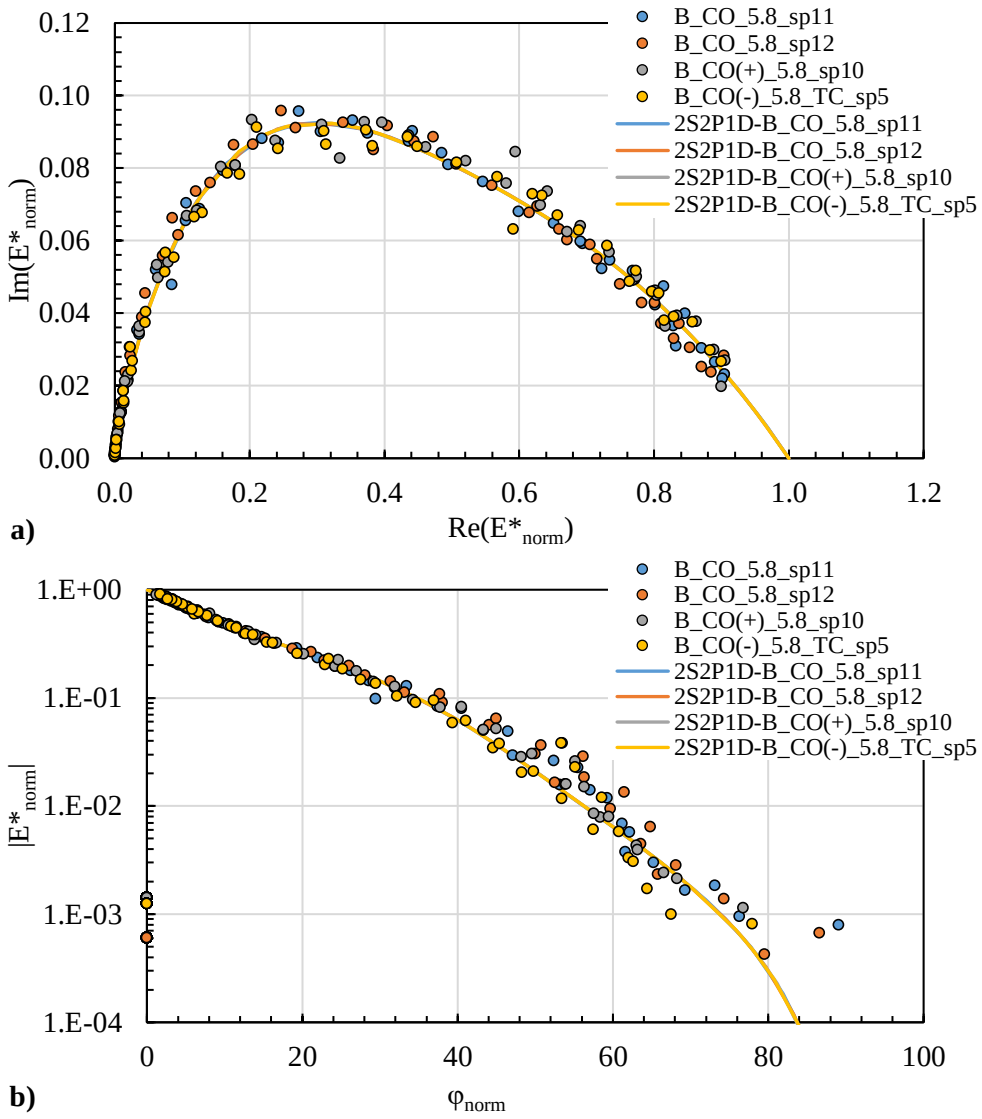

Figure 7-17 *Normalised complex modulus of mixtures with silane-treated aggregates (B_CO_5.8(+)_sp10 and B_CO_5.8(-)_sp5) and control mixtures (B_CO_5.8_sp11 and B_CO_5.8_sp12): a) in Black diagram, b) in Cole-Cole plot. 2D2P1D models were added for each mixture.*

Table 7-7 *2S2P1D constants and WLF parameters of mixtures with silane-treated aggregates (B_CO_5.8(+)_sp10 and B_CO_5.8(-)_sp5) and control mixtures (B_CO_5.8_sp11 and B_CO_5.8_sp12)*

	2S2P1D constants							WLF parameters		
	E_{00} (MPa)	**E_0 (MPa)**	**k** -	**h** -	**δ** -	**τ_0 (s)**	**β** -	**T_{ref} (°C)**	**C_1** -	**C_2 (°C)**
B_CO_5.8_sp11	45	32000	0.17	0.54	1.9	0.035	100	15	28.1	175.6
B_CO_5.8_sp12	20	33000	0.17	0.54	1.9	0.022	100	15	27.2	175.2
B_CO(+)_5.8_sp10	45	31800	0.17	0.54	1.9	0.015	100	15	27.9	177.1
B_CO(-)_5.8_sp5	40	32000	0.17	0.54	1.9	0.016	100	15	27.7	175.4

7.5.2 Resistance to fatigue, stiffness at 15°C/10Hz and water sensitivity

The resistance to fatigue of mixtures was evaluated through two fatigue tests:

- 2-PB test on trapezoidal specimen at 10°C/25Hz according to European standards (AFNOR 2012c), described in Section 3.1.2.1. 18 specimens were tested at various strain amplitudes for each mixture (B_CO_5.8, B_CO(o)_5.8, B_CO(+)_5.8 and B_CO(-)_5.8). The analysis of fatigue test results was developed in Section 4.2.1.
- TC test on cylindrical specimen at 10°C/10Hz (described in Section 3.1.2.2). 9 specimens were tested at various strain amplitude for B_CO_5.8, B_CO(+)_5.8 and B_CO(-)_5.8. The analysis of fatigue test results included five failure criteria (some were discussed in Section 2.3.4.4). Three "macroscopic" criteria were tested: half of the initial modulus criterion "$N_{f,50\%}$", the inflexion point criterion "$N_{f,\ inflexion}$" that marks the moment at which the curve of modulus plotted against the number of cycle becomes concave, and the maximum of phase angle criterion $N_{f,\ \varphi}$. Additionally, two "local" failure criteria were implemented: the extensometer amplitude discrepancy criterion $N_{f,\Delta\varepsilon}$ which is reached when the amplitude of one extensometer differs of at least 25% from the average signal amplitude, and the extensometer phase angle discrepancy criterion $N_{f,\Delta\varphi}$ which is reached when the phase angle of one extensometer differs of 5° from the average signal phase angle (see Figure 2-38).

The stiffness at 15°C/10Hz of mixtures was evaluated through complex modulus tests on 2-PB apparatus according to European standard (AFNOR 2012d).The water sensitivity was studied with Indirect Tensile Strength Ratio (ITSR) test, also according to European norm (AFNOR 2018d).

The complete fatigue test results obtained with 2-PB test and TC test are compiled respectively in Appendices 2.2.1. and 2.2.2. An illustrative example of fatigue test result obtained with TC geometry is displayed in Figure 7-18. The five failure criteria ($N_{f,50\%}$, $N_{f,\ inflexion}$, $N_{f,\ \varphi}$, $N_{f,\Delta\varepsilon}$ and $N_{f,\Delta\varphi}$) are also represented in this example. Moreover, the Wöhler curves and their associated linear regressions of the mixtures with aggregates treated with silanes (B_CO(+)_5.8 and B_CO(-)_5.8) and of the control mixture (B_CO_5.8) are plotted

for each failure criterion in Figure 7-19. From a general perspective, the Wöhler lines were almost parallel. The main difference between failure criteria was the value of the regression parameter ε_6 (i.e. the strain amplitude that corresponds to a life duration of 10^6 cycles). The different values are listed in Table 7-8. The inflection point criterion $N_{f,\ inflexion}$ appeared always underestimating ε_6 relatively to the other four criteria, that tended lead to very close results across the tested mixtures. In particular, the local criteria $N_{f,\Delta\varepsilon}$ and $N_{f,\Delta\varphi}$ coincided quite well with the classical "half-modulus" criterion $N_{f,50\%}$, as the maximal discrepancy equalled respectively 6.6 and 2.1 µm/m. The maximal phase angle criterion $N_{f,\ \varphi}$ coincided very well $N_{f,50\%}$, with a maximal discrepancy of only 1.3µm/m.

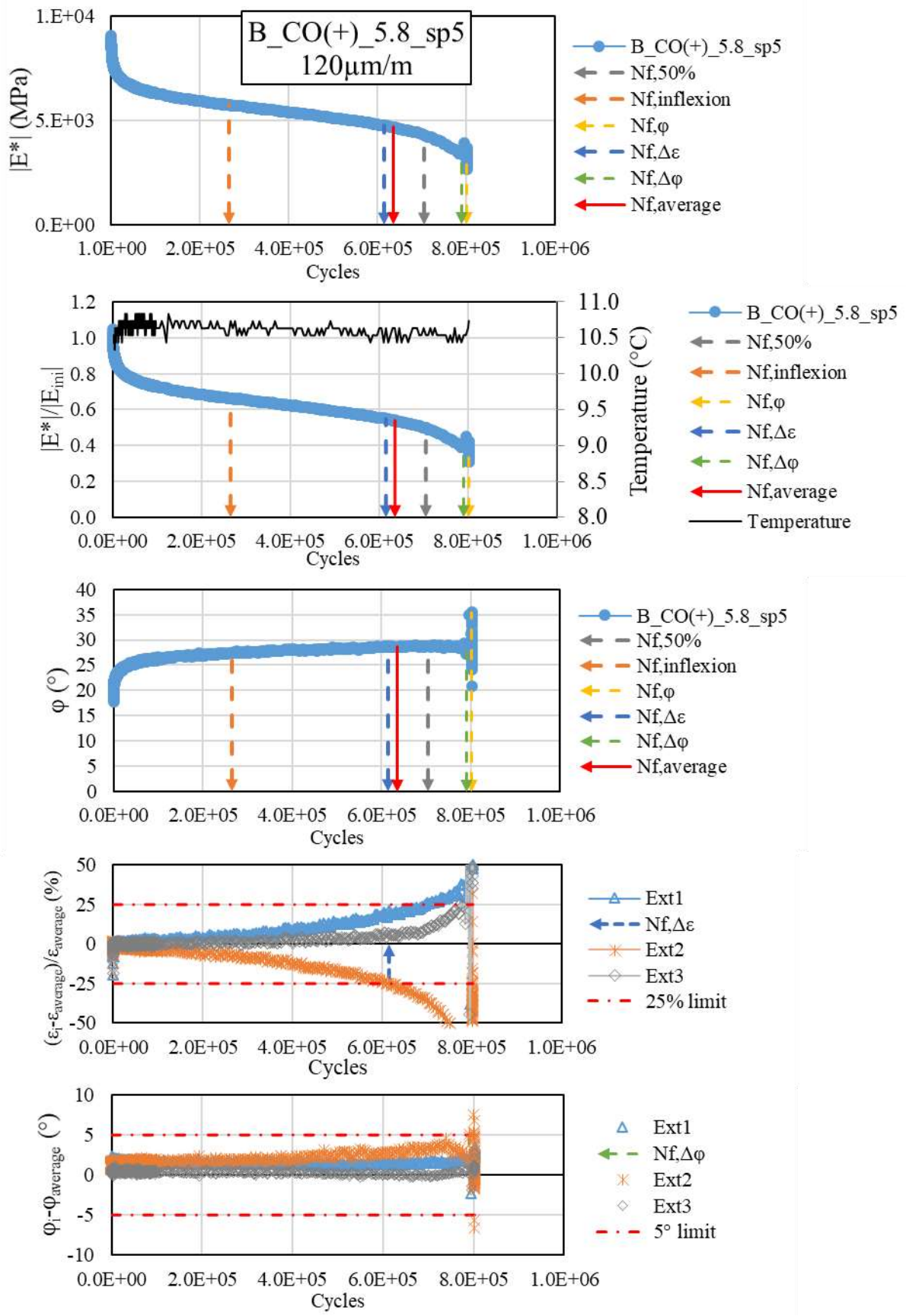

Figure 7-18 *fatigue test results of B_CO(+)_5.8_sp5 with TC test at 10°C/10Hz, and a strain amplitude of 120µm/m*

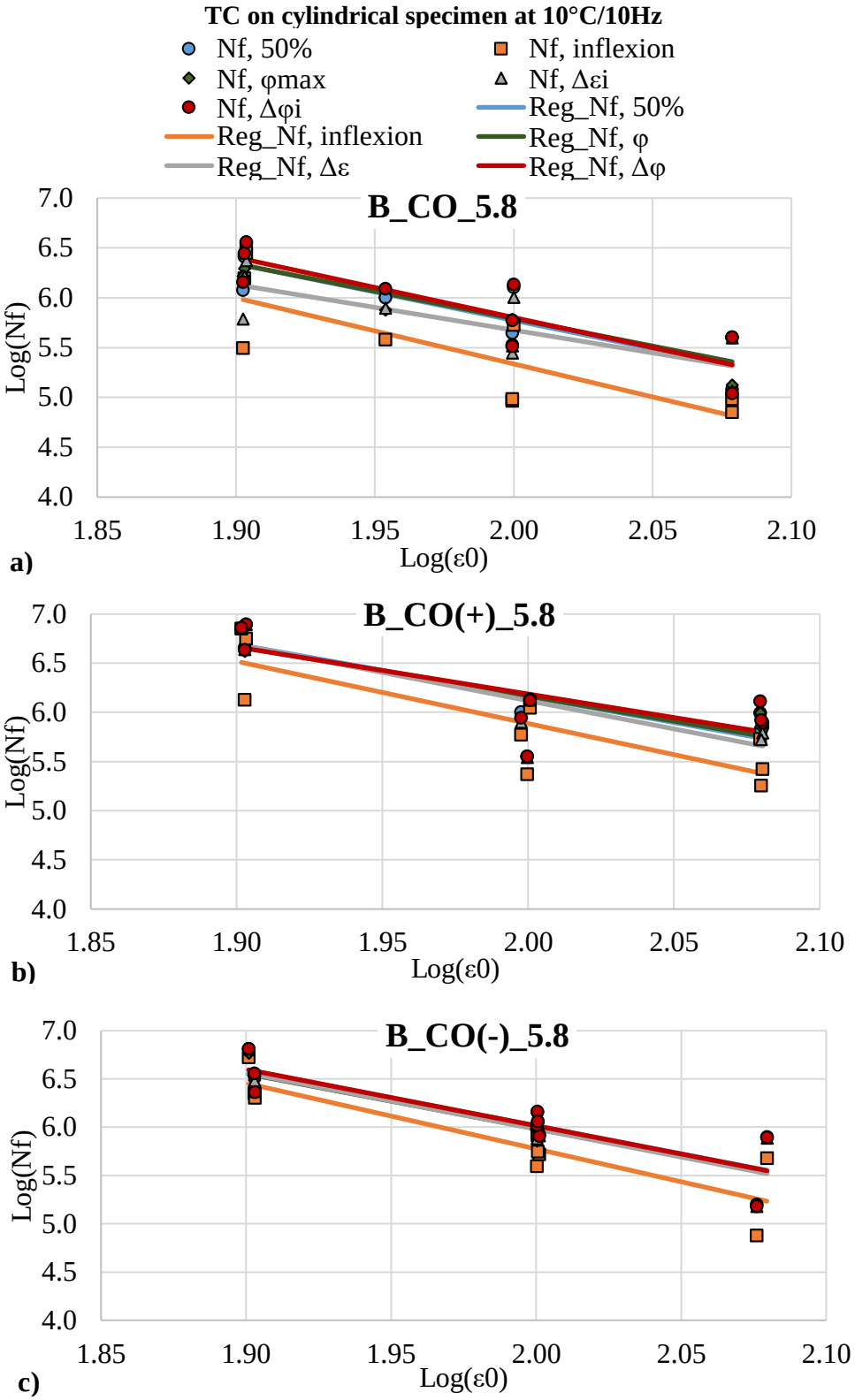

Figure 7-19 *Wöhler curves with five different failure criteria obtained with TC on cylindrical specimen at 10°C/10Hz for a) control mixture B_CO_5.8, b) mixture with aggregates treated with anti-stripping silane B_CO(+)_5.8, c) mixture with aggregates treated with pro-stripping silane B_CO(-)_5.8*

Table 7-8 *ε_6 values with five different failure criteria obtained with TC on cylindrical specimen at 10°C/10Hz for control mixture B_CO_5.8, B_CO(+)_5.8 and B_CO(-)_5.8*

Mixture	ε_6 (µm/m)				
	$N_{f,50\%}$	$N_{f,inflexion}$	$N_{f,\varphi}$	$N_{f,\Delta\varepsilon}$	$N_{f,\Delta\varphi}$
B_CO_5.8	91.22	79.39	91.60	84.88	92.71
B_CO(+)_5.8	107.29	95.95	107.77	104.87	109.39
B_CO(-)_5.8	100.63	92.69	99.38	99.26	100.60

The Wöhler lines obtained with 2-PB test on trapezoidal specimen at 10°C/25Hz and with TC test on cylindrical specimen at 10°C/10Hz are compared for all mixtures in Figure 7-20. The Wöhler curves were established with the classical failure criterion $N_{f,50\%}$. It should be reminded that the control mixture that underwent the silanisation procedure without silane (B_CO(o)_5.8) was not tested with the TC test geometry. Additionally, a focus on the regression parameter ε_6 obtained with both fatigue tests is presented in Figure 7-21. In Figure 7-20, all Wöhler lines were parallel. Consequently, the linear regressions possessed very close slope factors, regardless of the fatigue test type or the tested mixture. For any mixture, the increase of ε_6 value between the 2PB test and the TC test was consistently comprised between +25.4 and +28.4 µm/m.

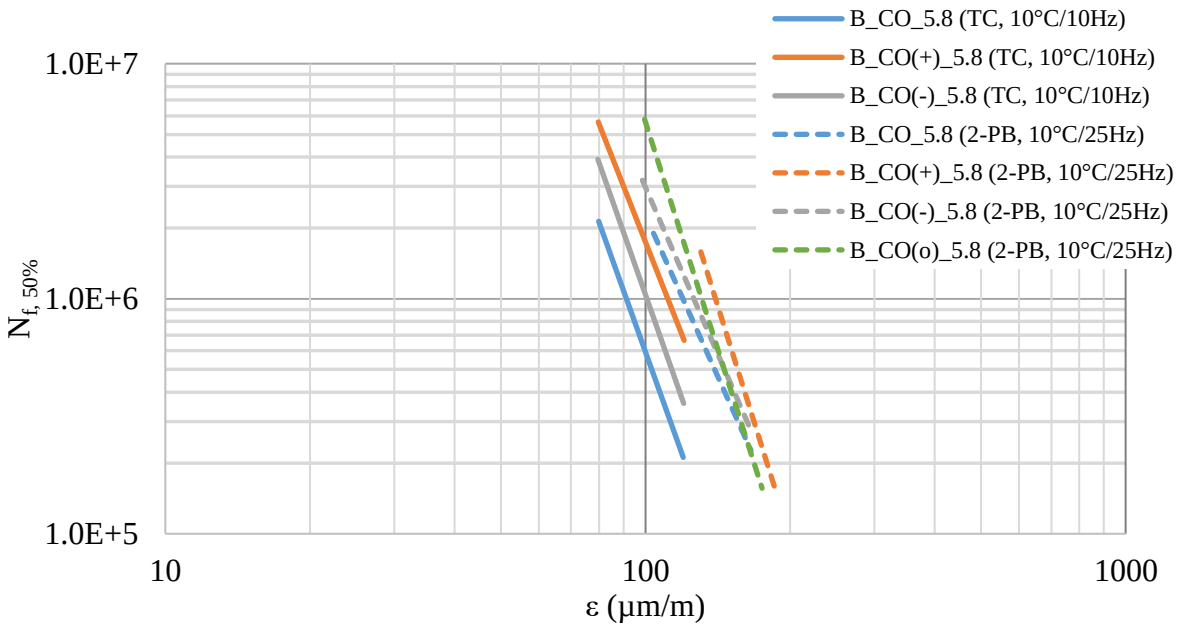

Figure 7-20 *Regression lines of Wöhler curves of mixtures with silane-treated aggregates (B_CO(+)_5.8 and B_CO(-)_5.8) and of control mixture B_CO_5.8, obtained with TC on cylindrical specimen at 10°C/10Hz and on 2-PB on trapezoidal specimen at 10°C/25Hz*

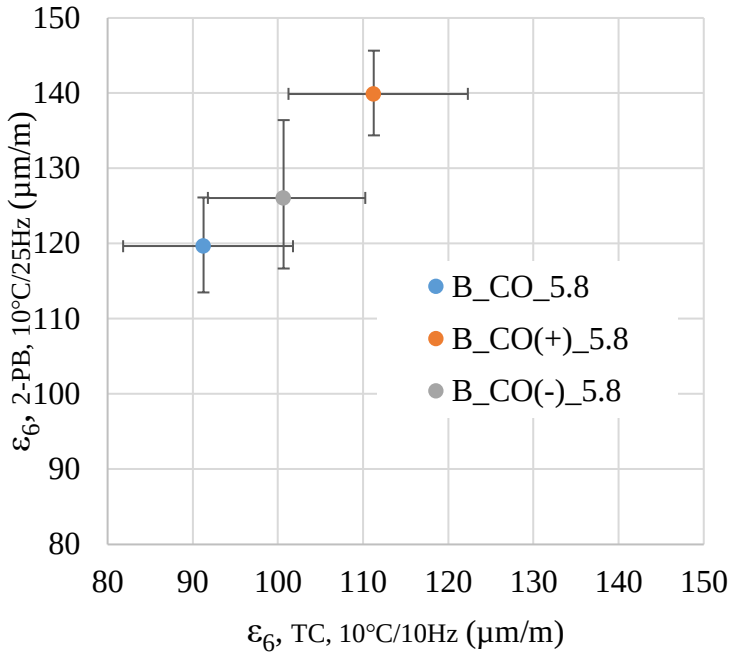

Figure 7-21 *ε_6 obtained with 2-PB on trapezoidal specimen at 10°C/25Hz as a function of ε_6 obtained with TC on cylindrical specimen at 10°C/10Hz, for mixtures with silane-treated aggregates (B_CO(+)_5.8 and B_CO(-)_5.8) and control mixture B_CO_5.8. Error bars represent 95% confidence intervals. The failure criterion was $N_{f,50\%}$ for both test type.*

Regarding the influence of the bitumen-aggregate modification on the fatigue performance, the linear regression parameters obtained with the 2-PB fatigue test for all tested mixtures were listed in Figure 7-22, in addition to the previous Figures Figure 7-20, Figure 7-21 and Table 7-8. In Figure 7-21, the mixtures with silane-treated aggregates showed higher ε_6 (i.e. better resistance to fatigue according to European standard) for both fatigue test types. The anti-stripping silane (adhesion promoter) yielded the best mixture performances, with a remarkable increase of 20µm/m of ε_6 compared to the untreated mixture. To put this increase of fatigue performance into perspective, an increase of 20µm/m of ε_6 corresponded to the use of polymer modified bitumen over pure bitumen (see Figure 4-3) for the mixtures studied in campaign I. Still in Figure 7-21, the pro-stripping silane (adhesion inhibitor) slightly increased ε_6 about 6 to 9µm/m (close to the limit of the 95% confidence interval). This observation was unexpected, since the bitumen-aggregate affinity was known to be undermined compared to the original rock substrate, as proven in Section 7.3.2.2. This apparent contradiction was erased with the analysis of the fatigue performances of the control mixture that underwent the silanisation procedure without silane (B_CO(o)_5.8). Indeed, in Figure 7-22, the silanisation procedure induced an increase of ε_6 (+11µm/m from B_CO_5.8 to B_CO(o)_5.8). From this point, the nature of the silane either improved (+9µm/m from B_CO(o)_5.8 to B_CO(+)_5.8) or reduced (-5µm/m from B_CO(o)_5.8 to B_CO(-)_5.8) the resistance to fatigue of mixtures. Overall, the sole modification of aggregates surface with hydroalcoholic solution (the procedure was described in Section 7.2.1) improved the resistance to fatigue to mixtures with fixed constituent and mix design parameters. The selection of the silane further modifying the aggregate surface, by either promoting or undermining the bitumen-aggregate adhesion, respectively lead to a better and worse resistance to fatigue.

The stiffness of mixtures was evaluated with the norm of complex modulus taken at 15°C and 10Hz $|E^*|(15°C/10Hz)$. The experimental results are shown in Figure 7-22. The silanisation procedure appeared to lower the norm of complex modulus about 10% (on average with B_CO(o)_5.8, B_CO(+)_5.8 and B_CO(-)_5.8) compared to the value obtained with the untreated control mixture B_CO_5.8. The modulus of the mixtures that underwent the silanisation procedure did not vary significantly with the type of silane (or the absence of silane). The same comments could be made with the initial equivalent modulus of the 2-PB fatigue tests at 10°C/25Hz, $|E^*|_{ini}$, represented in Figure 7-22. Moreover, this trend on the complex modulus matched the conclusions of the prior study of the LVE behaviour in Section 7.5.1; the effect of the silanisation procedure on stiffness was limited and the influence of the silane type was negligible.

The water sensitivity of mixtures was evaluated with *ITSR*. The experimental results are displayed in Figure 7-22. The errors bars for *ITSR* corresponded to the confidence interval of repeatability (+/-15%) according to the European standards (AFNOR 2018d). This wide confidence interval (in regards to the experimental results), however, was not based on a scientific consensus, as specified in the normative document. An extensive study on the moisture sensitivity evaluation for mixtures showed the extreme variations in *ITS* (Indirect Tensile Strength) scattering between specimens, in either wet or dry conditions (from 0.7% to 25.5% depending on the mixture) (Adorjányi 2008). The repeatability of the resulting *ITSR* values is obviously strongly dependent on the repeatability of the average *ITS* values (for dry and wet specimens). Since this aspect of the ITSR method has not been clearly treated, the analysis of the influence of the aggregate surface treatment with silane should be taken cautiously. The control mixtures B_CO_5.8 and B_CO(o)_5.8 shared same *ITSR* (77 and 79%). On the other hand, the mixtures with aggregates treated with both anti-stripping and pro-stripping silanes showed improved resistance to moisture with higher *ITSR* values (88 and 85%). The fact that the pro-stripping agent lowered the moisture sensitivity of the mixture could be considered unexpected. However, the fluorinated chains of the pro-stripping silane that were coated on the aggregates proved to increase the hydrophobicity of CO rock substrates in Section 7.3.2.1. Since most moisture damage mechanisms mainly depends on the debonding of the bitumen-aggregate interface (Caro et al. 2008a) which is natural from the thermodynamic work of adhesion theory in presence of water, super-hydrophobic agents such as the nonafluorotriethoxysilane (Figure 3-17 b)) could possibly make the debonding less favourable, even if the bitumen-aggregate adhesion appeared undermined in dry condition. This possibility might be the case, as the bitumen affinity of CO aggregate treated with pro-stripping silane was clearly worse than with the untreated substrate (Figure 7-8), the resistance to moisture appeared better. The distinction of the bitumen-aggregate adhesion in dry and wet conditions should be taken cautiously by paving technologists who wishes to improve the thermomechanical performances of bituminous mixtures by modifying the bitumen-aggregate interface.

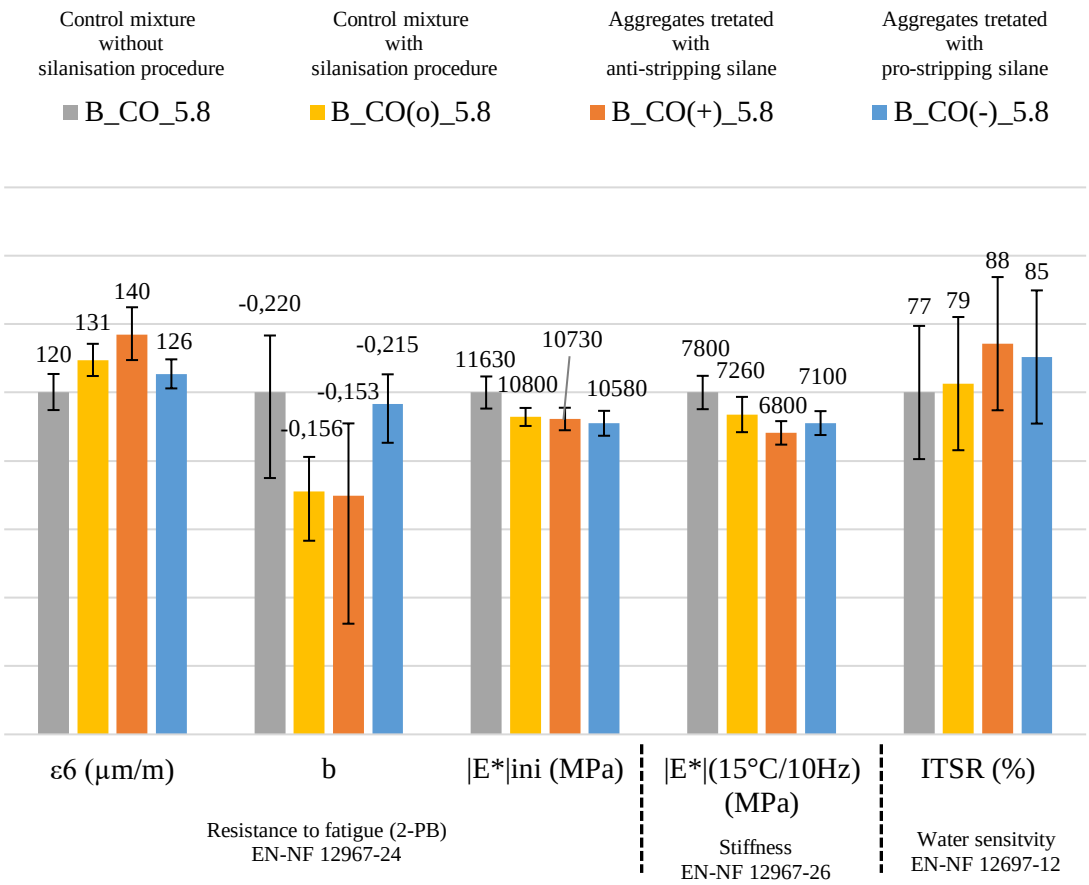

Figure 7-22 *Resistance to fatigue with 2-PB apparatus, stiffness and water sensitivity of mixtures with silane-treated aggregates (B_CO(+)_5.8 and B_CO(-)_5.8) and of control mixtures B_CO_5.8 and B_CO_5.8(o). Error bars for the linear regression parameters ε_6 and b represent 95% confidence interval. Error bars for $|E^*|_{ini}$ and |E*|(15°C/10Hz) represent the observed standard deviation. Error bars for the ITSR represent the 95% confidence interval of repeatability (non-consensual value)*

7.6 Conclusion of Campaign IV

The fourth and final campaign of this thesis focused on studying the influence of aggregate surface treatment with silanes on the thermomechanical performances of bituminous mastics and mixtures.

A new silanisation procedure to modify the surface properties of road aggregates and glass substrates was developed using a hydroalcoholic solution. Two silanes were tested: an anti-stripping silane (lipophilic with a long carbon chain) to promote bitumen-aggregate adhesion and a pro-stripping silane (with a short fluorinated chain) to undermine bitumen-aggregate adhesion.

The surface analysis of silane-treated substrates was performed with X-ray Photoelectron Spectroscopy (XPS). The XPS revealed the presence of molecules of silane at the very surface of the modified substrates, confirming the effectiveness of the silanisation procedure. The physicochemical properties of silane-treated substrates was evaluated with contact angle method. The test results proved that the silane coating changed the physicochemical properties of the substrates; both silanes effectively increased the hydrophobicity of the rock and glass substrates, and the pro-stripping silane reduced the bitumen-aggregate affinity. However, the quantitative approach using the surface free energy theory did not yield reliable predictions due to the lack of complementary tests.

The influence of silane treatment of glass beads on the thermomechanical behaviour of mastics was investigated. The LVE behaviour was studied with complex shear modulus test using ASR. The silane-treated and control mastics followed the TTSP and shared the same shift factors. The 2S2P1D model was successfully calibrated for all mastics. They shared several 2S2P1D constants (at least h, k and β), inherited from their constituent bitumen B. Overall, the silane modification appeared to play little if no role at all on the LVE behaviour of mastics. The behaviour of silane-treated and control mastics during Load and Rest Periods (LRP) test was also investigated. The silane treatment with anti-stripping silane did not seem to alter the behaviour during LRP. The LRP test and its analysis complexity was probably not the simplest way to study the influence of bitumen-aggregate interface on mastic behaviour.

The influence of silane treatment of aggregates on the thermomechanical behaviour of bituminous mixture was also investigated. The LVE behaviour of mixtures was studied with complex modulus test in TC on cylindrical specimen. The mixtures followed the TTSP and shared the same shift factors. The 2S2P1D model was successfully calibrated for all mixtures. They shared four 2S2P1D constants (h, k, δ and β). The surface modification of aggregates did not influence the LVE behaviour of mixtures, except a limited shift on τ_0.

The resistance to fatigue of mixtures was evaluated through the lens of two different fatigue tests: 2-PB test at 10°C/25Hz from the European standards and TC on cylindrical specimen at 10°C/10Hz. The stiffness of mixtures and the water sensitivity were also studied according to the European standards, respectively with the complex modulus at 15°C/10Hz and the Indirect Tensile Strength Ratio (ITSR). The silanisation procedure on aggregates without silane improved the resistance to fatigue of the mixture (around +10µm/m on ε_6). The silanisation of aggregates with anti-stripping silanes further increase the fatigue performances (+20m/m) compared to the untreated mixture, whereas the use of pro-stripping silane limited the fatigue performance enhancement (only +5µm/m). Regarding stiffness, the silanisation procedure caused a slight diminution of modulus, regardless of the silane type. Regarding water sensitivity, the presence of hydrophobic silanes at the bitumen-aggregate interface lead to an increase in *ITSR* (for both anti-stripping and pro-stripping silanes) compared to the untreated control mixture and the control mixture with aggregates that underwent the silanisation procedure without silanes. Both control mixtures shared the same ITSR, and that the hydroalcoholic solution did not change the water sensitivity of the mixture (the ethanol would not repel water), although it changed its resistance to fatigue.

In conclusion, this campaign showed the possibility to modify the bitumen-aggregate interface of bituminous mixtures without changing the constituent materials nor the mix design parameters. The bitumen-aggregate adhesion played a significant role on the resistance to fatigue and the water sensitivity of bituminous mixtures and a limited role on the LVE behaviour of mixtures.

8 Conclusions and perspectives

This thesis explored the relationship between the thermomechanical performances of bituminous binders and mixtures with a particular attention to the role of the bitumen-aggregate adhesion. The scope of the study was narrowed down to four distinct campaigns. Each campaign was built independently, with a set of objectives and detailed conclusions. Only the most important conclusions were summarised below.

Campaign I focused on the influence of bitumen and aggregate on bituminous mixtures thermomechanical performances. The campaign comprised an extensive parametric study on three thermomechanical performances of mixtures according to the European standards: Stiffness (complex modulus at 15°C/10Hz), resistance to fatigue (Wöhler curves obtained with fatigue tests using 2-PB apparatus) and water sensitivity (Indirect Tensile Strength Ratio). Different bitumen properties (bitumen origin, polymer modification and binder content) and aggregate nature (five different mineral substrates) were tested. The cross effects have been evaluated with a full factorial plan. In addition to the parametric study, fatigue tests on the four bitumens of the study were performed with DSR. The main conclusions of Campaign I were drawn as follow:

- The stiffness was mainly influence by the binder content, the bitumen origin and the aggregate nature, without cross effects.
- The resistance to fatigue of bituminous mixtures was determined mainly by the bitumen origin, secondarily by the polymer modification and marginally by the binder content.
- The water sensitivity of mixtures was influenced by the bitumen origin, the polymer modification and also by the aggregate nature with important cross effects.
- The biasing effect of steric hardening on the equivalent modulus during fatigue test of bitumen was identified and quantified. This phenomenon occurred over several hours, and should be taken into account in laboratory testing of bitumen
- The linear regression of the Wöhler curves of bitumens were established. The values of the slope factor *b* (consistently between -0.3 and -0.35) for pure and polymer modified bitumens appeared to be different from the mixture (around -0.2). This could constitute a standard value range for the slope factor of bitumens tested with DSR in general, since similar previous studies converged to the same results.
- The resistance to fatigue of the constituent bitumen, evaluated by the shear strain amplitude corresponding to fatigue life of 10^6 cycles (γ_6), seemed to be an indicator of the corresponding mixture performance (ε_6).
- A predictive equation of fatigue performances of bituminous mixtures was proposed, based on a regression on stiffness and water sensitivity test results and bitumen properties.

Campaign II focused on the thermomechanical behaviours of four bitumens and a glass-bead mastic. The linear viscoelastic (LVE) behaviour and the behaviour during Load and Rest Periods (LRP) of two pure bitumens, two PmB and of a bituminous mastic made with 40% of glass beads were tested. The LVE behaviour was characterised with complex shear modulus tests with Annular Shear Rheometer (ASR) and DSR, whereas the LRP test was performed only with ASR apparatus, at 10°C and 10Hz. The main conclusions of Campaign II were drawn as follow:

- All binders respected the Time-Temperature Superposition Principle (TTSP). The polymer modification did not influence the shift factors.
- The 2S2P1D model was successfully used to fit the complex modulus test results of all binders. Obtained simulations are good, except for the polymer-modified bitumen at low equivalent frequencies (high temperatures / low frequencies).
- The glass-bead mastic inherited the LVE properties of its constituent bitumen.

- All bitumens exhibited the capacity to recover from a 50% modulus loss during long rest periods (up to five days).
- The reversible phenomena occurring during LRP were identified: nonlinearity, self-heating and thixotropy. As expected, the effects of these phenomena on the equivalent shear modulus of the binder increased with the loading amplitude.
- A correction to take into account the effects of temperature change (due to self-heating induced by dissipated energy) and nonlinearity was proposed. Based on the corrected results, the remaining phenomena (thixotropic breakdown and damage during loading, thixotropic build-up and healing during rest) were clearly distinguished. The phase angle monitoring was essential to differentiate the phenomena.
- The healing phenomenon occurred over particularly long rest period (several days). Even after total complex modulus recovery, the successive LRP proved that the material ability to resist cyclic loading could be significantly undermined. In other words, the rate of damage of bituminous binders depended on the history of loading rather than on punctual stiffness evaluation.

In Campaign III, a new interface test on bitumen thin film trapped between two rock cylinders was proposed. The thin film specimen fabrication and the axial test set-up were described. The axial strains in the rock and in the bitumen phases were both measured thanks to a system of two pairs of short and long extensometers. An analytical solution to the homogeneous confined film under uniaxial tension-compression (TC) in isotropic linear elasticity (ILE) was proposed. The thin film geometry was simulated in ILE conditions with numerical finite element (FE) method. A FE parametric study with varying bitumen properties (E, υ) and bitumen film aspect ratio (ratio of thickness to diameter) was done to provide axial modulus for different film thicknesses as well as different bitumen and rock properties. The analytical solution could be obtained as an asymptotic case for low aspect ratio. Finally, the experimental testing of the real thin film specimen included LVE behaviour characterisation and pull-off tests. The main conclusions of Campaign III were drawn as follow:

- The fabrication procedure for the thin film specimen included metallic foil spacers to ensure a constant film thickness with micrometric precision.
- The analytical solution for the homogeneous ILE thin film was found. For particularly stiff rock phase (almost rigid), it lead to a bitumen film confined in oedometric TC (no radial strain allowed) and a rock phase in uniaxial TC (negligible radial stress).
- The analytical solution matched the FE simulation very well over a large range of realistic bitumen parameters for aspect ratios below 1/250 (which corresponded to the aspect ratio of the tested specimens). Hence, the thin film geometry proved to be able to test bitumen in confined condition without a conventional triaxial test set-tup.
- For high temperatures (from 30 to 50°C), the oedometric modulus of the bitumen followed the Time-Temperature Superposition Principle. With the additional knowledge of the complex shear modulus obtained from bitumen LVE characterisation in Campaign II, it was possible to calculate the Poisson ratio of the bitumen, which was very close to 0.5 (nearly incompressible). Indeed, the ratio of oedometric modulus to uniaxial modulus ranged from 10^2 to 10^4 in order of magnitude.
- The pull-off tests revealed the presence of strains due to flexion during tension, but did not give sufficient data to characterise the bitumen-rock interface. Nevertheless, the thin film test introduced the possibility to conduct very precise strain-controlled pull-off tests, which are not possible with classical pull-off tests.

In Campaign IV, the influence of aggregate surface treatment with silanes on mastic and mixture thermomechanical performances, was investigated. A new silanisation procedure to modify the surface properties of glass and road aggregates was developed. The substrates were treated with anti-stripping and pro-stripping silanes in order to evaluate the effects of the bitumen-aggregate interface modification. The silane-treated surfaces were analysed with X-ray Photoelectron Spectroscopy and the physicochemical properties of silane-treated and control substrates were assessed with contact angle method. Then, the LVE behaviour and the behaviour during LRP of bituminous mastics made with silane-treated glass beads were characterised (same tests as Campaign II). The LVE behaviour of bituminous mixtures with silane-treated aggregates was assessed with uniaxial complex modulus test on cylindrical specimens. Additionally, the resistance to fatigue of these mixtures was investigated with fatigue tests using either TC on cylindrical specimen or 2-PB flexion on trapezoidal specimen. Finally, the stiffness (complex modulus at 15°C/10Hz) and the water sensitivity (ITSR) of these mixtures were tested (same tests as Campaign I). The main conclusions of Campaign I were drawn as follow:

- The new silanisation procedure, which was based on a hydroalcoholic solution, was successfully applied to glass and mixtures aggregates. The procedure allowed to make, in laboratory, mixtures with exactly the same constituents and mix design parameters, but with different bitumen-aggregate adhesion.
- The silanes were found at the very surface (molecular scale) of silane-treated substrates with XPS, confirming the effectiveness of the silanisation procedure.
- The contact angle method proved that the silanisation changed the physicochemical properties of the substrates. Silane-treated substrates were more hydrophobic as expected and the bitumen-aggregate affinity was significantly undermined by the pro-stripping silane.
- All bituminous mastics and mixtures followed the TTSP, and the 2S2P1D model successfully modelled their LVE behaviour.
- The modification of bitumen-aggregate interface with silanes did not affect the LVE properties of both bituminous mastic and mixtures.
- The effect of silane treatment was not visible with the complex LRP tests on mastics.
- The resistance to fatigue of mixtures were improved by the silanisation procedure alone (without silane). The selection of the anti-stripping silane (long carbon chain) further improved the resistance to fatigue. On the other hand, the pro-stripping silane (short fluorinated chain) diminished the performance improvement observed with the silanisation procedure alone, but still yielded better fatigue results than the control mixture with untreated aggregates. The bitumen-aggregate interface appeared as an important factor that should be worth considering as paving technologist.
- The water sensitivity of mixtures was significantly reduced by both anti-stripping and pro-stripping silanes, which were particularly hydrophobic. The silanisation procedure alone did not modify the water sensitivity. This was a clear reminder to systematically differentiate the bitumen-aggregate adhesion in dry conditions, which apparently dictates important thermomechanical behaviour of mixtures such as the resistance to fatigue, from the adhesion in wet conditions, which address only moisture susceptibility.

Some perspectives arose from the four campaigns of this thesis.

- The relationship between the Wöhler curves of mixtures and their constituent bitumens should be further studied, since the fatigue performances of the bitumen appeared to be an important predictive parameter (γ_6 of bitumens vs. ε_6 of mixtures).

- The behaviour of bituminous binders during LRP revealed that the resistance to fatigue (or the rate of damage) depended on the history of loading rather than on the punctual measurement of stiffness, suggesting that microcraks do not heal completely. The visual observation of these microcraks and their evolution using rheo-optical techniques would constitute a great leap in the understanding of the complex damage process during fatigue. The thin film geometry could be advantageous in this scope.
- Another way of detecting a fundamental change in the microstructure during load and rest periods could be by monitoring other physical properties than the complex modulus of the bulk bitumen, such as the dielectric constant. The ASR and/or the thin film geometry could be adequate for that matter.
- The thin film test could be exploited to perform much more extended complex modulus tests with rigid metallic caps instead of fragile rock cylinders, for instance at lower temperatures. The combined study of oedometric and shear moduli of bitumen give access to the 3D LVE behaviour of bitumens over a wide temperature and frequency range with a quite good precision. Indeed, if bulky specimens of bitumen in triaxial cells would ultimately flow under their own weight, and therefore constrain the test to low temperature (0°C), the thin film geometry did not appear limited at all.
- The impact of strain rate of the pull-off test on the cohesive strength of bitumen should be further studied.
- The silanisation of road aggregates could be greatly optimised with a sharper approach from chemistry specialists, potentially unveiling more influence from the bitumen-aggregate interface on the mixture performances. The link between the proposed silanisation procedure and the classical adhesion promoting approach, which simply blends the anti-stripping agents in the bulk of bitumen, should also be studied (since chemicals companies claim that the agents migrate at the bitumen-aggregate interface and effectively coat the aggregates).
- The silane-treated substrates could be used in pull-off test campaigns to measure the impact of silanisation on the adhesive strength between bitumen and rock aggregate in dry conditions.

References

A. L. Babadopulos, Lucas F. de, Cédric Sauzéat, and Hervé Di Benedetto. 2017. 'Thermomechanical Coupling in Bituminous Mixtures Considered as Bonded Granular Media'. In *Poromechanics VI*, 610–17. Paris, France: American Society of Civil Engineers. https://doi.org/10.1061/9780784480779.075.

AASHTO M 320. 2017. 'AASHTO M 320 Standard Specification for Performance-Graded Asphalt Binder'.

AASHTO T 283. 2014. 'AASHTO T 283 Standard Method of Test for Resistance of Compacted Asphalt Mixtures to Moisture-Induced Damage'.

AASHTO T 313. 2019. 'AASHTO T 313 Standard Method of Test for Determining the Flexural Creep Stiffness of Asphalt Binder Using the Bending Beam Rheometer'.

AASHTO T 314. 2012. 'AASHTO T 314 Standard Method of Test for Determining the Fracture Properties of Asphalt Binder in Direct Tension'.

AASHTO T 315. 2019. 'AASHTO T 315 Standard Method of Test for Determining the Rheological Properties of Asphalt Binder Using a Dynamic Shear Rheometer'.

AASHTO T 324. 2019. 'AASHTO T 324 Standard Method of Test for Hamburg Wheel-Track Testing of Compacted Asphalt Mixtures'.

Adams, Robert D., ed. 2005. *Adhesive Bonding: Science, Technology and Applications*. Boca Raton : Cambridge: CRC Press ; Woodhead Pub.

Adamson, A. W. 1977. 'Physical Chemistry of Surfaces'. *Journal of The Electrochemical Society* 124 (5): 192C. https://doi.org/10.1149/1.2133374.

Adorjányi, Kálmán. 2008. 'Proceedings-4th Eurasphalt & Eurobitume Congress: Asphalt-Roads for Life. WATER SENSITIVITY EVALUATION OF AC MIXES WITH ANTISTRIPPING ADDITIVES BY DIFFERENT MECHANICAL TESTS'. https://doi.org/10.13140/2.1.2234.2400.

AFNOR. 2005. 'NF EN 933-5 July 2005 Tests for Geometrical Properties of Aggregates - Determination of Percentage of Crushed and Broken Surfaces in Coarse Aggegate Particles'.

———. 2006. 'NF EN 13108-5 December 2006 Bituminous Mixtures - Material Specifications Part 5: Stone Mastic Asphalt'.

———. 2007a. 'NF EN 12697-31 August 2007 - Bituminous Mixtures - Specimen Preparation with Gyratory Compactor'.

———. 2007b. 'NF EN 12697-33 September 2007 - Bituminous Mixtures - Specimen Preapared by Roller Compactor'.

———. 2008a. 'NF EN 933-4 June 2008 Tests for Geometrical Properties of Aggregates - Determination of Particle Shape - Shape Index'.

———. 2008b. 'NF EN 12620 June 2008 Aggregates for Concrete'.

———. 2010. 'NF EN 1097-2 June 2010 Tests for Mechanical and Physical Properties of Aggregates - Methods for the Determination of Resistance to Fragmentation'.

———. 2011. 'NF EN 1097-1 August 2011 Tests for Mechanical and Physical Properties of Aggregates - Determination of Resistance to Wear (Micro-Deval)'.

———. 2012a. 'NF EN 933-1 May 2012 Tests for Geometrical Properties of Aggregates - Determination of Particle Size Distribution'.

———. 2012b. 'NF EN 933-3 March 2012 Tests for Geometrical Properties of Aggregates - Determination of Particle Shape - Flawkiness Index'.

———. 2012c. 'NF EN 12697-24 August 2012 Bituminous Mixtures - Resistance to Fatigue'.

———. 2012d. 'NF EN 12697-26 June 2012 - Bituminous Mixtures - Stiffness'.

———. 2012e. 'NF EN 14770 August 2012 - Bitumen and Bituminous Binders - Determination of Complex Shear Modulus and Phase Angle'.

———. 2013a. 'NF EN 933-9 June 2013 Tests for Geometrical Properties of Aggregates - Assessment of Fines - Methylene Blue Test'.

———. 2013b. 'NF EN 12697-11 May 2013 - Bituminous Mixtures - Determination of the Affinity between Aggregate and Bitumen'.

———. 2013c. ‘NF EN 12697-22 December 2013 Test Methods for Hot Mix Asphalt - Wheel Tracking’.
———. 2013d. ‘NF EN 12697-46 Bitumnious Mixtures - Low Temperature Cracking and Properties by Uniaxial Tension Tests’.
———. 2014. ‘NF EN 12595 December 2014 Bitumen and Bituminous Binders - Determination of Kinematic Viscosity’.
———. 2015. ‘NF EN 933-8 July 2015 Tests for Geometrical Properties of Aggregates - Assessment of Fines -Sand Equivalent Test’.
———. 2017a. ‘NF EN 12697-35 August 2017 - Bituminous Mixtures - Laboratory Mixing’.
———. 2017b. ‘NF EN 13398 December 2017 Bitumen and Bituminous Binders - Determination of Elsatic Recovery Modified Bitumen’.
———. 2017c. ‘NF EN 13588 November 2017 - Bitumen and Bituminous Binderd - Determination of Cohesion of Bituminous Binders with Pendulum Test’.
———. 2018a. ‘NF EN 1426 January 2018 Bitumen and Bituminous Binders - Determination of Needle Penetration’.
———. 2018b. ‘NF EN 1427 January 2018 Bitumen and Bituminous Binders - Determination of the Softening Point’.
———. 2018c. ‘NF EN 12593 August 2018 Bitumen and Bituminous Binders - Determination of the Fraass Breaking Point’.
———. 2018d. ‘NF EN 12697-12 June 2018 - Bituminous Mixtures - Determination of the Water Sensitivity of Bituminous Specimens’.
Ahmed, Abubeker Worake, Safwat Fadhil Said, Xiaohu Lu, and Håkan Carlsson. 2019. ‘Pavement Performance Follow-up and Evaluation of Polymer-Modified Test Sections’. *International Journal of Pavement Engineering* 20 (12): 1474–87. https://doi.org/10.1080/10298436.2018.1435878.
Airey, G. D., B. Rahimzadeh, and C. Collop. 2003. ‘Viscoelastic Linearity Limits for Bituminous Materials’. *Mater. Struct.* 36 (264): 643–647. https://doi.org/10.1617/14081.
Airey, Gordon, Andrew Collop, and Raj Dongre. 2002. ‘Linear Viscoelastic Limits of Bituminous Binders’. *Association of Asphalt Paving Technology*.
Al-Humeidawi, Basim, Haider H. Aodah, and Kassim K. Hameed. 2016. ‘Evaluation of Moisture Damage and Stripping of Asphalt Concrete Prepared with New Additives of Polymer Modified Bitumen’. *Jornal of Babylon University* 24 (1).
Anderson, David A., Donald W. Christensen, Hussain U. Bahia, Raj Dongre, M. G. Sharma, and Charles. E. Antle. 1994. ‘SHRP-A-369 Binder Characterization and Evaluation. Volume 3: Physical Characterization’.
Apostolidis, Panos, Cor Kasbergen, Amit Bhasin, Athanassios Scarpas, and Sandra Erkens. 2018. ‘Study of Asphalt Binder Fatigue with a New Dynamic Shear Rheometer Geometry’. *Transportation Research Record: Journal of the Transportation Research Board* 2672 (28): 290–300. https://doi.org/10.1177/0361198118781378.
Arkles, Barry. 1977. ‘Tailoring Surfaces with Silanes’. In , edited by Chemtech. Chemtech.
———. 2011. *Hydrophobicity, Hydrophilicity and Silane Surface Modification (Gelest, Inc.)*.
Arrhenius, Svante. 1889. ‘Über Die Reaktionsgeschwindigkeit Bei Der Inversion von Rohzucker Durch Säuren [On the Reaction Velocity of the Inversion of Cane Sugar by Acids]’. *Zeitschrift Für Physikalische Chemie* 4: 226–48.
Aschenbrener, Tim. 1993. ‘Investigation of the Lottman Test to Predict the Stripping Performance of Pavements in Colorado’.
———. 1995a. ‘Evaluation of Hamburg Wheel-Tracking Device to Predict Moisture Damage in Hot-Mix Asphalt’. *Transportation Research Record* 1492.
———. 1995b. ‘Investigation of Low Temperature Thermal Cracking in Hot Mix Asphalt’. CDOT-DTD-R-95-7. FHWA.
Asphalt Institute, and Eurobitume. 2015. ‘The Bitumen Industry Third Edition’.
ASTM D3625. 2012. ‘ASTM D3625 Standard Practice for Effect of Water on Bituminous-Coated Aggregate Using Boiling Water’.

Azarhoosh, Alireza, Hossein Fallahi Abandansari, and Gholam Hossein Hamedi. 2019. 'Surface-Free Energy and Fatigue Performance of Hot-Mix Asphalt Modified with Nano Lime'. *Journal of Materials in Civil Engineering* 31 (9): 04019192. https://doi.org/10.1061/(ASCE)MT.1943-5533.0002836.

Baaj, H. 2003. 'Fatigue of Mixes: An Intrinsic Damage Approach'. In *Sixth International RILEM Symposium on Performance Testing and Evaluation of Bituminous Materials*, 394–400. Zurich, Switzerland: RILEM Publications SARL. https://doi.org/10.1617/2912143772.049.

Baaj, Hassan. 2002. 'Comportement à La Fatigue Des Matériaux Granulaires Traités Aux Liants Hydrocarbonés'. PhD Thesis, ENTPE.

Baaj, Hassan, Hervé Di Benedetto, and Pierre Chaverot. 2005. 'Effect of Binder Characteristics on Fatigue of Asphalt Pavement Using an Intrinsic Damage Approach'. *Road Materials and Pavement Design* 6 (2): 147–174. https://doi.org/10.1080/14680629.2005.9690003.

Babadopulos, Lucas. 2017. 'Phenomena Occuring during Cyclic Loading and Fatigue Tests on Bituminous Materials: Identification and Quantification'. Lyon: ENTPE, University of Lyon.

Babadopulos, Lucas F. de A. L., Cédric Sauzéat, and Hervé Di Benedetto. 2017. 'Softening and Local Self-Heating of Bituminous Mixtures during Cyclic Loading'. *Road Materials and Pavement Design* 18 (sup2): 164–77. https://doi.org/10.1080/14680629.2017.1304260.

Babadopulos, Lucas F. de A.L., Gabriel Orozco, Cédric Sauzéat, and Hervé Di Benedetto. 2019. 'Reversible Phenomena and Fatigue Damage during Cyclic Loading and Rest Periods on Bitumen'. *International Journal of Fatigue* 124 (July): 303–14. https://doi.org/10.1016/j.ijfatigue.2019.03.008.

Babadopulos, Lucas, Gabriel Orozco, Salvatore Mangiafico, Cédric Sauzéat, and Hervé Di Benedetto. 2019. 'Influence of Loading Amplitude on Viscoelastic Properties of Bitumen, Mastic and Bituminous Mixtures'. *Road Materials and Pavement Design* 20 (sup2): S780–96. https://doi.org/10.1080/14680629.2019.1628428.

Baldi-Sevilla, Alejandra, Mavis L. Montero, José P. Aguiar-Moya, Luis G. Loria-Salazar, and Amit Bhasin. 2017. 'Influence of Bitumen and Aggregate Polarity on Interfacial Adhesion'. *Road Materials and Pavement Design* 18 (sup2): 304–317. https://doi.org/10.1080/14680629.2017.1304265.

Barhamian, Anone. 2012. 'Evaluating Surface Energy of Asphalt Binders Using Wilhelmy Plate and Sessile Drop Techniques - Degree Project'.

Bari, Javed, and M. W. Witczak. 2006. 'Development of a New Revised Version of the Wtczak E* Predictive Model for Hot Mix Asphalt Mixtures'. *Journal of the Association of Asphalt Paving Technologists* 75.

Barnes, Howard A. 1997. 'Thixotropy—a Review'. *Journal of Non-Newtonian Fluid Mechanics* 70 (1–2): 1–33. https://doi.org/10.1016/S0377-0257(97)00004-9.

Basquin, O. H. 1910. 'The Exponential Law of Endurance Tests'. *American Society for Testing and Materials Proceedings* 10: 625–30.

Bazin, P., and J. Saunier. 1967. 'Deformability, Fatigue and Healing Properties of Asphalt Mixes'. In *Proceedings of the International Conference on the Structural Design of Asphalt Pavement*, 438–51.

Bhasin, Amit. 2006. 'Development of Methods to Quantify Bitumen-Aggregate Adhesion and Loss of Adhesion Due to Water'. Texas A&M University.

Bhasin, Amit, and Dallas N. Little. 2007. 'Characterization of Aggregate Surface Energy Using the Universal Sorption Device'. *Journal of Materials in Civil Engineering* 19 (8): 634–41. https://doi.org/10.1061/(ASCE)0899-1561(2007)19:8(634).

Bhasin, Amit, Eyad Masad, Dallas Little, and Robert Lytton. 2006. 'Limits on Adhesive Bond Energy for Improved Resistance of Hot-Mix Asphalt to Moisture Damage'. *Transportation Research Record* 1970 (1): 2–13. https://doi.org/10.1177/0361198106197000101.

Biot, M. A., and Shell Development Company. 1958. 'Linear Thermodynamics and the Mechanics of Solids'. In *Proceedings of the Third U. S. National Congress of Applied Mechanics, American Society of Mechanical Engineers*, 1–18.

Boëda, Eric, Jacques Connan, and Sultan Muhesen. 2002. 'Bitumen as Hafting Material on Middle Paleolithic Artifacts from the El Kowm Basin, Syria'. In *Neandertals and Modern Humans in Western Asia*, edited by Takeru Akazawa, Kenichi Aoki, and Ofer Bar-Yosef, 181–204. Boston: Kluwer Academic Publishers. https://doi.org/10.1007/0-306-47153-1_12.

Boulangé, Laurence, Estelle Bonin, and Michel Saubot. 2013. 'Physicochemical Characterisations of the Bitumen–Aggregate Interface to Get a Better Understanding of Stripping Phenomena'. *Road Materials and Pavement Design* 14 (2): 384–403. https://doi.org/10.1080/14680629.2013.803494.

Braham, A. F., and B. S. Underwood. 2016. *State of the Art and Practice in Fatigue Cracking and Evaluation of Asphalt Pavements*. Vol. Version 1.0. Lino Lakes, U.S.A.: Association of Asphalt Paving Technologists.

Braithwaite, F. 1854. 'ON THE FATIGUE AND CONSEQUENT FRACTURE OF METALS.' *Minutes of the Proceedings of the Institution of Civil Engineers* 13: 463–67. https://doi.org/10.1680/imotp.1854.23960.

Brennan, M. J., G Lohan, and J. M. Golden. 1990. 'A Laboratory Study of the Effect of Bitumen Content, Bitumen Grade, Nominal Aggregate Graging and Temperature on the Fatigue Performance of Dense Bitumen Macadam'. In *Proceedings of the IVth Internationl Rilem Symposium*, 358–66. Budapest, Hungary.

Brulé, B., Y. Brion, and A. Tanguy. 1988. 'Paving Asphalt Polymer Blends: Realationship between Composition, Structure and Properties'. *Asphalt Paving Technology* 57: 41–64.

Burmister, D. M. 1945. 'The General Theory of Stresses and Displacements in Layered Systems. I'. *Journal of Applied Physics* 16 (2): 89–94. https://doi.org/10.1063/1.1707558.

Canestrari, Francesco, Fabrizio Cardone, Andrea Graziani, Felice Ausilion Santagata, and Hussain U. Bahia. 2010. 'Adhesive and Cohesive Properties of Asphalt-Aggregate Systems Subjected to Moisture Damage'. *Road Materials and Pavement Design* 11 (Special issue 1): 11–32. https://doi.org/10.1080/14680629.2010.9690325.

Caro, S., E. Masad, A. Bhasin, and D. N. Little. 2008a. 'Moisture Susceptibility of Asphalt Mixtures, Part 1: Mechanisms'. *International Journal of Pavement Engineering* 9 (2): 81–98. https://doi.org/10.1080/10298430701792128.

———. 2008b. 'Moisture Susceptibility of Asphalt Mixtures, Part 2: Characterisation and Modelling'. *International Journal of Pavement Engineering* 9 (2): 99–114. https://doi.org/10.1080/10298430701792144.

Chaturabong, Preeda, and Hussain U. Bahia. 2018. 'Effect of Moisture on the Cohesion of Asphalt Mastics and Bonding with Surface of Aggregates'. *Road Materials and Pavement Design* 19 (3): 741–53. https://doi.org/10.1080/14680629.2016.1267659.

Christensen, D. W., and D. A. Anderson. 1992. 'Interpretation of Dynamic Mechanical Test Data'. *Journal of the Association of Asphalt Paving Technologists* 61.

Christensen, D. W., Terhi Pellinen, and Ramon Bonaquist. 2003. 'Hirsch Model for Estimating the Modulus of Asphalt Concrete'. In *Association of Asphalt Paving Technologists Proceedings of the Technical Sessions*, 72:97–121.

Christensen, Donald W., and Ramon Bonaquist. 2015. 'Improved Hirsch Model for Estimating the Modulus of Hot-Mix Asphalt'. *Road Materials and Pavement Design* 16 (sup2): 254–74. https://doi.org/10.1080/14680629.2015.1077635.

Christensen, R. M. 1982. *Theory of Viscoelasticity: An Introduction*. 2nd Edition. New York, U.S.A.: Academic Press Inc.

Clark, William G. 1971. 'Fracture Mechanics in Fatigue: Paper Presents a Review of the Current State of the Art of Fracture-Mechanics Approach to Fatigue'. *Experimental Mechanics* 11 (9): 421–28. https://doi.org/10.1007/BF02327647.

Claudy, P., J.M. Letoffe, G.N. King, and J-.P. Planche. 1992. 'Characterization of Asphalt Cements by Thermomicroscopy and Diffrential Scanning Calorimetry: Correlation to Classical Physical Properties'. *Fuel Science and Technology International* 10 (4–6): 735–65. https://doi.org/10.1080/08843759208916019.

Cole, K. S., and R. H. Cole. 1941. 'Dispersion and Absorption in Dieletrics Alternating Current Characteristics'. *Journal of Chemical Physics* 9: 341–51.

Collins, J.H., M.G. Bouldin, R. Gelles, and A. Berker. 1991. 'Improved Performance of Paving Asphalts by Polymer Modification'. *Asphalt Paving Technology* 60: 43–79.

Connan, Jacques, and Thomas Van de Velde. 2010. 'An Overview of Bitumen Trade in the Near East from the Neolithic (*c.* 8000 BC) to the Early Islamic Period'. *Arabian Archaeology and Epigraphy* 21 (1): 1–19. https://doi.org/10.1111/j.1600-0471.2009.00321.x.

Corté, Jean-François, and Hervé Di Benedetto. 2004. *Matériaux Routiers Bitumineux 1: Description et Propriétés Des Constituants*. Lavoisier. https://doi.org/10.3166/rcma.23.139-153.

cypraegean-neftegaz Ltd. 2020. 'Www.Cypraegean-Neftegaz.Com'. https://cypraegean-neftegaz.com/roads--bitumen.html.

Daniel, Jo Sias, and Y. R. Kim. 2002. 'Development of a Simplified Fatigue Test and Analysis Procedure Using a Viscoelastic, Continuum Damage Model (with Discussion)'. *Journal of the Association of Asphalt Paving Technologists* 71: 619–50.

De la Roche, Chantal. 1996. 'Module de Rigidité et Comportement En Fatigue Des Enrobés Bitumineux : Expérimentations et Nouvelles Perspectives d'analyses'. Châtenay-Malabry, France: Ecole Centrale de Paris.

De la Roche, Chantal, Fehrat Hammoum, Jean-Michel Piau, and Christian Stéfani. 2003. 'Comportement Du Bitumen En Film Mince Au Pseudo-Contact Entre Deux Granulats'. *Bulletin de Liaison Des Laboratoires Des Ponts et Chaussées*.

DeCarlo, Christopher, Eshan V. Dave, Jo E. Sias, Gordon Airey, and Rajib Mallick. 2020. 'Comparative Evaluation of Moisture Susceptibility Test Methods for Routine Usage in Asphalt Mixture Design'. *Journal of Testing and Evaluation* 48 (1): 20180908. https://doi.org/10.1520/JTE20180908.

Delaporte, Brice. 2007. 'Etude de La Rhéologie Des Mastics Bitumineux à l'aide d'un Rhéomètre à Cisaillement Annulaire'. PhD Thesis, ENTPE.

Delaporte, Brice, Hervé Di Benedetto, Pierre Chaverot, and Gilles Gauthier. 2007. 'Linear Viscoelastic Properties of Bituminous Materials: From Binders to Mastics'. *Journal of the Association of Asphalt Paving Technologists, Vol. 76, p. 455-494*.

Delorme, J. -L., C. de la Roche, and L. Wendling. 2007. 'LPC Bituminous Mixtures Design Guide'. Laboratoire Central des Ponts et Chaussées.

DeMonredon-Senani, Sophie. 2004. 'Interactions Organosilanes/Silice de Précipitation Du Milieu Hydro-Alcoolique Au Milieu Aqueux'. PhD Thesis, Université Pierre et Marie Curie Paris VI.

Di Benedetto, H., and C. de la Roche. 1998. 'State of the at of Stiffness Modulus and Fatigue of Bituminous Mixtures'. In *RILEM Report 17 - Bituminous Binders and Mixes: State of the Art and Interlaboratory Tests on Mechanical Behaviour and Mix Design*, Francken L., 137–80. London: E & FN Spon.

Di Benedetto, Hervé, and Jean-François Corté. 2005. *Matériaux Routiers Bitumineux 2: Constitution et Propriétés Thermomécaniques Des Mélanges*. Lavoisier.

Di Benedetto, Hervé, François Olard, Cédric Sauzéat, and Brice Delaporte. 2004. 'Linear Viscoelastic Behaviour of Bituminous Materials: From Binders to Mixes'. *Road Materials and Pavement Design* 5 (sup1): 163–202. https://doi.org/10.1080/14680629.2004.9689992.

Di Benedetto, Hervé, C. de La Roche, H. Baaj, A. Pronk, and R. Lundström. 2004. 'Fatigue of Bituminous Mixtures'. *Materials and Structures* 37 (3): 202–216. https://doi.org/10.1007/bf02481620.

Di Benedetto, Hervé, Ayasher Soltani, and Pierre Chaverot. 1996. 'Fatigue Damage for Bituminous Mixtures: A Pertinent Approach'. *Asphalt Paving Technology: Association of Asphalt Paving Technologists-Proceedings of the Technical Sessions* 65: 142–58.

Doan, T.H. 1977. 'Les Études de Fatigue Des Enrobés Bitumineux Au LCPC'. *Bulletin de Liaison Des Laboratoires Des Ponts et Chaussées* Numéro spécial V: 215–28.

Doubbaneh, Elias. 1995. 'Comportement Mécanique Des Enrobés Bitumineux Des "Petites" Aux "Grandes" Déformations'. Lyon: ENTPE-INSA Lyon.

Draper, Norman Richard, and Harry Smith. 1998. *Applied Regression Analysis*. 3rd ed. Wiley Series in Probability and Statistics. New York: Wiley.

Epps, J. A., and C. L. Monismith. 1969. 'Influence of Mixtures Variables on the Flexural Fatigue Properties of Asphalt Concrete'. *Journal of the Association of Asphalt Paving Technologists* 38: 423–58.

Ewing, J. A., and J. C. W. Humphrey. 1903. 'The Fracture of Metals under Repeated Alternations of Stress'. *Proceedings of the Royal Society of London* 71: 467–76. https://doi.org/10.1098/rspl.1902.0065.

Federal Highway Administration. 2014. 'Federal Highway Statistics'.

Forough, Seyed Arash, Fereidoon Moghadas Nejad, and Ali Khodaii. 2014. 'A Comparative Study of Temperature Shifting Techniques for Construction of Relaxation Modulus Master Curve of Asphalt Mixes'. *Construction and Building Materials* 53 (February): 74–82. https://doi.org/10.1016/j.conbuildmat.2013.11.060.

Fowkes, Frederick M. 1964. 'ATTRACTIVE FORCES AT INTERFACES'. *Industrial & Engineering Chemistry* 56 (12): 40–52. https://doi.org/10.1021/ie50660a008.

Freire, Reuber, Hervé Di Benedetto, Cédric Sauzéat, Simon Pouget, and Didier Lesueur. 2018. 'Linear Viscoelastic Behaviour of Geogrids Interface within Bituminous Mixtures'. *KSCE Journal of Civil Engineering* 22 (6): 2082–88. https://doi.org/10.1007/s12205-018-1696-9.

Gauthier, Gilles, Didier Bodin, Emmanuel Chailleux, and Thibaud Gallet. 2010. 'Non Linearity in Bituminous Materials during Cyclic Tests'. *Road Materials and Pavement Design* 11 (sup1): 379–410. https://doi.org/10.1080/14680629.2010.9690339.

Gayte, Pierre, Hervé Di Benedetto, Cédric Sauzéat, and Quang Tuan Nguyen. 2015. 'Influence of Transient Effects for Analysis of Complex Modulus Tests on Bituminous Mixtures'. *Road Materials and Pavement Design* 17 (2): 271–289. https://doi.org/10.1080/14680629.2015.1067246.

Gent, A. N., and P. B. Lindley. 1959. 'Internal Rupture of Bonded Rubber Cylinders in Tension'. *Proceedings of the Royal Society of London. Series A. Mathematical and Physical Sciences* 249 (1257): 195–205. https://doi.org/10.1098/rspa.1959.0016.

Glass, Nick R., Ricky Tjeung, Peggy Chan, Leslie Y. Yeo, and James R. Friend. 2011. 'Organosilane Deposition for Microfluidic Applications'. *Biomicrofluidics* 5 (3): 036501. https://doi.org/10.1063/1.3625605.

Griffith, A. A. 1921. 'VI. The Phenomena of Rupture and Flow in Solids'. *Philosophical Transactions of the Royal Society of London. Series A, Containing Papers of a Mathematical or Physical Character* 221 (582–593): 163–98. https://doi.org/10.1098/rsta.1921.0006.

Grönniger, Jens, Michael P. Wistuba, and Peter Renken. 2010. 'Adhesion in Bitumen-Aggregate-Systems: New Technique for Automated Interpretation of Rolling Bottle Tests'. *Road Materials and Pavement Design* 11 (4): 881–98. https://doi.org/10.1080/14680629.2010.9690311.

Hartman, A. M., and M. D. Gilchrist. 2004. 'Evaluating Four-Point Bend Fatigue of Asphalt Mix Using Image Analysis'. *Journal of Materials in Civil Engineering* 16 (1): 60–68. https://doi.org/10.1061/(ASCE)0899-1561(2004)16:1(60).

Harvey, John T., J. A. Deacon, B. -W. Tsai, and C. L. Monismith. 1995. 'Fatigue Performance of Asphalt Concrete Mixes and Its Relationship to Asphal Concrete Pavement Performance in California'. RAT-65W48-2. Asphalt Research Program. University of California, Berkeley, U.S.A: Institute of transportation Studies.

Harvey, John T., and Qing Lu. 2005. 'Investigation of Conditions for Moisture Damage in Asphalt Concrete and Appropriate Laboratory Test Methods'. Institute of Transporation Studies.

Harvey, John T., and Bor-Wen Tsai. 1996. 'Effects of Asphalt Content and Air Void Content on Mix Fatigue and Stiffness'. *Transportation Research Record: Journal of the Transportation Research Board* 1543 (1): 38–45. https://doi.org/10.1177/0361198196154300105.

Hefer, Arno, and Dallas Little. 2005. 'Adhesion in Bitumen-Aggregate Systems and Quantification of the Effects of Water on the Adhesive Bond'. International Center for Aggregate Research.

Hefer, Arno W., Amit Bhasin, and Dallas N. Little. 2006. 'Bitumen Surface Energy Characterization Using a Contact Angle Approach'. *Journal of Materials in Civil Engineering* 18 (6): 759–67. https://doi.org/10.1061/(ASCE)0899-1561(2006)18:6(759).

Hekeulom, W., and J. G. Klomp. 1964. 'Road Design and Dynamic Loading'. In *Proceedings of the Association of Asphalt Pavement Technologists*, 33:92–125.

Hertz, Heinrich. 1895. *Gesammelete Werke (Collected Works)*. Leipzig.

Hicks, R. G., and T. V. Scholz. 2003. 'Life Cycle Costs for Lime in Hot Mix Asphalt'. National Lime Association.

http://transporturbain.canalblog.com/. 2019. ‘Nancy : Du Trolleybus Au Tramway En Passant Par l’aventure TVR’. Blog. *Transporturbain* (blog). 2019. http://transporturbain.canalblog.com/.

Huet, C. 1963. *Etude Par Une Méthode d’impédance Du Comportement Viscoélastique Des Matériaux Hydrocarbonés*. Laboratoire Central des Ponts et Chaussées.

Islam, Md Rashadul, and Rafiqul A. Tarefder. 2015. ‘Coefficients of Thermal Contraction and Expansion of Asphalt Concrete in the Laboratory’. *Journal of Materials in Civil Engineering* 27 (11): 04015020. https://doi.org/10.1061/(ASCE)MT.1943-5533.0001277.

Jura, George, and William D. Harkins. 1944. ‘Surfaces of Solids. XI. Determination of the Decrease (π) of Free Surface Energy of a Solid by an Adsorbed Film’. *Journal of the American Chemical Society* 66 (8): 1356–62. https://doi.org/10.1021/ja01236a046.

Kachanov, L. M. 1958. ‘Time of the Rupture Process under Creep Conditions’. *Izvestiia Akademii Nauk SSSR* 8: 26–31.

———. 1986. *Introduction to Continuum Damage Mechanics*. Dordrecht: Springer Netherlands. http://public.ebookcentral.proquest.com/choice/publicfullrecord.aspx?p=3106040.

Khandal, P. S., C. Y. Lynn, and F. Parker Jr. 1998. ‘Charaterization Tests for Mineral Fillers Related to Performance of Asphalt Paving Mixtures’.

Kim, Y. Richard, and Dallas N. Little. 1990. ‘One-Dimensional Constitutive Modeling of Asphalt Concrete’. *Journal of Engineering Mechanics* 116 (4): 751–72. https://doi.org/10.1061/(ASCE)0733-9399(1990)116:4(751).

Kim, Yong-Rak, D. N. Little, and R. L. Lytton. 2003. ‘Fatigue and Healing Characterization of Asphalt Mixtures’. *Journal of Materials in Civil Engineering* 15 (1): 75–83. https://doi.org/10.1061/(ASCE)0899-1561(2003)15:1(75).

Kinloch. 1987. *Adhesion and Adhesives*. Springer Netherlands. https://doi.org/10.1007/978-94-015-7764-9.

Kok, Baha Vural, and Mehmet Yilmaz. 2009. ‘The Effects of Using Lime and Styrene–Butadiene–Styrene on Moisture Sensitivity Resistance of Hot Mix Asphalt’. *Construction and Building Materials* 23 (5): 1999–2006. https://doi.org/10.1016/j.conbuildmat.2008.08.019.

Krchma, L. C., and D. W. Gagle. 1974. ‘A U.S.A. History of Asphalt Refined from Crude Oil and Its Distribution’. In *Association of Asphalt Paving Technologists Proc*, 43A:25–88.

Kringos, N., and A. Scarpas. 2005. ‘Raveling of Asphaltic Mixes Due to Water Damage: Computational Identification of Controlling Parameters’. *Transportation Research Record: Journal of the Transportation Research Board* 1929 (1): 79–87. https://doi.org/10.1177/0361198105192900110.

Kringos, N., A. Scarpas, and C. Kasbergen. 2007. ‘Three Dimensional Elasto-Visco-Plastic Finite Element Model for Combined Physical-Mechanical Moisture Induced Damage in Asphaltic Mixes’. *Asphalt Paving Technology: Association of Asphalt Paving Technologists-Proceedings of the Technical Sessions* 76: 495–524.

Kriz, Pavel, Daniel L. Grant, Bibiana A. Veloza, Mary J. Gale, Alan G. Blahey, John H. Brownie, Ralph D. Shirts, and Sam Maccarrone. 2014. ‘Blending and Diffusion of Reclaimed Asphalt Pavement and Virgin Asphalt Binders’. *Road Materials and Pavement Design* 15 (sup1): 78–112. https://doi.org/10.1080/14680629.2014.927411.

Kriz, Pavel, Jiri Stastna, and Ludo Zanzotto. 2008. ‘Glass Transition and Phase Stability in Asphalt Binders’. *Road Materials and Pavement Design* 9 (sup1): 37–65. https://doi.org/10.1080/14680629.2008.9690158.

Lesueur, Didier. 2009. ‘The Colloidal Structure of Bitumen: Consequences on the Rheology and on the Mechanisms of Bitumen Modification’. *Advances in Colloid and Interface Science* 145 (1–2): 42–82. https://doi.org/10.1016/j.cis.2008.08.011.

Lesueur, Didier, Joëlle Petit, and Hans-Josef Ritter. 2013. ‘The Mechanisms of Hydrated Lime Modification of Asphalt Mixtures: A State-of-the-Art Review’. *Road Materials and Pavement Design* 14 (1): 1–16. https://doi.org/10.1080/14680629.2012.743669.

Lindsey, G., Richard Schapery, M. Williams, and A. Zak. 1963. ‘The Triaxial Tension Failure of Viscolestic Materials’.

Little, D. N., and D. Jones. 2003. ‘Chemical and Mechanical Mechanisms of Moisture Damage in Hot Mix Asphalts Pavements’. In . San Diego, U.S.A.

Little, D. N., R. L. Lytton, D. Williams, and C. W. Chen. 2001. 'Microdamage Healing in Asphalt Concrete. Volume 1: Microdamage and Microdamage Healing, Project Summary Report'. 7229. FHWA.

Little, Dallas N., and Amit Bhasin. 2007. 'Exploring Mechanism of H Ealing in Asphalt Mixtures and Quantifying Its Impact'. In *Self Healing Materials*, edited by Sybrand van der Zwaag, 100:205–18. Springer Series in Materials Science. Dordrecht: Springer Netherlands. https://doi.org/10.1007/978-1-4020-6250-6_10.

Lu, Qing, and John T. Harvey. 2006. 'Evaluation of Hamburg Wheel-Tracking Device Test with Laboratory and Field Performance Data'. *Transportation Research Record: Journal of the Transportation Research Board* 1970 (1): 25–44. https://doi.org/10.1177/0361198106197000103.

Lu, X., U. Isacsson, and J. Ekblad. 2003. 'Influence of Polymer Modification on Low Temperature Behaviour of Bituminous Binders and Mixtures'. *Materials and Structures* 36 (10): 652–56. https://doi.org/10.1007/BF02479497.

Lundström, Robert, and Ulf Isacsson. 2004. 'Linear Viscoelastic and Fatigue Characteristics of Styrene–Butadiene–Styrene Modified Asphalt Mixtures'. *Journal of Materials in Civil Engineering* 16 (6): 629–38. https://doi.org/10.1061/(ASCE)0899-1561(2004)16:6(629).

Luo, Rong, Derun Zhang, Zhe Zeng, and Robert L. Lytton. 2015. 'Effect of Surface Tension on the Measurement of Surface Energy Components of Asphalt Binders Using the Wilhelmy Plate Method'. *Construction and Building Materials* 98 (November): 900–909. https://doi.org/10.1016/j.conbuildmat.2015.08.125.

Lytton, R. L., E. Masad, C. Zollinger, R. Bulut, and D. N. Little. 2005. 'Measurements of Surface Energy and Its Relationship to Moisture Damage'. Texas Transportation Institute.

Mandel, J. 1955. 'Sur Les Corps Viscoélastiques à Comportement Linéaire'. In , 241:1910–12. Paris.

Mangiafico, S., L. F. A. L. Babadopulos, C. Sauzéat, and H. Di Benedetto. 2018. 'Nonlinearity of Bituminous Mixtures'. *Mechanics of Time-Dependent Materials* 22 (1): 29–49. https://doi.org/10.1007/s11043-017-9350-3.

Mangiafico, S., C. Sauzéat, Hervé Di Benedetto, S. Pouget, F. Olard, and L. Planque. 2015. 'Quantification of Biasing Effects during Fatigue Tests on Asphalt Mixes: Non-Linearity, Self-Heating and Thixotropy'. *Road Materials and Pavement Design* 16 (sup2): 73–99. https://doi.org/10.1080/14680629.2015.1077000.

Mangiafico, Salvatore. 2014. 'Linear Viscoelastic Properties and Fatigue of Bituminous Mixtures Produces with Reclaimed Asphalt Pavement and Corresponding Binder Blends'. PhD Thesis, ENTPE.

Masad, E., V. T. F. Castelo Branco, D. N. Little, and R. Lytton. 2008. 'A Unified Method for the Analysis of Controlled-Strain and Controlled-Stress Fatigue Testing'. *International Journal of Pavement Engineering* 9 (4): 233–46. https://doi.org/10.1080/10298430701551219.

Mazzoni, Giorgia, Arianna Stimilli, Fabrizio Cardone, and Francesco Canestrari. 2017. 'Fatigue, Self-Healing and Thixotropy of Bituminous Mastics Including Aged Modified Bitumens and Different Filler Contents'. *Construction and Building Materials* 131 (January): 496–502. https://doi.org/10.1016/j.conbuildmat.2016.11.093.

Mazzoni, Giorgia, Amedeo Virgili, and Francesco Canestrari. 2019. 'Influence of Different Fillers and SBS Modified Bituminous Blends on Fatigue, Self-Healing and Thixotropic Performance of Mastics'. *Road Materials and Pavement Design* 20 (3): 656–70. https://doi.org/10.1080/14680629.2017.1417150.

McCrum, N. G., C. P. Buckley, and C. B. Bucknall. 1997. *Principles of Polymer Engineering*. 2nd ed. Oxford ; New York: Oxford University Press.

McNally, Tony, ed. 2011. *Polymer Modified Bitumen: Properties and Characterisation*. Woodhead Publishing in Materials. Oxford ; Philadelphia: Woodhead Publishing Ltd.

Md. Yusoff, Nur Izzi, Damien Mounier, Ginoux Marc-Stéphane, Mohd. Rosli Hainin, Gordon D. Airey, and Hervé Di Benedetto. 2013. 'Modelling the Rheological Properties of Bituminous Binders Using the 2S2P1D Model'. *Construction and Building Materials* 38 (January): 395–406. https://doi.org/10.1016/j.conbuildmat.2012.08.038.

Mewis, Jan, and Norman J. Wagner. 2009. 'Thixotropy'. *Advances in Colloid and Interface Science* 147–148 (March): 214–227. https://doi.org/10.1016/j.cis.2008.09.005.

———. 2011. ‘Thixotropy’. In *Colloidal Suspension Rheology*, 228–51. Cambridge: Cambridge University Press. https://doi.org/10.1017/CBO9780511977978.

Miller, J. S., and W. Y. Bellinger. 2014. ‘Distress Identification Manual for the Long-Term Pavement Performance Program (Fifth Revised Edition)’. FHWA-HRT-13-092.

Min, Yahong, Ying Fang, Xiaojun Huang, Yinhui Zhu, Wensheng Li, Jianmin Yuan, Ligang Tan, Shuangyin Wang, and Zhenjun Wu. 2015. ‘Surface Modification of Basalt with Silane Coupling Agent on Asphalt Mixture Mosture Damage’. *Applied Surface Science* 346 (August): 497–502. https://doi.org/10.1016/j.apsusc.2015.04.002.

Miner, M. A. 1945. ‘Cumulative Damage in Fatigue’. *Journal of Applied Mechanics* 12: 159–64.

Moghadas Nejad, F., Gh. H. Hamedi, and A. R. Azarhoosh. 2013. ‘Use of Surface Free Energy Method to Evaluate Effect of Hydrate Lime on Moisture Damage in Hot-Mix Asphalt’. *Journal of Materials in Civil Engineering* 25 (8): 1119–26. https://doi.org/10.1061/(ASCE)MT.1943-5533.0000650.

Moreno-Navarro, Fernando, Gema García-Travé, María Del Carmen Rubio-Gámez, and Maria José Martinez-Echevarria. 2014. ‘Analysis of Th Moisture Susceptibility of Hot Bituminous Mixes Based on the Comparison of Laboratory Test Methods’. *DYNA* 81 (183): 49. https://doi.org/10.15446/dyna.v81n183.30893.

Mouillet, Virginie, Chantal De la Roche, Emmanuel Chailleux, and Philippe Coussot. 2012. ‘Thixotropic Behavior of Paving-Grade Bitumens under Dynamic Shear’. *Journal of Materials in Civil Engineering* 24 (1): 23–31. https://doi.org/10.1061/(ASCE)MT.1943-5533.0000354.

Moulder, John F., William F. Stickle, Peter E. Sobol, and Kenneth D. Bomben. 1992. *Handbook of X-Ray Photoelectron Spectroscopy*. Jill Chastain. Eden Prairie, Minnesota, U.S.A.: Perkin-Elmer Corporation.

Moutier, F. 1992. ‘Utilisation de La Presse à Cisaillement Giratoire et de l’orniérieur Dans La Méthode Française En Formulation Des Enrobés’. In *Proceedings of the 5th Eurobitume Congress*, 546–54. Stockholm, Sweden.

Murakami, Sumio. 2012. *Continuum Damage Mechanics*. Vol. 185. Solid Mechanics and Its Applications. Dordrecht: Springer Netherlands. https://doi.org/10.1007/978-94-007-2666-6.

Nguyen, M. D., F. Froiio, B. Cambou, H. Di Benedetto, and C. Sauzéat. 2016. ‘Simulation of the Asymptotic Behaviour of Bituminous Mixtures Using the Discrete Element Method’. In *8th RILEM International Conference on Mechanisms of Cracking and Debonding in Pavements*, edited by Armelle Chabot, William G. Buttlar, Eshan V. Dave, Christophe Petit, and Gabriele Tebaldi, 13:39–45. RILEM Bookseries. Dordrecht: Springer Netherlands. https://doi.org/10.1007/978-94-024-0867-6_6.

Nguyen, Quang Tuan. 2011. ‘Comportement Thermomechanique Des Enrobés Bitumineux Sous Sollicitations Cycliques Dans Les Domaines Linéaire et Non-Linéaire’. ENTPE.

Nguyen, Quang Tuan, Hervé Di Benedetto, and Cedric Sauzeat. 2014. ‘Linear Viscoelastic Domain for Bituminous Mixtures’. In *Pavement Materials, Structures, and Performance*, 59–68. Shanghai, China: American Society of Civil Engineers. https://doi.org/10.1061/9780784413418.007.

Nguyen, Quang Tuan, Hervé Di Benedetto, and Cédric Sauzéat. 2015. ‘Linear and Nonlinear Viscoelastic Behaviour of Bituminous Mixtures’. *Materials and Structures* 48 (7): 2339–51. https://doi.org/10.1617/s11527-014-0316-5.

Olard, François. 2012. ‘GB5 Mix Design: High-Performance and Cost-Effective Asphalt Concretes by Use of Gap-Graded Curves and SBS Modified Bitumens’. *Road Materials and Pavement Design* 13 (sup1): 234–59. https://doi.org/10.1080/14680629.2012.657074.

Olard, François, and Hervé Di Benedetto. 2003. ‘General 2S2P1D Model and Relation Between the Linear Viscoelastic Behaviours of Bituminous Binders and Mixes’. *Road Materials and Pavement Design* 4 (2): 185–224. https://doi.org/10.1080/14680629.2003.9689946.

Orozco, Gabriel. 2016. ‘Etude Du Comportement Thermomécanique d’un Bitume à l’aide d’un Rhéomètre à Isaaillement Annulaire’. Master Thesis, Nantes: Ecole Centrale de Nantes, Université de Nantes.

Orozco, Gabriel, Cédric Sauzéat, Jules Galipaud, and Hervé Di Benedetto. 2018. 'Modifying Surface Properties of Model and Pavement Aggregates with Silanes'. In *Poulikakos L., Cannone Falchetto A., Wistuba M., Hofko B., Porot L., Di Benedetto H. (Eds) RILEM 252-CMB-Symposium on Chemo Mechanical Characterization of Bituminous Materials*, 20:90–95. RILEM Bookseries.

Owens, D. K., and R. C. Wendt. 1969. 'Estimation of the Surface Free Energy of Polymers'. *Journal of Applied Polymer Science* 13 (8): 1741–47. https://doi.org/10.1002/app.1969.070130815.

Park, Sun Woo, Y. Richard Kim, and Richard A. Schapery. 1996. 'A Viscoelastic Continuum Damage Model and Its Application to Uniaxial Behavior of Asphalt Concrete'. *Mechanics of Materials* 24 (4): 241–55. https://doi.org/10.1016/S0167-6636(96)00042-7.

Park, S.W., and R.A. Schapery. 1999. 'Methods of Interconversion between Linear Viscoelastic Material Functions. Part I—a Numerical Method Based on Prony Series'. *International Journal of Solids and Structures* 36 (11): 1653–75. https://doi.org/10.1016/S0020-7683(98)00055-9.

Pell, P. S., and I. F. Taylor. 1962. 'Fatigue Characteristics of Bitumen and Bituminous Mixes'. In *Proceedings of the First International Conference on the Structural Design of Asphalt Pavements*. Ann Arbor, Michigan, U.S.A.

Pfeiffer, J. P., and P. M. Van Doormaal. 1936. 'The Rheological Properties of Asphaltic Bitumens'. *Journal of the Institute of Petroleum Technologists* 22: 414–40.

PIARC. 2019. 'Road Dictionary'. In . https://www.piarc.org/en/activities/Road-Dictionary-Terminology-Road-Transport.

Piau, J.M., and G. Rousset. 1983. 'Modélisation Thermomécanique Du Comportement Des Enrobés Bitumineux'. Palaiseau, France: Ecole Poylytechnique.

Planche, J. -P., D. A. Anderson, G. Gauthier, Y. M. Le Hir, and D. Martin. 2004. 'Evaluation of Fatigue Properties of Bituminous Binders'. *Materials and Structures* 37 (5): 356–59. https://doi.org/10.1007/BF02481683.

Plueddemann, Edwin P. 1991. *Silane Coupling Agents*. Springer US. https://doi.org/10.1007/978-1-4899-2070-6.

Pocius, Alphonsus V. 2012. *Adhesion and Adhesives Technology: An Introduction*. 3rd ed. Munich : Cincinnati: Hanser Publishers ; Hanser Publications.

Polacco, Giovanni, Sara Filippi, Filippo Merusi, and George Stastna. 2015. 'A Review of the Fundamentals of Polymer-Modified Asphalts: Asphalt/Polymer Interactions and Principles of Compatibility'. *Advances in Colloid and Interface Science* 224 (October): 72–112. https://doi.org/10.1016/j.cis.2015.07.010.

Pronk, A.C., and Rijkswaterstaat Dienst Weg-en Waterbouwkunde. 1995. *Evaluation of the Dissipated Energy Concept for the Interpretation of Fatigue Measurements in the Crack Initiation Phase*. P-DWW. https://books.google.fr/books?id=aDMbcgAACAAJ.

Qabur, Ali. 2018. 'Fatigue Characterization of Asphalt Mixes with Polymer Modified Asphalt Cement'. PhD Thesis.

Ramirez Cardona, Diego Alejandro, Simon Pouget, François Olard, and Hervé Di Benedetto. 2015. 'Viscoelastic Behaviour Characterization of a Gap-Graded Asphalt Mixture with SBS Polymer Modified Bitumen'. *Materials Research* 18 (2): 373–81. https://doi.org/10.1590/1516-1439.332214.

Randow, C. L., C. A. Williams, T. C. Ward, D. A. Dillard, J. G. Dillard, and J. P. Wightman. 1997. 'An Investigation of the Cling of Thin Polymeric Films'. *The Journal of Adhesion* 63 (4): 285–307. https://doi.org/10.1080/00218469708017224.

Rankine, W J M. 1843. 'ON THE CAUSES OF THE UNEXPECTED BREAKAGE OF THE JOURNALS OF RAILWAY AXLES; AND ON THE MEANS OF PREVENTING SUCH ACCIDENTS BY OBSERVING THE LAW OF CONTINUITY IN THEIR CONSTRUCTION.' *Minutes of the Proceedings of the Institution of Civil Engineers* 2: 105–7. https://doi.org/10.1680/imotp.1843.24600.

Read, John, and David Whiteoak. 2003. *The Shell Bitumen Handbook 5th Edition*. Thomas Telford.

Riara, Martin, Ping Tang, Liantong Mo, Barugahare Javilla, and Shaopeng Wu. 2018. 'Investigation into Crack Healing of Asphalt Mixtures Using Healing Agents'. *Construction and Building Materials* 161 (February): 45–52. https://doi.org/10.1016/j.conbuildmat.2017.11.074.

Riccardi, C., A. Cannone Falchetto, M. Losa, and P. Leandri. 2017. 'Estimation of the SHStS Transformation Parameter Based on Volumetric Composition'. *Construction and Building Materials* 157 (December): 244–52. https://doi.org/10.1016/j.conbuildmat.2017.09.083.

Rossi, Cesare Oliviero, Paolino Caputo, Noemi Baldino, Elisabeta Ildyko Szerb, and Bagdat Teltayev. 2017. 'Quantitative Evaluation of Organosilane-Based Adhesion Promoter Effect on Bitumen-Aggregate Bond by Contact Angle Test'. *International Journal of Adhesion and Adhesives* 72 (January): 117–122. https://doi.org/10.1016/j.ijadhadh.2016.10.015.

Rowe, G. M., G. Baumgardner, and M. J. Sharrock. 2008. 'A Generalized Logistic Function to Describe the Master Curve Stiffness Properties of Binder Mastics and Mixtures'. Presented at the 45th Petersen Asphalt Research Conference, Laramien Wyoming, U.S.A.

Rowe, Geoff. 1993. 'Performance of Asphalt Mixtures in the Trapezoidal Fatigue Test'. *Journal of the Association of Asphalt Paving Technologists* 62: 344–84.

Rowe, Geoffrey M. 2016. 'Vialit Cohesion and Cracking Performance'. In *Proceedings of 6th Eurasphalt & Eurobitume Congress*. Czech Technical University in Prague. https://doi.org/10.14311/EE.2016.216.

Salençon, Jean. 2009. *Viscoelasticité Pour Le Calcul Des Structures*. Palaiseau, France: Editions de l'Ecole Polytechnique.

Sayegh, G. 1965. 'Variation Des Modules de Quelques Bitumes Purs et Bétons Bitumineux'. PhD Thesis, Université de Paris.

Schapery, R. A. 1969. 'On the Characterization of Nonlinear Viscoelastic Materials'. *Polymer Engineering and Science* 9 (4): 295–310. https://doi.org/10.1002/pen.760090410.

———. 1975. 'A Theory of Crack Initiation and Growth in Viscoelastic Media: III. Analysis of Continuous Growth'. *International Journal of Fracture* 11 (4): 549–62. https://doi.org/10.1007/BF00116363.

———. 1987. 'Deformation and Fracture Characterization of Inelastic Composite Materials Using Potentials'. *Polymer Engineering and Science* 27 (1): 63–76. https://doi.org/10.1002/pen.760270110.

Schapery, Richard. 1966. 'A Theory of Nonlinear Thermoviscoelasticity Based on Irreversible Thermodynamics'.

———. 1981. 'On Viscoelastic Deformation and Failure Behavior of Composite Materials with Distributed Flaws'. In . Vol. AD-01.

Shan, Liyan, Yiqiu Tan, B. Shane Underwood, and Y. Richard Kim. 2011. 'Separation of Thixotropy from Fatigue Process of Asphalt Binder'. *Transportation Research Record: Journal of the Transportation Research Board* 2207 (1): 89–98. https://doi.org/10.3141/2207-12.

Shan, Liyan, Yiqiu Tan, Shane Underwood, and Y. Richard Kim. 2010. 'Application of Thixotropy to Analyze Fatigue and Healing Characteristics of Asphalt Binder'. *Transportation Research Record: Journal of the Transportation Research Board* 2179 (1): 85–92. https://doi.org/10.3141/2179-10.

SHRP. 1994. 'SHRP-A-379 The SUPERPAVE Mix Design System Manual of Specifications, Test Methods, and Practices'.

Singh, Bhupendra, and Praveen Kumar. 2019. 'Effect of Polymer Modification on the Ageing Properties of Asphalt Binders: Chemical and Morphological Investigation'. *Construction and Building Materials* 205 (April): 633–41. https://doi.org/10.1016/j.conbuildmat.2019.02.050.

Soenen, H., and B. Eckmann. 2000. 'Fatigue Testing of Bituminous Binders with a Dynamic Shear Rheometer'. In *Proceedings of the Papers Submitted for Review at the 2nd Eurasphalt and Eurobitume Congress*, 1:827–34. 1. Barcelona, Spain: Foundation Eurasphalt.

Soenen, Hilde, Chantal de La Roche, and Per Redelius. 2003. 'Fatigue Behaviour of Bituminous Materials: From Binders to Mixes'. *Road Materials and Pavement Design* 4 (1): 7–27. https://doi.org/10.1080/14680629.2003.9689938.

Soltani, Ayasher. 1998. 'Comportement En Fatigue Des Enrobés Bitumneux'. Lyon: INSA - ENTPE.

Somé, Cyrile, and Michel Saubot. 2015. 'Campagne EAPIC Série 14 - Détermination de La Sensibilité à l'eau d'un Enrobé Hydrocarboné'.

Stowe, Richard L. 1969. *Strength and Deformation Properties of Granite, Basalt, Limestone, and Tuff at Various Loading Rates*. Vol. 61. Waterways Experiment Station.

Sultana, Sharmin, Amit Bhasin, and Kenneth M. Liechti. 2014. 'Rate and Confinement Effects on the Tensile Strength of Asphalt Binder'. *Construction and Building Materials* 53 (February): 604–11. https://doi.org/10.1016/j.conbuildmat.2013.12.004.

Tapsoba, Nouffou. 2012. 'Comportement Des Enrobés Bitumineux à Partir de Matériaux Recyclés et/Ou Fabriqués à Température Réduite'. PhD Thesis, ENTPE.

Tucker, William Burns. 1938. 'Surface Tension by Pendant Drops'. Massachussets Institute of Technology.

Ugé, P., G. Gest, A. Gravois, and F. Bonnaure. 1977. 'Nouvelle Méthode de Calcul Du Module Complexe Des Mélanges Bitumineux'. *Bulletin de Liaison Des Laboratoires Des Ponts et Chaussées* Numéro spécial V: 199–213.

Underwood, B. Shane, Y. Richard Kim, and Murthy N. Guddati. 2010. 'Improved Calculation Method of Damage Parameter in Viscoelastic Continuum Damage Model'. *International Journal of Pavement Engineering* 11 (6): 459–76. https://doi.org/10.1080/10298430903398088.

Van Oss, Carel J., Manoj K. Chaudhury, and Robert J. Good. 1988. 'Interfacial Lifshitz-van Der Waals and Polar Interactions in Macroscopic Systems'. *Chemical Reviews* 88 (6): 927–941. https://doi.org/10.1021/cr00088a006.

Van Oss, Carel J., L. Ju, M. K. Chaudhury, and R. J. Good. 1989. 'Estimation of the Polar Parameters of the Surface Tension of Liquids by Contact Angle Measurements on Gels'. *Journal of Colloid and Interface Science* 128 (2): 313–319. https://doi.org/10.1016/0021-9797(89)90345-7.

Van Rompu, Julien, Hervé Di Benedetto, Maël Buannic, Thibault Gallet, and Carole Ruot. 2012. 'New Fatigue Test on Bituminous Binders: Experimental Results and Modeling'. *Construction and Building Materials* 37 (December): 197–208. https://doi.org/10.1016/j.conbuildmat.2012.02.099.

Vassaux, S., V. Gaudefroy, L. Boulangé, A. Pévère, V. Mouillet, and V. Barragan-Montero. 2017. 'Towards a Better Understanding of Wetting Regimes at the Interface Asphalt/Aggregate during Warm-Mix Process of Asphalt Mixtures'. *Construction and Building Materials* 133 (February): 182–195. https://doi.org/10.1016/j.conbuildmat.2016.12.015.

Vignard, N, D Bodin, E Chailleux, M Leguern, and C de La Roche. 2009. 'Fatigue Behaviour of Bitumen in Tension-Compression Loading Mode: Rheological Analysis and Comparison with Mix Fatigue'. In *Advanced Testing and Characterization of Bituminous Materials*, edited by Andreas Loizos, Manfred Partl, Tom Scarpas, and Imad Al-Qadi. CRC Press. https://doi.org/10.1201/9780203092989.ch74.

Wang, Di, Augusto Cannone Falchetto, Lily Poulikakos, Bernhard Hofko, and Laurent Porot. 2019. 'RILEM TC 252-CMB Report: Rheological Modeling of Asphalt Binder under Different Short and Long-Term Aging Temperatures'. *Materials and Structures* 52 (4): 73. https://doi.org/10.1617/s11527-019-1371-8.

Williams, M. L., R. F. Landel, and J. D. Ferry. 1955. 'The Temperature Dependence of Relaxation Mechanisms in Amorphous Polymers and the Glass-Forming Liquids'. *Journal of American Chemical Society* 77: 3701–7.

Witczak, M. W., and O. A. Fonseca. 1996. 'Revised Predictive Model for Dynamic (Complex) Modulus of Asphalt Mixtures'. *Transportation Research Record: Journal of the Transportation Research Board* 1540 (1): 15–23. https://doi.org/10.1177/0361198196154000103.

Wöhler, A. 1890. 'Über Die Festitigkeitversuche Mit Eisen Und Stahl'. *Zeitschrift Für Bauwesen* 20: 73–106.

Wool, R. P., and K. M. O'Connor. 1981. 'A Theory Crack Healing in Polymers'. *Journal of Applied Physics* 52 (10): 5953–63. https://doi.org/10.1063/1.328526.

Yildirim, Ismail. 2001. 'Surface Free Energy Characterization of Powders'. Blacksburg, Virginia: Faculty of the Virginia Polytechnic Institute and State University.

Yusoff, Md., Emmanuel Chailleux, and Gordon Airey. 2011. 'A Comparative Study Onf the Influence of Shitf Factor Equations on Master Curve Construction'. *Internation Journal of Pavement Research and Technology* 4.

Yusoff, Md., N. I. Monieur D., and Airey G. D. 2010. 'The 2S2P1D: An Excellent Linear Viscoelastic Model'. *Journal of Civil Engineering, Science and Technology* 1 (2): 1–7. https://doi.org/10.33736/jcest.76.2010.

Yusoff, N.I.Md., G.D. Airey, and M.R. Hainin. 2010. 'Predictability of Complex Modulus Using Rheological Models'. *Asian Journal of Scientific Research* 3 (1): 18–30. https://doi.org/10.3923/ajsr.2010.18.30.

Zaidi, Syed Bilal Ahmed, Gordon D. Airey, James Grenfell, Naveed Ahmad, and Imtiaz Ahmed. 2020. 'Moisture Susceptibility Assessment of Hydrated Lime Modified Asphalt Mixture and Surface Energy'. *International Journal of Pavement Engineering*, May, 1–13. https://doi.org/10.1080/10298436.2020.1763347.

Zhang, Feng, Jianying Yu, and Shaopeng Wu. 2010. 'Effect of Ageing on Rheological Properties of Storage-Stable SBS/Sulfur-Modified Asphalts'. *Journal of Hazardous Materials* 182 (1–3): 507–17. https://doi.org/10.1016/j.jhazmat.2010.06.061.

Zhang, Jizhe, Gordon D. Airey, James Grenfell, Alex K. Apeagyei, and Martyn Barrett. 2016. 'Development of a Composite Substrate Peel Test to Assess Moisture Sensitivity of Aggregate–Bitumen Bonds'. *International Journal of Adhesion and Adhesives* 68 (July): 133–41. https://doi.org/10.1016/j.ijadhadh.2016.02.013.

Zhang, Jizhe, Gordon D. Airey, and James R. A. Grenfell. 2015. 'Experimental Evaluation of Cohesive and Adhesive Bond Strength and Fracture Energy of Bitumen-Aggregates Systems'. *Materials and Structures* 49 (7): 2653–2667. https://doi.org/10.1617/s11527-015-0674-7.

Zofka, Adam, Maciej Maliszewski, and Alexander Bernier. 2014. 'Alternative Moisture Sensitivity Test'. In *9th ICEE Selected Papers*. Vilnius, Lithuania: Vilnius Gediminas Technical University Press Technika [etc. http://enviro.vgtu.lt/index.php/enviro2013/enviro9.